A 3-mm Imaging Line Survey of The Central Molecular Zones of M 82 and IC 342

Dissertation

zur

Erlangung des Doktorgrades (Dr. rer. nat.)

der

Mathematisch-Naturwissenschaftlichen Fakultät

der

Rheinischen Friedrich–Wilhelms–Universität Bonn

vorgelegt von

Céline Chidiac

aus

Achkout, Libanon

Bonn 2019

Angefertigt mit Genehmigung der Mathematisch-Naturwissenschaftlichen Fakultät der Rheinischen Friedrich–Wilhelms–Universität Bonn
Prepared with the permission from the Faculty of Mathematics and Natural Sciences of the University of Bonn

1. Gutachter: Prof. Dr. J. Anton Zensus

2. Gutachter: Prof. Dr. Frank Bertoldi

Tag der Promotion: 28. April 2020
Erscheinungsjahr: 2020

Diese Dissertation ist auf dem Publikationsserver der Universität Bonn mit der URN https://nbn-resolving.org/urn:nbn:de:hbz:5-58787 elektronisch publiziert.

The Astronomer

By Gibran KAHLIL GIBRAN

In the shadow of the temple my friend and I saw a blind man sitting alone.

And my friend said, “Behold the wisest man of our land.”

Then I left my friend and approached the blind man and greeted him.

And we conversed.

After a while I said, “Forgive my question; but since when has thou been blind?”

“From my birth,” he answered.

Said I, “And what path of wisdom followest thou?”

Said he, “I am an astronomer.”

Then he placed his hand upon his breast saying, “I watch all these suns and moons and stars.”

“The lights of stars that were extinguished ages ago still reach us. So it is with great men who died centuries ago, but still reach us with the radiations of their personalities.“

Gibran Khalil Gibran

Abstract

The central molecular zones of two nearby galaxies M 82 and IC 342 are among the most prominent extragalactic molecular sources in the northern hemisphere. While M 82 is a relatively small late type starburst galaxy, IC 342 is a spiral galaxy similar to the Milky Way in many respects, but seen face-on. While the two galaxies share many properties such as global molecular gas mass, H_2 column densities, and density of bulk gas, they differ in their star formation rates. In order to investigate how the star formation rate depends on the physical environments, conditions, and chemistries, the molecular content of the central molecular zones of M 82 and IC 342 has been studied, and different environmental conditions, e.g. shocks, hot cores, photo-dissociation regions were traced.

A spectral mapping survey targeting the central molecular zones of M 82 and IC 342 (with a spatial resolution of 43 and 50 pc for IC 342 and M 82 respectively), and covering almost the entire 3-mm range has been performed using the Plateau de Bure Interferometre, now known as NOrthern Extended Millimetre Array (NOEMA). This survey provides an inventory of the molecular content and distribution in the central molecular zones of these galaxies. Among the molecules observed are tracers of shocks, dense gas, and photodissociation regions, which in turn are tracers of ongoing high mass star formation.

In M 82, 15 molecular species were detected, in addition to three radio Hα recombination lines. In IC 342, 22 molecular species were detected. Most notably, SiO and HNCO (both shock tracers), CH_3CN, and CH_3OH were detected in IC 342 but not in M 82. The only complex molecule detected in M 82 is CH_3CCH, which is believed to be a tracer of photo-dissociative radiation. In general, the abundance of molecules relative to $C^{18}O$ are higher in M 82 than they are in IC 342. The column densities observed in this study were compared to chemical models in order to relate the physical and chemical conditions of the molecular clouds. The chemical models show that the central molecular zone in M 82 and IC 342 have a cosmic-ray ionisation rate 5000 times higher than the local standard value, with a visual extinction of $\sim$50 mag. For a better understanding of the spatial distribution of the molecules, a principal component analysis has been applied to the data, thus associating, different chemical tracers with different physical locations in the galaxies. The principal component analysis showed a strong correlation between HCN and HCO^+, and between CCH and HCN in M 82. In IC 342, a strong correlation between HCN and HCO^+, and between $C^{18}O$ and ^{13}CO was observed. Moreover, the principal component maps showed that in IC 342, dense gas traced by HCN and HCO^+ is more concentrated in the centre of IC 342, while shocks (traced by HNCO) are more dominant on the outer sides of the central molecular zones of the galaxy.

The results showed that in M 82, the gas is affected by photo-dissociation regions and emission from massive stars, as traced by Hα lines. The detection of N_2H^+ in M 82 indicates the presence of a quiescent gas with a visual extinction higher than 20 mag, that can act as gas reservoir and fuel future star formation. On the other hand, in IC 342, shocks (traced by SiO and HNCO) are dominating the heating processes, thus halting the star formation.

Acknowledgements

The journey of my doctoral studies has been very rewarding, albeit being challenging and demanding. Now that I am at its end, the intellectual and personal reward it granted me helped shape the person I am today, and will accompany me for the years to come. However, this journey would not have been possible without the help, support, and encouragement of the many people I have met along the way. First and foremost, I would like to thank Prof. Dr. J. Anton Zensus, for giving me the opportunity to be a member of his distinguished team for so many years, and allowing me to be part of a group that is leading advancement in science. It has been an honour working with, and along side many members of the group. I am grateful for the opportunities I got to attend conferences, astronomy schools, and observatories, that were crucial for my studies.

A sincere and special thanks to my PhD supervisor Priv. Doz. Dr. Rainer Mauersberger who accompanied me day-to-day through this journey. He has been very patient, helpful, and inspiring, always sharpening my scientific and critical thinking skills. For his continuous support and help, I am very grateful. A special thanks go to Dr. Christian Henkel, who gave me insights and great advices in order to get the most and best out my project. The feedback he has given me after repeatedly reading my thesis, was very valuable and important.

This journey would have been a lot more challenging without the help of Dr. Rebecca Aladro Fernández, and Dr. Denise E. Riqueleme Vásquez who answered a lot of questions, helped with a lot of programmes and interpretations, and gave me a support that helped me push through the rocky parts of the journey. I would like to thank them sincerely for their support and help. I also like to thank Prof. Dr. Serena Viti for her help in comparing my data with her chemical models. Another special thanks goes to Dr. Sergio Martín Ruiz, who supervised my work, and welcomed me in his office in Chile for two months, and for ESO who financed my stay there. The help Dr. Martín has given me, gave my project the boost it needed, made many tasks easier, and helped me get more robust results. He has answered too many questions, he has helped me too many times, even when he had scarcely any time. Without this help, this journey would have been a lot longer and more challenging that it needs to be.

I would also like to thank Prof. Dr. Frank Bertoldi, for kindly agreeing to be the second referee of my thesis. Furthermore, I would like to thank Prof. Dr. Klaus Desch and Prof. Dr. med. Rainer Schalnus for joining the PhD examination committee.

I would like to offer my deepest gratitude to the International Max-Planck Research School for Astronomy and Astrophysics (IMPRS) for supporting me through this journey, ensuring a great working environment, and offering a supporting community.

This entire journey would not have been possible, without my parents and my family. My parents have believed in me, encouraged me, and supported me, in more ways than I can count, not only throughout my PhD journey, but also throughout the very long journey I started when I left Lebanon and came to Germany to pursue my studies. Their prayers, help, sacrifices, and encouragement, made even the hardest part of this journey seem easy. I owe them everything I am today, and for that I am eternally grateful.

Last but not least, I would like to say thanks to my best friend, my rock, and my husband, Jeffrey Kevin Kotula, who made me laugh even through the most difficult parts of this journey. He has helped me in many steps along the way, in so many ways. He has stood by me when things were tough and never let me give up. His love and support gave me the motivation, courage, strength, and the will I needed to finish this journey. Thank you for everything.

Contents

Chapter 1

Introduction

1.1 Context

The basic stages of star formation are thought to be understood, at least in general terms. Imaging of star formation regions and the theoretical modelling of star formation have witnessed important breakthroughs in recent years. For instance, advances have been made in understanding the formation of binary stars using the Smoothed Particles Hydrodynamics (SPH) numerical method (Bate 2000; Lomax et al. 2015; Sigalotti et al. 2018; Riaz et al. 2018 and van der Plas et al. 2019), and the detailed structure of many molecular clouds where star formation takes place (Williams and Viti 2005) is now better known. Important details of the process, however, remain unclear such as the formation of low mass stars from both a theoretical and observational perspective, the dependence of star formation on the initial mass functions and other initial conditions of the clouds where the stars form, and the lower and upper mass cut-offs of the initial mass function, the role of the collapsing cloud environment (radiation fields, winds, ...), the influence of recent high-mass star formation on the ongoing star formation, or the role that metallicity plays in the star forming process (e.g. Wu et al. 2019). The formation of pre-stellar cores and their abundances, the role of turbulence, magnetic fields, gravity, kinematics, and pressure in the formation of molecular clouds are still not fully understood (Liu et al. 2018). The details of the bimodal star formation (that is, low mass stars form due to cloud collapse, while high mass stars may either form through cloud collapse, or due to competitive accretion of gas in a very dense interstellar medium), and the details of mass accumulation for high mass star formation are still unclear (Yuan et al. 2018).

Since star formation is still ongoing (Yusef-Zadeh et al. 2017), maybe even accelerating in molecular clouds (Palla and Stahler 2002; Lee et al. 2015 and Caldwell and Chang 2018) and is closely correlated with galaxy evolution (Larson 1996), understanding the mechanisms driving the star forming process is crucial to comprehend galaxy formation and evolution, as well as the chemical composition of the interstellar medium. Advances in technology and observational facilities promise high resolution data and advanced analysis software that help reveal more details about the mechanisms and processes of star formation.

For instance, the Atacama Large Millimetre/sub-millimetre Array (ALMA)[1] allows to observe detailed images of star forming regions and gas clouds with high resolution and sensitivity obser-

---

[1] http://www.almaobservatory.org/

vations of the molecular gas and dust, which are the main components of star formation (Aalto 2015; Favre et al. 2016; Yusef-Zadeh et al. 2017; Scoville et al. 2017 and Cyganowski et al. 2017). With the Atacama Pathfinder EXperiment (APEX)[2], one can study cold dust, and gas in galaxies, trace thermal continuum emission and analyse spectral lines at high radio and sub/-millimetre frequencies. This allows for a better understanding of the chemistry and structure of individual star forming regions, as well as, on much larger scales, of galaxies undergoing star formation (Leurini et al. 2019). The NASA/DLR Stratospheric Observatory for Infrared Astronomy(SOFIA) (Heyminck et al. 2012 and Temi et al. 2014) allows for high-resolution spectroscopy and diffraction-limited imaging, since it observes above 99% of the atmospheric water vapour of the Earth, enabling thus the detailed study of the interstellar medium (ISM), the magnetic fields in star forming regions, and probing the chemistry and evolution of proto-planetary disks in the THz regime (Röllig et al. 2009).

One approach to study star formation is to investigate the chemical content of the central molecular zones (CMZs) in galaxies. The star formation rate (SFR) is a good indicator of a galaxy's degree of activity with respect to star formation. Understanding the dense CMZs in the centre of galaxies is crucial, as they play an important role in the molecular chemical evolution of the galaxies and can underline different physical processes. These CMZs can fuel massive star formation and AGN activity, and therefore are catalyst of their host galaxy's evolution (Izumi et al. 2016). Moreover, it is important to investigate the chemical composition of the CMZs, as it can shed light on the chemical evolution that the host galaxy underwent, as a result of different heating sources from star formation regions, AGN, shocks, and other mechanical and radiative processes (Izumi et al. 2016).

The nearby galaxies M 82 (D=3.53 ± 0.26 Mpc, Karachentsev and Kashibadze 2006) and IC 342 (D=3.28 ± 0.27 Mpc, Karachentsev and Kashibadze 2006) are among the most prominent and prototypical molecular lighthouses in the northern hemisphere. M 82 is a late type spiral SBc galaxy (spiral barred (SB) galaxy with c as arm tightness; Mayya et al. 2005), in a late starburst stage, seen edge-on (with an inclination of 80°, de Vaucouleurs et al. 1991). On the other hand, IC 342 (also known as Cadwell 5) is an intermediate spiral galaxy of type SAB(rs)cd, that is, it is classified between unbarred and barred, and between ringed and spindle, with an arm tightness between c and d (de Vaucouleurs et al. 1976). IC 342 is therefore a spiral galaxy resembling the Milky Way, seen face-on, rendering it easier to study its nuclear region than that of the Milky Way (MW).

Moreover, the three galaxies (M 82, IC 342, and the Milky Way) share many characteristics, such as gas mass, gas temperature, gas density, and the fact that the gas temperature is well in excess of the dust temperature (Mauersberger et al. 1986, 2003 and Ao et al. 2013).

Further studies revealed stronger similarities between IC 342 and the Milky Way: Sakamoto et al. 1999 showed that giant molecular clouds in the bar of IC 342 have similar linear sizes as the Sgr A and Sgr B2 molecular clouds in the centre of the Milky Way and Meier (2014) summarised the many similarities between IC 342 and the Milky Way, such as ionising photon rate, X-ray luminosity, and mass of the largest CMZ in the galaxies.

However, despite all their similarities, the SFR in M 82 is significantly higher than those in IC 342 and the Milky Way. In an attempt to understand the difference in SFR, to explore the highly efficient star formation in M 82, and to study the nuclear region of IC 342, this work maps the CMZs of M 82 and IC 342 in almost the entire 3-mm range in molecules and the continuum using the Plateau de Bure Interferometre (PdBI), now known as NOrthern Extended Millimetre Array (NOEMA) in the French Alps. The observations are backed by chemical abundance models with

---

[2] http://www.apex-telescope.org/

different excitation conditions and distinct physical environments such as photo-dissociation regions (PDRs), very dense gas with different metallicities and cosmic ray (CR) fluxes (using the models presented by Viti 2017). Since the different stages of star formation leave different chemical fingerprints, different environmental conditions such as shocks, hot cores, quiescent gas, and PDRs can be traced. Tracers of shocks, hot cores, photon-, CR-, or X-ray dominated regions show clues of physical mechanisms affecting the gas. Chemical abundance maps will be related to the physical environment. The spatial distributions of transitions will be compared to chemical models and other tracers of star formation. Different kinds of chemistry will be related to morphological and kinematical features to explain the nature of the giant molecular clouds and the gas influenced by their orbital environment. To ease this task, a Principle Component Analysis (PCA) will be applied. Detection of isotopologues such as $H^{12}CO^+$ and $H^{13}CO^+$ can be potentially used as a tracer for the isotopic abundance ratio. The isotopic ratios of secondary to primary isotopes provide clues to the gas metallicity and the influence of massive versus low mass stellar ejecta, which helps constraining the origin of the gas. The CMZ sources of the Milky Way can be used as a template for the extragalactic studies (Turner 1989 and van der Wiel et al. 2009).

1.2 Objectives

An unbiased imaging survey that covers almost the entire 3-mm spectral window and includes the central molecular zones is still missing for extragalactic objects like M 82 and IC 342. Previous studies performed line surveys targeting solely selected molecular transitions. Moreover, a high resolution line survey that resolves the innermost few hundred parsec of a galaxy has not been done so far. Studies such as Meier and Turner (2005); Martín et al. (2010) and Aladro et al. (2011b) have targeted specific molecules in M 82 and IC 342. Molecular line surveys, such as presented by Aladro et al. (2011a) and Aladro et al. (2015) have used data obtained by a single-dish telescope, which lacks spatial resolution.

The data used in this work is the first high resolution survey covering the 3-mm range and targeting the innermost few 100 pc of the M 82 and IC 342 CMZs. This survey offers an unbiased spatially resolved inventory of the molecular contents of these galaxies.

The molecular content of the galaxies will help find reliable indicators of PDRs that are a strong tracers of star formation regions. Moreover, finding reliable indicators of shocks, and cosmic ray dominated regions (CR-regions) can shed light on the physical activity in the central molecular zones. The application of the statistical method Principal Component Analysis (PCA), the association of different chemistries to different physical locations in the galaxies will facilitate the understanding of the chemical distribution within the central molecular zones, and its relation to physical boundary conditions and star formation.

Chapter 2

Physical and Mathematical Concepts

In this chapter, some fundamental physical and mathematical concepts relevant for this thesis will be outlined. Section 2.1 will discuss in general terms the interstellar medium (ISM) and the different heating mechanisms. Section 2.1.5 will discuss briefly the central molecular zones of galaxies, the CMZs. Section 2.2 will explain temperatures and thermodynamical equilibrium. Radiative transfer will be presented in Section 2.3. The basic concept of radio interferometry and its application will be laid out in Section 2.4. Finally, in Section 2.5, the principal component analysis and its application in this study will be briefly described in this chapter.

2.1 The Interstellar Medium

The interstellar medium (ISM) has many phases ranging from the hot ionised diffuse gas where temperatures are higher than 10^5 K and densities $\sim 4 \times 10^{-3}\,\mathrm{cm}^{-3}$ to the cold dense molecular gas where temperatures are between 10 and 50 K and the densities reach $10^3 - 10^6\,\mathrm{cm}^{-3}$(Draine 2011). This leads to different chemical states of the matter in ISM: radiation and high temperatures can lead to hot ionised atomic gas, while colder and denser clouds allow for molecule formation. These phases are dynamic and heavily influenced by the different physical processes that take place in the ISM. For instance, strong UV radiation from hot stars can ionise the surrounding gas. On the other hand, line and continuum emission can cool a hot gas to temperatures low enough to allow the formation of molecules.

While it is possible to observe each phase of the ISM separately for the Galactic ISM, this becomes a challenge for extragalactic sources. The reason is that even for nearby galaxies, single-dish mm-telescopes such as the IRAM 30-m telescope have a spatial resolution of several hundred pc. This makes interferometric observations necessary in order to disentangle the different phases and to resolve giant molecular clouds. For example, the 3-mm observations toward two nearby galaxies in this study, result in a spatial resolution of $\sim$ 50 pc, comparable to the size of the giant molecular clouds. As targets, two galaxies were chosen that are similar in many respects but have radically different star formation rates: M 82 and IC 342.

M 82 is a known late-type starburst galaxy where H II regions traced by hydrogen recombination lines were detected, and IC 342 is a galaxy that resembles the Milky Way but seen face-on. The star formation rate in M 82 is significantly higher than in IC 342 and the Milky Way, despite the fact that these three galaxies share many similarities (see Chapter 1.1). Interferometric observations with high spatial resolution ($\sim$ 50 pc) allow for the detailed studies of the central molecular zones in these galaxies and can highlight signature chemistries of the different stages of a starburst. By tracing the different phases of the ISM and their physical processes, such as shocks, ionising and dissociating radiation, one can reveal clues of physical mechanisms affecting the gas. In the following subsections, those phases and processes, that will become essential to the understanding of results presented in this thesis, will be described.

2.1.1 H II Regions

The formation of hot massive stars can significantly alter the chemistry of the parent molecular cloud. Young massive stars emit FUV radiation capable of ionising hydrogen, and irradiating the molecular cloud with electrons. The H II regions are then formed, emitting a free-free continuum emission observable at radio wavelengths (Draine 2011). After being ionised in H II regions, a certain percentage of ionised hydrogen (H^+) recombines with electrons to form a new neutral hydrogen atom. In an H II region, there is a certain equilibrium between H I and H II. This electron in the newly formed neutral hydrogen atom, can be at any energy level, but then cascades to the ground state ($n = 1$). As it cascades, the electron will emit photons at each transition. These regions are therefore characterised by strong emission of hydrogen recombination lines (eg. Hα). If the newly formed neutral atom emits a photon causing its electron to fall from energy level $n + 1$ to energy level n ($\Delta n = 1$), the transition is then known as the H$n\alpha$ line. For instance, the H41α line is emitted when the electron of the hydrogen atom falls from the energy level $n+1$ =42 to the energy level n =41. The Hα recombination lines are often used as tracers of ionised hydrogen regions, and thus, regions of massive star formation.

2.1.2 Molecular Clouds

In the Milky Way, the interstellar medium has a mass ranging between 10-15 % of the total mass of the disk (Ferrière 2001). Hydrogen accounts for $\sim$ 70 % of the mass of the ISM, helium accounts for $\sim$ 28 %, while metals (elements heavier than He) account for the remaining $\sim$ 2 % of the ISM mass (Ferrière 2001). In the Milky Way, molecular hydrogen (H_2) has a mass of $(1.0 \pm 0.3) \times 10^9\,M_\odot$ (Heyer and Dame 2015), while atomic hydrogen (H I) has a mass of $2.5 \times 10^9\,M_\odot$ (Nakanishi and Sofue 2003).
The densest regions of the ISM, molecular clouds, mainly consist of H_2 molecules and He atoms. For molecular clouds to form, the gas should be dense enough to allow for self-shielding from UV-photons that can dissociate molecules. In gas with roughly solar metallicities, the threshold column density for the molecular phase to set in, is $N(H_2) = 5 \times 10^{20}\,\mathrm{cm}^{-2}$ (Stecher and Williams 1967; Hollenbach et al. 1971 and Federman et al. 1979). Interstellar H_2 was first detected in FUV by Carruthers (1970) in absorption towards diffuse interstellar gas. Since H_2 is a symmetrical molecule, it lacks a permanent electric dipole moment, therefore dipole transitions between rotation levels are forbidden. Quadrupole transitions (e.g. J=2-0) can be observed in the IR. Due to the low moment of inertia of H_2, J=2 is at 500 K above ground level. Such quadrupole transitions can be observed towards very warm gas (Snell et al. 2019). This make H_2 hard to detect in cold molecular clouds (Dame et al. 2001). Therefore, most of the molecular cloud mass evades direct astronomical detection, in the cold environment of the molecular clouds. Observable tracers such as molecules with an electric dipole moment are instead used. Dust emission in the mm and sub-mm range, or dust extinction are used to trace molecular clouds at shorter wavelength, mostly in IR but also at mm/sub-mm wavelengths. The most commonly used H_2 tracer is CO, as it is the molecule with the highest relative abundance in the ISM after H_2 (the fractional abundance of CO relative to H_2 is (1.4-2.5)$\times 10^{-4}$, Heyer and Dame 2015).

It also possesses a permanent dipole moment, unlike H_2, and it is much heavier than molecular hydrogen, and therefore, its rotational transitions can be observed at accessible frequencies in the mm- and sub-mm range.

Star are formed in molecular clouds. One can classify molecular clouds in different categories, depending on their visual extinctions A_v (visual extinction can be related to the column density of hydrogen: $\frac{N_{\mathrm{H}}}{A_v} \approx 1.8 \times 10^{21} \mathrm{cm}^{-2}\,\mathrm{mag}^{-1}$, Reina and Tarenghi 1973) by the dust they contain, which can widely vary from 1 mag $< A_v$ to $A_v \gtrsim 100\,\mathrm{mag}$ (Draine 2011 Chapter 32, and references therein). Star formation usually occurs in Star-forming Clumps with typical sizes between 0.1 and 2 pc, densities $N_{\mathrm{H}} \sim 10^3 - 10^5\,\mathrm{cm}^{-3}$, and masses ranges from 10 to $10^3\,\mathrm{M}_\odot$ (Klessen 2011). These clumps, where water molecules (H_2O) and other ices can be found on the surface of dust grains[1], are dark, dense, and gravitationally bound (Draine 2011 Chapter 1).

2.1.3 Photodissociation Regions (PDRs)

Massive stars emit strong far ultra-violet (FUV) radiation (6 eV $< h\nu < 13.6$ eV, Hollenbach and Tielens 1997) that can dissociate and ionise the surrounding gas. This photo-ionised gas has temperatures that can reach 10^4 K (Draine 2011), and can become highly-pressurised, resulting in a compressive wave that might cause the flow of the ionised gas from the high pressure regions into regions with lower pressure (Draine 2011). Photodissociation regions (PDRs) are defined as the interface between the ionisation front of the H II region and the dense molecular cloud, where molecules can be effectively dissociated by radiation.

Figure 2.1 shows the propagation of the UV-radiation through the ISM. High-mass O/B stars emit strong UV-radiation. In the near vicinity of such stars, the UV-radiation reaches energies higher than 13.6 eV, and is thus ionising hydrogen atoms. These regions are called H II regions. The ionisation front is defined as the region where half of the hydrogen is ionised (Draine 2011). After the ionisation front, ionised Hydrogen (H^+) and other atoms recombine with electrons to form atomic hydrogen, however molecules cannot be formed since they would be rapidly dissociated by radiation. This region is therefore called the Photo-Dissociation Region (PDR). The ionisation front does not sharply divide the H II regions from the PDR. The ionisation front can advance with a velocity v_{IF}, and the overlap between the ionisation front and the PDR forms a region where the Lyman continuum photons are absorbed[2]. Photons with energies lower than 13.6 eV (FUV-photons) continue their propagation into the PDR. The low-energy FUV-radiation of the PDR cannot ionise Hydrogen, but can dissociate molecular hydrogen into atomic hydrogen, and can ionise heavier elements such as carbon (Goicoechea et al. 2016). A strong FUV flux will also prevent ionised carbon (C^+) and O from forming CO. However, polycyclic aromatic hydrocarbon (PAH) can form, and they emit strong mid-IR emission (Goicoechea et al. 2016).

The dissociation front, which is not sharply defined, separates a PDR from a region where molecules can exist, and is rich in C^+. After the dissociation front, H starts forming molecular hydrogen. This is known as the H/H_2 transition zone. In this zone, observations show a peak in the H_2^* vibrational transition (Goicoechea et al. 2016). It is also in this zone, that HCO^+ emission becomes intense (Goicoechea et al. 2016). After the H/H_2 transition zones, occurs the C^+/CO transition zone, since C has a lower ionisation energy. Assuming a FUV radiation that is irradiating the cloud uniformly from one direction, the FUV flux will be attenuated by dust

---

[1] Interstellar dust is composed of small solid particles of mainly carbon, silicon, and oxygen, magnesium, sulfur, and iron, with a size smaller than 1 μm (Chlewicki and Mayo Greenberg 1984; Li and Greenberg 1997).

[2] Lyman continuum photons are photons emitted from stars with an energy higher than the Lyman limit which is given in terms of wavelength as 912 Å, or in terms of photon energy as 13.6 eV.

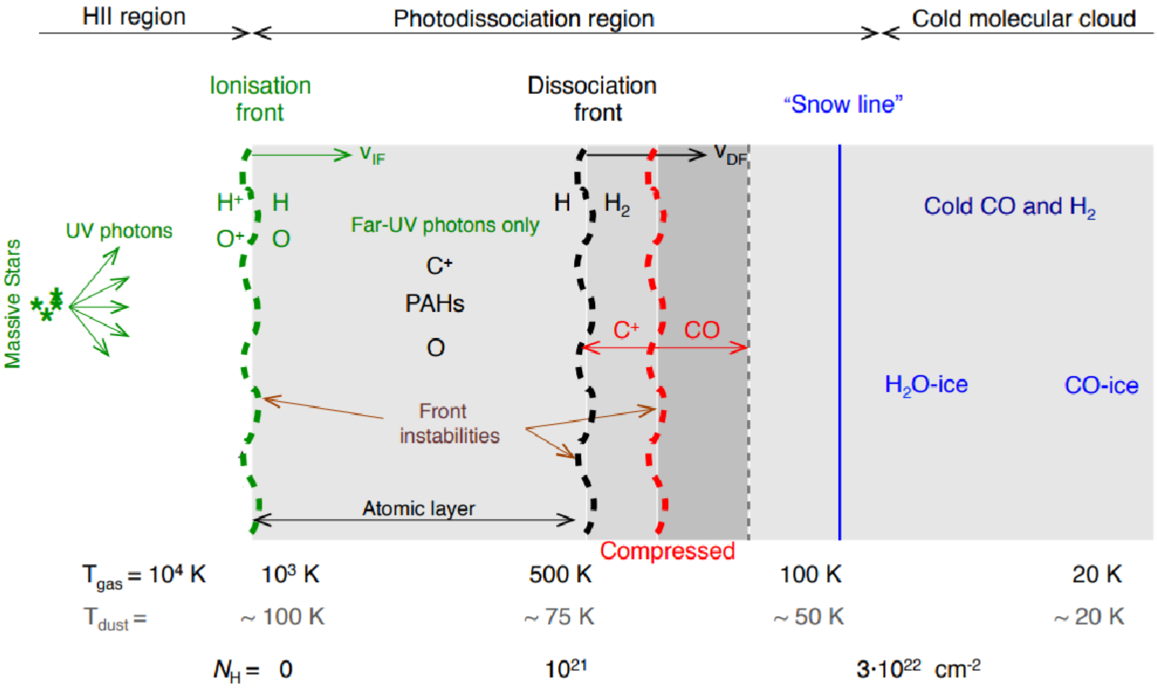

Figure 2.1: Diagram representing the structure of a PDR between the H II region and the molecular cloud (Goicoechea et al. 2016).

absorption and scattering as it propagates further into the cloud. Therefore, the ISM after the dissociation front is cold, and the photo-dissociation rate decreases. Thus, after the C^+/CO transition zones, starting from the snow line where the dust temperature drops to 50 K, the molecules start to freeze onto dust surfaces. With temperature reaching ~ 20 K, the molecular clouds are relatively cold and dense ($n_{\rm H} = 3 \times 10^{22}\,{\rm cm}^{-2}$), allowing for the formation of ice grains, such as H_2O and CO.

2.1.4 Shocks

In the interstellar medium, phenomena such as strong stellar winds, cloud collisions, novae and supernovae explosions, spiral density waves, expanding H II regions, jets and outflows from star forming regions, cause a pressure-driven turbulence in the ISM that propagates with speeds higher than those of compressive waves, and increases the entropy of the medium, thus causing irreversible changes in the surrounding cloud. This turbulence results in shocks. Shocks are common in the interstellar medium, and have a strong effect on the chemistry and the evolution of the molecular clouds, and they are closely related to the evolution of a galaxy as well.

The effects of a shock on the interstellar medium depends strongly on the speed of that shock, the temperature of the post-shock gas, and on the presence of a magnetic field. The speed of a shock is defined relative to the speed of sound in the medium where the shock is propagating. The speed of sound in an isothermal ideal gas depends solely on the temperature and the mean molecular weight of the gas and is given as:

$$\text{Speed of sound :} \quad c_s = \sqrt{\gamma \frac{P}{\rho}} = \sqrt{\gamma \frac{k_B T}{\mu}} \tag{2.1}$$

$$\text{Ideal gas equation of state :} \quad P = \frac{\rho k_B T}{\mu} \tag{2.2}$$

where P and T are the gas pressure and temperature respectively, ρ is the density of the gas, k_B is the Boltzmann constant given as $1.38 \times 10^{-16}\,\mathrm{cm^2\,g\,s^{-2}\,K^{-1}}$, and μ is the mean molecular weight (Tielens 2005). For an atomic gas, the mean molecular weight is usually assumed to be $\mu = 1.5 \times m_H$; for molecular gas, a value of $\mu = 2.7 \times m_\mathrm{H}$ is usually used, and for a fully ionised gas, the mean molecular weight is $\mu = 0.7 \times m_\mathrm{H}$. The specific heat ratio γ is expressed as function of constant pressure (c_P) and constant volume (c_V): $\gamma = \frac{c_P}{c_V}$. For mono-atomic gas, γ is given as $\frac{5}{3}$, and for di-atomic gas, $\gamma = \frac{7}{5}$. The Mach number $M = \frac{v}{c_s}$ is the ratio of the speed of the shock (v) to the speed of sound in a medium (c_s) (Tielens 2005).

There are two broad types of shocks: the jump shocks (J-shocks) that are fast shocks causing sharp changes in density, temperature, and velocity of the medium where they occur, and the continuous shocks (C-shocks), that are shocks which allow for a continuous change without sharp changes of the characteristics of the medium. The main difference between the two types of shock lies in the velocity and temperature of these shocks, where the J-shocks have higher velocities and temperature than the C-shocks (Tielens 2005).

J-shocks

When a shock has a high velocity that will cause a sharp change in the temperature, velocity and pressure of the cloud, these changes are called a jump. Jump shocks (J-shocks), thus alter the properties of the cloud. J-shocks are fast shocks with $M \gg 1$. Assuming the gas in which the J-shocks propagate is atomic ($\gamma = \frac{5}{3}$), the gas velocity will increase to $\frac{3}{4} v_s$ (v_s is the shock velocity), the temperature will be proportional to $\frac{3}{16} v_s^2$, and the gas density will increase by a factor of 4, leading to a compressed gas (Tielens 2005). The J-shocks have a velocity that is higher than $40 - 50\,\mathrm{km\,s^{-1}}$ (Hollenbach and McKee 1989; Tielens 2005). The shocks can dissociate and ionise the gas, but will also lead to molecule formation in the zones behind the shock. The chemistry of these zones depends on the post-shock temperatures. If the post-shock temperature is less than 10^4 K, H_2 is not dissociated. However, reactions with O are possible, leading to the formation of H_2O (Tielens 2005). Other abundant molecules under such conditions are CO, H_2, O_2, CH^+, SiO, and H_2S (Tielens 2005). However, for post-shock temperatures higher than 10^4 K, with shock velocities higher than $50\,\mathrm{km\,s^{-1}}$, molecular hydrogen (H_2) dissociates, and the gas becomes predominantly atomic (Draine and McKee 1993; Tielens 2005).

The emitted radiation of these shocks depends on their velocity. The temperature of the gas directly behind the shock front depends on the velocity of the shock, where $T(\mathrm{K}) \propto 10^5 \left(\frac{v_s}{100\,\mathrm{km\,s^{-1}}}\right)^2$ (Tielens 2005). Ionising shocks with velocities higher than $50\,\mathrm{km\,s^{-1}}$ cause post-shocks temperature to reach 10^6 K. Such high temperatures lead to bright X-ray emissions. Slower non-dissociating shocks lead to UV and optical emission. This UV-radiation results in photo-dissociation and photo-ionisation in the cloud. After the photo-ionisation of hydrogen in these clouds, optical recombination lines are observed in the post-shock gas. Moreover, for temperatures lower than 5000 K, fine-structure line emission of neutral hydrogen and other ions can be observed, as well as rotational emission at IR and radio frequencies from molecules formed due to the shock (Tielens 2005).

The UV-radiation caused by shocks can be distinguished from the UV-radiation of PDRs by the resulting chemistry. In shocked regions, one can detect strong lines from low-excitation species. For instance, in the optical regime, the line intensities of [S II]$\lambda 6717$, and [O I]$\lambda 6300$ are much higher relative to the optical Hβ line (Tielens 2005). In ionisation regions of shocks, one can also detect [Fe II] lines, and high ratios of $\frac{\text{[Fe II]}1.644\mu\text{m}}{\text{Br}\gamma 2.166\mu\text{m}}$. In the IR-regime, one can distinguish between shocks and PDR regions, by the lack of PAH emission that is typical for PDRs (Tielens 2005). Moreover, the ratio $\frac{\text{[O I]}\lambda 63\mu\text{m}}{\text{[C II]}\lambda 158\mu\text{m}}$ is much lower in PDRs than it is in shock regions (Hollenbach and McKee 1989).

C-shocks

In strongly magnetised clouds, C-shocks occur. The magneto-sonic waves (longitudinal waves propagating in a magnetised plasma perpendicular to the magnetic field), have a velocity of:

$$v_{ms} = \sqrt{c_s^2 + v_A^2} \tag{2.3}$$

where v_A is the Alfvén speed defined as $v_A = \frac{B}{\sqrt{4\pi\rho}}$ (B is the magnetic field strength, and ρ is the density of the gas). The speed of the magneto-sonic wave is significantly higher than the speed of sound c_s. Therefore, it is possible for a supersonic wave to propagate at speeds lower than the magneto-sonic wave speed. There is then, a wide range of shock velocities that are slower than magneto-sonic waves. The magneto-sonic waves can then travel ahead of the shock wave, "preparing" the cloud for the incoming shock, causing a continuous change in the cloud properties, hence the name, continuous-shock or C-shock. These shocks are colder than the J-shocks, have a maximum velocity of $40\,\text{km}\,\text{s}^{-1}$ (Tielens 2005), but are still able to partially dissociate some molecules. Other molecules such as H_2O, and OH are formed abundantly. In regions where the post-shock temperature increases, and O is abundant, reactions with OH, and CH^+ take place, and the formation of CH_3OH, and SiO in gas phase becomes enhanced (Jiménez-Serra et al. 2008). C-shock regions can be observed at IR and radio wavelengths. One detects strong fine-structure line emission such as [O I] at 63, and 146 μm, [C I] at 370, and 610 μm, and [S I] at 25 μm. Via molecular rotational lines one can detect molecules such as CH_3OH, SiO, HNCO, and H_2O (eg. Jiménez-Serra et al. 2008). In C-shocks, ion abundance is low, therefore one can use the detection of hydrogen recombination lines, and fine-structure line emission of Ne II at 12.8 μm, Si II at 35 μm, and Fe II at 26-36 μmm as indicators of a C-shock chemistry (Hollenbach and McKee 1989).

2.1.5 Central Molecular Zones of Galaxies

In the Milky Way, the central molecular zone (CMZ) is defined as a region of particularly strong molecular emission located within a radius of 200 pc from the centre of the Galaxy (Morris and Serabyn 1996). This zone is characterised by high densities ($n_{\text{H}_2} \gtrsim 10^4\,\text{cm}^{-3}$), where molecular hydrogen H_2 contributes a mass of $1.9 \times 10^7\,\text{M}_\odot$, while atomic hydrogen (H I) contributes a mass of only $1.6 \times 10^6\,\text{M}_\odot$ (Ferrière et al. 2007). The CMZ in the Milky Way has a projected size of 500×300 pc (Ferrière et al. 2007), and has a total molecular gas mass of $\sim 3 \times 10^7\,\text{M}_\odot$ (Dahmen et al. 1998). Within this CMZ, many dense and massive molecular clouds are detected (eg. Sgr A, B, C, D, E), filament-shaped clouds, and dust-lanes (Bally et al. 1988 and Morris and Serabyn 1996). Among others, molecules such as SiO, HCO^+, and $H^{13}CO^+$ are wide-spread in the CMZ of the Milky Way (Riquelme et al. 2010), while the molecular cloud Sgr B2 is possibly the richest molecular source of the entire sky (e.g. Belloche et al. 2013).

In other galaxies, such as M 82, IC 342, and NGC 253 similar molecular regions have been identified, bearing similar characteristics in mass, density, and chemical composition to the CMZ in the Milky Way (eg. Meier and Turner 2005; Martín et al. 2010; Aladro et al. 2011b,a; Meier 2014; Aladro et al. 2015 and Ginard et al. 2015). Therefore, these regions have also been called central molecular zones (CMZs). These CMZs are of high interest, in particularly those even more active than the CMZ of the Milky Way. The CMZs in M 82 and IC 342 will be the focus of this thesis and the work presented here.

2.2 Thermodynamical Equilibrium and Temperatures

2.2.1 Temperatures and Local Thermodynamic Equilibrium (LTE)

Assuming the existence of a population of particles with a number of atoms N_a that has an energy of E_a, with a statistical weight g_a and another population of particles with a number of atoms N_b that has an energy of E_b, with a statistical weight g_b, the excitation temperature T_{ex} between two levels defines the temperature at which one can expect to find this population ratio in a given system. This temperature is described by the Boltzmann equation (where k is the Boltzmann constant):

$$\frac{N_b}{N_a} = \frac{g_b}{g_a} e^{-\frac{(E_b - E_a)}{kT_{\text{ex}}}} \tag{2.4}$$

Under the extreme conditions of the interstellar medium, the level populations can be described by a single temperature, only in rare cases. Depending on the nature of the involved levels, one speak of e.g. rotational temperature T_{rot}. T_{rot} can be calculated using eq. 2.4 where the statistical weights are given as $2J{+}1$ (J is the rotational quantum number).
For a certain frequency, the spectral radiance B_ν can be described by the Planck function:

$$B_\nu = \frac{2h\nu^3}{c^2(e^{\frac{h\nu}{kT}} - 1)} \tag{2.5}$$

where $h = 6.626 \times 10^{-34}\,\text{J s}$ is the Planck's constant. Since in radio astronomy, the frequencies observed are usually low, one often applies the Rayleigh-Jeans approximation $h\nu \ll kT$, and equation 2.5 becomes:

$$B_\nu = \frac{2k\nu^2 T}{c^2} \tag{2.6}$$

The brightness temperature is defined as the temperature at which at a certain frequency, a source can emit a radiation intensity of I_ν. Therefore, substituting T for the **brightness temperature** T_B, one obtains:

$$I_\nu = B_\nu(T_B) = \frac{2k\nu^2 T_B}{c^2} \tag{2.7}$$

Thermodynamical equilibrium occurs when all processes can be described by a single temperature, that is, all the temperatures are the same:

$$T = T_{\text{ex}} = T_{\text{kin}} = T_B \tag{2.8}$$

Even though, thermodynamical equilibrium is rarely observed in the interstellar medium, one can assume that equilibrium occurs locally, in regions where the difference in temperatures is small enough. In other terms, if the mean free path[3] of the particles and photons (distance travelled between collisions) is significantly smaller than the distance required for the temperature to change remarkably or smaller than the scales at which energy exchange with the surrounding environment occurs, local thermodynamical equilibrium (LTE) is assumed.

2.2.2 Einstein Coefficients

In its most simple form, thermodynamical equlibrium is assumed when a process (e.g. emission) occurs at the same rate as its inverse process (e.g. absorption). Assuming that a photon is passing near a particle, be it an atom or a molecule, one can infer an interaction between the photon and the particle (interaction between matter and radiation). These interactions will then result in transitions between two energy levels of the particle, the lower energy level E_l and the upper energy level E_u, with statistical weights g_u and g_l for the upper and the lower level respectively. There are three forms of such transitions:

- **Spontaneous emission:** A particle can get spontaneously de-excited from an upper level (u) to a lower level (l). A photon is then emitted, with an energy of $E = h\nu_{ul}$, where ν_{ul} is the frequency of the emitted photon. The probability of such a spontaneous photon emission is then described by the Einstein coefficient of spontaneous emission A_{ul} and is given in units of s^{-1}. Therefore a particle in the upper level u has a lifetime of $t = \frac{1}{A_{ul}}$ in seconds. After the emission, the population in the upper and lower level will change. Assuming a density of n_u for the upper level, the contribution of spontaneous emission to the changes in the population levels is given by $n_u A_{ul}$.

- **Stimulated emission:** The de-excitation of a particle can occur because of an incident photon that has interacted with a particle, causing the emission of a photon from an upper to a lower level. This is the result of incoming radiation that is affecting the particle. The probability for a stimulated emission is proportional to the Einstein coefficient of stimulated emission B_{ul} in units of $\mathrm{erg}^{-1}\,\mathrm{cm}^2\,\mathrm{sr}\,\mathrm{Hz}$. The photon emitted through this de-excitation has an energy of $E = h\nu_{ul}$, where ν_{ul} is its frequency. Like in the case of a spontaneous emission, the population in the different levels will change. This change is affected by the intensity of the radiation field I. The contribution of stimulated emission to the population exchange is given as $n_u B_{ul} I_\nu$.

- **Absorption:** Much like in the case of the stimulated emission, a radiation field can cause a particle to absorb a photon with a frequency of ν_{ul}, and thus an energy $E = h\nu_{ul}$. This photon will then excite a particle from the lower level l to the upper level u. The Einstein coefficient of absorption B_{lu} in units of $\mathrm{erg}^{-1}\,\mathrm{cm}^2\,\mathrm{sr}\,\mathrm{Hz}$ describes such a process. The contribution of absorption to the change in the population in the different energy levels is then given by $n_l B_{lu} I_\nu$.

In order to achieve equilibrium, emission processes should happen at the same rate as absorption. Therefore, thermodynamical equilibrium is fulfilled when $n_u A_{ul} + n_u B_{ul} I_\nu = n B_{lu} I_\nu$ or $n_u A_{ul} = (n_l B_{lu} - n_u B_{ul}) I_\nu$. This condition can be written as:

---

[3] The mean free path is the average distance travelled between 2 collisions and is defined as: $l = \frac{1}{n\sigma}$ where n is the number density of atoms, $\sigma = 4\pi a^2$ is the collision cross section of an atom and a its radius. It is also defined as $l = \frac{1}{\kappa_\nu \rho}$ where κ_v is the frequency-dependent opacity of a medium and ρ its density.

$$I_\nu = \frac{A_{ul}}{\frac{n_l}{n_u}B_{lu} - B_{ul}} \tag{2.9}$$

Moreover, the Boltzmann equation (eq. 2.4) describes the ratio of the populations of two different levels $\frac{n_u}{n_l}$. Therefore, $\frac{n_l}{n_u}$ is then given as $\frac{g_l}{g_u}e^{-\frac{h\nu}{kT}}$, with T representing the excitation and, in case of local thermodynamic equilibrium, also the kinetic temperature. Furthermore, the intensity is described by the Planck Law (eq. 2.5). Thus, eq. 2.9 will be written as:

$$I_\nu = \frac{A_{ul}}{\frac{g_l}{g_u}e^{-\frac{h\nu}{kT}}B_{lu} - B_{ul}} = \frac{2h\nu^3}{c^2(e^{\frac{h\nu}{kT}} - 1)} \tag{2.10}$$

If equation 2.10 holds, this then implies that:

$$\begin{aligned} g_l B_{lu} &= g_u B_{ul} \\ A_{ul} &= \frac{2h\nu^3}{c^2} B_{ul} \end{aligned} \tag{2.11}$$

2.2.3 Line Thermalisation, Column Density and Critical densities

Under the Rayleigh-Jeans approximation, the observed brightness temperature T_{Line} of a molecular emission or absorption line is given as a function of the background temperature T_{bg} ($T_{bg} = T_{CMB} + T_s$, where $T_{CMB} = 2.73\,\mathrm{K}$ is the cosmic microwave background temperature, and T_s is the temperature of a possible background continuum source), excitation temperature T_{ex} and optical depth τ. In cases where the observed molecular cloud and the background sources do not fill the telescope beam, beam filling factors of the emitting gas (f_{cl}), and of the background sources (f_{bg}), should be introduced. Moreover, one should take into account the fraction of the background source that is covered by the observed cloud (f_{frac}) (Wilson et al. 2012). In those cases, the observed line temperature is:

$$T_{Line} = (f_{cl}T_{ex} - f_{frac}f_{bg}T_{bg})(1 - e^{-\tau_\nu}) \tag{2.12}$$

From the observed radiation temperature, one can calculate the column density of molecules in level u, as a function of the Einstein coefficient of spontaneous emission A_{ul} and the frequency of the line (ν_{ul}), and by converting from frequency to velocity units through $d\nu = \frac{\nu}{c}dv$:

$$N_u = \frac{8\pi k\nu_{ul}^2}{A_{ul}hc^3}\int T_{Line}dv \tag{2.13}$$

In order to derive the total column density of the observed molecule, one needs the partition function which, for an energy E_i of the level i and a degeneracy g_i, is given as:

$$Z = \sum_{i=1}^{\infty} g_i e^{-\frac{E_i}{kT}} \tag{2.14}$$

Using the partition function, one can then obtain the total column density of the molecular species (Wilson et al. 2012):

$$N_{\text{molecule}} = \frac{ZN_u}{g_u}e^{\frac{E_u}{KT_{rot}}} \tag{2.15}$$

The relative abundance of a molecular species is defined as:

$$X_{\text{molecule}} = \frac{N_{\text{molecule}}}{N_{\text{H}_2}} \tag{2.16}$$

The critical density (n_{crit}) is defined as the density at which collisional de-excitation (with a collision coefficient of C_{ul}) and radiative de-excitation (described by the Einstein coefficient of spontaneous emission A_{ul}) are equally important in populating energy levels in a gas. It is defined as (Tielens 2005):

$$n_{crit} = \frac{A_{ul}}{C_{ul}} \tag{2.17}$$

If the density of the gas increases to values considerably higher than the critical density n_{crit}, collisions would dominate the population of energy levels, and the excitation temperature would approach the kinetic temperature, and LTE can hold. At such densities, the molecular line is thermalised. If the density of the gas is lower than the critical density, radiation dominates the population of energy levels.

2.3 Radiative Transfer

As a ray of light propagates, emission and absorption processes change its intensity. This increase in intensity dI_ν is related to the wavelength of the photons, and the distance ds they travelled. Assuming that only spontaneous emission processes occur, while absorption and scattering processes are suppressed, the increase in intensity can be described as:

$$dI_\nu = j_\nu ds \tag{2.18}$$

The emissivity of the gas at a given frequency (ν), j_ν, is given in units of power per unit volume per unit frequency per unit solid angle

$$j_\nu = \frac{1}{4\pi} n_u A_{ul} h\nu\phi_\nu \tag{2.19}$$

where ϕ_ν describes the probability that the photon emitted has a frequency between ν and $\nu + d\nu$. However, one definitely needs to take processes such as absorption and scattering into account, as they influence changes in the intensity. Equation 2.20 describes the decrease in intensity due to absorption and stimulated emission:

$$dI_\nu = -\kappa_\nu I_\nu ds \tag{2.20}$$

The real increase in intensity is obtained by combining eq. 2.20 and eq. 2.18:

$$dI_\nu = -\kappa_\nu I_\nu ds + j_\nu ds \tag{2.21}$$

where κ_ν is the attenuation coefficient at a given frequency (ν), and has a dimension of (length)$^{-1}$. Therefore, the rate and the manner at which the intensity of a beam of photons changes depend strongly on the rate at which emission and absorption processes are occurring.

One can describe the changes in the intensity independently from κ_ν (and therefore from length), by using the optical depth (τ_ν) of a medium, described as $d\tau_\nu \equiv \kappa_\nu ds$. In the case where the emission is optically thin ($\tau \ll 1$), radiation will experience little absorption along its path. However, if the emission is optically thick ($\tau \gg 1$), the radiation will be partially or highly absorbed. Moreover, one can define the **source function** as $S_\nu \equiv \frac{j_\nu}{\kappa_\nu}$. Thus, the radiative transfer equation can now be written as:

$$dI_\nu = -I_\nu d\tau_\nu + S_\nu d\tau_\nu \tag{2.22}$$

In order to solve this equation, one can rewrite eq. 2.22 as:

$$e^{\tau_\nu}(dI_\nu + I_\nu d\tau_\nu) = e^{\tau_\nu}(S_\nu d\tau_\nu) \tag{2.23}$$

The first part of the equation is simply the derivative of $e^{\tau_\nu} I_\nu$, and therefore, one can write:

$$d(e^{\tau_\nu} I_\nu) = e^{\tau_\nu}(S_\nu d\tau_\nu) \tag{2.24}$$

The integration goes from $\tau_\nu = 0$ to τ_ν, where $I_\nu(0)$ is the initial value for $\tau_\nu = 0$:

$$[e^{\tau_\nu} I_\nu]_0^{\tau_\nu} = \int_0^{\tau_\nu} e^{\tau_\nu'}(S_\nu d\tau_\nu') \tag{2.25}$$

$$[e^{\tau_\nu} I_\nu - I_\nu(0)] = \int_0^{\tau_\nu} e^{\tau_\nu'}(S_\nu d\tau_\nu') \tag{2.26}$$

Now, one can multiply both sides of the equations by $e^{-\tau_\nu}$, and assume that the source function S_ν is a constant:

$$[e^{\tau_\nu} I_\nu - I_\nu(0)]\, e^{-\tau_\nu} = \int_0^{\tau_\nu} e^{\tau_\nu'} e^{-\tau_\nu}(S_\nu d\tau_\nu') \tag{2.27}$$

$$[e^{\tau_\nu} I_\nu - I_\nu(0)]\, e^{-\tau_\nu} = \int_0^{\tau_\nu} e^{\tau_\nu' - \tau_\nu}(S_\nu d\tau_\nu') \tag{2.28}$$

$$I_\nu - I_\nu(0)e^{-\tau_\nu} = \left[S_\nu e^{(\tau_\nu' - \tau_\nu)}\right]_0^{\tau_\nu} \tag{2.29}$$

$$I_\nu - I_\nu(0)e^{-\tau_\nu} = S_\nu(1 - e^{-\tau_\nu}) \tag{2.30}$$

The solution for the radiative transfer is given as:

$$I_\nu = I_\nu(0)e^{-\tau_\nu} + S_\nu(1 - e^{-\tau_\nu}) \tag{2.31}$$

2.4 Radio interferometry

Radio astronomy opened up the observation of the cold universe, which is obscured at other wavelengths, and widened the observable wavelengths range of Earth-bound observatories. In this section, a broad introduction to radio astronomy and interferometry will be presented, with a summary of how radio interferometers work, their advantages, and short-comings. For more details about radio astronomy, and radio interferometers, please refer to Wilson et al. (2012).

2.4.1 Advantages and Challenges of Radio Astronomy

Radio astronomy offers many advantages and new diagnostic tools with respect, to optical astronomy, to the field of astrophysics. It allows for observations in daytime, as well as nights, and greatly expands the range of observable wavelengths. Since the atmosphere does not block radio waves, Earth-bound telescopes can detect radiation from 15 MHz, up to 1.5 THz (Wilson et al. 2012). Of course, one has to account for water vapour (particularly at 22.2, and 183 GHz) and O_2 (at 65 GHz) in the atmosphere, as they can absorb some of the incoming radio radiation (Wilson et al. 2012). Radio frequencies are less obscured by interstellar dust, and thus one can pierce through dense molecular clouds, and dust clouds. This allows for the detailed studies of dust properties and the composition of molecular clouds. Since the rotational transitions of molecules emit mostly in radio wavelengths, radio telescopes allowed the observations of molecular clouds. The detection of molecular species and the estimation of their column density and abundance allowed astronomers to study in more details the chemistry of the molecular clouds. Radio observations also allowed to observe cool hydrogen clouds through molecular proxies such as CO, that were undetected at optical wavelengths. Some objects can be more easily detected by radio telescopes such as hot gas around a black hole, and radio lobes of radio galaxies, that are not detected in optical.

However, single dish radio telescopes have their limitations. The resolution of a telescope is given by $\theta = \frac{1.2 \times \lambda}{d}$ (Wilson et al. 2012), where θ is the angular resolution of the telescope in radians, λ is the wavelength of the observed radiation, and d is the diameter of the telescope. Radio wavelengths (in mm-range) are significantly longer than optical wavelengths (in μm-range). Due to the long wavelengths and the mechanical limitations in construction, a single dish telescope tends to have a resolution which is much inferior to the resolution of an optical telescope. For a fixed wavelength, the only possibility to improve angular resolution of a single-dish radio telescope, is to maximise the diameter of the dish. The current technology and materials allow for a maximum diameter of $d = 500$ metres when supported by a valley (for example, the Five-hundred-meter Aperture Spherical radio Telescope (FAST) in China), or $d = 100$ metres for a steerable antenna (Effelsberg, and the Green Bank Telescope), limiting the resolution to few arcseconds. Moreover, the cosmic radio waves are weak compared to the earth-made radio signals. Radio communications on Earth (satellites, mobile phone services, ...) can interfere with radio observations. Therefore, radio telescopes are built in remote areas, where such interferences are less likely to occur.

2.4.2 Aperture Synthesis

In order to improve the resolution and increase the collecting area, one can use several single dish telescopes, separated by a distance larger than their diameters, forming thus a radio interferometer. The antennas will usually be connected by cables, and a correlator. For an interferometer with multiple antennas, the collecting area is then $\frac{\pi N d^2}{4}$, as it is now related to the number of the antennas N, and their diameter d. This also improves the angular resolution of system significantly as the resolution is now depending on the largest distance between the antennas $D_{\max}$ (order of $\sim$ 50 m to transcontinental distances, even up to 30 Earth diameters, if using space antennas) which is much larger than the diameter of the antennas, allowing for resolutions reaching the micro-arcsecond range ($\theta = \frac{1.2\lambda}{D}$). This improved resolution is comparable or even higher than the state-of-the-art optical telescopes, and it allows then for observations of substructures and details in -for instance- molecular clouds. With such resolution, one can resolve astronomical objects that were previously undetected (for example, the first image of the shadow of the supermassive black hole at the centre of M 87, Event Horizon Telescope Collaboration et al. 2019), the proto-planetary disks (Zhu et al. 2010; Ansdell et al. 2016). Moreover since the molecular rotational transitions emit in the mm- and sub-mm regime, interferometry allows for the spectral mapping of molecular species, shedding light on the chemical composition and distribution in molecular clouds.

2.4.3 Observations with Radio Interferometry

For an interferometer with N antennas, there are $\frac{N(N-1)}{2}$ baselines[4]. The $uv-$plane is the plane of the spatial frequencies corresponding to the projected baselines. A sampling function is used to produce the $uv-$plane. The $uv-$axes are usually given as a function of wavelength (it is a measure of wavelengths per baseline, see Fig. 2.2). For each baseline (each pair of antennas), one measures the complex visibilities resulting from the correlation of the individual signals. The resulting visibility function ($V(u,v)$) in the $uv-$plane is the Fourier transform of the brightness distribution of the source in the plane of the sky ($T(l,m)$).

$$\begin{aligned} V(u,v) &= \int\int T(l,m) e^{-2i\pi(ul+vm)} dl\, dm \\ T(l,m) &= \int\int V(u,v) e^{2i\pi(ul+vm)} du\, dv \end{aligned} \tag{2.32}$$

The visibility function can be derived from the electromagnetic signal detected by the antennas. In a pair of antennas (A1 and A2), the electromagnetic signal would reach antenna A1, before it reaches antenna A2 (Fig. 2.3). This causes a time delay caused by the geometry of the antennas, and thus called a geometric delay. The geometric delay is defined as $\tau_{geo} = \frac{b\, sin\theta}{c}$ where b is the distance between two antennas (baseline), c is the speed of light, and θ is the source angle relative to the zenith plane. This time delay will introduce a phase difference between the signals $\Delta\phi = 2\pi\,\nu\,\tau_{geo}$ (ν is the frequency of the radio signal). The electromagnetic signal (E2) detected by antenna A2 will then be shifted by a phase $\Delta\phi = 2\pi\,\nu\,\tau_{geo}$ to account for that delay and multiplied by the electromagnetic signal (E1) detected by antenna A1. The result of this multiplication is called the multiplicative response of the interferometer. This response is averaged over a certain period of time (integrated).

The calibration of the interferometric observations consist of the following basic steps. The bandpass calibration is done to compensate for the frequency-dependent gain response of the system. For this a bandpass calibrator (a bright source with a known spectrum) is observed once for each observation track. Moreover, it is important to calibrate the phase to account for signal delays. Phase calibration can be done by observing a source with a known shape and position, usually a point source, regularly during the observation track (usually every few minutes). In order to account and compensate for the flux loss due to atmospheric opacity and instrumental losses, the amplitude should also be calibrated. The amplitude calibration is done by observing a spatially unresolved source with a known flux density. This source can be an independently calibrated and radio source that does not vary its intensity over time. The calibrated response is the visibility function of the baseline. The visibility function of an interferometer is the sum of all the visibility functions of each baseline.

---

[4] Baseline is the separation between 2 antennas

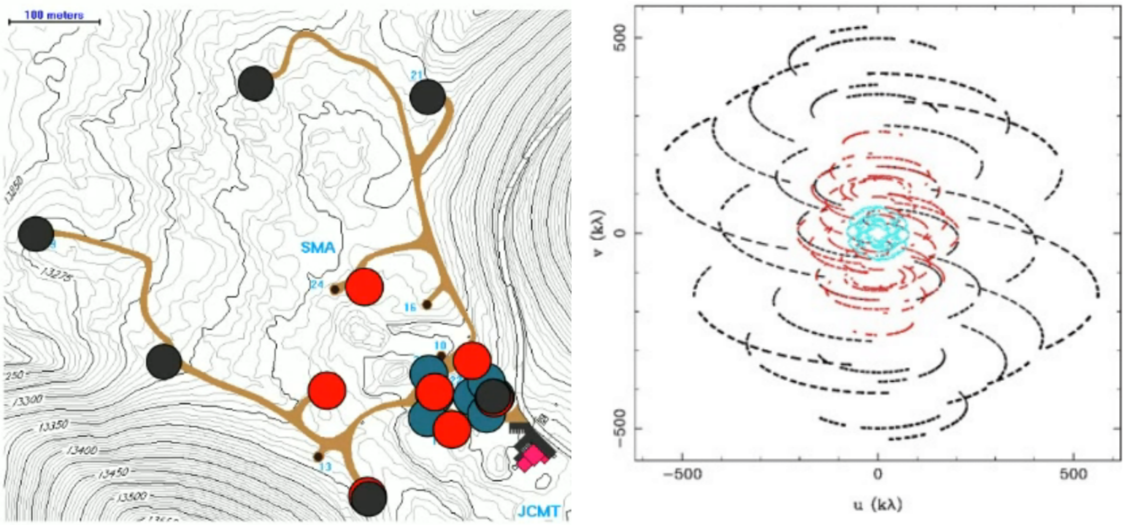

Figure 2.2: Example of 3 antenna configurations of the Sub-Millimeter Array (SMA) (left), and the resulting $uv-$coverage obtained when combining 3 different observation tracks (right). The $uv-$axes are given as a function of wavelength. (Credit: David Wilner, Harvard-Smithsonian Center for Astrophysics).

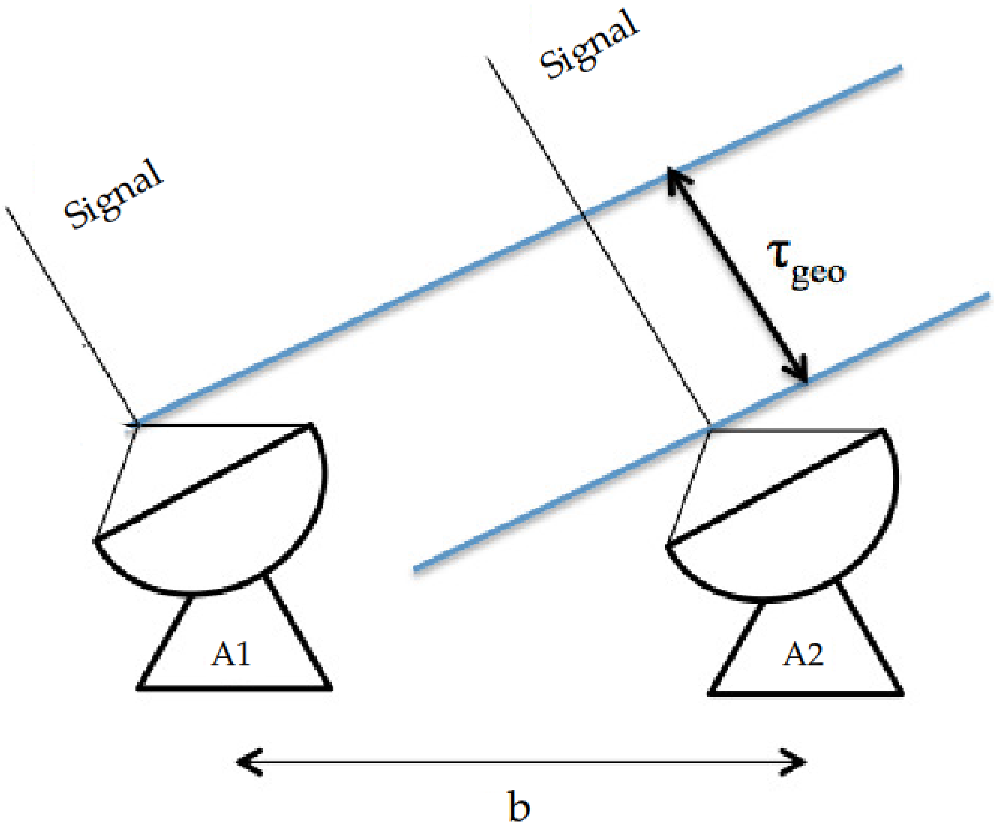

Figure 2.3: The geometric delay of the signal occurs because the radio signal of a source will reach antenna A1 before it reaches antenna A2 (Credit: Avison and George 2012, edited).

A Fourier transform of the $uv-$plane sampling function will give the image of the dirty beam, or the point-spread function. To get the dirty image one applies an inverse Fast Fourier Transform on the visibility function. However, since the visibilities are not provided on a regularly spaced grid, one has to sample the visibilities by a gridding function. One can also multiply the visibility function by a weighting function, which can minimise the side-lobes and change the shape of the point-spread function, as well as decrease the noise of the output image. In order to get the clean image, one needs to deconvolve the dirty image from the point-spread function. The details of that deconvolution are described in Chapter 4 Section 4.2.

2.4.4 Challenges in Radio Interferometry

However, the radio interferometer has its own challenges, not encountered when carrying out single-dish observations, such as the missing flux problem, in which some of the flux or intensity of an observed source is lost due to an incomplete coverage of the uv-plane, due to missing short- and zero-spacing. Moreover, the spatial scales recovered by an interferometer are limited to:

$$\frac{\lambda}{b_{\mathrm{max}}} < \theta < \frac{\lambda}{b_{\mathrm{min}}}$$

where b_{min} is the minimum separation between two antennas, and b_{max} is the maximum separation between two antennas. This indicates, that structures with an angular resolution smaller than $\frac{\lambda}{b_{\mathrm{max}}}$ will remain unresolved, and thus setting a limit to the resolution of an interferometer, and structures with an angular resolution larger than $\frac{\lambda}{b_{\mathrm{min}}}$ won't be detected. To overcome this issue, observations with small antennas in a compact configuration, or a large single dish telescope can be used.

2.5 Principal Component Analysis (PCA)

Data with more than three dimensions are hard to visualise with normal imaging programmes, and the interpretation of the results can become challenging. Furthermore, high dimensional data often contain a large number of redundant features that makes the interpretation of the data particularly difficult, without providing any additional or useful information. One method to overcome such difficulties and eliminate redundancy within a data set, is the Principal Component Analysis (PCA). In this section, a brief explanation of the mathematical theory and computation method will be described. A short mathematical derivation of the principal components will be provided as presented in Jolliffe (2002). The PCA has been applied already to astronomical data, for instance, by Ungerechts et al. (1997); Jones et al. (2013) and Riquelme et al. (2018).

Statistics are important to understand any given data set. The mean value of a data set and the variance $var(x) = \frac{\sum_{i=1}^{n}(x_i - \bar{x})^2}{n-1}$ are prominent examples. However, the variance is a measure that can only be calculated for a one-dimensional data set. For a two-dimensional data set, the covariance shows how the data points in each dimension vary from their mean value with respect to the other dimension. A covariance explores the correlation between two dimensions and is expressed as:

$$cov(x, y) = \frac{\sum_{i=1}^{n}(x_i - \bar{x})(y_i - \bar{y})}{n-1} \tag{2.33}$$

where x_i, y_i are individual data points in the x- and y-dimensions with $\bar{x}$ and $\bar{y}$ as their mean value, respectively. The covariance between a dimension and itself will result in the variance of this dimension, $cov(x, x) = var(x)$. For a data set with three dimensions or more, the best way to explore the correlation between all possible dimensions is to calculate the covariance of all the different dimensions and write them in a matrix called the Covariance Matrix $C_{n\times n}$, where n is the number of dimensions in the data set. For instance, the covariance matrix of a three-dimensional data set will be:

$$C_{3\times 3} = \begin{pmatrix} cov(x,x) & cov(x,y) & cov(x,z) \\ cov(y,x) & cov(y,y) & cov(y,z) \\ cov(z,x) & cov(z,y) & cov(z,z) \end{pmatrix} \tag{2.34}$$

The covariance matrix is a square symmetrical matrix around the diagonal.

Principal Component Analysis (PCA) can be used to reduce the dimensions of a data set without reducing the amount of valuable information. In some cases, it can be used to reduce the noise of a data set. In order to do so, PCA searches for the components that contain the highest variances. To illustrate the work of PCA, the example mentioned and the notations used in Jolliffe (2002) will be also used here.

In a 2-D data set as in Fig. 2.4 (a), the observations are plotted along an *xy*-axis that represents physical properties of the data. This gives a first insight on how the observables are distributed, but does not yet lead to a better understanding of the underlying structures or properties.

In the illustrated example, one notices that the data is most spread along the z_1-axis (Fig. 2.4, (b)). This is the direction where the highest variance of the data is. The z_1-axis is then the first principal component axis. The second principal component axis is orthogonal to the first principal component axis (in order to span the whole spread of the data along the *xy*-axis effectively), and has the second highest variance (Fig. 2.4, (c)).

Plotting the data along the principal component axes offers a certain advantage against plotting them in the *xy*-axis, as it better represents the underlying properties of the data (Fig. 2.4, (d)). However, in order to plot the data along the principal component axes, one must perform a linear transformation on the observables. After the linear transformation, the new axes (z_1-z_2-axes) hold no obvious physical meaning. For instance, if the *xy*-plane represents a time vs space correlation, the new z_1-z_2-plane loses this physical association. The interpretation of the new axes is largely dependent on the data set on which the PCA has been performed.

In a 2-D data set, it is fairly easy to calculate and plot the directions on which most variance is spread. For a data set with higher dimension, finding the principal components is not as trivial. PCA is applied to such high dimensional data sets in order to remove some unnecessary dimensions while maintaining most of the variations. This is done by transforming the data into a new set of uncorrelated, independent variables called the principal components (PCs). This new set of variables, or PCs are ordered in such a way that the first components contain most of the variabilities.

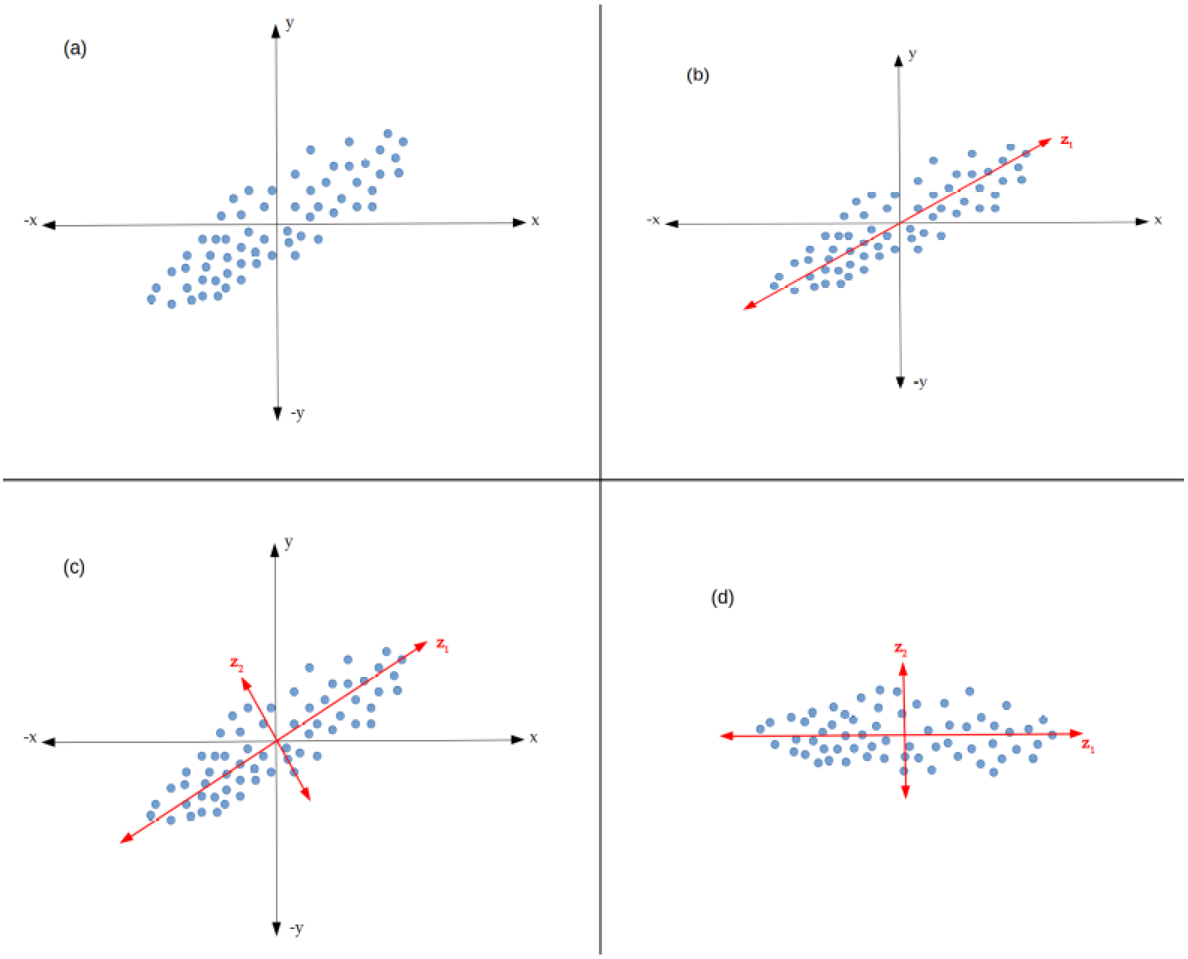

Figure 2.4: (a) Set of observations plotted on an *xy*-axis. (b) Data set with the first principal component axis. (c) Data set with both first and second principal component axes. (d) Data set plotted along the principal component axes.

In this example, the set of random variables **p** are described by a vector **X**. Before starting the analysis, one has to normalise the vector X by removing the mean of X, and dividing by its standard deviation. The new normalised vector x is then given as:

$$\mathbf{x_i} = \frac{\mathbf{X_i} - \bar{\mathbf{X}}}{\sigma_{\mathbf{X}}} \tag{2.35}$$

The correlations and covariances between the variables are important for the interpretation of the results. In a set of **p** variables, one has $\frac{1}{2}p(p-1)$ such correlations or covariances. Instead of analysing $\frac{1}{2}p(p-1)$ different correlations, which in a large data set can reach a considerable number, one can look for the most important variables, where most of the variability is, and study their correlations.

As described before, the first step is to find the linear transformation that allows the user to go from the original *xy*-axis to the principal component axes. This linear transformation is denoted as $\mathbf{a}'_1$ where $\mathbf{a}'_1$ is a transpose of $\mathbf{a_1}$, a vector of **p** elements or constants denoted as $\mathbf{a_{1p}}$. It should be noted that $\mathbf{a}'_1\mathbf{a_1} = \mathbf{1}$.

$$z_1 = a'_1 x = a_{11}x_1 + a_{12}x_2 + ... + a_{1p}x_p = \sum_{j=1}^{p} a_{1j}x_j \tag{2.36}$$

Now, one can calculate and maximise the variance of $\mathbf{z_1}$, so that it has the highest variance of the data set. For the second highest variance, one has to find a linear transformation $\mathbf{z_2} = \mathbf{a_2'x}$ that is uncorrelated with $\mathbf{z_1} = \mathbf{a_1'x}$. Therefore, for the k^{th} highest variance, one has to find the linear transformation $\mathbf{z_k} = \mathbf{a_k'x}$, and it should be uncorrelated with all the previous linear transformations ($\mathbf{a_k'a_p} = \mathbf{0}$, for $\mathrm{k} = 1, 2, ..., \mathrm{p} - 1$ and $\mathbf{a_k'a_k} = \mathbf{1}$). In order to maximise the variance, one can define a Lagrangian multiplier λ. It can be shown that $var(z_1) = a_1'\Sigma a_1$ where Σ is the covariance matrix of x. The variance $var(z_1)$should be maximised subject to $a_1' a_1 = 1$. Explicitly written, $f(x,y) = var(z_1) = a_1'\Sigma a_1$ is subject to $g(x,y) = a_1'a_1 - 1 = 0$. Therefore, in order to find the highest variance of $\mathbf{z_1}$, one has to maximise $a_1'\Sigma a_1 - \lambda(a_1'a_1 - 1)$. This leads to $\Sigma = \lambda_1 I_p$ where $\mathbf{I_p}$ is an identity matrix of the same dimension of Σ, and λ_1 is the highest variance of $\mathbf{z_1}$ and largest eigenvalue of Σ.

If the vector **x** has a known covariance matrix Σ, then the $(i,j)^{th}$ element of this matrix is the known covariance between the i^{th} and the j^{th} elements of **x**, if *i* and *j* are different. If, however, *i*=*j*, then $(i,j)^{th}$ element is the variance of the j^{th} element. It can also be proven that the highest variance of $\mathbf{z_k}$ is $var(z_k) = \lambda_k$. Therefore, it can also be shown that if *k* is an element from **p**, then the k^{th} PC is described as $\mathbf{z_k} = \mathbf{a_k'x}$, with $\mathbf{a_k}$ being an eigenvector of Σ that corresponds to the k^{th} highest eigenvalue $\lambda_\mathbf{k}$. For the mathematical details, check Jolliffe (2002). The eigenvector of each component describes the direction in which most of the variability is to be found. The eigenvalue of this eigenvector is then the number that quantifies the variance or the variability along this direction.

In this project, the PCA has been extracted based on the data matrix. This is done by using the Non-linear Iterative Partial Least Squares (NIPALS) method. Since the method relies on the data matrix to extract the principal components, it is less computationally intensive and can be faster than the other methods that rely on the covariance or the correlation matrices for the extraction of the principal components. However, NIPALS (the algorithm will be explained in the following section) is not suitable for data sets with a high number of principal components, because of the accumulations of machine-precision errors[5].

From data cube to principal components

The data set used in this study is composed of 7 maps for M 82 and 5 maps for IC 342 each containing the flux distribution of an emission line along a region of 256 by 256 pixels (65 536 pixels). Therefore, the data set is seen as 65 536 points in 7 and 5 dimensions for M 82 and IC 342 respectively, one dimension for each emission line. This means that the maximum number of principal components[6] is 7 and 5 for M 82 and IC 342 respectively. The flux distribution of each line can be described as a matrix, that can be flattened into a vector. That means, that is the image matrix has a dimension of N×N, the vector would have N^2. If one wishes to apply PCA on k images each with N×N, one will have dimensions, one gets k vectors, each with N^2 elements. Therefore, the data matrix would have dimensions of $k \times \mathrm{N}^2$. In the example of this thesis, the data matrix would have dimensions of (7×65 536) for M 82, and of (5×65 536) for IC 342. For the analysis, a code has been developed by Dr. Maria Cunningham in Python. The code has been used in different works such as Jones et al. (2013) and Riquelme et al. (2018). In this code, the data set is prepared by centring the mean and standardising the data by removing the mean and dividing by the standard deviation. This allows for an accurate comparison between the

---

[5] https://support.sas.com/documentation/onlinedoc/stat/141/hpprincomp.pdf

[6] There is a maximum for the number of principal components in a data matrix. This maximum number is defined as the smallest dimension of the data matrix: If the data matrix has a dimension of (m×n), then p=min(m,n) is the maximum number of principal components.

different components. The code used the PCA module from the Python library[7]. The procedure of the code and its operation are described in details in the documentation of the Python PCA Module[8].

The data matrix **X** (centred and standardised) is decomposed into a structure matrix $\mathbf{TP^T}$ ($\mathbf{P^T}$ is the transpose of **P**) and a noise matrix **E**. The matrix **E** is also called the residual matrix. The data matrix has a dimension of $k \times \mathrm{N}^2$, the structure matrix $\mathbf{T}$ has a dimension of $\mathrm{N}^2 \times k$, while P has a dimension of $k \times k$. Therefore, $\mathbf{X} = \mathbf{TP^T} + \mathbf{E}$..The structure matrix $\mathbf{TP^T}$ is the important one as it contains the scores **T** and the loadings **P** matrices of the PCA. The aim is to store most of the variance in the structure matrix and leave the noise in the **E**-matrix. The scores t are stored in a **T**-matrix in such a way that the first column holds the score of the first PC, and the second holds the scores of the second components and so on. It is useful to plot the scores of each PC, as it gives a visual representation of the PC, called the PC map. The loadings p stored in the **P**-matrix describe the weight or the contribution of each component on the scores of each PCs. In the example of this study, it describes the influence of each emission line on the scores of the PCs. The loadings can also be plotted and it shows how the variables are distributed against the principal components. It is useful to plot the loading of the first PC against those of the second PC. The loadings of each PC are normalised, so that: $\Sigma_i p_i^2 = 1$.

This module uses the NIPALS algorithm in order to find the eigenvectors and eigenvalues of the data set. If **X** is the mean centred data matrix, then as a first step, the noise or residual matrix **E** is set to be equal to **X**, and the t vector is set to be a column in **X**. The iteration goes from one to the number of components (7 and 5 for M 82 and IC 342 respectively). The first step of the algorithm is to project **X** onto t, in order to calculate the corresponding loading p. The second step consists of normalising the loading vector to 1, then projecting **X** onto the loading vector p to find its corresponding score vector t. Thus, the first PC is estimated. Then, the estimated PC is removed from the **E**-matrix, and then the code resumes from the first step, until the code has gone through all the components.

The PCA has been used in several astronomical studies and papers as a way to reduce dimensions and to find correlations between the different components. Most notably, the PCA has been applied in the work of Ungerechts et al. (1997); Meier and Turner (2005); Lo et al. (2009); Jones et al. (2013), and Riquelme et al. (2018). However, with the exception of the work done by Meier and Turner (2005), the PCA has been applied to single-dish data, almost exclusively. In this work, PCA will be applied to a 3-mm line survey performed by Plateau de Bure Interferometre (now known as NOrthern Extended Millimitre Array, or NOEMA) targeting the innermost few hundred pc of the central molecular zones (CMZs) of M 82 and IC 342.

PCA has its limitations when applied to physical problems. In its nature, PCA is a mathematical tool, therefore lacking the ability to analyse and interpret physical phenomena or concepts. It also fails to guarantee a meaningful physical solution to every problem that one wishes to solve with this method. It is therefore important to carefully interpret the results giving by this application.

---

[7] https://folk.uio.no/henninri/pca_module/

[8] https://folk.uio.no/henninri/pca_module/pca_nipals.pdf

Chapter 3

The Sources

3.1 M82

The galaxy M 82 (also known as NGC 3034, Arp 337, UGC 5322, 3C 231, CGCG 333-008)[1] is located at a distance of $3.5 \pm 0.3\,\mathrm{Mpc}$ (Karachentsev and Kashibadze 2006). M 82 has a right ascension RA (J2000): $09^{\mathrm{h}}55^{\mathrm{m}}52^{\mathrm{s}}.7$ and a declination DE (J2000): $+69^{\circ}40'46''$. Its inclination is around 80° perpendicular to the plane of the sky, and the position angle of the major axis is 65° (de Vaucouleurs et al. 1991). With a dynamical mass of only $10^{10}\,\mathrm{M}_{\odot}$ within a radius of 4 kpc (Greco et al. 2012) and a Holmberg diameter of $14\,\mathrm{kpc}$ (Appleton et al. 1981), it is a rather small galaxy compared to the Milky Way that has a dynamical mass ranging between $0.8 \times 10^{12}\,\mathrm{M}_{\odot}$ (Kafle et al. 2014) and $1.3 \times 10^{12}\,\mathrm{M}_{\odot}$ (McMillan 2017) and a radius >$31\,\mathrm{kpc}$ (López-Corredoira et al. 2018). It is the second member of the M 81 galaxy group, which is one of the closest to the Local Group (Karachentsev 2005). M 82 has been observed all over the electromagnetic spectrum, and is among the brightest extragalactic near infra-red sources in the sky (Jarrett et al. 2003; Hutton et al. 2014): M 82 is around five times more luminous in optical and near infra-red frequencies than the Milky Way, with its central region being ten times more luminous than the central molecular zone of the Milky Way (Barker et al. 2008). With a receding velocity of of $203 \pm 4\,\mathrm{Km\,s^{-1}}$, M 82 has a high surface brightness of $5.7 \times 10^{4}\,\mathrm{L_{\odot}pc^{-2}}$ in a region of 150×45 pc (O'Connell and Mangano 1978). Being one of the nearest starburst galaxies, M 82 is one of the most prominent molecular lighthouses in the northern hemisphere, and it has a starburst in a late stage of evolution (Aladro et al. 2011b). M 82 is interacting with the larger and more massive galaxy M 81 ($\mathrm{M} = 5 \times 10^{10}\,\mathrm{M}_{\odot}$ and Diameter=$27.2\,\mathrm{kpc}$ (Stoyan et al. 2008)): An interaction between those two galaxies is thought to have occurred around few 10^{8} years ago (Gottesman and Weliachew 1977; Yun et al. 1994). This interaction has been made responsible for the high star formation rate of around $10\,\mathrm{M_{\odot}yr^{-1}}$ in this rather small galaxy (de Grijs et al. 2001) and the period of vigorous star formation in recent times that resulted in the formation of around 150 star clusters within the innermost 100 pc M 82 (Barker et al. 2008; Divakara Mayya and Carrasco 2009).

Along side a still active starburst, supernova remnants, compact X-ray sources, maser sources, super winds and outflows can be observed in M 82 (eg. Wills et al. 1997; Allen and Kronberg 1998; McDonald et al. 2002; Chiang and Kong 2011; Fossey et al. 2014). This renders this

---

[1] https://ned.ipac.caltech.edu/

galaxy an ideal source to study and monitor, as it provides a multi-wavelength insight on its formation and dynamics. The structure of M 82 and the different sources observed in this galaxy will be discussed in the following sections.

Figure 3.1: Multi-wavelength Image of M 82: The bright blue colour represents the X-ray emission at 1.5 keV, taken by Chandra - ACIS. The green colour is optical emission at 440 nm captured by HST - ACS. The orange colour represents optical emission at 656 nm taken by HST - ACS. Finally, the red colour is the infra-red emission at 8.0 μm captured by Spitzer - IRAC. Credit: NASA/JPL-Caltech/STScI/CXC/UofA/

Figure 3.1 shows a mutli-wavelength image of M 82 taken by the Hubble Space Telescope - Advanced Camera for Surveys (HST - ACS), Spitzer's Infra-Red Array Camera (Spitzer - IRAC), and Chandra's Advanced CCD Imaging Spectrometre (Chandra - ACIS), on 24 April 2006. The X-shaped outflows in orange are Hydrogen clouds being expelled from the central regions of the galaxy, where star formation is up to 10 times more efficient than in the Milky Way. This outflow is hot enough to emit at X-ray wavelengths.

3.1.1 Structure and Morphology

A large number of studies conducted observations at optical and infra-red wavelengths, in order to investigate the structure and the morphology of M 82. Observations at optical wavelengths revealed the existence of many star clusters within the inner $600\,\mathrm{pc}$ of the galaxy (O'Connell and Mangano 1978 observations between 500 and $680\,\mathrm{nm}$). These clusters outline the regions of recent starburst activity in the centre of M 82, these regions are characterised by a high surface brightness. The low mass-to-light ratio of $\frac{M(\mathrm{M}_\odot)}{L(\mathrm{L}_\odot)} \sim 0.1$ provides an upper limit for the cluster age estimates of around 5×10^7 years (O'Connell and Mangano 1978). Evidence for ongoing star formation in the centre of the galaxy is found, with few localised starbursts that have ended around 2×10^7 years ago (O'Connell and Mangano 1978). O'Connell and Mangano (1978) proposed the existence of hot stars in the central clusters, and that optical dust scattering dominates line radiation outside of the inner $600\,\mathrm{pc}$ of M 82. They also concluded that M 82 had had a tidal encounter with M 81, which stripped M 82 from a significant portion of its interstellar gas. This stripped gas is now orbiting and falling into the galaxy, forming filaments and a cool halo interacting with the residual gas, leading to new waves of starbursts (O'Connell and Mangano 1978).

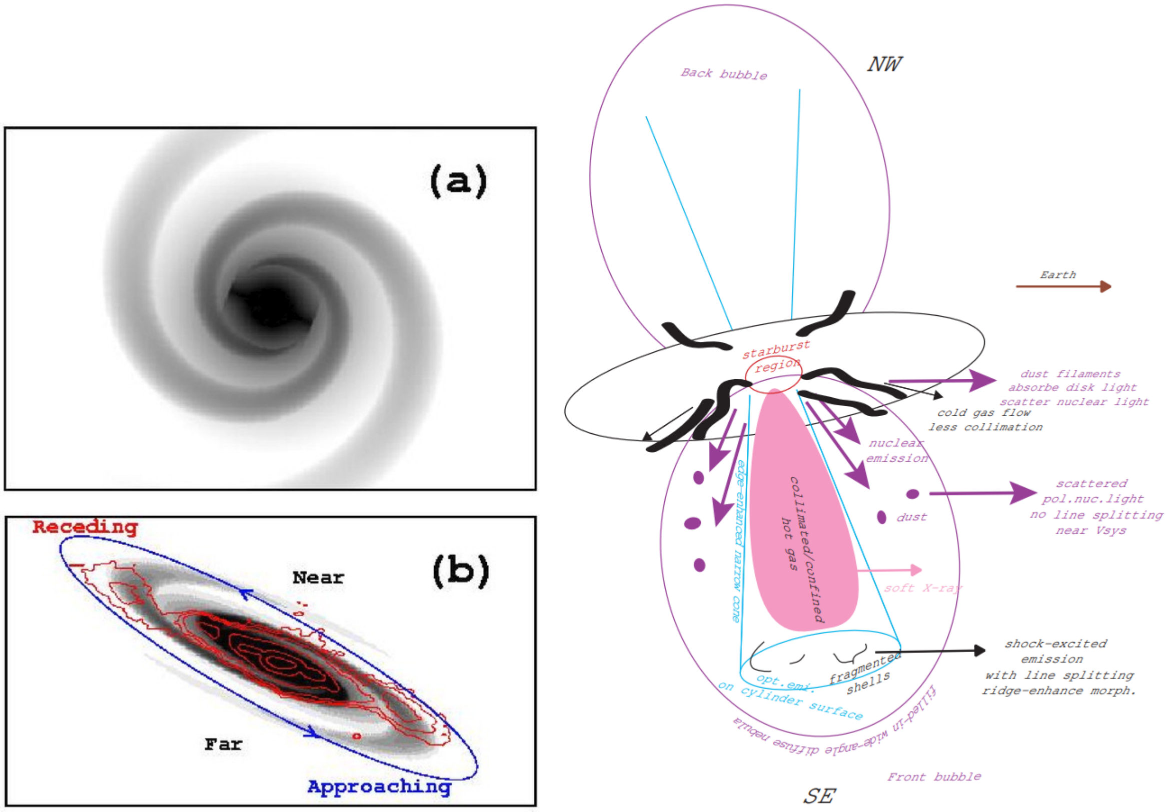

Figure 3.2: The Structure of M 82. Left Top Panel (a): The galaxy seen face on, with the exponential disk removed, showing the best-fit model galaxy. Left Bottom Panel (b): The galaxy viewed edge-on, with $\lambda = 2\,\mu\mathrm{m}$ K-band residual image (with the exponential disk removed) contours (in red). The ellipse in blue indicates the stellar rotation from the trailing spiral arms, where (neglecting the systematic velocity) the Southeastern Part of M 82 is moving toward the Milky Way, while the Northeastern part is receding (from Mayya et al. 2005). Right Panel: M 82 view as seen side-on, depicting the main components of the galaxy (starburst region, wind, outflow,...) as published by Ohyama et al. 2002. Here, one can see the diffuse and the ridge-dominated cylindrical components of the super-wind, with the dust filaments that are scattering the stellar light. For more details, check the text and refer to Ohyama et al. 2002.

Later studies by Yun et al. (1993, 1994) estimated that the interaction between M 82 and M 81 occurred between $(2-5)\times10^8$ years ago, by modelling the HI gas distribution of M 82 using Very Large Array (VLA) data. This interaction formed a bar in M 82, and triggered star formation through an inflow of gas into the nuclear region (Wills et al. 2000). From near infra-red observations, Götz et al. (1990) found that the central stellar concentration observed at $2\,\mu$m, has a low mass-to-luminosity ratio of $\sim 0.3\,\frac{\mathrm{M}_\odot}{\mathrm{L}_\odot}$ (for comparison, the mass-to-luminosity ratio in the Galactic Centre is $3\,\frac{\mathrm{M}_\odot}{\mathrm{L}_\odot}$). Using CO (v=2-0) absorption at $2.3\,\mu$m, Gaffney et al. (1993) estimated the size of the M 82 nuclear bulge to be around $\sim 7.5\,\mathrm{pc}$ in diameter, and calculated a conservative mass for the bulge of $M(r < 7.5\,\mathrm{pc}) = (3 \pm 1) \times 10^7 \mathrm{M}_\odot$[2]. Some studies have interpreted this bulge to be a supermassive black hole (SMBH) in the centre of M 82 with a mass of $3 \times 10^7\,\mathrm{M}_\odot$ (e.g. Gurzadyan et al. 2015 and Pfeffer et al. 2017), but this interpretation should be considered with skepticism, since no evidence was presented to support this assumption. This estimate of the nuclear mass of M 82 is similar to the mass of the same region in the Galactic Centre ($3 \times 10^7\,\mathrm{M}_\odot$, McGinn et al. 1989). Therefore, the newly estimated mass-to-light ratio within $r < 7.5\,\mathrm{pc}$ of M 82 is similar to the mass-to-light ratio within the same radius in the Milky Way (contrary to the estimations by Götz et al. (1990), and the previous estimation of O'Connell and Mangano 1978).

Due to its inclination, high surface brightness, and strong optical obscuration, the galaxy was originally classified as a dwarf irregular type-II galaxy, with a mass of $6 \times 10^9\,\mathrm{M}_\odot$ (Lynds and Sandage 1963; Sandage and Brucato 1979; McKeith et al. 1995; Sofue et al. 1998a). However, infra-red (IR) mapping of M 82 at $2\,\mu\mathrm{m}$ revealed a bar of $\sim 1\,\mathrm{kpc}$ in length ($\sim 60''$) (Telesco et al. 1991). Later near infra-red (NIR) observations corroborated the existence of such a bar and revealed spiral arms in the disk, where the disk covers a scale of $48'' \sim 0.84\,\mathrm{kpc}$ (Mayya et al. 2005). These structures have been obscured by optically thick dust. Therefore, M 82 is now classified as a small late-type spiral barred SBc galaxy[3] (Mayya et al. 2005)). Figure 3.2 presents the structure of M 82 with the disk, the bar and the spiral arms, obtained from K-band observation of M 82 with a field of view of $5'.5 \times 5'.5$ (Mayya et al. 2005).

Starburst

Through interaction with the dominant group member, M 81, starburst activities have been triggered at different stages, with a star formation rate (SFR) several times that of the larger Milky Way (SFR in M 82 $\sim 10\,\mathrm{M}_\odot\,\mathrm{yr}^{-1}$ (de Grijs et al. 2001), while SFR in Milky Way is $\sim 0.68 - 1.45\,\mathrm{M}_\odot\,\mathrm{yr}^{-1}$ (Robitaille and Whitney 2010)). The interaction also caused an outflow along the minor axis of M 82. Many of the sources associated with the starburst activities (massive stars, SN, SN remnants) that were triggered around 20 Myr ago, are found in the central ∼500 pc of the galaxy (O'Connell 2002; Barker et al. 2008). Most of these sources are heavily obscured at optical wavelengths due to the optically thick dust surrounding the centre of M 82, but one can identify high surface brightness clumps at optical wavelengths, corresponding to sources detectable at X-ray, radio, and infra-red wavelengths (Barker et al. 2008). There is evidence that the tidal interaction with M 81 has triggered two different bursts of star formation, resulting in two distinct super star clusters (Brouillet et al. 1991; O'Connell 2002). It is estimated that the earlier starburst activity occurred around $\sim 6 \times 10^8$ years ago, in a region extending between 400 and 1000 pc to the north-east from the galaxy centre (Brouillet et al. 1991; O'Connell 2002). This region hosts a super star cluster containing around 100 luminous clusters, with a mean luminosity of $4 \times 10^6\,\mathrm{L}_\odot$ (O'Connell 2002).

Another bright super star cluster is found in a region closer to the centre of the galaxy. This one has an extremely high surface brightness of $\mu_V \sim 14.5\,\mathrm{mag\,arcsec}^{-2}$, containing young stars that are around 5×10^6 years old (O'Connell 2002). Around 150 bright stellar clusters have been detected within the innermost 100 pc of the galaxy, with ages between $\sim 2.5 \times 10^6$ and 6×10^6 years and an average mass of $\sim 10^5\,\mathrm{M}_\odot$ (Barker et al. 2008). The nuclear starburst region is surrounded by optically thick dust, making the detection of such sources challenging. However,

---

[2] Considering that the Milky Way has a diameter of >31 kpc (López-Corredoira et al. 2018), and a bulge of $\sim 3\,\mathrm{kpc}$ (Gerhard 2002), the bulge of M 82 is significantly smaller, even when considering that M 82 has a diameter of 14 kpc.

[3] Spiral Barred (SB) galaxy. The "c" refers to the tightness of the arms

using infra-red imaging, 12 compact sources were identified with ages ranging between 6×10^6 and 10^7 years (Satyapal et al. 1997). The hot gas in that region has been linked to a galactic wind observable in the $\mathrm{H}\alpha$ recombination lines. This suggests that the star clusters observed in these regions are driving the galactic wind.

Outflows and Winds

The galactic wind along the minor axis of M 82 is observed at different wavelengths and apparently forms a bipolar outflow. This ionised gas consists of complex loops and filaments that extend out to distances of few kpc from the high-altitude halo along the minor axis (Ohyama et al. 2002), with a cone opening of around $\sim 30°$ (Götz et al. 1990). From measurement of the disk inclination, kinematic studies and conical outflow modelling, it is suggested that the southern outflow is blue-shifted, while the northern outflow is red-shifted (McKeith et al. 1995).
Ohyama et al. (2002) presented a schematic view of M 82 as seen side-on, depicting the starburst regions, the outflow and the wind of hot gas (Fig. 3.2, right panel). Using the 8.2 m Subaru Telescope, they also identified two components with different origins and different morphologies related to the emission nebula of the galaxy that were caused by the super-wind (Ohyama et al. 2002). The first component is cylinder-shaped and ridge-dominated, containing filament and loop substructures. These structures are caused by local shocks between the matter inside the galaxy that is colliding with the outer interstellar medium (Ohyama et al. 2002). This component is similar in morphology to the hot plasma detected in soft X-rays, and has a diameter that is similar to the diameter of the nuclear starburst region (Ohyama et al. 2002). The sharp boundaries of this component are indicative of radiative shocks caused by the expansion of hot gas. Therefore, this component is shock-driven with a collimated structure (Ohyama et al. 2002).
The second component is diffuse, and has an opening wider than the size of the nuclear starburst region. This component originates from stellar light scattering due to dust grains in the high-altitude dusty halo of M 82 (Ohyama et al. 2002). These dust grains are also responsible for the dark lanes seen above and below the galaxy's disk, forming an X-shaped morphology (Ichikawa et al. 1994, 1995). These dark lanes can be seen across the disk of M 82, and seem to originate from the nuclear starburst region. It is also suggested that, since the dust has a conical morphology, the dust grains are expelled from the nuclear regions through outflows probed by soft X-ray and optical emissions, forming a dusty super-wind. This, along with the absence of boundaries within the diffuse component, implies that the dust lanes and the high-latitude dusty halo are created by the same mechanisms (Ohyama et al. 2002). Furthermore, there have been suggestions that the dusty super-wind is dynamically acting on the high-latitude gas, thus associating the outflow with the cold molecular and atomic gas found at high latitudes (Yun et al. 1993). The expansion of high-pressure gas of the super-wind is pushing out the dusty gas around the nucleus, leading then to this dusty, and cold outflow (Ohyama et al. 2002). It is also suggested that the bipolar outflow of M 82 is driven by supernova explosions that are occurring in the galaxy at a rate of $\sim 0.1\,\mathrm{yr}^{-1}$ (Lynds and Sandage 1963; Shopbell and Bland-Hawthorn 1998; de Grijs et al. 2000).

3.1.2 Compact Sources in M 82

M 82 observations revealed a large number of compact sources in radio, as well as in X-rays. Wills et al. (1997) and Allen and Kronberg (1998) identified around 26 compact radio sources in the nucleus of M 82. Using VLA data at 15 GHz complemented by Multi-Element Radio-Linked Interferometer Network (MERLIN) observations at 5 GHz, McDonald et al. (2002) identified 20 additional compact sources. Of the 46 identified compact objects, 30 are classified as supernova (SN) remnants, while 16 of these sources are identified as H II regions. The locations of the H II regions seem to coincide with the regions where the large-scale ionised gas distribution peaks and their spectra are steep and inverted at high resolutions, indicating that H II regions might be optically thick between 5 and 15 GHz (McDonald et al. 2002). The large number of sources ($\sim$ 65% of the sources) that are identified as SN remnants, further indicate that M 82 is at an advanced stage of a starburst. Another 15 compact sources were discovered but remain unidentified, bringing the total number of compact sources in the nucleus of M 82 to 61. These unidentified sources are most likely older SN remnants (McDonald et al. 2002).

A rare radio supernova, SN 2008 iz, was discovered by Brunthaler et al. (2009). Having a peak flux density of around 90 mJy at 22 GHz, this source was the brightest radio source in M 82 (Brunthaler et al. 2009). The flux density faded to $\sim$ 11 mJy at 22 GHz within a month (Brunthaler et al. 2009). The lack of X-ray emission from its progenitor suggests that a black hole (stellar or intermediate-mass) could not be the progenitor, making a radio supernova the best explanation for this source. Later observations showed that the SN 2008 iz is most likely a Type II SN, originating from a large dense molecular cloud ($\mathrm{N_{H_2}} = 5.4 \times 10^{22}\,\mathrm{cm^{-2}}$) with high visual extinction of $A_v = 24.4\,\mathrm{mag}$ (Brunthaler et al. 2010).

Two ultra-luminous X-ray sources (ULX) were observed in the centre of M 82, designated as M 82 X-1 and M 82 X-2, separated by $5''$, with high luminosities of $10^{41}\,\mathrm{erg\,s^{-1}}$ and $1.8 \times 10^{40}\,\mathrm{erg\,s^{-1}}$ respectively, at 0.3-10 keV (Bachetti et al. 2014). From the X-ray luminosity, a mass of $\gtrsim 500\mathrm{M_\odot}$ was estimated for M 82 X-1, making it a candidate for an intermediate-mass black hole (Kaaret et al. 2001). The detection of quasi-periodic oscillation in the X-ray emission of M 82 X-1, allowed for an estimation of the black hole mass to be $\sim 428 \pm 105\,\mathrm{M_\odot}$ (Pasham et al. 2014). However relativistic precession modelling lead to a more accurate estimation of $415 \pm 63\,\mathrm{M_\odot}$ (Pasham et al. 2014). Therefore, M 82 X-1, the bright X-ray source in M 82, is the most prominent candidate for an intermediate black hole.

Being an active starburst, M 82 is the host of many X-ray sources. Between 1999 and 2007, 58 X-ray sources were identified in M 82, exhibiting long term flux variability (Chiang and Kong 2011). Three X-ray sources were identified as supernovae (Chiang and Kong 2011). This strong and long term X-ray variability observed in M 82 is a strong indication of a high number of X-ray binaries within M 82 (Chiang and Kong 2011). Other observations also showed that M 82 contains many UV and X-ray sources (Spaans and Meijerink 2007). Spaans and Meijerink (2007) suggested that the X-ray radiation has two main sources, one being the super-wind from the starburst leading to thermal X-ray emission, and the other being a compact hard source from the nuclear region of M 82, but there is no evidence to suggest that this compact source is an AGN.

Since the hard component of the X-ray spectrum of M 82 showed variability on scales ranging from minutes to months, from $3 \times 10^{40}\,\mathrm{erg\,s^{-1}}$ to $10^{41}\,\mathrm{erg\,s^{-1}}$, Matsumoto and Tsuru (1999a) attributed this variability and the hard component of the X-ray spectrum (that seems to originate from the central region of M 82 with a column density of $\mathrm{N_H} = 3 \times 10^{21}\,\mathrm{cm^{-2}}$ (Matsumoto and Tsuru 1999a and Matsumoto and Tsuru 1999b) to a variable compact source: a putative AGN with low luminosity in the centre of M 82. Many studies have presented candidates for this AGN in M 82. Wills et al. (1997); Seaquist et al. (1997) and Wills et al. (1999) suggested the source 44.1+59.6 as an AGN candidate: the source is located near the centre of M 82 as well as the 2.2 $\mu\mathrm{m}$ peak. Moreover, 44.01+59.6 has a positive index spectrum and a strong low-frequency turnover, which is untypical for a SN remnant, but similar to other AGNs, such as the one in Cen A (Seaquist et al. 1997 and Wills et al. 1999). A compact radio source 0951+699 was detected with a position that coincides with the kinematic centre of M 82, and has a brightness temperature of 10^{11} K, that is typical for AGNs, but also typical for some radio supernovae ~ 100 days following the explosion (Sokolovsky et al. 2014).

3.1.3 Previous Studies of Dense Molecular Gas and Related Components

Many observations and surveys targeted the dense gas in the central regions of M 82 in order to study and understand its chemical composition, distribution, and the physical properties and processes in these regions.

Molecular Gas

A molecular ring rotating around the nucleus of M 82 has been detected in CO emission with a mean radius of 250 pc and a width of 170 pc (Loiseau et al. 1990). Shen and Lo (1995) detected CO emission from the spiral arms at 125 and 390 pc from the central region. In the spiral arms of M 82, the H_2 mass does not follow the CO distribution: traced by $C^{18}O$ emission, the H_2 mass peaks in the central regions of M 82, while CO seems to be smoothly distributed across the centre (Shen and Lo 1995). The distribution of C I emission follows closely that of CO (White et al. 1994). Moreover, the detected high C I abundance in M 82 was attributed to the strong flux of cosmic rays in the galaxy (White et al. 1994). Similarly, the distribution of ^{13}CO follows closely that of CO and exhibits the same double peak morphology observed by Shen and Lo (1995) (Neininger et al. 1998). Ammonia (NH_3) inversion lines the (J,K) = (1, 1), (2, 2), and (3, 3) transitions were first detected in M 82 by Weiß et al. (2001), with low abundances compared to H_2, due to photo-dissociation of NH_3 in PDR regions. Weiß et al. (2001) estimated a kinetic temperature of ~ 60 K for the molecular gas. Mauersberger et al. (2003) estimated the temperature of the molecular gas to be ~ 29 K from the NH_3 emission, indicating that the gas in central regions of M 82 is cold. However, using observations of H_2CO which is less affected by photo-dissociation, Mühle et al. (2007) suggested that the molecular gas in the central regions of M 82 is warm with a kinetic temperature of $T_{kin} \sim 200$ K, and dense with a density of $n_{H_2} = 7 \times 10^3\,\mathrm{cm}^{-3}$.

Interferometric observations with the IRAM Plateau de Bure Interferometer showed three regions where different chemistries dominate in M 82 (Ginard et al. 2015): A super-shell that is associated with a supernova, where no massive stars are forming but where one can observe knots of N_2H^+ with high intensity, an outer orbit where H41α detection indicates the formation of massive stars, and an inner orbit where a photo-dissociation region (PDR) is located, and where a high N_2H^+ abundance is observed. The high abundance of N_2H^+ observed in the different regions indicates that the gas reservoir needed for star formation is not yet completely exhausted, allowing for future star formation across the galaxy (Ginard et al. 2015).

Aladro et al. (2011b) determined a molecular gas mass of $5.2 \times 10^8\,\mathrm{M}_\odot$ within a 12″-beam of the 30-m IRAM single dish telescope, while the neutral hydrogen mass $\mathrm{M_{HI}}$ is around $1.3 \times 10^9\,\mathrm{M}_\odot$. They further showed that a significant part of the molecular emission in M 82 originates from regions with $\mathrm{n_{H_2}}$ densities of $10^5 - 10^6\,\mathrm{cm}^{-3}$. However, outside the Giant Molecular Clouds (GMCs), the bulk gas maintains a density of $10^4\,\mathrm{cm}^{-3}$ (Aladro et al. 2011b).

Outflow of Molecular Gas

M 82 is known for its strong outflow and super-wind that can be detected at different wavelengths (radio, X-rays, ...) (e.g. Ohyama et al. 2002; Fuente et al. 2008). This outflow is observed in the Hα recombination lines (Walter et al. 2001; Ohyama et al. 2002), N II and O III spectral lines (Shopbell and Bland-Hawthorn 1998), and even at X-ray energies (Walter et al. 2001), and shows a maximum velocity of $\sim 240\,\mathrm{km\,s^{-1}}$ (Walter et al. 2002). Shen and Lo (1995) indicated that the molecular outflow is moving at a velocity of $230\,\mathrm{km\,s^{-1}}$. It is estimated that more than $3 \times 10^8\,\mathrm{M_\odot}$ of molecular gas is in the outflows (Walter et al. 2002). Molecular mass estimates of the outflow range between $M = 2.6 \times 10^8\,\mathrm{M_\odot}$ and $M = 1.0 \times 10^9\,\mathrm{M_\odot}$ (Salak et al. 2013). These CO and ionised gas outflows are suggested to have a cylindrical shape and were detected $\sim 2\,\mathrm{kpc}$ above the galactic plane in M 82 (Salak et al. 2013). The existence of such gas is due to a warm/hot component in the outflows, that could have temperatures reaching $10^8\,\mathrm{K}$ (Fuente et al. 2008). Beirão et al. (2015) calculated the mass of the warm component to be between $M_{warm} = 5 \times 10^6 \mathrm{M_\odot}$ and $M_{warm} = 1.7 \times 10^7 \mathrm{M_\odot}$. Their observations showed that low-velocity shocks ($v < 40\,\mathrm{km\,s^{-1}}$) are exciting the warm gas in the outflow, where the molecular gas seems to have densities ($\mathrm{n_H}$) ranging between 10^2 and $10^4\,\mathrm{cm^{-2}}$ (Beirão et al. 2015). Moreover, SiO has been detected in these outflows, up to 500 pc above the galactic plane, forming a super-shell with a diameter of 150 pc, and expanding at a speed of $\sim 40\,\mathrm{km\,s^{-1}}$ (García-Burillo et al. 2001). This SiO super-shell is suspected to be feeding the outflow with $\sim 10^7\,\mathrm{M_\odot}$ of molecular gas (García-Burillo et al. 2001).

Velocity Structure

Interferometric observations of CO emission in M 82 revealed the presence of several peaks, attributed to radial velocity components ranging from 70 to $225\,\mathrm{km\,s^{-1}}$ which is due to the rotation of the galactic plane (Shen and Lo 1995). Moreover, Shen and Lo (1995) determined a systematic LSR velocity of $\sim 225\,\mathrm{km\,s^{-1}}$ for the galaxy.

Spectral Line Scans

Several single-dish observations targeted the central molecular zone of M 82. Aladro et al. (2011a,b) and Aladro et al. (2015) scanned the central zones of M 82 at 1.3, 2, and 3 mm, thus providing the most extensive molecular content catalogue of M 82. In addition to molecular lines (see Table. 3.1), many Hα recombination lines (H42α, H41α, H40α, H39α, and H38α) were detected (Aladro et al. 2015).

The abundance of ethyl acetylene CH_3CCH compared to H_2 ($1.1 \times 10^{-8}\,\mathrm{cm^{-2}}$) in M 82 is four times higher than that of CS, and ten times higher than that of HC_3N (Aladro et al. 2011b). This is unexpected as CH_3CCH is easily photo-dissociated, but it can be due to the fact that CH_3CCH is formed through neutral-neutral reactions, or through reactions between ions and molecules, while the others are created from dust grains. It is more abundant in M 82 than in other typical starburst galaxies (Aladro et al. 2011b). It is possible that this molecule originates from dense regions ($\sim 10^5\mathrm{cm^{-3}}$) that are not affected by the UV-radiation of the PDRs. Aladro et al. (2011a) detected for the first time in M 82 molecules like H_2S, CH_3CN, H_2CS, NO, and NH_2CN. Other single dish surveys covering the 3-mm range found molecules such as SiO, $C^{18}O$, ^{13}CO, $C^{17}O$, HNCO, CH_3CN, and recombination lines such as H41α, and H39α. (Aladro et al. 2015). Moreover, the extended PDR regions that were created by strong UV radiation from the starburst, are further traced by Hα recombination lines and HOC^+, HCO, and CH_3CCH that show brighter lines in M 82 than in other starburst galaxies (Aladro et al. 2015).

In previous studies, Fuente et al. (2005) reported that the $\frac{\mathrm{CN}}{\mathrm{HCN}}$ ratio ~ 5 within 650 pc of M 82 indicates a giant and dense PDR region excited by a strong radiation field. Furthermore, they reported the detection of $HOC^+(1\text{-}0)$, with a ratio of $\frac{\mathrm{HCO}^+}{\mathrm{HOC}^+} \sim 40$, further confirming the presence of a strong PDR region in the centre of M 82 (Fuente et al. 2005). van der Tak et al. (2008) detected extragalactic H_3O^+ in M 82. This molecule traces oxygen chemistry and can help to estimate the ionisation rate in dense gas. The column density of $H_3O^+ \sim 10^{14}\,\mathrm{cm}^{-2}$ can be explained through an XDR or a PDR with a high cosmic-ray ionisation rate (van der Tak et al. 2008). The prototypical starburst galaxy M 82 showed low abundances of shock tracers and complex molecules such as SiO, CH_3OH and HNCO (Mauersberger and Henkel 1993; Martín et al. 2006a,b, 2009).

Table 3.1: List of detected molecules in M 82

Molecules	Reference	Molecules	Reference
CCH	Aladro et al. 2011a and Aladro et al. 2015	HOC^+	Aladro et al. 2011a and Aladro et al. 2015
NO	Aladro et al. 2011a	**OCS**	Aladro et al. 2011a
CH_3CCH	Aladro et al. 2011a,b and Aladro et al. 2015	HNCO	Aladro et al. 2011a and Aladro et al. 2015
CS	Aladro et al. 2011a,b and Aladro et al. 2015	**C_2S**	Aladro et al. 2011a
CH_3OH	Aladro et al. 2011a and Aladro et al. 2015	**$c\text{-}C_3H$**	Aladro et al. 2011a
H_2CO	Aladro et al. 2011a	**C_2D**	Aladro et al. 2011a
H_2S	Aladro et al. 2011a	**CH_2NH**	Aladro et al. 2011a
$c\text{-}C_3H_2$	Aladro et al. 2011a and Aladro et al. 2015	**^{13}CS**	Aladro et al. 2011a
HCO	Aladro et al. 2011a	**$HOCO^+$**	Aladro et al. 2011a
SO	Aladro et al. 2011a and Aladro et al. 2015	NS	Aladro et al. 2011a and Aladro et al. 2015
H_2CS	Aladro et al. 2011a	**$HN^{13}C$**	Aladro et al. 2011a
HC_3N	Aladro et al. 2011a,b and Aladro et al. 2015	SiO	Aladro et al. 2011a and Aladro et al. 2015
SO_2	Aladro et al. 2011a	**DCN**	Aladro et al. 2011a
NH_2CN	Aladro et al. 2011a	**DNC**	Aladro et al. 2011a
$C^{34}S$	Aladro et al. 2011a and Aladro et al. 2015	**N_2D^+**	Aladro et al. 2011a
CH_3CN	Aladro et al. 2011a and Aladro et al. 2015	$HC^{18}O^+$	Aladro et al. 2015
$H^{13}CN$	Aladro et al. 2011a and Aladro et al. 2015	HCO^+	Aladro et al. 2015
$H^{13}CO^+$	Aladro et al. 2011a and Aladro et al. 2015	N_2H^+	Aladro et al. 2015
$C^{18}O$	Aladro et al. 2011a and Aladro et al. 2015	CH_3CHO	Aladro et al. 2015
CN	Aladro et al. 2011a and Aladro et al. 2015	^{13}CO	Aladro et al. 2015
HCN	Aladro et al. 2011a and Aladro et al. 2015	$C^{17}O$	Aladro et al. 2015
HNC	Aladro et al. 2011a and Aladro et al. 2015	CO	Aladro et al. 2015
CO^+	Aladro et al. 2011a	NH_3	Weiß et al. 2001

Molecules in boldface are the molecules for which only upper limits of column densities were measured

Isotopic Ratios in M 82

From the observations of different isotopologues observed in spectral scans and surveys, one can determine the isotopic ratios in M 82. Different isotopic ratios can shed light on the evolution of the galaxy, as well as the influence of massive stars on the ISM.

- $\frac{^{12}\mathrm{C}}{^{13}\mathrm{C}}$ is a good tracer of chemical evolution in a given galaxy: ^{12}C is a direct product of nucleosynthesis through helium burning in massive stars, whereas ^{13}C is a secondary nuclear product of ^{12}C (Henkel et al. 1998; Martín et al. 2010). The high $\frac{^{12}\mathrm{C}}{^{13}\mathrm{C}}$ isotope ratio also indicates an enhancement of ^{12}C through nucleosynthesis in massive stars. Henkel et al. (1998) measured isotope ratios of $\frac{^{12}\mathrm{C}}{^{13}\mathrm{C}} > 40$, which is much higher than the value of ~ 20 estimated for the Galactic Centre (Wilson and Rood 1994). From observations of CCH, ^{13}CCH, and C^{13}CH, Martín et al. (2010) concluded that the $\frac{^{12}\mathrm{C}}{^{13}\mathrm{C}}$ isotope ratio could be much higher than previously thought, giving a lower limit of ~ 138 for the ratio. From the $\frac{^{12}\mathrm{C}}{^{13}\mathrm{C}}$ isotope ratio, Martín et al. (2010) derived a lower limit for the column density of molecular hydrogen, $\mathrm{N}_{\mathrm{H}_2} > 2.6 \times 10^{22}\,\mathrm{cm}^{-2}$, by assuming that the conversion factor $\frac{\mathrm{CO}}{\mathrm{H}_2} = 8.5 \times 10^{-5}$.

- Using the IRAM 30-m Telescope, Sage et al. (1991) used C^{18}O observations to determine an $\frac{^{18}\mathrm{O}}{^{17}\mathrm{O}}$ isotope ratio of 8.3 ± 1.3 in M 82. The ratio found in M 82 is significantly higher than the ratios of $\sim 2.5 - 3.5$ in the central zone of the Milky Way (Zhang et al. 2015) and of 3-5 across the Galaxy (Wouterloot et al. 2005). Different hypotheses were presented in order to explain this high $\frac{^{18}\mathrm{O}}{^{17}\mathrm{O}}$ isotope ratio. For instance, Sage et al. (1991) explained that it is likely, that high mass star formation is favoured in M 82, leading to higher abundances for ^{18}O (since ^{18}O is mainly produced in massive stars), and lower abundances for isotopes produced in stars of intermediate mass such as ^{17}O. Sage et al. (1991) also stated, that if the supernovae are the main mechanism by which ^{18}O is enriched, the abundance of that isotope will then be strongly enhanced relative to other isotopes such as ^{17}O. Similarly, Heikkila et al. (1998) suggests that a high $\frac{^{18}\mathrm{O}}{^{17}\mathrm{O}}$ implies that the starburst activity favoured the formation of massive stars, and that the high isotope ratio is indicative of the high metallicity of the surrounding ISM.

- Henkel et al. (1998) measured an isotope ratio of $\frac{^{16}\mathrm{O}}{^{18}\mathrm{O}} > 90$ in M 82. However, Martín et al. (2010) used previous ^{13}CO observations to derive a lower limit of $\frac{^{16}\mathrm{O}}{^{18}\mathrm{O}} > 350$, which is similar to the value of $\frac{^{16}\mathrm{O}}{^{18}\mathrm{O}} \sim 330$ that is estimated in the Galactic Centre (Wilson and Rood 1994).

- Martín et al. (2009) derived a column density of $(14 \pm 4) \times 10^{13}\,\mathrm{cm}^{-2}$ for CS, and $(8.1 \pm 1.9) \times 10^{12}\,\mathrm{cm}^{-2}$ for C^{34}S, within a 25″-beam of the 30-m IRAM single dish telescope. This gave a factor of ~ 17.5 for $\frac{^{32}\mathrm{S}}{^{34}\mathrm{S}}$, indicating an isotopical enrichment of ^{34}S through the formation of massive stars. In Galactic Disk, the isotopic ratio $\frac{^{32}\mathrm{S}}{^{34}\mathrm{S}}$ is ~ 24 (Chin et al. 1996).

- Using observations of HC^{14}N and HC^{15}N, Henkel et al. (1998) derived a lower limit of 100 for the $\frac{^{14}\mathrm{N}}{^{15}\mathrm{N}}$ isotopic ratio. The Galactic Centre has an isotopic ratio of $\frac{^{14}\mathrm{N}}{^{15}\mathrm{N}} \sim 120 - 400$ (Adande and Ziurys 2012). This isotopic ratio is thought to be a good indicator of the nucleosynthesis processes that are taking place. The isotope ^{14}N can be synthesised in stars starting from H and He, or from either ^{13}C or ^{17}O in both cold and hot CNO cycles (Adande and Ziurys 2012). However, ^{15}N can only be synthesised from ^{15}O in hot CNO cycles, and possibly in Type Ia and Type II supernovae (Adande and Ziurys 2012). Therefore, this ratio can give insights on the type of stars formed in the observed region.

3.2 IC 342

IC 342 is one of the most prominent molecular sources in the northern hemisphere. Also known as Cadwell 5, it is an intermediate spiral galaxy of type SAB(rs)cd[4] (de Vaucouleurs et al. 1976). Located at a distance of 3.3 Mpc from the Milky Way (Saha et al. 2002, for more details see Section 3.2.1), it has a right ascension RA (J2000): $03^{\mathrm{h}}46^{\mathrm{m}}48^{\mathrm{s}}.5$, a declination DE (J2000): $+68°05'46''$, a radial velocity of $31 \pm 3\,\mathrm{km\,s^{-1}}$, and an inclination of $25°$ (Newton 1980). It is the second brightest galaxy in the IC 342/Maffei group, and it is the brightest in the IC 342 group, which is the closest galaxy group to the Local Group (Karachentsev 2005). Hodge and Kennicutt (1983) counted 666 separate H II regions in IC 342 using Hα images. IC 342 has an H II nucleus (Ho et al. 1997). Meier (2014) made the case that IC 342 is very similar to the Milky Way, as they share similar dynamical and molecular gas mass, similar photon ionisation rate, and similar X-ray luminosity. However, the central region of IC 342 (132×132 pc) has a star formation rate of $\sim 0.15\,\mathrm{M_{\odot}\,yr^{-1}}$(Balser et al. 2017), assuming a distance of 3.3 Mpc. For comparison, the total star formation rate in the Milky Way has been estimated around $\sim 1.7\,\mathrm{M_{\odot}\,yr^{-1}}$ (Robitaille and Whitney 2010).

3.2.1 Distance to IC 342

Its position near the Galactic equator makes IC 342 difficult to observe at optical wavelengths. In particular, it makes it difficult to determine its distance from the Local Group. Early estimates vary between 1.3 and 8 Mpc (Sandage and Tammann 1974; McCall 1989), due to uncertainties in the absorption, the extinction of IC 342, and the Galactic extinction (Sandage and Tammann 1974; McCall 1989; Karachentsev and Tikhonov 1993). Originally, Edwin Hubble classified IC 342 as a possible member of the Local Group (Hubble 1936). However, Karachentsev and Tikhonov (1993) later discovered, using extinction values from Ables (1971) that, IC 342 has a distance of at least 2.08 Mpc, and thus is halfway between M 81/NGC 2403 and the Local Group, which means, it cannot be a part of the Local Group. Saha et al. (2002) used the photometry of 20 Cepheids to estimate a value of 3.28 ± 0.26 Mpc. Tikhonov and Galazutdinova (2010) measured a distance of 3.93 ± 0.10 Mpc to IC 342 using the tip of the red giant branch method, stating that it offers more accurate resutls than the Cepheid photometry method. This difference in distances affects the determination of the physical parameters of IC 342, such as its luminosity and its mass ($M \propto D$ and $L \propto D^2$). The different calculated distances to IC 342 can also affect spatial resolution[5] l ($l \propto D$)and the star formation rate[6] (since SFR $\propto D^2$). From the infra-red tip of the red giant branch, Wu et al. (2014) estimated a distance of $\sim 3.31 \pm 0.20\,\mathrm{Mpc}$. In the recent literature, the distance of $\sim 3.3\,\mathrm{Mpc}$ is widely used (eg. Aladro et al. 2011b; Lebrón et al. 2011; Balser et al. 2017). Therefore, in this work, a value of 3.3 Mpc for the distance to IC 342 is adopted, in order to simplify and facilitate the comparison of the obtained results with those of previous studies.

---

[4] It is classified as intermediate between unbarred (SA) and barred galaxy (SB), thus it has the type SAB. It is also an intermediate type between ringed (r), and spindle (s), which makes it an (rs) type. Finally, the tightness of the arms is halfway between c and d, and therefore it is a cd type.

[5] The angular resolution $\theta = \frac{l}{2D}$, where l is the spatial resolution and D is distance to the galaxy.

[6] The SFR is proportional to the luminosity of a galaxy (Buat 2015), and therefore, proportional to D^2

3.2.2 Structure and Morphology

Being a nearby galaxy and one of the most luminous infra-red galaxies in the northern hemisphere, many studies targeted this source to study its structure and morphology, especially its disk and arms. Maps of CO($J = 1 - 0$) show a ring-like structure with a non-circular gas motion in the inner nuclear regions of IC 342, which is typical for barred spiral galaxies (Ishizuki et al. 1990). Through VLA observations of H I, the kinematics of IC 342 have been studied by Crosthwaite et al. (2000) who found evidence of a density wave in the inner disk and four-arm patterns in the outer disk and identified interconnected spiral segments between 2 and 5 kpc. These spiral arms are consistent with the material arms resulting from gravitational instabilities (Crosthwaite et al. 2000). Radio observations showed an enhancement of CO($J = 1 - 0$) in the spiral arms, and revealed two components for the H_2 gas, the nuclear region and a molecular disk (Sage and Solomon 1991). Interferometric observations in IC 342, showed spatial differences in the distribution of ^{12}CO and ^{13}CO (Meier et al. 2000). The spatial differences indicate that the bulk of the dense molecular gas (traced by ^{13}CO) was observed to have temperatures between 10 and 20 K, this bulk is surrounded by PDRs (traced by ^{12}CO), with temperatures reaching higher than 50 K (Meier et al. 2000). These temperatures were derived from the line ratios of $\frac{^{13}\mathrm{CO}(2-1)}{^{13}\mathrm{CO}(1-0)}$ and $\frac{^{12}\mathrm{CO}(2-1)}{^{12}\mathrm{CO}(1-0)}$ (Meier et al. 2000). However, lower transitions of CO and its isotopologues cannot always uniquely disentangle whether the excitation is mainly due to a high H_2 density, a high kinetic temperature, or a combination of both (e.g. Mauersberger et al. 1999). Using several NH_3 transitions, Mauersberger et al. (2003) found two components in the molecular gas of IC 342: a cold component with a temperature of $\sim 53\,\mathrm{K}$ and a hot component with a temperature of $\sim 443\,\mathrm{K}$. Later, Lebrón et al. (2011) determined temperatures between 23 and 920 K, using the same NH_3 transitions.

The dynamical mass of IC 342 within 100 pc is around $\sim 2 \times 10^8\,\mathrm{M}_\odot$ (Meier 2014), which is similar to the mass within the same radius in the Milky Way (Meier 2014 and reference therein). Radio observations from the Effelsberg 100-m telescope and the VLA aimed at the magnetic fields in IC 342, which proved to be typical of barred spiral galaxies (Beck 2015). They detected a radio continuum disk which is much more intense in the centre than in the outer parts of the disk. The radio continuum emission seems to follow the infra-red dust emission, whereas the polarised emission seems to be concentrated in the spiral arms, suggesting a compression induced by a density wave (Beck 2015) (evidence for a density wave in IC 342 is presented in Turner and Hurt 1992; Crosthwaite et al. 2000).

Figure 3.3 is an infra-red image of IC 342, showing the dust structure of the galaxy. The star forming regions appear in bright red-yellow, due to the higher temperature of dust, compared to the other regions. The bar of dust seen on both sides of the centre, is fuelling this star-formation burst that is happening in the centre. This burst is highlighted by a strong and bright IR-emission. The galaxy IC 342 is situated close to the Galactic Plane, which makes obscuration measurements difficult. The low surface brightness of IC 342 is in part due to a low star-density, and in part due to Galactic extinction due to its location close to the Galactic plane.

From the infra-red analysis, it was estimated that if a supermassive black hole exists in IC 342, its mass is limited by $< 5 \times 10^5\,\mathrm{M}_\odot$ (Böker et al. 1999). Any SMBH in IC 342 would be then at least an order of magnitude less massive than the SMBH in the Milky Way (Eckart and Genzel 1997; Ghez et al. 1998, 2008). There has been some discussion on whether or not the presumable SMBH of IC 342 is in fact active. High resolution X-ray observations suggested that an AGN can be contributing to the total X-ray emission from IC 342 that may be dominated by starburst emission, however, this possibility was neither confirmed nor excluded (Mak et al. 2008).

Rigopoulou et al. (2013) suggested that the CO excitation in IC 342 can be fully explained by

PDRs without the need to invoke additional heating mechanisms. Moreover, based on chemical studies, Nakajima et al. (2018) could not detect any significant effect of an AGN or starburst on the chemistry of IC 342 on scales of about 1 kpc.

Figure 3.3: Infra-red image of IC 342: Blue shows the infra-red emission at 3.6-4.5 μm. Red shows the infra-red emission at 5.8-8 μm. The image has been captured by Spitzer IRAC. This image shows the web-structured dust in red. The low surface brightness of the galaxy is indicative of a low star-density (stars are seen in blue). The centre and the disk of the galaxy are very bright (red-white), due to the warm dust found in the central regions of the galaxy. The strong brightness of the centre is indicative of a strong star formation burst, that is taking place in small regions in the centre. This figure has been captured by Spitzer's - Infra-Red Array Camera (Spitzer - IRAC) on 20 July 2011. The scale of the image is $33'.3 \times 28'.4$ or $33.88\,\mathrm{kpc} \times 28.89$ kpc. Credit: NASA/JPL-Caltech/J. Turner (UCLA)

3.2.3 Star Formation in IC 342

Many studies have investigated star formation in IC 342, and discussed the possibility of a early-age starburst in the nuclear region of the galaxy. The galaxy exhibited a strong 6-cm radio continuum emission in the nuclear region indicative of enhanced starburst activity, that is fuelled by the large amount of molecular gas that is detected in the bars (Ishizuki et al. 1990). Moreover, the diffuse component of the X-ray emission has a similar morphology to that of the 1.4 GHz emission and the emission of Hα (Bregman et al. 1993). This diffuse component can be interpreted in terms of a hot gas bubble, with an estimated age of $\sim 2 \times 10^5$ years, confined within the disk, suggesting that IC 342 could be a starburst galaxy in its early stages (Bregman et al. 1993). Later near infra-red observations of the central 110 pc revealed a cluster of young and massive supergiants ($\sim 10^7$ years old with masses between 12 and 18 $\mathrm{M}_\odot$) surrounded by a molecular gas ring that extends up to a diameter of 70 pc (Boker et al. 1997). The molecular ring encompasses H II complexes with an age of $\sim 5 \times 10^6\,\mathrm{M}_\odot$ which implies that the star formation is propagating from the inside of the ring, in an outward direction (Boker et al. 1997). High-resolution infrared observations in the K-band showed a cluster with a mass of $\sim 6 \times 10^6 \mathrm{M}_\odot$, and a velocity dispersion of $\sigma = (33 \pm 3)\,\mathrm{km\,s^{-1}}$ within few hundred pc from the centre of IC 342 (Böker et al. 1999). The age of the cluster is estimated to be between 10^6 and 10^8 years, and its mass-to-light ratio of around 0.047 $\frac{\mathrm{M}_\odot}{\mathrm{L}_\odot}$ (Böker et al. 1999). Different mechanisms seem to be causing a possible starburst in IC 342, where cloud-cloud collisions and gravitational instabilities provoke the star formation in the central region of the galaxy while gravitational instability dominates the star formation in the disk (Pan et al. 2014). It has also been suggested that the star formation is more efficient in the centre of the galaxy than in the disk, due to the existence of more dense gas in the centre (Sage and Solomon 1991). Interferometric spectral studies revealed that the centre of IC 342 is mostly dominated by PDRs (Meier and Turner 2005). However, star formation events can reoccur in the nucleus of IC 342, as the gas inflow of $\sim 0.14\,\mathrm{M}_\odot\,\mathrm{yr}^{-1}$ is sufficient to sustain re-occuring star formation events (Schinnerer et al. 2003).

The spiral galaxy IC 342 showed evidence of an early-stage starburst (eg. Bregman et al. 1993) and of a number of PDRs that are dominating the heating mechanism of the molecular clouds (eg. Meier et al. 2000; Rigopoulou et al. 2013). However, there have been evidence to suggest that IC 342 cannot be classified as a starburst galaxy. With a star formation rate of $\sim 0.15\,\mathrm{M}_\odot\,\mathrm{yr}^{-1}$ in the central region (Balser et al. 2017) (which is consistent with previous estimation of SFR of $\sim 0.1\,\mathrm{M}_\odot\,\mathrm{yr}^{-1}$of Turner and Hurt 1992), the star formation in IC 342 is less efficient than in the Milky Way, which has a star formation rate of $\sim 1.7\,\mathrm{M}_\odot\,\mathrm{yr}^{-1}$ (Robitaille and Whitney 2010). Moreover, IC 342 has a ratio of infrared luminosity versus isophotal area, $\log\left(\frac{L_{FIR}}{D_{25}^2}\right)$ $(\mathrm{L}_\odot\,\mathrm{kpc}^{-2})$ below 7.25 (D_{25} is the optical linear size given in kpc), indicating that IC 342 is not a starburst galaxy (Mao et al. 2010).

3.2.4 X-ray Point Sources in IC 342

Both diffuse and point source X-ray emission can be observed in the central regions of IC 342 (Bregman et al. 1993). Kong (2003) detected around 37 X-ray point sources, most of them in the spiral arms. The sources had a typical luminosity of $\sim 10^{37}\,\mathrm{erg\,s^{-1}}$ (Kong 2003). Among the detected sources, several were ultra-luminous. The three most prominent sources are denoted as X7, X13, and X21 by Kong (2003) and as IC 342 X-1, IC 342 X-2, and IC 342 X-3 respectively by Mak et al. (2011). The ULX IC 342 X-1 (X7) is suggested to be a black hole with a mass ranging from 10 to 30 $\mathrm{M}_\odot$ (Kubota et al. 2002; Kong 2003). IC 342 X-2 is suggested to be a binary system accreting matter, however, more studies are needed to determine its nature (Mak et al. 2011). The ULX IC 342 X3 (or X21) is located around $\sim 3''$ from the dynamical centre of IC 324 (Kong 2003). The nature of this source is still debated. Kong (2003) suggested that it is either an intermediate-mass black hole with a mass of at least $\sim 120\,\mathrm{M}_\odot$, or a stellar mass black hole with strong wind.

3.2.5 Spectroscopic Data

Being nearby and similar to the Milky Way (Meier 2014), the early-stage starburst galaxy IC 342 has been the target of a number of spectroscopic studies. Knapp et al. (1980) detected CO(2-1) in IC 342, revealing an optically thick molecular line. Using the Effelsberg 100-m telescope, Martin and Ho (1986) detected three transitions of NH3 in the innermost 1 kpc of IC 342, corroborating the existence of warm gas ($50 - 70\,\mathrm{K}$) in the nuclear region of the galaxy. Martin and Ho (1986) suggested that this gas is the result of OB star formation near the nucleus. Interferometric IRAM observations showed that the 3.4 mm continuum is due to free-free emission (Downes et al. 1992). From this study, the first extragalactic molecular line intensity ratios were derived revealing a ratio of $\sim$ 7 for $\frac{\mathrm{CO}}{\mathrm{HCN}}$(J=1-0), and a ratio of $\sim$2 for both $\frac{^{13}\mathrm{CO}}{\mathrm{HCN}}$(J=1-0) and $\frac{\mathrm{HCN}}{\mathrm{NH_3}}$ (Downes et al. 1992). Downes et al. (1992) also noted that there are only moderate star formation activities, thus concluding that the gas is most likely heated through turbulence. The HCN maps showed that the emission regions for HCN and IR emission are smaller than the emission regions of CO(1-0), suggesting that HCN is well correlated with the IR emission, unlike CO, but neither trace star formation (Downes et al. 1992).

The maps of ^{12}CO and ^{13}CO obtained from the Owens Valley Millimeter Array showed that ^{12}CO maps are tracing warm PDRs, while ^{13}CO traces the colder bulk of the molecular gas (Meier et al. 2000). Schulz et al. (2001) argued that no additional heating mechanism other than PDR are required to explain the density and temperature gradients, and CO and C II lines tracing the warm gas ($\sim 50\,\mathrm{K}$). However, they also argued that for the cold gas ($\lesssim 30\,\mathrm{K}$), PDR excitation becomes negligible as a heating mechanism, giving way to turbulence and cosmic rays (Schulz et al. 2001). The fact that the molecular gas in IC 342 is composed of two components with different temperatures and densities is corroborated by the VLA observations conducted by Montero-Castaño et al. (2006). In these observations, they detected $\mathrm{NH_3}$(6-6) for the first time in an extragalactic source. Further observations of $\mathrm{NH_3}$(6-6) suggested that the lack of detection of $\mathrm{NH_3}$ in lower transitions is indicative of a maser in the $\mathrm{NH_3}$(6-6) transition (Lebrón et al. 2011).

Despite numerous detections of PDR tracers, the shock tracers SiO and $\mathrm{H^{13}CO^+}$ were detected mainly in a region of around $\sim 300\,\mathrm{pc}$ off the centre in the northern spiral arm of IC 342, and from a smaller region in the nuclear ring (Usero et al. 2006). The differences in the intensity ratios of $\frac{\mathrm{SiO}}{\mathrm{H^{13}CO^+}}$, where the ratio is significantly higher in the spiral arm than in the nuclear ring, shows that shocks are influencing the molecular gas chemistry in IC 342 (Usero et al. 2006). By comparing the SiO emission to the emission of another shock tracer, $\mathrm{CH_3OH}$, they determined that the shock velocity is similar in the two emission regions of SiO (Usero et al. 2006). However, Usero et al. (2006) concluded that the SiO emission revealed large-scale shocks predating the starburst phase, and mostly caused by cloud-cloud collisions in the bar of IC 342. Baan et al. (2008) identified PDR regions from the $J = 1 - 0$ ratios $\frac{\mathrm{HCO^+}}{\mathrm{HCN}} = 0.51 \pm 0.06$, and $\frac{\mathrm{HNC}}{\mathrm{HCN}} = 0.34 \pm 0.02$, while the ratio of $\frac{\mathrm{HNC}}{\mathrm{HCO^+}} = 0.65 \pm 0.07$ indicated the presence of X-ray dominated regions. Moreover, unlike in M 82, different transitions of HNCO were detected in both the central and the offset regions of IC 342, indicating that the starburst in IC 342 is still in its early stages, as HNCO is easily destroyed by radiation from PDRs (Martín et al. 2009).

Targeted spectroscopic observations revealed ratios of $\frac{^{18}\mathrm{O}}{^{17}\mathrm{O}} \gtrsim 5.5$ (Sage et al. 1991), $\frac{^{16}\mathrm{O}}{^{18}\mathrm{O}} > 125$ and $\frac{^{12}\mathrm{C}}{^{13}\mathrm{C}} > 30$ (Henkel et al. 1998). These ratios showed that, even though the star formation is less active in IC 342 than in M 82, massive star formation is preferred in both galaxies (Sage et al. 1991; Henkel et al. 1998). CS (J = 2 - 1) emission has been mapped by Mauersberger and Henkel (1989). The morphology is s similar to the CO(3 - 2) maps published by Steppe et al. (1990). The CS emission seems to originate from confined regions close to the nucleus of IC 342, where the $\mathrm{H_2}$ density is high ($n_{\mathrm{H_2}} \leqslant 10^5\,\mathrm{cm^{-3}}$), but it is not clear whether the emission region forms a bar-like structure or simply two unresolved emission regions (Mauersberger and Henkel 1989). Higher resolution studies of the composition of IC 342 have been conducted more recently. Interferometric imaging mapped the emission of molecules and better defined their emission regions. For instance, eight molecules have been mapped and detected using the Owens Valley Millimeter Array: C_2H, $C^{34}S$, N_2H^+, CH_3OH, HNCO, HNC, HC_3N, and SO (Meier and Turner 2005). With the exception of SO, all molecules showed bright emission and a correlation with each other of the zeroth order. This indicates that all those molecules are emitted from dense molecular clouds. However, Meier and Turner (2005) have been able to distinguish between three different emission regions. Dense molecular cloud tracers such as N_2H^+, HNC, and HCN are bright and widespread: however, PDR tracers such as C_2H, and $C^{34}S$ were only found within the innermost 50-100 pc of the central region. This central region is the location where high radiation fields are expected. Finally, CH_3OH (a shock tracer) is correlated well with HNCO (another shock tracer), which places their emission region at bar-induced orbital shock locations. Moreover, Meier and Turner (2005) found that HC_3N is correlated well with the 3-mm continuum emission, which led to the conclusion that the warmest and densest molecular gas can be found in young starbursts. Aladro et al. (2011b) detected CS, and different transitions of HC_3N and CH_3CCH in both M 82 and IC 342, however, CH_3CCH was significantly less abundant in IC 342 than in M 82. Moreover, IC 342 exhibits strong density gradients between different regions, leading to a more evolved star formation in the nuclear region of IC 342, and an early-stage star formation in the outer regions (Meier and Turner 2005; Aladro et al. 2011b).

3.3 Similarities between M 82 and IC 342

Table 3.2: Parameters overview of M 82, IC 342, Milky Way

Galaxy	M 82	IC 342	Milky Way
Type	Barred Spiral (Mayya et al. 2005)	Barred Spiral (de Vaucouleurs et al. 1976)	Barred Spiral (Ortiz and Lepine 1993)
Distance from MW^a	3.5-3.8 Mpc	3.3±0.3 Mpc^b	-
CMZ View	Edge-on	Face-on	Edge-on
Global Molecular Gas Mass ($M_\odot$)	10^8 (Aladro et al. 2011b)	10^8 (Aladro et al. 2011b)	$(0.2-0.6)\times10^8$ (Sodroski et al. 1995)
Dynamical Mass ($M_\odot$)	2×10^9 (R<500 pc) (Greco et al. 2012)	2×10^8 (R<100 pc) (Balser et al. 2017)	2×10^8 (R<100 pc) (Balser et al. 2017)
Density of 25% gas in CMZ (n_{H_2} in cm^{-3})	10^5-10^6 (Aladro et al. 2011b)	10^5-10^6 (Aladro et al. 2011b)	10^5-10^6 (Aladro et al. 2011b)
Density of Bulk Gas (cm^{-3})	10^4 (Aladro et al. 2011b)	10^4 (Balser et al. 2017)	10^4 (Aladro et al. 2011b)
Column Density of H_2 (cm^{-2})	2.6×10^{22} (Martín et al. 2010)	10^{22} (Meier and Turner 2005)	
Heating mechanisms in CMZs	PDRs	PDRs, Shocks	Shocks
Star Formation Rate ($M_\odot$ yr^{-1})	$\sim$10 (Aladro et al. 2011b)	$\sim$ 0.15 (Balser et al. 2017)	$\sim 0.68-1.45$ (Robitaille and Whitney 2010)

a) In this work, a distance of 3.6 Mpc was adopted for M 82, and of 3.3 Mpc for IC 342
b) See Chapter 3, Section 3.2, Subsection 3.2.1 for the discussion about distance measurements in IC 342

Both galaxies M 82 and IC 342 have a similar H_2 mass of around 10^8 $M_\odot$ in their central molecular zones (CMZ) (Aladro et al. 2011b), while in the Milky Way, the $\mathrm{H_2}$ mass is around $0.2-0.6\times10^{8}\,\mathrm{M_\odot}$ within 100 pc radius (Sodroski et al. 1995), and a total $\mathrm{H_2}$ mass of $2.5\times10^{9}\,\mathrm{M_\odot}$ (Combes 1991).

Multilevel studies of molecules with high dipole moment (e.g. $\mathrm{HC_3N}$ or $\mathrm{CH_3CN}$) show that 25% of the gas in the CMZ of M 82, IC 342, and the Milky Way, has densities $\mathrm{n_{H_2}}=10^{5}-10^{6}\,\mathrm{cm^{-3}}$ (de Vicente et al. 1996 and Aladro et al. 2011b), while the density of the bulk of the gas is still $10^{4}\,\mathrm{cm^{-3}}$ (de Vicente et al. 1996; Aladro et al. 2011b and Balser et al. 2017). A parameter overview summarising the properties of all three galaxies is presented in Table. 3.2.

Chapter 4

Observation and Data Reduction

4.1 Observations

The data used in this study have been observed with the IRAM Plateau de Bure Interferometer (PdBI), now known as The Northern Extended Millimetre Array (NOEMA). The observations covered the 3-mm range from 85.7 to 115.1 GHz, with a six-antenna interferometer in configurations A, B and C on 25 April 2012 , and between January and October 2013. The 15 baselines between 6 antennas[1] (each antenna has a diameter of 15 m) range from 88 to 452 metres. The targets of this line survey were the innermost few hundred pc of the central molecular zones in IC 342 and M 82. The maximum field of view is $57.9'' \times 57.9''$, for M 82 and IC 342 at 87.1 GHz. For each source, there have been eight frequency-tunings centred at 87.1, 91.2, 94.8, 98.4, 102, 105.6, 109.2, and 112.8 GHz, each covering a bandwidth of 3.6 GHz and a total of 1843 channels of 2 MHz width. Typically, we integrated four hours on-source observing time per frequency tuning, resulting in a sensitivity of $\sigma = 2$ mJy for each frequency tuning. The spatial resolution for each of the frequency tunings was slightly different (see Tables 4.1,). For a better comparison, the spatial resolution has been smeared to $2.9'' \times 2.9''$ for M 82 and $2.7'' \times 2.7''$ for IC 342. The absolute flux calibration was obtained by observing the source MWC 349 with an assumed spectral flux density of 1.26 Jy. This source provides a calibration accuracy of $5 - 10\,\%$ throughout the 3-mm band (M. Krips, Private Communications). For some observations, other sources have been used for flux calibration. For phase calibration, the source 0954+658 has been observed every 22 minutes. The baseline calibration was done during the observations by the astronomer on duty (AoD). Data calibration was performed using the IRAM-pipeline with the Continuum and Line Interferometer Calibration (CLIC)[2] package of the Grenoble Image and Line Data Analysis Software or GILDAS[3], that takes the PdBI raw data format as input and gives uv-tables as output. These uv-tables only contain the calibrated visibilities of the observed sources.

---

[1] For N antennas, one has $\frac{N(N-1)}{2}$ baselines.

[2] https://www.iram.fr/IRAMFR/GILDAS/doc/pdf/clic.pdf

[3] http://www.iram.fr/IRAMFR/GILDAS/

Table 4.1: Observations of M 82 and IC 342 with a spectral resolution of 2 MHz. The velocity resolution is given as: $\Delta v = \frac{c\times\Delta\nu}{\nu}$ where $\Delta\nu$ is the spectral resolution and ν is the observed frequency.

Frequency	Source	Beam size	Beam size	Position Angle	Noise	Velocity Resolution
		Major Axis	Minor Axis			
MHz		arcsec	arcsec	degree	mJy/beam	$\mathrm{km\,s^{-1}}$
87 100	M 82	2.48±0.03	1.76±0.02	-225.74±1.24	1.35	6.88
91 200	M 82	1.79±0.01	1.34±0.01	108.65±0.55	1.70	6.57
94 800	M 82	1.47±0.01	1.34±0.001	67.99±1.43	1.30	6.32
98 400	M 82	1.74±0.01	1.33±0.01	81.01±0.69	0.30	6.09
102 000	M 82	1.58±0.001	1.23±0.001	33.66±0.40	1.93	5.88
105 600	M 82	2.85±0.11	1.43±0.06	61.26±2.07	2.21	5.68
109 200	M 82	1.25±0.01	0.99±0.01	81.84±1.28	2.65	5.49
112 800	M 82	1.98±0.02	1.49±0.02	21.06±1.77	2.24	5.32
87 100	IC 342	2.20±0.01	1.71±0.01	87.48±0.60	1.09	6.88
91 200	IC 342	2.10±0.01	1.54±0.01	48.02±0.44	1.27	6.57
94 800	IC 342	2.61±0.07	1.73±0.05	104.48±2.77	1.75	6.32
98 400	IC 342	2.51±0.01	1.52±0.001	10.61±0.28	1.77	6.09
102 000	IC 342	1.64±0.02	1.21±0.01	66.22±1.25	1.96	5.88
105 600	IC 342	2.67±0.01	1.67±0.01	38.71±0.31	2.28	5.68
109 200	IC 342	1.99±0.01	1.59±0.01	-16.93±0.94	1.95	5.49
112 800	IC 342	2.19±0.02	2.03±0.02	96.01±4.08	2.58	5.32

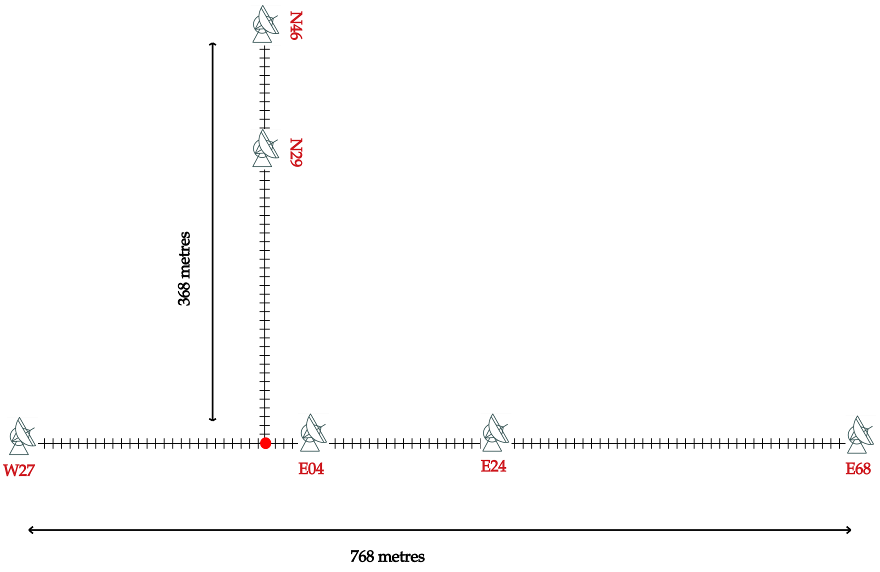

Figure 4.1: Example: The Plateau de Bure Interferometer in configuration A with 6 antennas. One distance unit is 8 metres. The distance is always counted from the intersection point between the tracks, represented by the red dot.

In Table. 4.1, the initial values of the major and minor axes of the beams for each observation are presented, as well as their position angles and the noise per beam. The tables 4.2, and 4.3, list the sources used for calibration. If the source flux is fixed, the values are noted with an (f), otherwise, if the flux of the source has been computed from another main calibrator, the values are denoted with (c). The antennas are denoted with the number of the antennas, followed by their configuration. The eastern antennas are denoted with "E", western antennas with "W", and the northern antennas with an "N". The distances between the intersection point of the tracks and the antennas are given by the number of distance units (1 unit = 8 metres) from the intersection to the antenna. For instance, if the antenna is described as 6A-E68: E04N29N46W27E24, this means there are 6 antennas in the configuration A (6A), without the antenna E68 (-E68), which is the eastern antenna that is at a distance of 544 metres (8×68 metres) from the intersection point, followed by a list of the antennas used which are two eastern antennas at 32 and 192 metres (8×4 metres and 8×24 metres, respectively), two northern antennas at 232 and 368 metres (8×29 metres and 8×46 metres respectively), and a western antenna at 216 metres (8×27 metres). Figure 4.1 depicts the distribution of the antennas at the Plateau de Bure Interferometer, where the longest baseline extending from the west to the east is 768 metres.

4.2 Data Reduction: Imaging and Extraction of Spectra (GILDAS)

For the reduction of data, different packages of the Grenoble Image and Line Data Analysis Software or GILDAS[4] were used. The MAPPING package was used for the imaging of the calibrated data, the cleaning, and the imaging of the cleaned data. With this package, the moments of the observed molecular lines were extracted, which showed the flux, velocity, and width distribution of each line. For the spectral analysis, the Continuum and Line Analysis Single-dish Software (CLASS)[5] was used. This package allowed the extraction of spectra from each data cube and, the subtraction of the baselines from the observed spectra. The spectra were averaged, and plotted. The lines were also identified and fitted using this package. CLASS is usually used to reduce data from single-dish telescopes with a ".30m" format. However, it can also be used to analyse interferometric data with a ".pdb" extension and format. For further line identification, fitting, abundances and excitation temperature calculations, MAdrid Data CUBe Analysis (MADCUBA) (Martin et al. in prep) was used. This software, equipped with different line catalogues, uses spectra from single-dish telescopes, and interferometres as input and allows an easy analysis and line identification.

For this project, there are no dedicated zero-spacing, and no short-spacing data. However, the results of the interferometric data of M 82 and IC 342 obtained from this study have been compared to single dish observation results of the IRAM-30m telescope done by Aladro et al. (2011b) and Aladro et al. (2015). In order to calculate the correlation between different emission regions, a principal component analysis (PCA) has been applied to the data, for which a python script has been used[6].

---

[4] http://www.iram.fr/IRAMFR/GILDAS

[5] https://www.iram.fr/IRAMFR/GILDAS/doc/pdf/class.pdf

[6] The python script has been written by Dr. Maria Cunningham from the university of New South Wales, Australia. The PCA module can be found online (http://folk.uio.no/henninri/pca_module/)

Table 4.2: Calibration Information for M 82. Values with an (f) are the assumed values in the calibration and values with (c) are computed. (P) represents the observations where polarisation has been detected.

Frequency	Date	Flux calibrator	Flux Calibrator	Phase/amplitute Calibrator	Antennas
GHz		MWC349	Other sources	0954+658	
87.1	25 April 2012	1.10 (f)	-	1.49 (c) (P)	6A-E68: E04N29N46W27E24
87.1	25 April 2012	1.10 (f)	-	1.07 (c) (P)	6C: W09E10N11N17W12E04
87.1	25 April 2012	1.00 (f)	-	1.05 (c) (P)	6C: W09E10N11N17W12E04
87.1	25 April 2012	0.80 (c)	-	1.10 (f) (P)	6A-E68: E04N29N46W27E24
87.1	25 April 2012	1.10 (f)	-	1.07 (c) (P)	6C: W09E10N11N17W12E04
87.1	25 April 2012	1.00 (c)	15.94 (3C 84) (f)	1.05 (c) (P)	6C: W09E10N11N17W12E04
91.2	1 January 2013	1.13 (f)	-	1.32 (c) (P)	6C: E04W09E10N17N11W12
91.2	28 February 2013	1.07 (c)	-	0.75 (f) (P)	6B: E12W12E23N46N20W27
91.2	4 March 2013	1.13 (f)	-	0.98 (c)	6B: E12W12E23N46N20W27
91.2	8 March 2013	-	17.77 (3C 84) (f)	0.92 (c)	6B: E12W12E23N46N20W27
94.8	2 January 2013	1.16 (f)	-	1.24 (c)	6C: E04W09E10N17N11W12
94.8	4 March 2013	-	16.90 (3C 84) (f)	0.77 (c)	6B: E12W12E23N46N20W27
94.8	9 March 2013	-	4.28 (0923+392) (f)	0.90 (c) (P)	6B: E12W12E23N46N20W27
94.8	14 March 2013	-	4.16 (0923+392) (f)	0.86 (c)	6B: E12W12E23N46N20W27
94.8	4 April 2013	-	15.67 (3C 84) (f)	0.99 (f)	6C-E10+E23: E04W09E23N17N11W12
94.8	9 April 2013	-	15.61 (3C 84) (f)	0.99 (c)	6C: E04W09E10N17N11W12
98.4	10 March 2013	1.19 (f)	-	1.04 (c)	6B: E12W12E23N46N20W27
98.4	10 March 2013	-	17.07 (3C 84) (f)	0.75 (c) (P)	6B: E12W12E23N46N20W27
98.4	19 April 2013	1.19 (f)	-	1.36 (c) (P)	6C-E04: W09E10N17N11W12
98.4	21 April 2013	1.19 (f)	-	1.26 (c) (P)	6C: E04W09E10N17N11W12
102	9 March 2013	1.15 (c)	-	0.90 (c) (P)	6B: E12W12E23N46N20W27
102	25 April 2013	-	5.56 (0923+392) (f)	1.23 (c) (P)	6C: E04W09E10N17N11W12
105.6	10 March 2013	-	14.74 (3C 84) (f)	0.82 (c) (P)	6B: E12W12E23N46N20W27
105.6	24 April 2013	1.24 (f)	-	1.17 (c) (P)	6C: E04W09E10N17N11W12
105.6	25 April 2013	1.24 (f)	-	1.22 (c) (P)	6C: E04W09E10N17N11W12
109.2	11 March 2013	0.93 (c)	-	0.89 (c) (P)	6B: E12W12E23N46N20W27
109.2	12 March 2013	-	17.42 (3C 84) (f)	+0.98 (c)	6B: E12W12E23N46N20W27
112.8	19 March 2013	-	2.38 (0059+581) (f)	1.07 (c)	6B: E12W12E23N46N20W27
112.8	22 March 2013	-	17.75 (3C 84) (f)	1.13 (c) (P)	6B: E12W12E23N46N20W27
112.8	4 April 2013	-	16.57 (3C 84) (f)	1.15 (c)	6C-E10+E23: E04W09E23N17N11W12
112.8	6 April 2013	-	10.57 (2200+420) (f)	1.17 (c)	6C: E04W09E10N17N11W12
112.8	9 April 2013	1.29 (f)	-	1.18 (c)	6C: E04W09E10N17N11W12
112.8	11 April 2013	1.29 (f)	-	1.30 (c)	6C: E04W09E10N17N11W12
112.8	16 April 2013	-	4.41 (0923+392) (f)	1.24 (c) (P)	6C-E04: W09E10N17N11W12
112.8	21 April 2013	-	4.47 (0923+392) (f)	1.27 (c) (P)	6C: E04W09E10N17N11W12

Table 4.3: Calibration Information for IC 342. Values with an (f) are the fixed values in the calibration and values with (c) are computed. (P) represents the observations where polarisation has been detected.

Frequency	Date	Flux calibrator	Flux Calibrator	Phase/amplitute Calibrator	Antenna
GHz		MWC349	Other sources	0224+671	
87.1	25 April 2012	1.10 (f)	-	0.63 (c) (P)	6A-E68: E04N29N46W27E24
87.1	25 April 2012	1.00 (c)	16.26 (3C 84) (f)	0.67 (c) (P)	6C: W09E10N11N17W12E04
87.1	25 April 2012	1.10 (f)	-	0.63 (c)	6A-E68: E04N29N46W27E24
91.2	23 March 2013	-	16.32 (3C 84) (f)	1.23 (c)	6B: E12W12E23N46N20W27
91.2	26 March 2013	1.13 (f)	-	1.49 (c) (P)	6B: E12W12E23N46N20W27
91.2	16 April 2013	0.94 (c)	8.23 (2200+420) (f)	1.12 (c) (P)	6C-E04: W09E10N17N11W12
94.8	30 March 2013	-	14.53 (3C 84) (f)	1.24 (c)	6B: E12W12E23N46N20W27
94.8	2 May 2013	1.08 (c)	4.25 (2013+370) (f)	1.06 (c) (P)	6C: E04W09E10N17N11W12
98.4	1 April 2013	1.19 (f)	-	1.46 (c)	6C: E04W09E10N17N11W12
98.4	2 May 2013	1.19 (f)	-	1.03 (c) (P)	6B: E12W12E23N46N20W27
102	1 April 2013	1.21 (f)	-	1.37 (c)	6B: E12W12E23N46N20W27
102	2 April 2013	1.21 (f)	-	1.46 (c)	6B: E12W12E23N46N20W27
102	25 April 2013	1.21 (f)	-	1.16 (c) (P)	6C: E04W09E10N17N11W12
105.6	3 April 2013	1.24 (f)	-	1.41 (c)	6B: E12W12E23N46N20W27
105.6	22 April 2013	1.10 (c)	4.48 (0923+392) (f)	1.16 (c)	6C: E04W09E10N17N11W12
105.6	24 April 2013	1.24 (f)	-	1.12 (c)	6C: E04W09E10N17N11W12
109.2	2 April 2013	-	17.29 (3C 84) (f)	1.46 (c) (P)	6B: E12W12E23N46N20W27
109.2	3 April 2013	1.26 (f)	-	1.41 (c)	6B: E12W12E23N46N20W27
109.2	21 April 2013	1.21 (c)	8.30 (2200+420) (f)	1.13 (c) (P)	6C: E04W09E10N17N11W12
112.8	22 March 2013	1.29 (f)	-	1.35 (c)	6B: E12W12E23N46N20W27
112.8	25 March 2013	-	9.78 (2200+420) (f)	1.19 (c)	6B: E12W12E23N46N20W27
112.8	30 March 2013	1.29 (f)	-	1.37 (c)	6B: E12W12E23N46N20W27
112.8	16 April 2013	1.29 (c)	-	1.14 (f)	6C-E04: W09E10N17N11W12
112.8	21 April 2013	1.29 (f)	-	1.18 (c) (P)	6C: E04W09E10N17N11W12
112.8	24 April 2013	1.31 (c)	7.91 (3C 273) (f)	1.13 (c)	6C: E04W09E10N17N11W12
112.8	28 April 2013	-	22.70 (3C 279) (f)	1.78 (c)	6C: E04W09E10N17N11W12
112.8	28 April 2013	1.29 (f)	-	1.11 (c) (P)	6C: E04W09E10N17N11W12
112.8	2 May 2013	1.29 (f)	-	1.07 (c)	6C: E04W09E10N17N11W12
112.8	3 May 2013	1.29 (f)	-	1.16 (c)	6C: E04W09E10N17N11W12

The calibrated data are stored as uv-tables (".uvt" extension), containing the calibrated visibilities of the sources. As an example the uv-coverage of an observation is shown in Fig. 4.2. In order to convert the uv-tables into images, the command " go uv_map" is used. This command created a map from the uv-tables, through a convolution function and a fast Fourier transform of the individual spectral channels. The output of this command is a ".lmv" extension file. This is an lmv cube with two coordinate axes and one velocity (or frequency) axis (x, y, velocity). For the analysis of the spectral line images, one must first subtract the continuum emission from the data cube. In order to do so, the continuum emission between emission lines was averaged using the "go uv_average" command in MAPPING (The emission lines were determined from the averaged spectrum in the bottom right frame as seen in the left plot in Fig.4.3). The average continuum emission was then subtracted from the initial data cube using the "go uv_subtract" command (see Fig. 4.3).

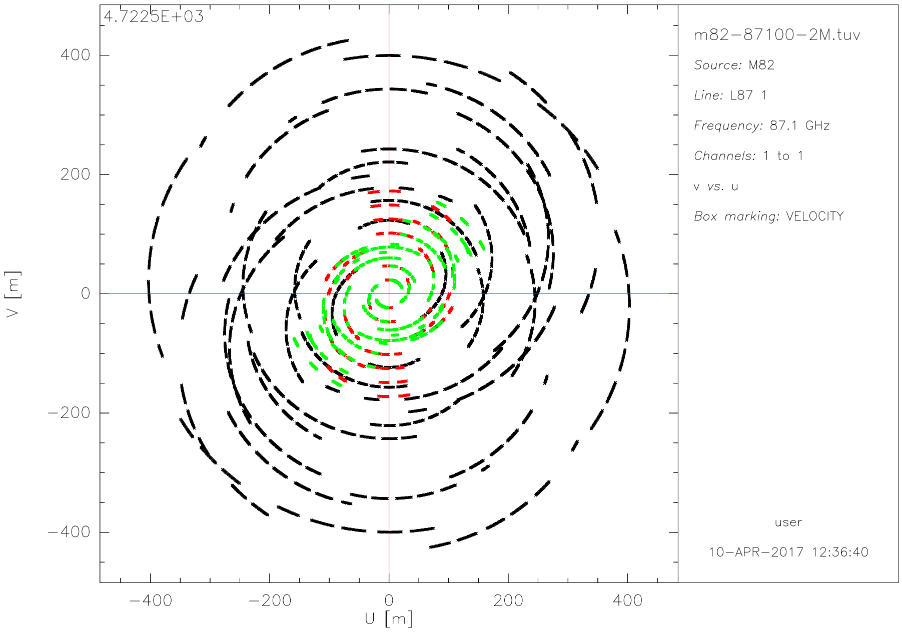

Figure 4.2: The uv-coverage of the observations at 87.1 GHz frequency tuning of M 82.

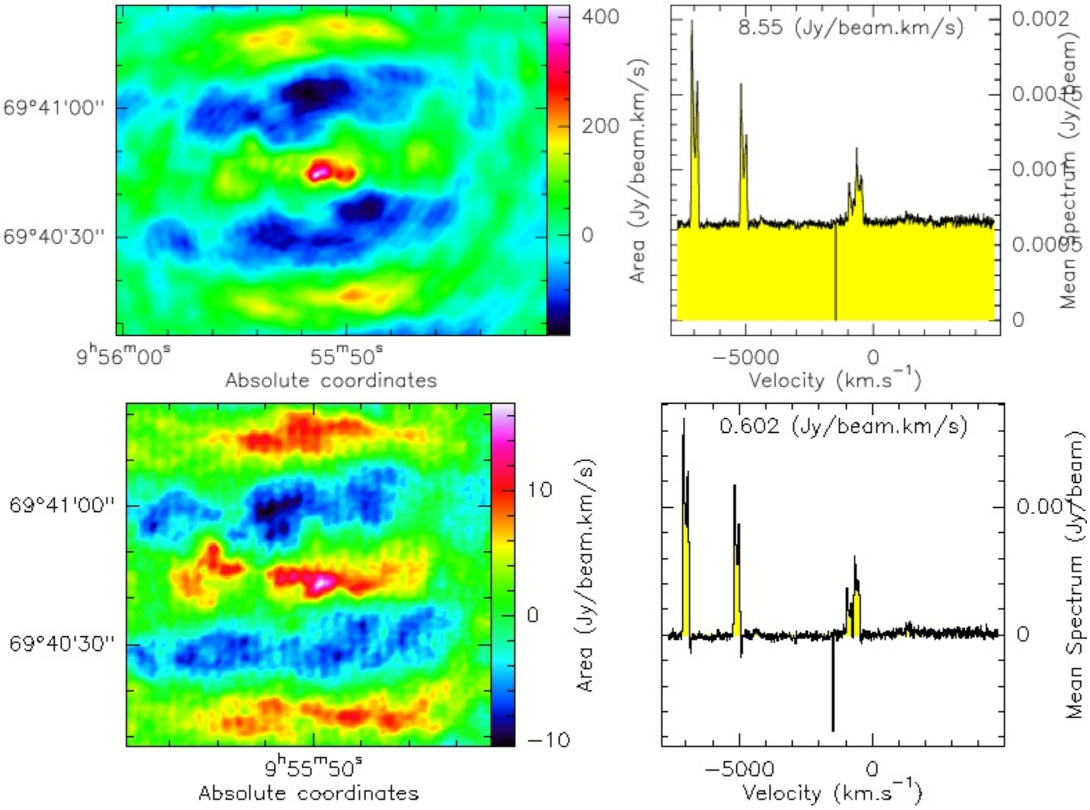

Figure 4.3: Top panel: Initial dirty data cube of M 82 at 87.1 GHz with continuum emission (left), and its spectrum (right). Bottom panel: Dirty data cube of M 82 at 87.1 GHz where continuum emission has been subtracted (left) and its spectrum (right).

The next step was to fix the beam size for the different data cubes for each galaxy, to allow for a reliable comparison and analysis of the emission lines at different frequencies. The sizes of both the major and minor axes were smeared to $2.9''$ for M 82 and to $2.7''$ for IC 342. Next, a polygon surrounding the centre region was defined as a "support region" to facilitate the cleaning procedure. This support region defines the region where the clean component (observed source) is located, and thus informing the programme that the other bright regions outside this support are simply side lobes. The deconvolution algorithm known as CLEAN HOGBOM method (Högbom 1974) has been used with 4000 iterations for both galaxies. It is considered the easiest approach to the iterative search[7]. This method first localises the pixel with the strongest intensity in the current map. It then adds the loop gain (the factor that controls convergence, and is usually between 0 and 2, where a high loop gain yields a faster convergence) of the maximum intensity pixel and its spatial position to the clean component list. The next step is to convolve the loop gain by the dirty beam. Finally, to remove the side lobes that are associated with the localised clean component, this convolution will be subtracted from the residual map. However, the convolution by the dirty beam is affected by the fact that the uv-sampling is incomplete. Therefore, one needs to apply a deconvolution process. Mathematically speaking, due to the incompleteness of the uv-sampling, there is an infinite number of intensity distributions that are compatible with the measured visibilities. Deconvolution helps find the intensity distribution that is most suited for the measured visibilities. To help the deconvolution process, a support region is usually defined. However, one must be careful when selecting a supporting region, as one can easily exclude real emission regions from parts of the sky. For more information about the cleaning algorithm used in GILDAS, please see the GILDAS software guide[8].

An example of a cleaned data cube is given in Fig. 4.4. After subtracting the continuum, the data will be saved into a file on its own. This continuum file is also imaged and cleaned (see Fig. 4.5). For some of the data cubes, the data reduction -especially the continuum subtraction- proved to be difficult due to low signal-to-noise ratios, or to the absence of emission lines. In order to solve this issue, the sources in the data were divided into regions (see Figure 5.1). From each region, the brightest spatial position ($0.66'' \times 0.66''$) in the 87.1 GHz frequency tuning was chosen to perform further spectral analysis (the frequency tuning of 87.1 GHz is chosen because it is the tuning where the regions are brightest and best defined). This method allowed the extraction of lines that might have been otherwise buried in the noise, or dominated by the continuum emission.

After the continuum subtraction and the cleaning of the data cube, one can extract individual lines from the initial map. This allows to visualise the emission of each line, and image their flux, velocity, and width distribution. As an example, the imaging of the HCN(1-0) line at 88.632 GHz and its moments are presented in Fig. 4.6.

---

[7] Assuming that the sky brightness distribution is a collection of point sources, the search for these sources is iterative: Each source is subtracted from the residual map and added to the list of clean components. The number of iteration describes the maximum number of clean components in the map. The typical value for iteration is 500.

[8] http://www.iram.fr/IRAMFR/GILDAS/

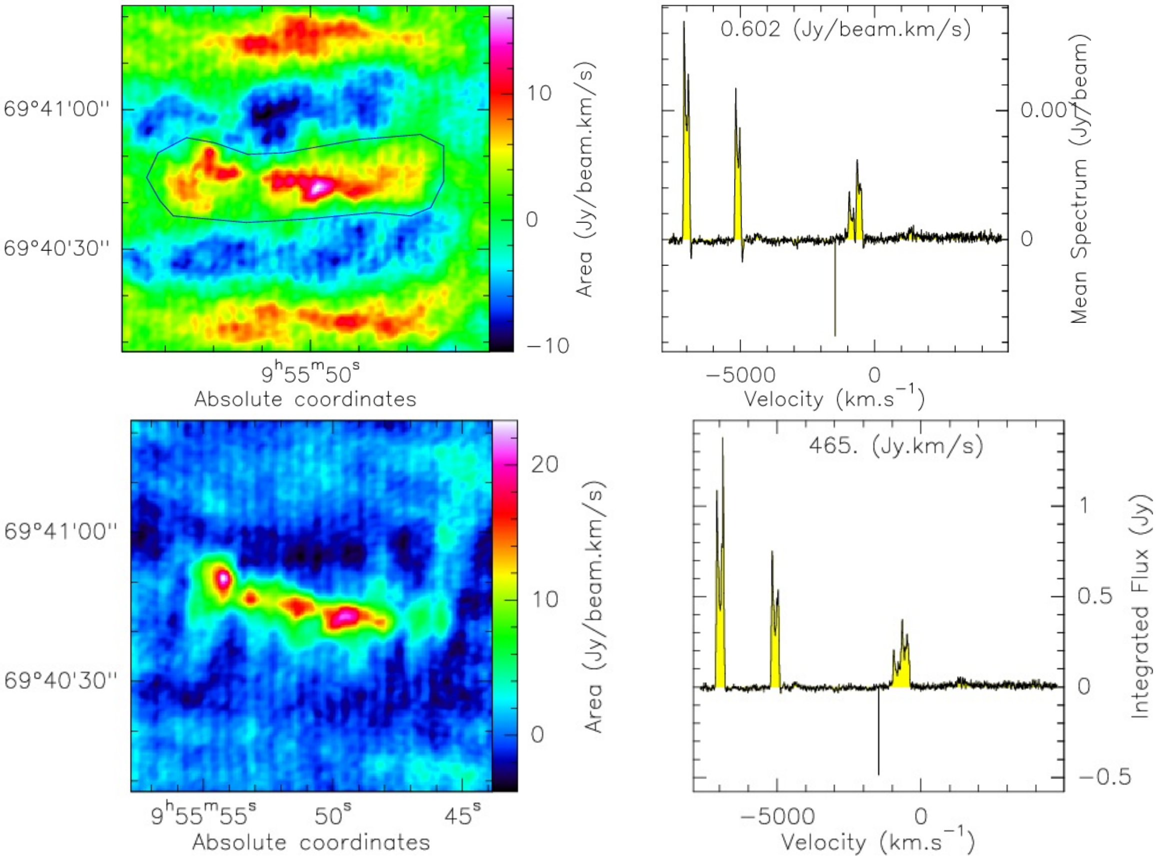

Figure 4.4: Top Panel: (left) Dirty data cube of M 82 at 87.1 GHz with no continuum emission. The polygon defines the support region for the cleaning process. The bright region outside the polygon are the side lobes associated with the clean component. (right) The spectrum of the dirty image with no continuum emission. Bottom Panel: (left) The clean image of the observation after implementing the cleaning algorithm, where the region inside the polygon shows the observed galaxies, and the side lobes are gone. (right) The clean spectrum of the observed galaxy at 87.1 GHz

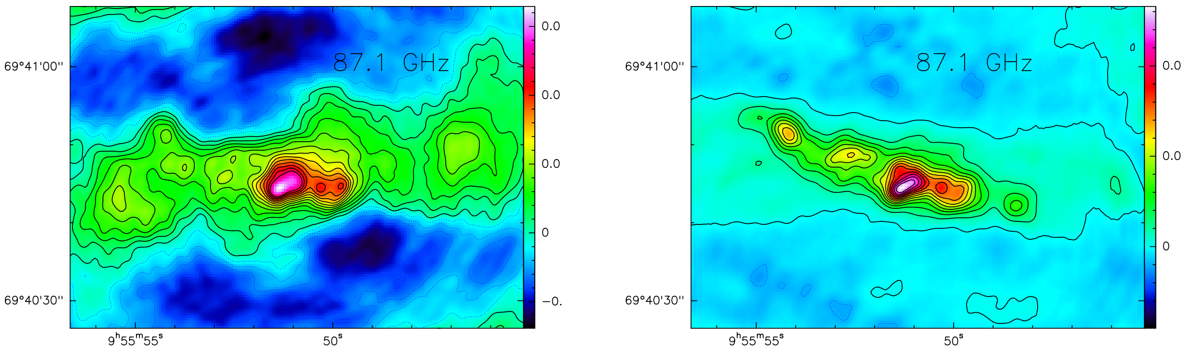

Figure 4.5: Left: Dirty continuum image of M 82 at 87.1 GHz. Right: Clean continuum image of M 82 at 87.1 GHz.

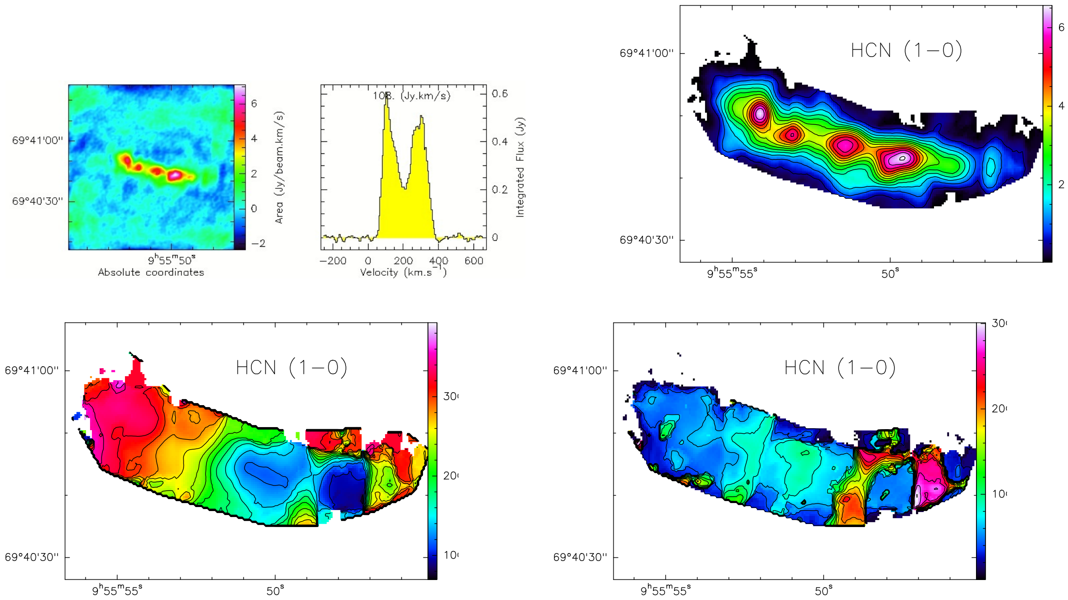

Figure 4.6: HCN (1-0) at 88.632 GHz in M 82 .Top left: line image with its spectrum. Top right: line flux distribution (moment zero) in M 82 (contour levels from 0.5 to 6.5 $\mathrm{Jy\,beam^{-1}\,km\,s^{-1}}$ by steps of 0.5 $\mathrm{Jy\,beam^{-1}\,km\,s^{-1}}$). Bottom left: line velocity distribution (moment one) (contour levels from 20 to 400 $\mathrm{km\,s^{-1}}$ by steps of 20). Bottom right: line width distribution (moment two) in M 82 (contour levels from 20 to 300 $\mathrm{km\,s^{-1}}$ by steps of 20).

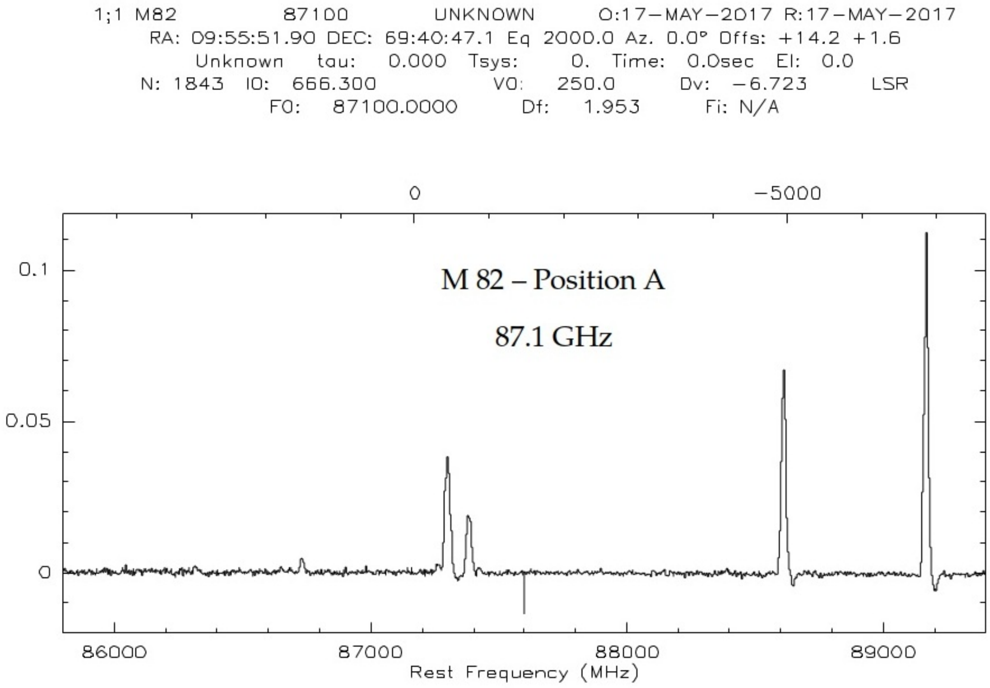

```
1;1 M82          87100          UNKNOWN        0:17-MAY-2017 R:17-MAY-2017
    RA: 09:55:51.90 DEC: 69:40:47.1 Eq 2000.0 Az. 0.0° Offs: +14.2 +1.6
        Unknown     tau:    0.000  Tsys:      0.  Time:  0.0sec  El:  0.0
   N: 1843  I0:  666.300             V0:   250.0     Dv:  -6.723        LSR
             F0:    87100.0000        Df:    1.953       Fi: N/A
```

Figure 4.7: The spectrum of M 82 at 87.1 GHz, plotted by CLASS, at an offset position of +14.2″ and +1.6″ from the right ascension and declination respectively, relative to the centre of M 82. The bottom x-axis shows the frequency in MHz and top x-axis shows the velocity in $\mathrm{km\,s^{-1}}$, where the frequency at 87.1 GHz is set at 0 $\mathrm{km\,s^{-1}}$. The y-axis shows the flux density in Jy.

For the extraction of the spectra from the map images, the Continuum and Line Analysis Single-dish Software (CLASS)[9] was used. This software only shows the calibrated, cleaned spectra, from which the continuum has been subtracted (see Fig. 4.7).

4.3 Missing Flux Calculation

It is important to check how much flux is actually missing from data obtained with an interferometer, which is not sensitive to low spatial frequencies due to the lack of the smallest baselines. For that purpose, the results of the data from this study have been compared with the results of single dish data published in Aladro et al. (2011b, 2015). Due to the difference in resolution between the interferometer and single dish data, the first step was to smooth the beam of the interferometric data to match the resolution of the single dish telescope. The data used in Aladro et al. (2011b, 2015) were collected using the IRAM 30-m telescope in Pico Veleta Spain[10]. The resolution of the IRAM 30-m telescope depends on the frequency that one is observing and it is given by[11]:

$$\theta'' = \frac{2460}{\nu} \tag{4.1}$$

where θ is the half power beam width, HPBW, given in arcseconds, and ν is the frequency in GHz. Moreover, the results (main beam brightness temperature) presented in Aladro et al. (2011b, 2015) are given in units of K. In order to compare them with the results in this work that are presented in Jy, one has to convert from Kelvin to Jy through:

$$\mathrm{S} = \frac{2.65\ \mathrm{T}\theta'^2}{\lambda^2} \tag{4.2}$$

where S is the flux density given in Jy, T is the brightness temperature in K, θ is the beam size in arcminute, and λ is the wavelength in cm (Wilson et al. 2012, Chapter 8, Section 2.2, page 180). The conversion factor a from Jy to K is then given as:

$$\begin{aligned} \mathrm{T(K)} &= \frac{\lambda^2}{2.65\theta'^2}\,\mathrm{S(Jy)} \\ a &= \frac{\lambda^2}{2.65\theta'^2} \end{aligned} \tag{4.3}$$

Given that the speed of light c is given as $c = 299792458\,\mathrm{ms^{-1}} = \lambda_\mathrm{m} \times \nu_\mathrm{Hz}$, the wavelength in cm can be written as $\lambda_\mathrm{cm} = \frac{29.9}{\nu_\mathrm{GHz}}$. Furthermore, one arcminute contains 60 arcseconds, giving then, $\theta' = \frac{\theta''}{60}$. By substituting these values in equations 4.2 and 4.3, one gets the following equations:

$$\mathrm{S(Jy)} = \frac{\nu^2\theta''^2}{1.21 \times 10^6}\mathrm{T(K)} \tag{4.4}$$

$$\begin{aligned} \mathrm{T(K)} &= \frac{1.21 \times 10^6}{\nu^2\theta''^2}\,\mathrm{S(Jy)} \\ a &= \frac{1.21 \times 10^6}{\nu^2\theta''^2} \end{aligned} \tag{4.5}$$

---

[9] https://www.iram.fr/IRAMFR/GILDAS/doc/pdf/class.pdf

[10] http://www.iram-institute.org/EN/30-meter-telescope.php

[11] http://www.iram.es/IRAMES/mainWiki/Iram30mEfficiencies

In the work of Aladro et al. (2015), the region observed toward M 82 was around 12″ or 204 pc centred around $9^{\mathrm{h}}55^{\mathrm{m}}51^{\mathrm{s}}.9$ and $69°40'47''$, with an offset position of $+13''$ and $+7.5''$ respectively. For a successful comparison, the HPBW beam of the interferometric data has been smoothed from $2.9''$ to $29''$,$27''$, $26''$ and $22''$ for M 82 (depending on the observed frequency). As for IC 342, the results from Aladro et al. (2011b) were used, where the observed region was $10.6''$ or 170 pc, centred around RA (J2 000) $3^{\mathrm{h}}46^{\mathrm{m}}48^{\mathrm{s}}.5$ and DEC (J 2000) $68°05'46''$. The synthesised beam in this study has been smoothed from $2.7''$ to $28''$,$26''$, $25''$ and $23''$ depending on the observed frequency. After doing so, the spectra have been extracted and analysed. The conversion factors are presented in Table. 4.3, while the integrated areas of the lines A and their peak main beam temperature T_{MB} have been compared and presented in Table. 4.3. Aladro et al. (2015) kindly provided the spectra of M 82 used in their study, in order to plot and compare the results of single-dish observations with those of interferometric observations. However, no such spectra were provided for IC 342 by Aladro et al. (2011b). Results referring to the missing flux are illustrated in Figure 4.8. Since Aladro et al. (2015) has only single pointing, the distribution of the missing flux could not be recovered.

From the given results, the interferometric data suffer from flux loss of about 50%. However, this loss does not affect the results of this work and their interpretation. Due to the differences in scales, Aladro et al. (2011b, 2015) are observing the sources on scales ranging from 400 to 500 pc, with a resolution of $23''$-$28''$, while in this work, the observed sources have scales around 50-100 pc, with a resolution of $2.9''$, the data observed in Aladro et al. (2011b, 2015) can also be picking up outflows and winds from these galaxies. The interferometric data from this work is not sensitive enough to pick up the emission from such outflows. An interferometer is only sensitive to emission with an angular scale of:

$$\frac{\lambda}{\mathrm{B_{max}}} < \theta < \frac{\lambda}{\mathrm{B_{min}}} \tag{4.6}$$

where λ is the observed wavelength, in this case $3\,\mathrm{mm}$, or $0.003\,\mathrm{m}$, $\mathrm{B_{min}}$ and $\mathrm{B_{max}}$ are the minimum and the maximum baseline separations respectively. From Table. 4.3, the value of $\mathrm{B_{min}}$ is $24\,\mathrm{m}$ and $\mathrm{B_{max}}$ is $427\,\mathrm{m}$. This then yields a sensitivity on angular scales between $1.44''$ and $25''$. Therefore, the angular scale for which the interferometer is sensitive, is smaller than the angular resolution $29''$.

Table 4.4: Conversion factor and resolution for M 82 and IC 342, using results from Aladro et al. 2011b and Aladro et al. 2015. a is the conversion factor from Jy to K, as in eq. 4.5.

Source	Line	Frequency in GHz	θ''	a	Reference
M 82	CCH (1-0)	83.317	29	0.20	Aladro et al. 2015
M 82	HCN (1-0)	88.632	29	0.18	Aladro et al. 2015
M 82	HCO^+ (1-0)	89.189	29	0.18	Aladro et al. 2015
M 82	CS (2-1)	97.981	27	0.17	Aladro et al. 2015
M 82	CN ($1_{0,1}$-$0_{0,1}$)	113.191	22	0.20	Aladro et al. 2015
M 82	CN ($1_{0,2}$-$0_{0,1}$)	113.491	22	0.19	Aladro et al. 2015
M 82	CS (2-1)	97.981	26	0.17	Aladro et al. 2011b
M 82	CH_3CCH (6_k-5_k)	102.548	22	0.24	Aladro et al. 2011b
IC 342	CS (2-1)	97.981	26	0.19	Aladro et al. 2011b
IC 342	HC_3N (10-9)	90.978	28	0.19	Aladro et al. 2011b
IC 342	HC_3N (11-10)	100.076	25	0.19	Aladro et al. 2011b
IC 342	HC_3N (12-11)	109.174	23	0.19	Aladro et al. 2011b

Table 4.5: Recovered flux results for M 82 and IC 342, using results from Aladro et al. 2011b and Aladro et al. 2015.

Source	Line	Frequency GHz	$\int T_{MB}\,dv$ from this work $\mathrm{K\,km\,s^{-1}}$	$\int T_{MB}\,dv$ from Aladro et al. 2015 $\mathrm{K\,km\,s^{-1}}$	Recovered value	T_{MB} from this work K	T_{MB} from Aladro et al. 2015 K	Recovered value
M 82	CCH (1-0)	83.317	5.18	20.61	25%	0.04	0.08	50%
M 82	HCN (1-0)	88.632	7.60	23.56	32.25%	0.07	0.18	36.67%
M 82	HCO^+ (1-0)	89.189	11.93	33.74	35.36%	0.10	0.24	43.33%
M 82	CS (2-1)	97.981	3.69	9.97	36.96%	0.04	0.08	50%
M 82	CN ($1_{0,1}$-$0_{0,1}$)	113.191	4.23	14.34	29.49%	0.02	0.07	32.80%
M 82	CN ($1_{0,2}$-$0_{0,1}$)	113.491	11.99	28.63	41.87%	0.09	0.19	47.36%

Source	Line	Frequency GHz	$\int T_{MB}\,dv$ from this work $\mathrm{K\,km\,s^{-1}}$	$\int T_{MB}\,dv$ from Aladro et al. 2011b $\mathrm{K\,km\,s^{-1}}$	Recovered value	T_{MB} from this work K	T_{MB} from Aladro et al. 2011b K	Recovered value
M 82	CS (2-1)	97.981	3.69	9.4	39.20%	0.04	0.09	46.50%
M 82	CH3CCH (6_k-5_k)	102.548	0.47	3.70	12.70%	0.02	0.03	66.67%
IC 342	CS (2-1)	97.981	1.85	5.00	37%	0.04	0.09	44.44%
IC 342	HC_3N (10-9)	90.978	0.037	0.7	5.28%	0.0027	0.015	18%
IC 342	HC_3N (11-10)	100.076	0.06	0.70	8.57%	0.0048	0.012	40%
IC 342	HC_3N (12-11)	109.174	0.072	0.7	10.28%	0.0064	0.012	53.33%

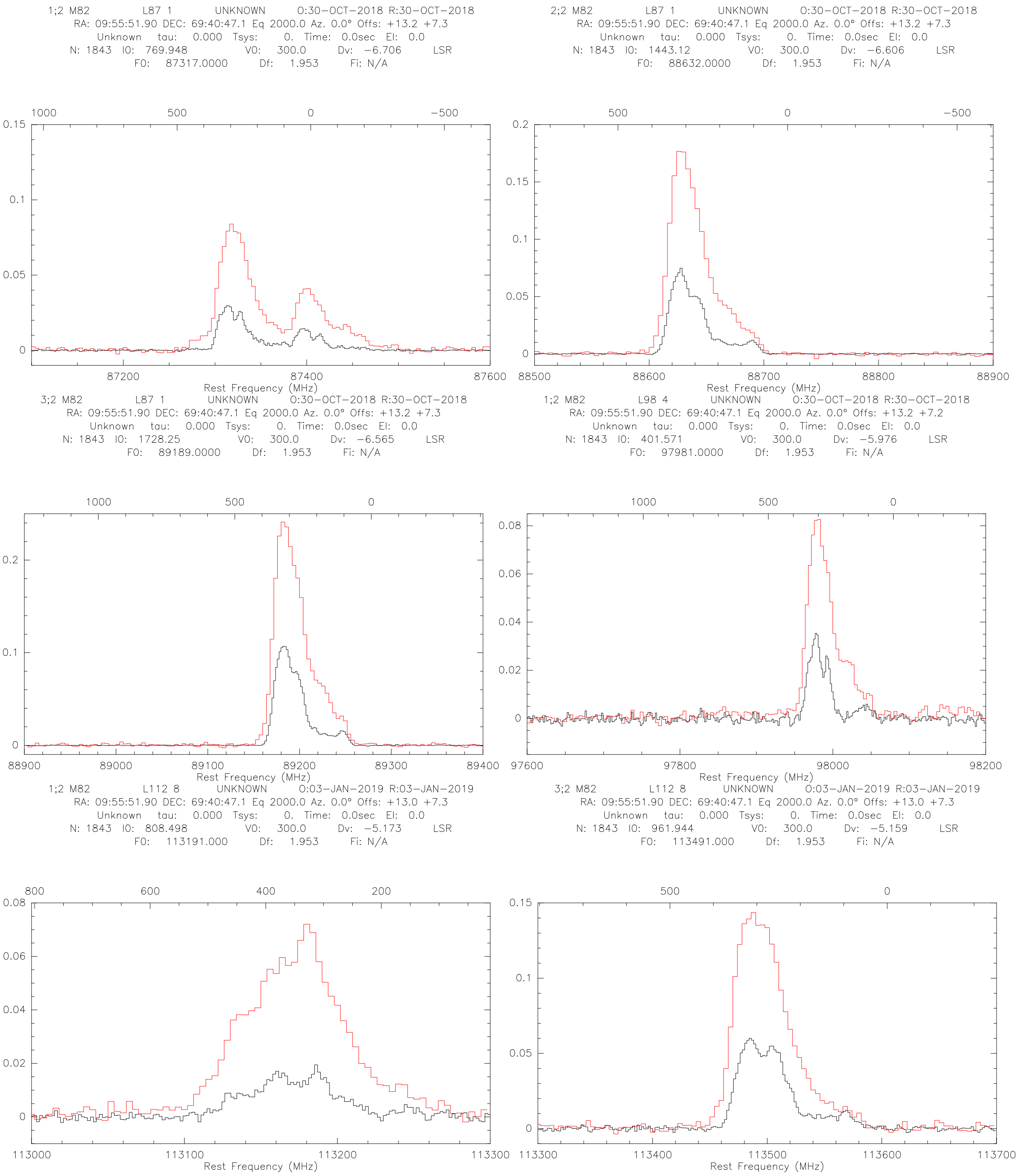

Figure 4.8: Flux comparison for M 82 using results from Aladro et al. 2015. Top left: CCH (1-0) at 87.317 GHz. Top right: HCN (1-0) at 88.632 GHz. Middle left: HCO+ (1-0) at 89.189 GHz. Middle right: CS (2-1) at 97.981 GHz. Bottom left: CN ($1_{0,1}$-$0_{0,1}$) at 113.191 GHz. Bottom right: CN ($1_{0,2}$-$0_{0,1}$) at 113.491 GHz. The red lines are the spectra from Aladro et al. 2015, the black lines are the spectra from this work, after smoothing the beam to the resolution used by Aladro et al. 2015. The bottom x-axis shows the frequency in MHz and the top x-axis shows the velocity in km s^{-1}. The y-axis is the main beam temperature given in K.

4.4 Spectral Analysis (with MADCUBA)

For the spectroscopic analysis of the extracted spectra and line identification, the MAdrid Data CUBe Analysis (MADCUBA)[12] programme has been used. The detailed description of the software, its computation and calculations can be found in Martin et al. (in prep). In the following, a short description of the software will be presented. One of the many useful extensions of MADCUBA is the Spectral Line and Identification and Modelling (SLIM). This is a spectroscopic analysis tool. SLIM is equipped with several spectroscopic databases, that are used to find and identify emission or absorption lines:

- Cologne Database for Molecular Spectroscopy[13] (CDMS) (Müller et al. 2001 and Müller et al. 2005)
- Jet Propulsion Laboratory (JPL) (Pickett et al. 1998)
- Spectral Line Atlas of Interstellar Molecules (SLAIM)[14] (F. J. Lovas, priv. comm., Remijan et al. 2007)
- Recommended Rest Frequencies for Observed Interstellar Molecular Microwave Transitions, 1991 revision (Lovas 1992)
- Recommended Rest Frequencies for Observed Interstellar Molecular Microwave Transitions, 2002 revision (Lovas 2004)

The CDMS, and the JPL catalogues enclose spectroscopic parameters that are necessary for the simulation or fitting of the lines. The software is also able to provide a synthetic spectrum with parameters similar to the observed spectral parameters. This synthetic spectrum can be either over plotted or fitted to the observed spectra, to thus derive the best spectroscopic parameters that describe the observed lines. The synthetic spectra and their spectroscopic parameters are calculated by assuming a Gaussian line profile and by varying the physical parameters of a line, such as the column density (N), the excitation temperature (T_{ex}) given in K, the velocity of the line (v) given in km s^{-1}, the source size (it is a fixed parameter) and finally, the full width at half maximum (FWHM) of the emission line (Δv) in km s^{-1}. By changing these parameters in the interactive window, the user can find the best set of parameters that describe all the observed transitions of a molecule and fit the synthetic or the simulated line to the observed one. The automatic fitting is done by performing a non-linear least-squares fitting of the molecular line emission or absorption. The errors in the fitted parameters are given by the standard deviations of those parameters. Therefore, all transitions of a molecule considered for the fit are taken into account when calculating the errors. For the time being, SLIM only models lines for molecular species.

In the following, a brief explanation of SLIM and its calculations will be presented. This explanation is based on the detailed work of Martín et al. (2019a). The main process of SLIM is to solve the radiative transfer equation, assuming local thermodynamical equilibrium (LTE), and an isothermal object in one dimension. Under the LTE assumption, the intensity of the source, noted as I_ν is described with the Planck Function, $B_\nu(T_B)$ (eq. 2.5) where T_B is the brightness temperature, so that the intensity of the source can be written as:

---

[12] http://cab.inta-csic.es/madcuba/MADCUBA_IMAGEJ/ImageJMadcuba.html

[13] https://www.astro.uni-koeln.de/cdms/catalog

[14] Available at http://www.splatalogue.net

$$I_\nu = B_\nu(T_B) = \frac{2h\nu^3}{c^2(e^{\frac{h\nu}{kT_B}} - 1)} = \frac{2k\nu^2}{c^2} J_\nu(T_B) \tag{4.7}$$

The intensity in temperature units is then $J_\nu(T) = \frac{h\nu}{k(e^{\frac{h\nu}{kT}}-1)}$. Under these definitions, the radiation temperature is then defined as $T_R = J_\nu(T_B)$. Thus, the source intensity is then described as:

$$I_\nu = \frac{2k\nu^2}{c^2} J_\nu(T_B) \sim \frac{2k\nu^2}{c^2} T_R \tag{4.8}$$

Under the Rayleigh-Jeans approximation, one can assume that $J(T) \sim T$. However, this assumption breaks down for high frequencies and regions of low temperatures. Therefore, instead of using the Rayleigh-Jeans approximation, SLIM solves the radiative transfer equation assuming a gas with an uniform temperature and density. Given the Cosmic Microwave Background (CMB) with a brightness temperature T_{bg} (by default, $T_{bg} = 2.73\,\mathrm{K}$), a background continuum source with a temperature of T_c, a gas of a given molecular species with an excitation temperature T_{ex}, and an optical depth of τ_ν, the solution to the radiative transfer equation can be written as:

$$T_R = J_\nu(T_{bg})e^{-\tau_\nu} + c_s J_\nu(T_c)e^{-\tau_\nu} + J_\nu(T_{ex})(1 - e^{-\tau_\nu}) \tag{4.9}$$

where c_s is the covering factor that accounts for continuum absorption by a foreground medium. However, only the line temperature T_L is of importance here, and it is calculated by removing the continuum contribution from the background source ($c_s J_\nu(T_c)$, and fixing $c_s = 1$, for simplicity reasons) and the CMB ($J_\nu(T_{bg})$). Thus the line temperature is given as:

$$T_L = (J_\nu(T_{ex}) - J_\nu(T_c) - J_\nu(T_{bg}))(1 - e^{-\tau_\nu}) \tag{4.10}$$

The calculation of the line temperature (eq. 4.10) can be simplified depending on the optical depth. If the medium is optically thin ($\tau_\nu \ll 1$), then the line temperature can be written as $J_\nu(T_L) = (J_\nu(T_{ex}) - J_\nu(T_c) - J_\nu(T_{bg}))\tau_\nu$. For the case of an optically thick medium with $\tau_\nu \gg 1$, the line temperature will be estimated as $J_\nu(T_L) = (J_\nu(T_{ex}) - J_\nu(T_c) - J_\nu(T_{bg}))$. The flux density (in units of Jy) and the main beam brightness temperature T_{MB} (in units of K) of a line are calculated from the line temperature, the solid angle of the source Ω_s, and the source convolved with the beam $\Omega_{s\star b}$:

$$\begin{aligned} &\text{Temperature in K}: \quad && T_{MB} = \frac{\Omega_s}{\Omega_{s\star b}} T_L \\ &\text{Flux Density in Jy}: \quad && S = 10^{23}\frac{2k\nu^2}{c^2}\Omega_{s\star b} T_L \end{aligned} \tag{4.11}$$

with 1 Jy = $10^{-23}\mathrm{erg\,s^{-1}\,cm^{-2}\,Hz^{-1}}$. The factor of 10^{23} is then the factor of conversion from a Jy unit to cgs units. The source solid angle is given in units of steradians, and it is a function of the source's or the beam's FWHM in the major and minor axis ($\Omega = 1.133\theta_{major}\theta_{minor}$), under the assumption that both the source and the telescope beam are described by Gaussian profiles. For simplicity reasons, SLIM assumes that $\theta_{major} = \theta_{minor}$. Therefore, in practice, the main beam brightness temperature is calculated as a function of the convolution of the Gaussian FWHM of the source θ_s and of the beam θ_b ($\theta_b = \sqrt{\theta_{major}\theta_{minor}}$), where the convolution is given as $\sqrt{\theta_s^2+\theta_b^2}$. Moreover, one can write the convolved solid angle as a function of θ_s and θ_b ($\Omega_{s\star b} = 1.133(\theta_s^2+\theta_b^2)$). Thus, the main beam brightness temperature is actually calculated as:

$$\begin{aligned}
&\text{Temperature in K}: && T_{MB} = [J_\nu(T_{ex}) - J_\nu(T_c) - J_\nu(T_{bg})](1-e^{-\tau_\nu})\left(\frac{\theta_s^2}{\theta_s^2+\theta_b^2}\right) \\
&\text{Flux Density in Jy}: && S = 10^{23}\frac{2k\nu^2}{c^2}1.133\theta_s^2\left([J_\nu(T_{ex}) - J_\nu(T_c) - J_\nu(T_{bg})]\,(1-e^{-\tau_\nu})\right)
\end{aligned} \tag{4.12}$$

For extended sources, θ_s^2 becomes much larger than θ_b^2. In this case, the beam filling factor $f = \left(\frac{\theta_s^2}{\theta_s^2+\theta_b^2}\right)$ tends to 1. SLIM works under the assumption that the velocity distribution of the molecules follows a Maxwellian distribution, and therefore the opacity will have a Gaussian shape. For an opacity τ_o at the central velocity v_o, the opacity is described as $\tau_v = \tau_o e^{-4ln2\frac{(v-v_o)^2}{\Delta v^2}}$, where Δv is the FWHM. In this case, the main beam brightness temperature will have a Gaussian shape for low opacities. For high opacities, the profile will be saturated, leading to a more flat-topped line shape.

The total column density of the observed line N is given as a function of the column density in the upper level N_u, the partition function Z, the energy in the upper level E_u, and the degeneracy (g_u) (see eq. 2.15 in Chapter 2, Section 2.2). The opacity at central velocity τ_0, or the maximum value of the optical depth for a given transition, is given as a function of N, g_u, Z, the Einstein coefficient for spontaneous emission A_{ul}, the FWHM, the excitation temperature T_{ex}, and the energies at lower and upper levels E_l, and E_u:

$$\tau_0 = \frac{N\, g_u\, A_{ul}\, c^3}{8.52\pi\, \Delta v\, Z\, \nu_{ul}^3}\left(e^{-\frac{E_l}{kT_{ex}}} - e^{-\frac{E_u}{kT_{ex}}}\right) \tag{4.13}$$

From the peak temperature of the spectral line T_L^0 (temperature of the line at $\tau = \tau_0$), one can derive the area of the line or the integrated line intensity:

$$A = \int_{-\infty}^{+\infty} T_L \delta v = (\sqrt{2\pi})\sigma T_L^0 = 1.06\,\Delta v\, T_L^0 \tag{4.14}$$

where σ^2 is the variance of the Gaussian, and Δv can be written as: $\Delta v = 2\sqrt{2ln2}\,\sigma = 2.35\sigma$. For more details about the computation and the calculation used in SLIM and MADCUBA, refer to Martín et al. (2019a).

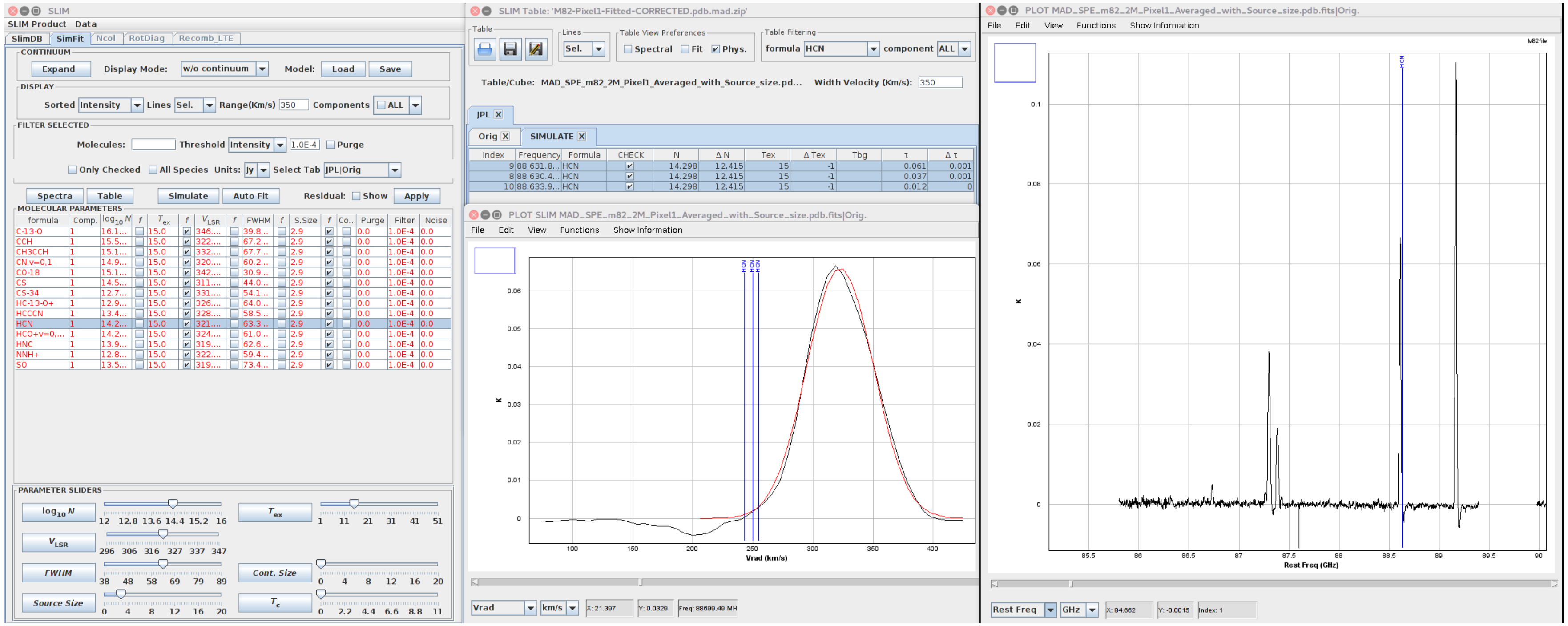

Display Mode: w/o continuum Model:

Sorted Intensity Lines Sel. Range(Km/s) 350 Components ☐ ALL

Molecules: Threshold Intensity 1.0E-4 ☐ Purge

☐ Only Checked ☐ All Species Units: Jy Select Tab JPL|Orig

Residual: ☐ Show

formula	Comp.	$\log_{10}N$	f	T_{ex}	f	V_{LSR}	f	FWHM	f	S.Size	f	Co...	Purge	Filter	Noise
C-13-O	1	16.1...	☐	15.0	☑	346....	☐	39.8...	☐	2.9	☑	☐	0.0	1.0E-4	0.0
CCH	1	15.5...	☐	15.0	☑	322....	☐	67.2...	☐	2.9	☑	☐	0.0	1.0E-4	0.0
CH3CCH	1	15.1...	☐	15.0	☑	332....	☐	67.7...	☐	2.9	☑	☐	0.0	1.0E-4	0.0
CN,v=0,1	1	14.9...	☐	15.0	☑	320....	☐	60.2...	☐	2.9	☑	☐	0.0	1.0E-4	0.0
CO-18	1	15.1...	☐	15.0	☑	342....	☐	30.9...	☐	2.9	☑	☐	0.0	1.0E-4	0.0
CS	1	14.5...	☐	15.0	☑	311....	☐	44.0...	☐	2.9	☑	☐	0.0	1.0E-4	0.0
CS-34	1	12.7...	☐	15.0	☑	331....	☐	54.1...	☐	2.9	☑	☐	0.0	1.0E-4	0.0
HC-13-O+	1	12.9...	☐	15.0	☑	326....	☐	64.0...	☐	2.9	☑	☐	0.0	1.0E-4	0.0
HCCCN	1	13.4...	☐	15.0	☑	328....	☐	58.5...	☐	2.9	☑	☐	0.0	1.0E-4	0.0
HCN	1	14.2...	☐	15.0	☑	321....	☐	63.3...	☐	2.9	☑	☐	0.0	1.0E-4	0.0
HCO+v=0,...	1	14.2...	☐	15.0	☑	324....	☐	61.0...	☐	2.9	☑	☐	0.0	1.0E-4	0.0
HNC	1	13.9...	☐	15.0	☑	319....	☐	62.6...	☐	2.9	☑	☐	0.0	1.0E-4	0.0
NNH+	1	12.8...	☐	15.0	☑	322....	☐	59.4...	☐	2.9	☑	☐	0.0	1.0E-4	0.0
SO	1	13.5...	☐	15.0	☑	319....	☐	73.4...	☐	2.9	☑	☐	0.0	1.0E-4	0.0

SLIM Table: 'M82-Pixel1-Fitted-CORRECTED.pdb.mad.zip'

Lines Sel. ☐ Spectral ☐ Fit ☑ Phys. formula HCN component ALL

Table/Cube: MAD_SPE_m82_2M_Pixel1_Averaged_with_Source_size.pd... Width Velocity (Km/s): 350

Index	Frequency	Formula	CHECK	N	Δ N	Tex	Δ Tex	Tbg	τ	Δ τ
9	88,631.8...	HCN	☑	14.298	12.415	15	-1		0.061	0.001
8	88,630.4...	HCN	☑	14.298	12.415	15	-1		0.037	0.001
10	88,633.9...	HCN	☑	14.298	12.415	15	-1		0.012	0

Vrad km/s X: 21.397 Y: 0.0329 Freq: 88699.49 MH

Rest Freq GHz X: 84.662 Y: -0.0015 Index: 1

Figure 4.9: Screenshot of MADCUBA. In this image, one can see on the left the lines that have been chosen from the JPL catalogue, and the physical terms that one can change in order to fit the line. In the top middle panel is the table that shows the values of the fit and its errors. In the bottom middle panel, the red line is the synthetic or simulated line, while the black line is the observed emission line. Finally, on the right panel, one can see the spectrum used for the analysis and the blue line shows the transitions of the emission line that is fitted.

Chapter 5

Results

After having outlined the details of the data analysis in Chapter 4, the results from the data analysis of the high resolution 3-mm survey targeting M 82 and IC 342 are presented here. First, the results of the galaxy imaging after the cleaning processes and the continuum subtraction are presented, where four main emission regions are identified in M 82 and three regions in IC 342. This is followed by a spectral analysis of the extracted spectra. From this spectral analysis, lines were fitted to get quantitative values for the flux density, flux, line width, radial velocity, and column densities. From these values, abundance ratios were derived. The distribution of line flux, velocities, and widths (respectively moment zero, one, and two) are shown and compared. Finally, results from a principal component analysis (PCA, see Chapter 2, Section 2.5) are presented, showing correlations and differences between the emission lines observed in the two galaxies.

5.1 Imaging and Spectral analysis

The imaging of the data cubes has been performed using the MAPPING Package in GILDAS. The details of the procedure are explained in Chapter 4, Section 4.2. Despite lower signal-to-noise ratios in some frequency tunings (for example, 98.4 GHz, 102 GHz), the quality of the data is generally good, and offers reliable results.

In Figure 5.1, the galaxies M 82 and IC 342 are shown. The line maps (with the continuum removed) are centred at a frequency of 87.1 GHz and have a bandwidth of 3.6 GHz. M 82 shows four distinct line emission regions (A, B, C, and D) (molecular line emission from $H^{13}CN$, CCH, HCN, and HCO^+), while IC 342 shows three line emission regions (A, B, and C) (molecular line emission from $H^{13}CN$, $H^{13}CO^+$, SiO, $H^{13}NC$, CCH, HNCO, HCN, and HCO^+). The molecular emission seen in both M 82 and IC 342 at 87.1 GHz is representative of the molecular distribution in these galaxies at different frequencies. The dynamical centre of M 82 (right ascension RA (J2000): $09^h55^m52.7^s$ and declination DE (J2000): $+69°40'46''$, see the NASA/IPAC Extragalactic Database (NED, http://ned.ipac.caltech.edu)) is thought to be between the regions B and C, as marked in Fig. 5.1. On the other hand, the centre of IC 342 (right ascension RA (J2000): $03^h46^m48.5^s$, a declination DE (J2000): $+68°05'46''$, see Crosthwaite et al. 2000) is located at the eastern edge of region C, as depicted in Fig. 5.1. The coordinates of the different regions are presented in Table. 5.1. Figure 5.2 presents the continuum emission in M 82 and IC 342 at 91.2 and 105.6 GHz. This shows that for both M 82 and IC 342, the continuum slightly changes across the 3-mm range (see Table. 5.3). The continuum flux densities in M 82 fluctuate significantly with frequency, whereas one would expect a fairly constant flux density across the

3-mm spectrum. The reason behind these fluctuations is unclear. These differences could be partly due to differences in signal-to-noise ratios at different frequency tunings, as well as to the difference in observation configurations, and number of observations carried at each frequency (see Tables 4.2, and 4.3), calibration error in the data, or to missing flux due to interferometric observations. However, fluctuations in the continuum flux densities in M 82 were also reported in single dish observations, where the continuum flux density dropped by 38% between 105 and 109 GHz observations (Aladro, priv. Comm.). The continuum images at all frequency tunings for both galaxies are presented in Appendix *A*.

From each of these regions (Regions A, B, C, and D in M 82 and Regions A, B, and C in IC 342), the brightest $0.66'' \times 0.66''$ pixel (called hereafter Position) at 87.1 GHz, has been selected. These Positions -now called Position A, Position B, Position C, and Position D (corresponding to Region A, B, C, and D respectively)- are used to perform the analysis, in order to optimise the signal-to-noise ratios. The same positions will be used for the analysis at other frequencies, to conserve spatial consistency. The coordinates of the positions selected for the analysis are presented in Table. 5.2.

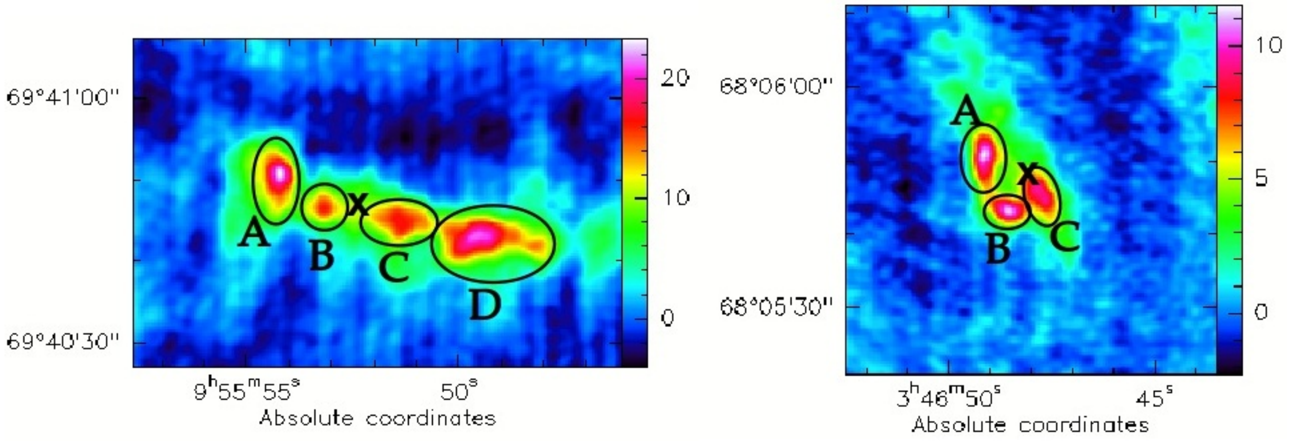

Figure 5.1: Left: The image shows the line emission of M 82 imaged at 87.1 GHz frequency tuning, with four distinct regions denoted as A, B, C, and D (the continuum emission at 87.1 GHz is subtracted). The "x" shows the centre of M 82 (RA (J2000): $09^{h}55^{m}52.7^{s}$ and a declination DE (J2000): $+69°40'46''$), on the 87.1 GHz frequency tuning. Right: The image shows the line emissions of IC 342 imaged at 87.1 GHz, with the three distinct regions A, B, and C (the continuum emission at 87.1 GHz is subtracted). The "x" shows the centre of IC 342 (RA (J2000): $03^{h}46^{m}48.5^{s}$, a declination DE (J2000): $+68°05'46''$), on the 87.1 GHz frequency tuning. The colour-coded flux density is given in units of Jy/beam.

Table 5.1: Coordinates of the main emission regions in M 82 and IC 342

	M 82 (RA(J2000) and DEC(2000))				IC 342 (RA(J2000) and DEC(2000))			
Regions	West ($9^{h}55^{m}$)	East ($9^{h}55^{m}$)	South ($69°40'$)	North ($69°40'$)	West ($3^{h}46^{m}$)	East ($3^{h}46^{m}$)	South ($68°05'$)	North ($68°05'$)
Region A	$53^{s}.8$	$55^{s}.7$	$38''$	$57''$	$49^{s}.4$	$48^{s}.1$	$46''$	$58''$
Region B	$52^{s}.3$	$53^{s}.5$	$41''$	$50''$	$47^{s}.8$	$49^{s}.3$	$41''.8$	$46''$
Region C	$50^{s}.6$	$52^{s}.4$	$37''$	$51''$	47^{s}	$48^{s}.2$	$37''$	$50''$
Region D	$47^{s}.3$	$50^{s}.5$	$35''$	$46''$	-	-	-	-

From each of the selected positions, spectra at different frequencies have been extracted, as seen in Fig. 5.3. From these spectra, one notices significant changes in the line intensities between the different regions in the same galaxy. Moreover, in IC 342 there are more emission lines than in M 82. Furthermore, one notices a difference in the overall flux densities of the lines between M 82 and IC 342. In fact, such differences in the spectra are seen in all regions of the two galaxies. These differences are quantified by the Gaussian fits to the lines. Spectra and Gaussian fit of the brightest positions in the different regions of both galaxies are presented in Appendix *B*. There is a 600 MHz gap between the frequency tunings at 87.1 and 91.2 GHz that is not covered by either bands. This gap is seen the spectra of both M 82 and IC 342 (see Figs. 5.3 and 5.4). In this gap, HOC$^+$(1-0) emission line at 89.4874 GHz could have been detected.

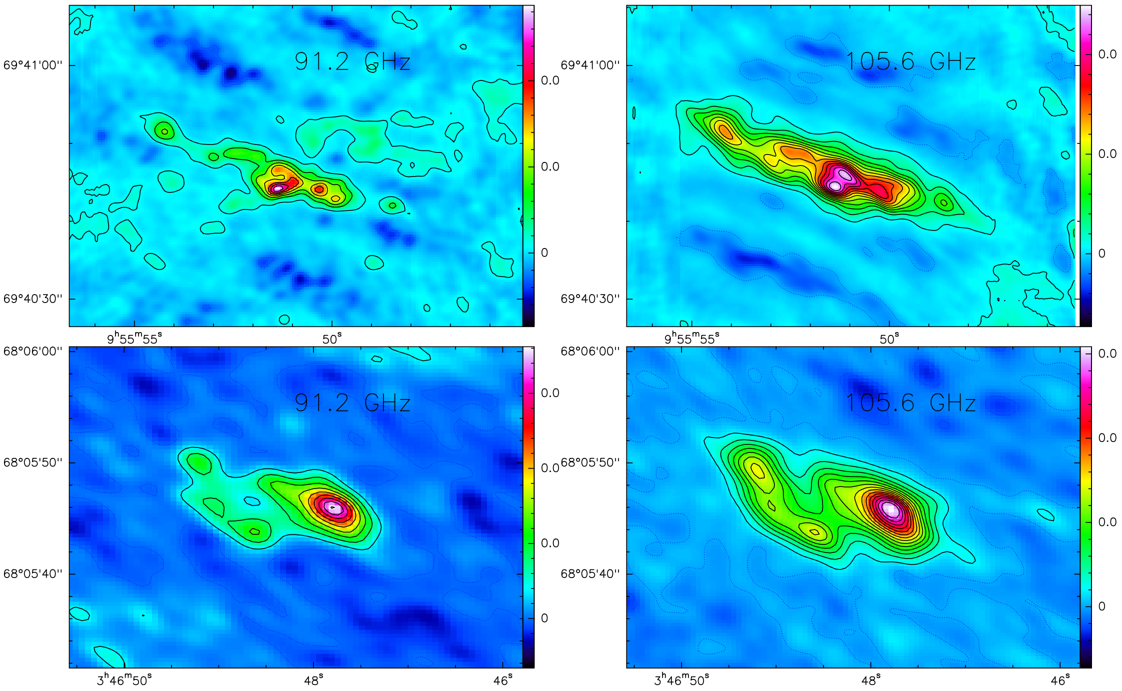

Figure 5.2: Continuum image of M 82 at 91.2 GHz (top left) (contour levels from -4 to 14 mJy beam^{-1} km s^{-1} by steps of 2 mJy beam^{-1} km s^{-1}), and 105.6 GHz (top right) (contour levels from -8 to 24 mJy beam^{-1} km s^{-1} by steps of 2 mJy beam^{-1} km s^{-1}). Continuum image of IC 342 at 91.2 GHz (bottom left) (contour levels from -0.4 to 1.8 mJy beam^{-1} km s^{-1} by steps of 0.2 mJy beam^{-1} km s^{-1}), and at 105.6 GHz (bottom right) (contour levels from -0.8 to 3 mJy beam^{-1} km s^{-1} by steps of 0.2 mJy beam^{-1} km s^{-1}).

Table 5.2: Positions central coordinates in M 82 and IC 342.

	M 82		IC 342	
Positions	(RA(J2000)	DEC(2000))	(RA(J2000)	DEC(2000))
Position A	$9^h55^m54^s.70$	$69°40'50''.54$	$3^h46^m49^s.12$	$68°05'50''.90$
Position B	$9^h55^m53^s.17$	$69°40'46''.50$	$3^h46^m48^s.53$	$68°05'43''.00$
Position C	$9^h55^m51^s.40$	$69°40'45''.10$	$3^h46^m47^s.82$	$68°05'46''.00$
Position D	$9^h55^m49^s.75$	$69°40'43''.10$	-	-

Table 5.3: Total continuum flux densities in M 82 and IC 342, not accounting for missing flux. The bandwidth of each frequency band is 3.6 GHz.

	M 82		IC 342	
Frequency GHz	Flux Density mJy	Noise mJy	Flux Density mJy	Noise mJy
87.1	437	1.12	19.3	0.05
91.2	151	0.48	10.5	0.05
94.8	184	0.23	14.2	0.05
98.4	514	0.55	16.1	0.06
102	455	0.54	19	0.05
105.6	489	0.87	20.2	0.07
109.2	39	0.24	14.2	0.07
112.8	212	0.61	21.3	0.08

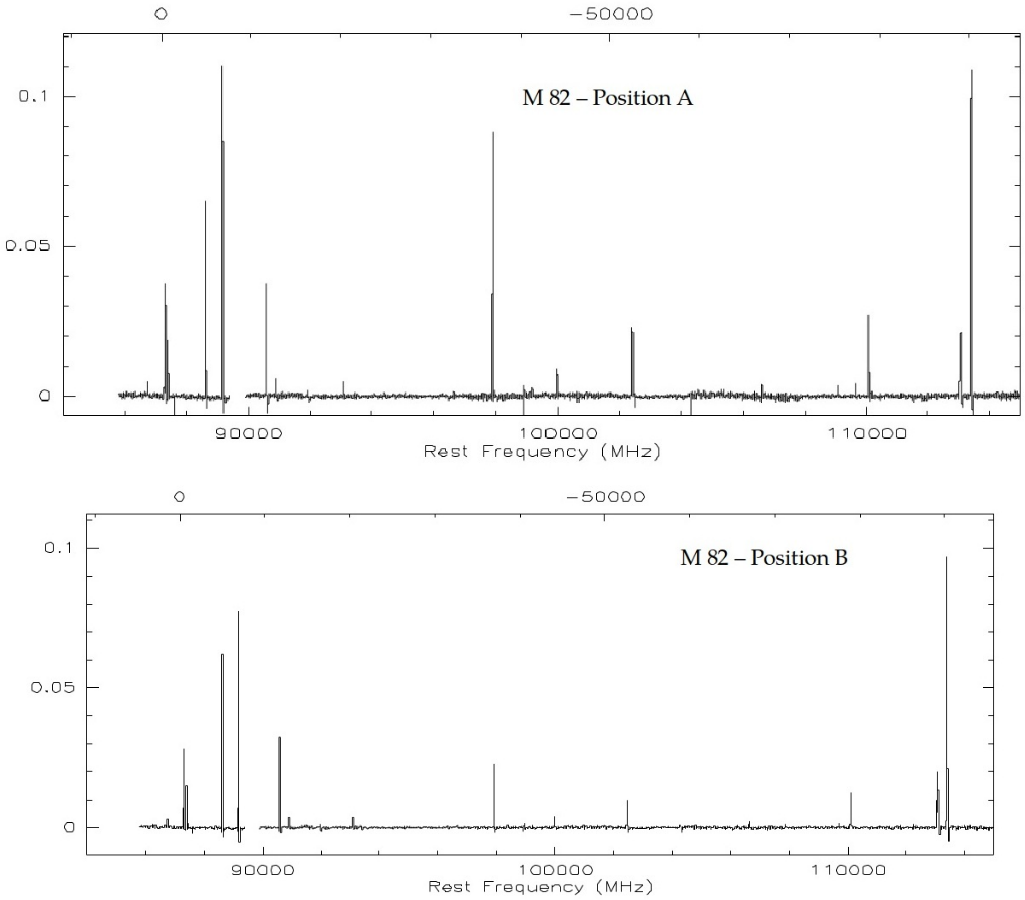

Figure 5.3: The combined spectrum of the brightest position from Region A in M 82 (top pannel), and from Region B in M 82 (bottom pannel). These spectra cover frequencies from 86 to 114 GHz. The bottom x-axis shows the frequency in MHz and the top x-axis shows the velocity in km s^{-1}, where the frequency at 87.1 GHz is set at 0 km s^{-1}. The y-axis shows the flux density in Jy.

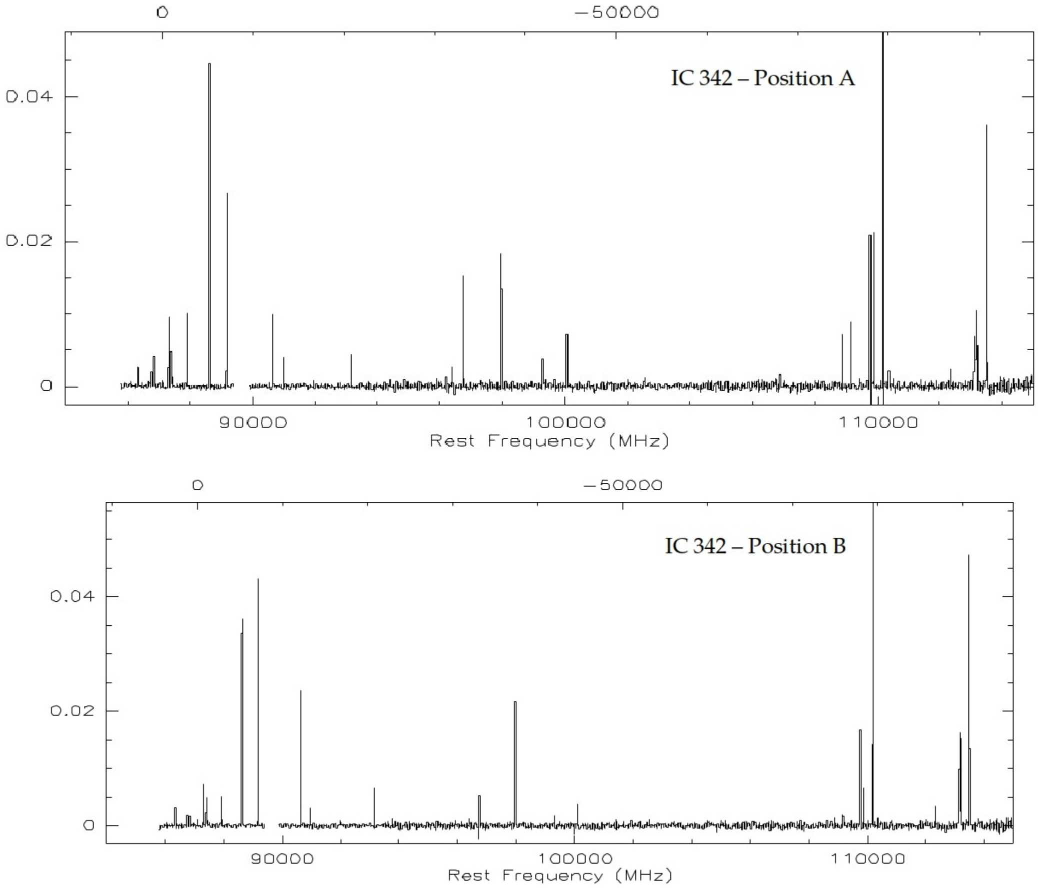

Figure 5.4: The combined spectrum of the brightest position from Region A in IC 342 (top pannel), and from Region B in IC 342 (bottom pannel). These spectra cover frequencies from 86 to 114 GHz. The bottom x-axis shows the frequency in MHz and the top x-axis shows the velocity in km s^{-1}, where the frequency at 87.1 GHz is set at 0 km s^{-1}. The y-axis shows the flux density in Jy.

5.2 Line Parameters

After analysing the spectra of the brightest positions in each region, the molecular emission has been summarised in Tables 5.4, 5.5, 5.6, 5.7, 5.8, 5.9, and 5.10.
The spectral analysis was performed using both GILDAS CLASS and MADCUBA_IJ. The details of the analysis procedure can be found in Chapter 4, Section 4.2, and Section 4.4. As a sanity check, the results from the two analysis tools were compared and found to be consistent with each other. Figure 5.5 shows the Gaussian fits of two different molecules (CCH and CN) in Position A in M 82 and IC 342. The fit results of all emission lines found in the different positions of M 82 and IC 342 can be found in Appendix *D*. The fitting analysis provides quantitative measurements of the flux (in $\mathrm{Jy\,km\,s^{-1}}$), the local standard of rest velocity, $\mathrm{V_{LSR}}$ in $\mathrm{km\,s^{-1}}$, the width of the line in $\mathrm{km\,s^{-1}}$, and the flux density of the line in Jy. Moreover, from the analysis done with MADCUBA, one gets the column density of the line in $\mathrm{cm^{-2}}$. The analysis is performed on the spectra obtained from the different positions of the galaxies.

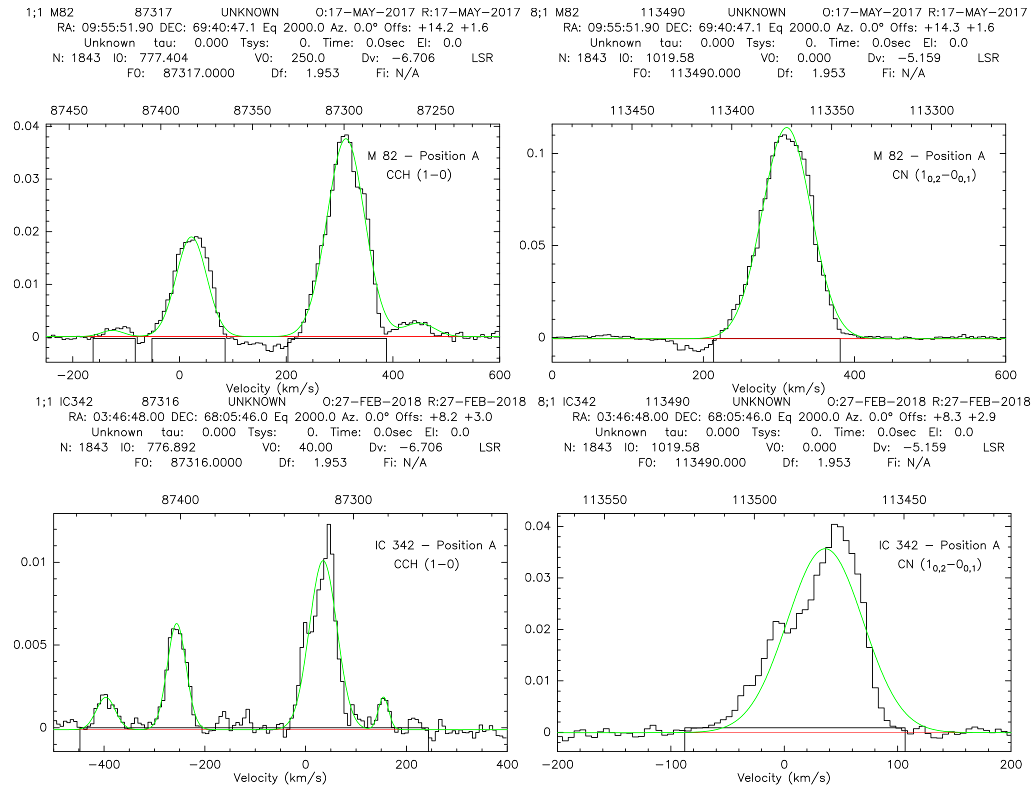

Figure 5.5: Gaussian fits to spectral lines using GILDAS CLASS. Top panel: CCH (1-0) at 87.316 GHz including hyperfine components (left) and $\mathrm{CN}\,(1_{0,2}-0_{0,1})$ at 113.490 GHz (right) in position A of M 82 (Offset of $14.2''$ and $1.6''$ from the galaxy's centre). Bottom Panel: CCH (1-0) at 87.316 GHz including hyperfine components (left) and $\mathrm{CN}\,(1_{0,2}-0_{0,1})$ at 113.490 GHz (right) in position A of IC 324 (Offset of $8.3''$ and $2.9''$ from galaxy's centre). The black box indicates the window in which the lines are to be found, the red line is the baseline at zero level, and the green line is the best fit for the respective features. The top x-axis shows the frequency in MHz and the bottom x-axis shows the velocity in km s^{-1}, where the rest frequency of the line (87.317 GHz and 113.49 GHz for CCH $(1_{2,2}-0_{1,1})$ and $\mathrm{CN}\,(1_{0,2}-0_{0,1})$ respectively) is set at 0 km s^{-1}. The y-axis shows the flux density in Jy.

Table 5.4: Fit results of the spectrum from the Position A in M 82

Line	Rest Frequency GHz	Flux Jy km s^{-1}	V$_{\rm LSR}$ km s^{-1}	Width km s^{-1}	Flux Density$^{(a)}$ mJy	Column Density 10^{14} cm^{-2}
$H^{13}CO^+$ (1 − 0)	86.75	0.29±0.02	325.38±1.74	58.81±3.87	4.69	(0.107±0.003)
CCH ($1_{2,1} - 0_{1,1}$)	87.28	0.19±0.07	330.39±4.49	63.88±6.71	2.78	(39.5±0.5)
CCH ($1_{2,2} - 0_{1,1}$)	87.32	3.32±0.07	310.43±6.71	82.34±6.71	37.90	(39.5±0.5)
CCH ($1_{1,1} - 0_{1,1}$)	87.40	1.56±0.07	315.34±0.82	72.29±6.71	20.30	(39.55±0.5)
CCH ($1_{1,1} - 0_{1,0}$)	87.45	5.59×10^{-2}±0.07	341.37±6.70	39.54±6.71	1.33	(39.5±0.5)
HCN (1 − 0)	88.63	4.67±0.03	316.22±0.21	65.41±0.47	67.00	(1.17±0.01)
HCO^+ (1 − 0)	89.19	7.31±0.04	323.01±0.19	62.96±0.43	110.00	(2.16±0.02)
HNC (1 − 0)	90.66	2.55±0.04	317.33±0.50	63.19±1.14	37.90	(1.13±0.02)
HC_3N (10 − 9)	90.98	0.38±0.02	326.76±1.57	60.41±3.82	5.87	(2.86±0.18)
H41α	92.03	0.14±0.02	339.67±4.37	63.48±9.65	1.98	-
N_2H^+ (1 − 0)	93.17	0.29±0.01	313.94±1.55	63.53±3.56	4.34	(0.0263±0.0024)
$C^{34}S$ (2 − 1)	96.41	8.16×10^{-2}±0.01	327.90±4.84	68.34±12.65	1.12	(0.0195±0.0021)
CS (2 − 1)	97.98	4.06±0.03	308.03±0.12	43.79±0.35	87.20	(3.73±0.12)
H40α	99.02	0.22±0.05	319.13±7.78	53.72±12.20	3.82	-
SO ($2_1 - 3_2$)	99.30	0.19±0.01	314.44±2.70	73.53±5.55	2.44	(0.189±0.032)
HC_3N (11 − 10)	100.08	0.61±0.02	323.36±0.87	61.22±1.95	9.31	(2.86±0.18)
CH_3CCH ($6_k - 5_k$)	102.55	1.64±0.03	336.94±0.62	68.64±1.46	22.40	(14.0±0.3)
H39α	106.74	0.19±0.02	332.16±2.51	48.04±6.64	3.68	-
HC_3N (12 − 11)	109.17	0.15±0.01	336.91±1.34	42.18±2.67	3.28	(2.86±0.18)
$C^{18}O$ (1 − 0)	109.78	7.21×10^{-2}±0.01	346.52±0.49	13.47±1.09	5.03	(14.1±1.0)
$C^{18}O$ (1 − 0)	109.78	3.94×10^{-2}±0.01	320.12±0.85	13.11±1.65	2.82	(3.79±1.09)
^{13}CO (1 − 0)	110.20	1.10±0.02	345.60±0.32	39.05±0.78	26.40	(182±8)
CN ($1_{0,1} - 0_{0,1}$)	113.19	3.40±0.04	381.91±0.87	150.97±1.77	21.10	(11.7±0.2)
CN ($1_{0,2} - 0_{0,1}$)	113.49	9.24±0.06	312.96±0.22	75.84±0.51	110.00	(11.7±0.2)

(a) The peak flux density of the fitted Gaussian has not been used for determining the column densities. It is a by-product of the GILDAS fits but the results are only indicative, since the fitted lines do not have a perfect Gaussian shape in all cases. This is why no errors are provided.

Table 5.5: Gaussian Fit of the spectrum from Position B in M 82

Line	Rest Frequency GHz	Flux $\mathrm{Jy\,km\,s^{-1}}$	$\mathrm{V_{LSR}}$ $\mathrm{km\,s^{-1}}$	Width $\mathrm{km\,s^{-1}}$	Flux Density$^{(a)}$ mJy	Column Density $10^{14}\,\mathrm{cm^{-2}}$
$\mathrm{H^{13}CO^{+}\,(1-0)}$	86.75	0.14±0.01	254.71±1.11	28.74±2.40	4.50	(0.05±0.003)
$\mathrm{CCH\,(1_{2,1}-0_{1,1})}$	87.28	1.66×10^{-2}±0.05	256.67±1.52	56.64±6.71	0.28	(15.6±0.2)
$\mathrm{CCH\,(1_{2,2}-0_{1,1})}$	87.32	1.97±0.05	244.68±6.71	59.33±6.71	31.20	(15.6±0.2)
$\mathrm{CCH\,(1_{1,1}-0_{1,1})}$	87.40	0.80±0.05	253.02±0.53	39.69±6.71	19.00	(15.6±0.2)
$\mathrm{CCH\,(1_{1,1}-0_{1,0})}$	87.45	0.12±0.05	265.78±6.70	72.84±6.71	1.58	(15.6±0.2)
$\mathrm{HCN\,(1-0)}$	88.63	3.86±0.03	258.37±0.18	50.58±0.42	71.80	(1.65±0.04)
$\mathrm{HCO^{+}\,(1-0)}$	89.19	5.44±0.13	259.72±0.56	46.57±1.24	110.00	(1.37±0.03)
$\mathrm{HNC\,(1-0)}$	90.66	1.66±0.02	253.31±0.25	38.08±0.61	40.90	(0.582±0.040)
$\mathrm{HC_3N\,(10-9)}$	90.98	0.16±0.01	255.33±1.15	32.42±2.85	4.76	(0.155±0.091)
$\mathrm{H41}\alpha$	92.03	8.30×10^{-2}±0.02	260.09±3.96	43.38±12.87	1.79	-
$\mathrm{N_2H^{+}\,(1-0)}$	93.17	0.17±0.01	259.84±1.07	31.65±2.67	5.06	(0.0439±0.0249)
$\mathrm{C^{34}S\,(2-1)}$	96.41	1.78×10^{-2}±0.01	261.16±2.17	15.71±5.39	1.06	(0.0305±0.004)
$\mathrm{CS\,(2-1)}$	97.98	1.62±0.02	254.71±0.20	35.89±0.51	42.40	(1.89±0.11)
$\mathrm{H40}\alpha$	99.02	0.14±0.04	271.18±8.68	67.22±22.97	1.96	-
$\mathrm{SO\,(2_1-3_2)}$	99.30	7.06×10^{-2}±0.01	247.84±4.07	46.67±9.33	1.42	(0.0452±0.011)
$\mathrm{HC_3N\,(11-10)}$	100.08	0.21±0.01	256.84±1.13	36.67±2.78	5.30	(0.155±0.091)
$\mathrm{CH_3CCH\,(6_k-5_k)}$	102.55	0.73±0.03	265.26±0.76	47.40±2.17	14.50	(15.6±1.8)
$\mathrm{H39}\alpha$	106.74	0.18±0.02	262.64±3.62	59.53±9.27	2.77	-
$\mathrm{HC_3N\,(12-11)}$	109.17	1.32×10^{-2}±0.001	263.56±0.59	5.36±13.769	2.31	(0.155±0.091)
$\mathrm{C^{18}O\,(1-0)}$	109.7	9.01×10^{-2}±0.01	254.65±2.13	44.06±4.08	3.00	(6.55±1.13)
$\mathrm{^{13}CO\,(1-0)}$	110.20	0.56±0.02	253.35±0.40	34.94±0.98	15.00	(91.8±8.2)
$\mathrm{C^{17}O\,(1-0)}$	112.36	8.32×10^{-2}±0.01	260.61±3.69	45.82±10.44	2.90	(8.32±1.39)
$\mathrm{CN\,(1_{0,1}-0_{0,1})}$	113.14	0.66±0.04	256.25±1.32	48.52±3.34	12.80	(12.4±0.2)
$\mathrm{CN\,(1_{0,1}-0_{0,1})}$	113.17	0.92±0.03	252.44±0.55	36.35±1.61	23.80	(12.4±0.2)
$\mathrm{CN\,(1_{0,1}-0_{0,1})}$	113.19	0.72±0.03	253.85±0.65	32.85±1.42	20.60	(12.4±0.2)
$\mathrm{CN\,(1_{0,2}-0_{0,1})}$	113.49	6.84±0.05	248.72±0.21	56.90±0.51	110.00	(12.4±0.2)

(a) The peak flux density of the fitted Gaussian has not been used for determining the column densities. It is a by-product of the GILDAS fits but the results are only indicative, since the fitted lines do not have a perfect Gaussian shape in all cases. This is why no errors are provided.

Table 5.6: Gaussian Fit of the spectrum from Position C in M 82

Line	Rest Frequency GHz	Flux $\mathrm{Jy\,km\,s^{-1}}$	$\mathrm{V_{LSR}}$ $\mathrm{km\,s^{-1}}$	Width $\mathrm{km\,s^{-1}}$	Flux Density$^{(a)}$ mJy	Column Density $10^{14}\,\mathrm{cm^{-2}}$
$\mathrm{H^{13}CO^{+}\,(1-0)}$	86.75	0.26±0.02	154.40±4.52	101.29±8.31	2.42	(0.06±0.002)
$\mathrm{CCH\,(1-0)}$	87.32	2.65±0.04	139.31±0.70	100.79±1.51	24.70	(25.8±0.5)
$\mathrm{CCH\,(1-0)}$	87.40	1.14±0.04	144.71±1.35	98.32±3.55	10.90	(25.8±0.5)
$\mathrm{HCN\,(1-0)}$	88.63	5.08±0.08	149.33±0.73	96.58±1.65	49.40	(2.29±0.05)
$\mathrm{HCO^{+}\,(1-0)}$	89.19	7.51±0.14	154.54±0.90	96.34±2.06	73.20	(2.36±0.04)
$\mathrm{HNC\,(1-0)}$	90.66	2.40±0.06	142.15±1.13	95.72±2.33	23.60	(0.67±0.02)
$\mathrm{HC_3N\,(10-9)}$	90.98	0.25±0.02	131.20±3.63	90.96±7.45	2.54	(0.017±0.01)
$\mathrm{H41}\alpha$	92.03	0.48±0.02	119.10±2.31	110.25±5.25	4.05	-
$\mathrm{N_2H^{+}\,(1-0)}$	93.17	0.18±0.02	139.36±5.71	98.62±12.93	1.76	(0.031±0.005)
$\mathrm{C^{34}S\,(2-1)}$	96.41	3.48×10^{-2}±0.01	168.33±4.91	37.15±10.26	0.88	(0.015±0.004)
$\mathrm{CS\,(2-1)}$	97.98	0.56±0.04	302.85±5.98	23.44±5.98	22.30	(0.58±0.013)
$\mathrm{CS\,(2-1)}$	97.98	1.44±0.04	146.76±5.98	95.38±5.98	14.20	(0.58±0.013)
$\mathrm{H40}\alpha$	99.02	0.46±0.01	124.76±1.17	85.33±2.44	5.09	-
$\mathrm{SO\,(2_1-3_2)}$	99.30	0.11±0.02	335.85±5.85	63.72±15.01	1.62	(0.013±0.01)
$\mathrm{HC_3N\,(11-10)}$	100.08	0.37±0.01	138.76±1.00	91.89±5.38	3.85	(0.17±0.08)
$\mathrm{CH_3CCH\,(6_k-5_k)}$	102.55	0.46±0.03	180.26±1.46	43.16±3.24	10.00	(4.66±0.34)
$\mathrm{H39}\alpha$	106.74	0.57±0.03	124.23±1.77	82.35±4.61	6.54	-
$\mathrm{HC_3N\,(12-11)}$	109.17	0.10±0.01	138.99±4.14	76.99±8.16	1.22	(0.17±0.08)
$\mathrm{C^{18}O\,(1-0)}$	109.78	0.13±0.01	137.04±0.85	25.58±2.40	4.63	(29.9±1.7)
$\mathrm{^{13}CO\,(1-0)}$	110.20	0.93±0.02	134.34±0.23	53.24±1.24	24.00	(50.6±4.5)
$\mathrm{CN\,(1_{0,1}-0_{0,1})}$	113.19	3.70±0.05	178.47±0.78	121.05±1.84	28.70	(20.5±1.1)
$\mathrm{CN\,(1_{0,2}-0_{0,1})}$	113.19	6.89±0.22	300.33±5.16	75.69±5.16	85.50	(20.5±1.1)
$\mathrm{CN\,(1_{0,2}-0_{0,1})}$	113.49	9.32±0.22	132.62±5.16	94.40±5.16	92.80	(20.5±1.1)

(a) The peak flux density of the fitted Gaussian has not been used for determining the column densities. It is a by-product of the GILDAS fits but the results are only indicative, since the fitted lines do not have a perfect Gaussian shape in all cases. This is why no errors are provided.

Table 5.7: Gaussian Fit of the spectrum from Position D in M 82

Line	Rest Frequency GHz	Flux $\mathrm{Jy\,km\,s^{-1}}$	$\mathrm{V_{LSR}}$ $\mathrm{km\,s^{-1}}$	Width $\mathrm{km\,s^{-1}}$	Flux Density$^{(a)}$ mJy	Column Density $10^{14}\ \mathrm{cm^{-2}}$
$\mathrm{H^{13}CO^{+}}$ $(1-0)$	86.75	0.21±0.02	104.58±2.03	47.48±6.13	4.15	(0.036±0.002)
CCH $(1_{2,2}-0_{1,1})$	87.32	2.83±0.03	101.75±0.38	73.81±0.97	36.00	(23.3±0.5)
CCH $(1_{1,1}-0_{1,1})$	87.40	1.32±0.03	110.28±0.57	65.23±1.60	19.00	(23.3±0.5)
CCH $(1_{1,1}-0_{1,0})$	87.45	0.15±0.03	110.02±3.03	46.49±10.22	3.10	(23.3±0.5)
HCN $(1-0)$	88.63	5.27±0.05	113.50±0.33	74.64±0.70	66.30	(0.85±0.03)
$\mathrm{HCO^{+}}$ $(1-0)$	89.19	7.71±0.14	118.09±0.66	75.39±1.50	96.10	(1.74±0.04)
HNC $(1-0)$	90.66	1.87±0.02	107.75±0.27	49.48±0.64	35.40	(0.61±0.04)
$\mathrm{HC_3N}$ $(10-9)$	90.98	0.13±0.01	96.11±0.86	24.83±2.68	4.83	(0.42±0.05)
$\mathrm{H41\alpha}$	92.034	0.23±0.02	93.57±2.13	65.08±5.04	3.37	-
$\mathrm{N_2H^{+}}$ $(1-0)$	93.17	0.24±0.01	97.54±1.19	43.27±3.01	5.16	(0.044±0.002)
$\mathrm{C^{34}S}$ $(2-1)$	96.41	0.10±0.01	118.21±2.91	58.27±6.01	1.67	(0.087±0.001)
CS $(2-1)$	97.98	2.17±0.02	111.77±0.21	58.26±0.47	34.90	(2.10±0.06)
$\mathrm{H40\alpha}$	99.02	0.23±0.01	111.65±2.30	84.92±4.26	2.56	-
SO (2_1-3_2)	99.30	7.01×10^{-2}±0.01	107.06±1.42	21.46±4.02	3.06	(0.16±0.04)
$\mathrm{HC_3N}$ $(11-10)$	100.08	0.21±0.02	107.90±2.42	58.96±5.075	4.85	(0.42±0.05)
$\mathrm{CH_3CCH}$ (6_k-5_k)	102.55	0.61±0.03	107.52±0.90	44.18±2.63	12.90	(10.02±0.6)
$\mathrm{H39\alpha}$	106.74	0.47±0.02	103.15±2.03	87.99±4.63	4.98	-
$\mathrm{C^{18}O}$ $(1-0)$	109.17	0.18±0.01	107.25±0.94	40.52±2.56	5.90	(5.08±0.52)
$\mathrm{^{13}CO}$ $(1-0)$	110.20	1.18±0.01	106.48±0.21	41.81±0.50	26.60	(219±12)
$\mathrm{C^{17}O}$ $(1-0)$	112.36	0.12±0.01	116.34±4.08	71.47±6.57	2.11	(8.24±0.10)
CN $(1_{0,1}-0_{0,1})$	113.14	0.35±0.03	95.64±0.69	27.89±2.86	11.90	(8.89±0.19)
CN $(1_{0,1}-0_{0,1})$	113.17	1.22±0.06	148.86±1.05	51.73±2.94	22.20	(8.89±0.19)
CN $(1_{0,1}-0_{0,1})$	113.19	0.62±0.05	98.80±090	30.40±1.90	19.10	(8.89±0.19)
CN $(1_{0,2}-0_{0,1})$	113.49	5.16±0.21	99.22±1.34	70.50±3.35	68.70	(8.89±0.19)

(a) The peak flux density of the fitted Gaussian has not been used for determining the column densities. It is a by-product of the GILDAS fits but the results are only indicative, since the fitted lines do not have a perfect Gaussian shape in all cases. This is why no errors are provided.

Table 5.8: Gaussian Fit of the spectrum from Position A in IC 342

Line	Rest Frequency	Flux	V_{LSR}	Width	Flux Density$^{(a)}$	Column Density
	GHz	$\mathrm{Jy\,km\,s^{-1}}$	$\mathrm{km\,s^{-1}}$	$\mathrm{km\,s^{-1}}$	mJy	$10^{14}\ \mathrm{cm^{-2}}$
$H^{13}CN(1-0)$	86.34	0.21±0.01	45.48±1.11	42.94±2.53	4.55	(0.046±0.002)
$H^{13}CO^+\ (1-0)$	86.75	8.25×10^{-2}±0.01	41.39±1.87	31.47±4.32	2.39	(0.027±0.002)
SiO $(2-1)$	86.85	0.26±0.01	43.17±0.83	44.19±1.92	5.53	(0.14±0.01)
$HN^{13}C(1-0)$	87.09	5.91×10^{-2}±0.01	40.61±2.99	63.77±10.15	1.51	(0.026±0.003)
CCH $(1_{2,1}-0_{1,1})$	87.28	4.41×10^{-2}±0.01	44.82±1.97	21.94±4.35	1.88	(6.00±0.10)
CCH $(1_{2,2}-0_{1,1})$	87.32	0.67±0.02	34.99±6.71	62.95±6.71	10.02	(6.00±0.10)
CCH $(1_{2,1}-0_{1,1})$	87.40	0.28±0.02	39.39±0.70	41.72±1.53	6.21	(6.00±0.10)
CCH $(1_{1,1}-0_{1,0})$	87.45	8.11×10^{-2}±0.02	52.99±2.41	40.44±5.57	1.88	(6.00±0.10)
HNCO $(4_{0,4}-3_{0,3})$	87.93	0.54±0.01	45.81±0.17	29.12±0.42	17.30	(2.51±0.13)
HCN $(1-0)$	88.63	2.89±0.01	48.60±0.09	52.86±0.19	51.30	(1.77±0.03)
$HCO^+\ (1-0)$	89.19	2.01±0.001	49.16±0.09	49.29±0.17	38.40	(0.86±0.014)
HNC $(1-0)$	90.66	0.76±0.01	45.08±0.20	37.20±0.47	19.20	(0.39±0.001)
$HC_3N\ (10-9)$	90.98	0.26±0.01	43.50±0.51	31.65±1.16	7.80	(2.56±0.32)
$CH_3CN\ (5_k-4_k)$	91.99	5.90×10^{-2}±0.01	62.64±3.48	47.55±7.69	1.17	(0.0518±0.01)
$N_2H^+\ (1-0)$	93.17	0.27±0.01	44.52±0.41	35.23±0.87	7.20	(0.0951±0.003)
$C^{34}S\ (2-1)$	96.41	0.13±0.01	50.49±1.02	27.79±2.11	4.25	(0.19±0.02)
$CH_3OH\ (2_k-1_k)$	96.74	0.80±0.01	58.48±0.27	34.43±0.65	21.90	(6.19±0.20)
CS $(2-1)$	97.98	1.17±0.01	22.20±0.19	37.10±0.44	29.70	(3.08±0.02)
SO (2_1-3_2)	99.30	0.19±0.01	44.01±1.32	37.21±3.85	4.82	(0.49±0.03)
$HC_3N\ (11-10)$	100.08	0.31±0.01	45.54±0.53	27.95±1.31	10.50	(2.56±0.32)
$CH_3CCH\ (6_k-5_k)$	102.55	7.99×10^{-2}±0.01	50.19±4.24	57.46±11.38	1.31	(1.73±0.10)
$^{13}CN\ (1-0)$	108.78	3.58×10^{-2}±0.01	33.20±3.72	28.22±7.62	1.19	(0.039±0.007)
$CH_3OH\ (0_0-1_{-1})$	108.89	0.27±0.01	47.87±0.47	23.59±1.09	10.80	(6.19±.020)
$HC_3N\ (12-11)$	109.17	0.40±0.01	46.73±0.29	27.24±0.71	13.60	(2.56±0.32)
$C^{18}O\ (1-0)$	109.78	1.09±0.02	47.93±0.21	27.59±0.47	37.10	(635±31)
HNCO $(5_{0,5}-4_{0,4})$	109.91	0.83±0.01	46.12±0.12	25.23±0.27	30.90	(2.51±0.13)
$^{13}CO\ (1-0)$	110.20	4.90±0.07	47.26±0.21	31.54±0.46	150.00	(1870±100)
$CH_3CN\ (6-5)$	110.38	8.75×10^{-2}±0.02	44.77±3.51	42.76±10.16	1.92	(0.052±0.01)
$CH_3CN\ (6-5)$	110.38	6.69×10^{-2}±0.01	4.71±1.74	23.16±3.35	2.70	(0.052±0.01)
$C^{17}O\ (1-0)$	112.36	0.10±0.01	44.75±0.87	22.67±2.17	4.32	(24.2±1.1)
CN $(1_{0,1}-0_{0,1})$	113.12	0.21±0.03	39.14±2.25	37.56±7.14	5.20	(7.94±0.18)
CN $(1_{0,1}-0_{0,1})$	113.14	0.20±0.02	44.62±1.00	25.18±3.03	7.32	(7.94±0.18)
CN $(1_{0,1}-0_{0,1})$	113.17	0.61±0.02	48.98±0.63	38.62±1.65	14.50	(7.94±0.18)
CN $(1_{0,1}-0_{0,1})$	113.19	0.49±0.02	46.30±0.73	34.35±1.60	13.40	(7.94±0.18)
CN $(1_{0,2}-0_{0,1})$	113.49	3.01±0.03	38.72±0.34	79.08±0.80	38.20	(7.94±0.18)

(a) The peak flux density of the fitted Gaussian has not been used for determining the column densities. It is a by-product of the GILDAS fits but the results are only indicative, since the fitted lines do not have a perfect Gaussian shape in all cases. This is why no errors are provided.

Table 5.9: Gaussian Fit of the spectrum from Position B in IC 342

Line	Rest Frequency GHz	Flux $\mathrm{Jy\,km\,s^{-1}}$	$\mathrm{V_{LSR}}$ $\mathrm{km\,s^{-1}}$	Width $\mathrm{km\,s^{-1}}$	Flux Density$^{(a)}$ mJy	Column Density $10^{14}\,\mathrm{cm^{-2}}$
$\mathrm{H^{13}CN(1-0)}$	86.34	0.16±0.01	21.82±1.15	37.20±3.004	4.10	(0.059±0.004)
$\mathrm{H^{13}CO^{+}\ (1-0)}$	86.75	0.11±0.01	21.06±1.21	30.07±2.89	3.52	(0.025±0.003)
$\mathrm{SiO\ (2-1)}$	86.85	9.73×10^{-2}±0.01	17.62±1.08	31.83±2.43	2.87	(0.202±0.008)
$\mathrm{HN^{13}C(1-0)}$	87.09	4.59×10^{-2}±0.01	16.93±2.37	24.22±6.54	1.78	(0.024±0.004)
$\mathrm{CCH\ (1_{2,1}-0_{1,1})}$	87.28	5.42×10^{-2}±0.01	26.69±3.12	36.91±6.40	1.38	(25.9±0.4)
$\mathrm{CCH\ (1_{2,2}-0_{1,1})}$	87.32	0.47±0.01	19.92±0.37	32.95±1.02	13.40	(25.9±0.4)
$\mathrm{CCH\ (1_{2,1}-0_{1,1})}$	87.40	0.31±0.01	20.72±0.62	41.29±1.69	6.91	(25.9±0.4)
$\mathrm{CCH\ (1_{1,1}-0_{1,0})}$	87.45	7.41×10^{-2}±0.01	26.67±3.78	53.19±9.93	1.31	(25.9±0.4)
$\mathrm{HNCO\ (4_{0,4}-3_{0,3})}$	87.93	0.31±0.01	35.18±0.75	53.26±1.48	5.49	(1.53±0.12)
$\mathrm{HCN\ (1-0)}$	88.63	2.91±0.01	23.80±0.08	49.01±0.19	55.70	(3.13±0.04)
$\mathrm{HCO^{+}\ (1-0)}$	89.19	2.32±0.01	25.01±0.10	42.44±0.24	51.20	(0.81±0.01)
$\mathrm{HNC\ (1-0)}$	90.66	1.05±0.01	20.13±0.13	28.90±0.30	34.10	(0.38±0.007)
$\mathrm{HC_3N\ (10-9)}$	90.98	0.14±0.01	17.98±0.57	21.30±1.38	5.99	(0.39±0.01)
$\mathrm{CH_3CN\ (5_{\mathit{k}}-4_{\mathit{k}})}$	91.99	3.70×10^{-2}±0.004	32.85±1.56	25.14±3.33	1.38	(0.025±0.004)
$\mathrm{N_2H^{+}\ (1-0)}$	93.17	0.37±0.01	18.77±0.20	25.81±0.45	13.50	(0.096±0.003)
$\mathrm{C^{34}S\ (2-1)}$	96.41	9.94×10^{-2}±0.01	23.20±1.92	32.05±3.91	2.910	(0.38±0.03)
$\mathrm{CH_3OH\ (2_k-1_k)}$	96.74	0.37±0.02	28.36±0.61	24.09±1.28	13.10	(5.35±0.45)
$\mathrm{CS\ (2-1)}$	97.98	1.00±0.01	-1.64±0.17	34.59±0.41	27.10	(1.59±0.02)
$\mathrm{SO\ (2_1-3_2)}$	99.30	9.73×10^{-2}±0.01	18.47±0.91	27.49±2.18	3.32	(0.48±0.04)
$\mathrm{HC_3N\ (11-10)}$	100.08	0.14±0.01	19.26±0.69	22.86±1.62	5.82	(0.39±0.01)
$\mathrm{CH_3CCH\ (6_k-5_k)}$	102.55	7.57×10^{-2}±0.01	27.504±2.56	38.88±5.48	1.83	(0.47±0.09)
$\mathrm{^{13}CN\ (1-0)}$	108.78	3.08×10^{-2}±0.001	30.31±1.64	22.47±3.00	1.29	(0.04.5±0.009)
$\mathrm{CH_3OH\ (0_0-1_{-1})}$	108.89	8.42×10^{-2}±0.01	25.81±1.48	24.77±3.73	3.19	(5.35±0.45)
$\mathrm{HC_3N\ (12-11)}$	109.17	0.11±0.01	22.02±0.77	21.25±1.89	4.95	(0.39±0.01)
$\mathrm{C^{18}O\ (1-0)}$	109.78	0.74±0.01	28.83±0.26	28.65±0.55	24.30	(497±17)
$\mathrm{HNCO\ (5_{0,5}-4_{0,4})}$	109.91	0.27±0.01	23.72±0.50	27.41±1.31	9.09	(1.53±0.12)
$\mathrm{^{13}CO\ (1-0)}$	110.20	3.74±0.01	28.42±0.04	30.16±0.08	120.00	(4430±130)
$\mathrm{CH_3CN\ (6-5)}$	110.38	8.79×10^{-2}±0.01	-1.01±3.28	53.17±7.52	1.55	(0.025±0.004)
$\mathrm{C^{17}O\ (1-0)}$	112.36	0.14±0.01	25.27±1.68	31.44±3.45	4.05	(52.0±2.1)
$\mathrm{CN\ (1_{0,1}-0_{0,1})}$	113.12	0.15±0.03	22.25±5.18	24.81±5.18	5.78	(8.55±0.21)
$\mathrm{CN\ (1_{0,1}-0_{0,1})}$	113.14	0.40±0.02	24.44±0.64	30.40±1.57	12.00	(8.55±0.21)
$\mathrm{CN\ (1_{0,1}-0_{0,1})}$	113.17	0.82±0.02	24.12±0.33	30.95±0.80	25.10	(8.55±0.21)
$\mathrm{CN\ (1_{0,1}-0_{0,1})}$	113.19	0.62±0.02	22.02±0.43	30.92±1.00	18.80	(8.55±0.21)
$\mathrm{CN\ (1_{0,2}-0_{0,1})}$	113.49	2.54±0.05	24.33±0.34	40.79±0.63	58.40	(8.55±0.21)

(a) The peak flux density of the fitted Gaussian has not been used for determining the column densities. It is a by-product of the GILDAS fits but the results are only indicative, since the fitted lines do not have a perfect Gaussian shape in all cases. This is why no errors are provided.

Table 5.10: Gaussian Fit of the spectrum from Position C in IC 342

Line	Rest Frequency GHz	Flux $\mathrm{Jy\,km\,s^{-1}}$	V_{LSR} $\mathrm{km\,s^{-1}}$	Width $\mathrm{km\,s^{-1}}$	Flux Density$^{(a)}$ Jy	Column Density $10^{14}\,\mathrm{cm^{-2}}$
$H^{13}CN(1-0)$	86.34	0.12±0.01	24.09±0.89	28.11±2.21	3.85	(0.35±0.02)
$H^{13}CO^+\,(1-0)$	86.75	0.12±0.01	24.64±1.22	30.50±2.60	3.70	(0.23±0.02)
$SiO\,(2-1)$	86.85	2.79×10^{-2}±0.01	21.08±3.36	21.09±10.21	1.24	(0.22±0.008)
$HN^{13}C(1-0)$	87.09	6.64×10^{-2}±0.01	22.44±1.66	28.02±4.33	2.23	(0.03±0.004)
$CCH\,(1_{2,1}-0_{1,1})$	87.28	7.76×10^{-2}±0.02	25.46±6.71	57.66±6.71	1.30	(7.83±0.14)
$CCH\,(1_{2,2}-0_{1,1})$	87.32	0.48±0.01	20.75±0.23	30.55±0.94	14.7	(7.83±0.14)
$CCH\,(1_{2,1}-0_{1,1})$	87.40	0.33±0.01	19.39±0.57	40.42±1.34	7.75	(7.83±0.14)
$CCH\,(1_{1,1}-0_{1,0})$	87.45	3.05×10^{-2}±0.01	19.49±2.41	20.12±4.77	1.42	(7.83±0.14)
$HNCO\,(4_{0,4}-3_{0,3})$	87.93	0.25±0.01	30.85±0.83	58.98±1.74	3.95	(12.3±1.1)
$HCN\,(1-0)$	88.63	2.91±0.01	25.57±0.08	43.41±0.20	63.00	(3.45±0.05)
$HCO^+\,(1-0)$	89.19	2.45±0.02	26.12±0.11	38.50±0.28	59.70	(1.52±0.02)
$HNC\,(1-0)$	90.66	0.72±0.01	23.72±0.14	27.20±0.34	24.90	(0.29±0.005)
$HC_3N\,(10-9)$	90.98	4.69×10^{-2}±0.01	21.77±1.21	20.39±2.55	2.16	(0.5±0.012)
$CH_3CN\,(5_k-4_k)$	91.99	1.63×10^{-2}±0.004	35.45±1.73	14.01±3.66	1.09	(0.22±0.018)
$N_2H^+\,(1-0)$	93.17	8.02×10^{-2}±0.01	20.69±0.73	20.27±1.47	3.72	(0.53±0.018)
$C^{34}S\,(2-1)$	96.41	3.31×10^{-2}±0.01	33.42±1.49	12.56±3.38	2.49	(0.45±0.038)
$CH_3OH\,(2_\mathrm{k}-1_\mathrm{k})$	96.74	7.84×10^{-2}±0.01	29.43±0.98	16.62±1.94	4.43	(5.40±0.15)
$CS\,(2-1)$	97.98	0.65±0.01	-0.90±0.28	29.01±0.63	21.20	(2.74±0.02)
$SO\,(2_1-3_2)$	99.30	5.88×10^{-2}±0.01	14.64±8.98	76.53±24.57	0.72	(0.95±0.065)
$HC_3N\,(11-10)$	100.08	3.40×10^{-2}±0.01	20.87±2.80	21.71±5.47	1.47	(0.504±0.012)
$CH_3CCH\,(6_\mathrm{k}-5_\mathrm{k})$	102.55	6.00×10^{-2}±0.01	32.61±2.23	28.17±4.66	2.00	(6.00±0.23)
$^{13}CN\,(1-0)$	108.78	2.80×10^{-2}±0.01	-21.26±3.27	23.39±5.26	1.12	(0.12±0.021)
$CH_3OH\,(0_0-1_{-1})$	108.89	7.04×10^{-2}±0.01	17.30±1.19	22.78±2.31	2.90	(5.40±0.15)
$HC_3N\,(12-11)$	109.17	5.45×10^{-2}±0.01	21.90±2.16	24.07±5.87	2.12	(0.504±0.012)
$C^{18}O\,(1-0)$	109.78	0.83±0.02	21.10±0.24	27.46±0.56	28.20	(386±13)
$HNCO\,(5_{0,5}-4_{0,4})$	109.91	0.21±0.02	15.01±0.97	27.24±2.15	7.39	(12.3±1.1)
$^{13}CO\,(1-0)$	110.20	4.53±0.02	22.74±0.07	33.14±0.17	130.00	(1560±50)
$CH_3CN\,(6-5)$	110.38	5.31×10^{-2}±0.01	-28.52±3.87	45.81±6.73	1.09	(0.22±0.018)
$C^{17}O\,(1-0)$	112.36	0.14±0.02	16.54±1.85	31.28±5.93	4.07	(1.02±4)
$CN\,(1_{0,1}-0_{0,1})$	113.12	0.16±0.02	21.68±1.45	29.72±5.82	5.09	(9.27±0.23)
$CN\,(1_{0,1}-0_{0,1})$	113.14	0.39±0.03	23.57±0.69	32.00±3.38	11.40	(9.27±0.23)
$CN\,(1_{0,1}-0_{0,1})$	113.17	0.71±0.03	27.27±5.17	29.14±1.28	23.00	(9.27±0.23)
$CN\,(1_{0,1}-0_{0,1})$	113.19	0.59±0.03	22.84±0.78	34.17±1.97	16.20	(9.27±0.23)
$CN\,(1_{0,2}-0_{0,1})$	113.49	3.01±0.03	24.66±5.16	39.02±5.16	72.50	(9.27±0.23)

(a) The peak flux density of the fitted Gaussian has not been used for determining the column densities. It is a by-product of the GILDAS fits but the results are only indicative, since the fitted lines do not have a perfect Gaussian shape in all cases. This is why no errors are provided.

From these tables, one notices a certain homogeneity in the integrated intensity, peak intensity, and the abundances for some molecules (HCN, SO, $CN\,(1_{0,1}-0_{0,1})$, ...) towards different positions, in the two galaxies. For other molecules ($CN\,(1_{0,2}-0_{0,1})$, HC_3N, HNCO, ...), the difference in peak intensities and abundances is more pronounced. However, one notices considerable differences in the velocity of the molecular lines between the different positions in M 82 and IC 342, ranging around 300, 250, 150, and 100 km s^{-1} for positions A, B, C, and D in M 82 respectively, and around 45, 25, and 20 km s^{-1}, for positions A, B, and C in IC 342 respectively. Moreover, one notices differences in the detected lines between M 82 and IC 342. For instance, three H_α radio recombination lines were observed in M 82 but not in IC 342. On the other hand, CH$_3$OH, SiO and HNCO molecules were detected in IC 342, but not in M 82. Methanol (CH$_3$OH) has been observed in regions A, B, and C in IC 342, but the estimated abundances should be considered with caution as they might be overestimated due to the low signal-to-noise ratio for this molecule. Other molecules such as H^{13}CN, HN^{13}C, and CH$_3$CN remain undetected in M 82 in this study. This could be due to their low abundances in M 82, and/or the low sensitivity and low signal-to-noise ratios of some frequency tunings. The column densities of the different molecules in each of the positions in the two galaxies are presented in Table. 5.13. The column densities were calculated in MADCUBA_IJ, assuming an excitation temperature T_{ex} of 15 K for both M 82 and IC 342. The peak flux densities are presented in Table. 5.11, and the flux is presented in Table. 5.12.

Table 5.11: Total Flux Densities (mJy): Comparison between M 82 and IC 342

Line	M 82				IC 342		
	Position A	Position B	Position C	Position D	Position A	Position B	Position C
H^{13}CN	-	-	-	-	4.55	4.10	3.85
H^{13}CO$^+$	4.69	4.50	4.00	4.15	2.39	3.52	3.70
SiO	-	-	-	-	5.53	2.87	1.24
HN^{13}C	-	-	-	-	1.51	1.78	2.23
CCH	62.30	52.10	35.60	58.10	33.10	28.80	31.70
HNCO	-	-	-	-	48.10	14.60	11.30
HCN	67.00	71.80	49.40	66.30	51.30	55.70	63.00
HCO$^+$	110.00	110.00	73.20	96.10	38.40	51.20	59.70
HNC	37.90	40.90	23.60	35.40	19.20	34.10	24.90
HC$_3$N	18.50	12.40	19.90	12.20	31.90	16.80	5.75
CH$_3$CN	-	-	-	-	5.80	2.93	2.18
H41α	1.98	1.79	4.05	3.37	-	-	-
N$_2$H$^+$	4.34	5.06	1.76	5.16	7.20	13.50	3.72
C^{34}S	1.12	1.06	0.88	1.67	4.25	2.91	2.49
CH$_3$OH	-	-	-	-	32.70	16.3	7.33
CS	87.20	42.40	36.50	34.90	29.70	27.10	21.20
H40α	3.82	1.96	5.09	2.56	-	-	-
SO	2.44	1.42	1.62	3.06	4.82	3.32	0.72
CH$_3$CCH	22.40	14.50	10.00	12.90	1.30	1.77	2.00
H39α	3.68	2.77	6.54	4.98	-	-	-
^{13}CN	-	-	-	-	1.19	1.29	1.12
C^{18}O	7.85	3.00	4.63	5.90	37.10	24.30	28.20
^{13}CO	26.4	15.00	30.40	26.60	0.15	0.12	0.13
C^{17}O	-	2.90	-	2.90	4.32	4.05	4.50
CN	131.00	167.00	207.00	122.00	98.00	150.00	157.00

Table 5.12: Total Flux ($\mathrm{Jy\,km\,s^{-1}}$): Comparison between M 82 and IC 342

Line	M 82				IC 342		
	Position A	Position B	Position C	Position D	Position A	Position B	Position C
$H^{13}CN$	**(0.07)**	**(0.02)**	**(0.03)**	**(0.03)**	0.20	0.16	0.12
$H^{13}CO^+$	0.29	0.14	0.16	0.21	0.08	0.11	0.12
SiO	**(0.07)**	**(0.02)**	**(0.03)**	**(0.02)**	0.26	0.09	0.03
$HN^{13}C$	**(0.07)**	**(0.02)**	**(0.03)**	**(0.03)**	0.06	0.05	0.07
CCH	5.13	2.90	3.79	4.30	1.06	1.06	1.05
HNCO	**(0.07)**	**(0.09)**	**(0.03)**	**(0.03)**	1.37	0.58	0.46
HCN	4.67	3.86	5.08	5.27	2.89	2.91	2.91
HCO^+	7.31	5.44	7.51	7.71	2.01	2.32	2.45
HNC	2.55	1.66	2.40	1.87	0.76	1.05	0.72
HC_3N	1.14	0.21	0.75	0.35	0.97	0.39	0.14
CH_3CN	**(0.07)**	**(0.03)**	**(0.04)**	**(0.03)**	0.21	0.12	0.07
$H41\alpha$	0.14	0.08	0.48	0.23	-	-	-
N_2H^+	0.29	0.17	0.18	0.24	0.27	0.37	0.08
$C^{34}S$	0.08	0.02	0.03	0.10	0.13	0.1	0.03
CH_3OH	**(0.06)**	**(0.03)**	**(0.02)**	**(0.02)**	1.07	0.45	0.15
CS	4.06	1.62	2.00	2.17	1.17	1.00	0.65
$H40\alpha$	0.22	0.14	0.46	0.23	-	-	-
SO	0.19	0.07	0.11	0.07	0.19	0.09	0.06
CH_3CCH	1.64	0.73	0.46	0.61	0.08	0.07	0.06
$H39\alpha$	0.19	0.18	0.57	0.47	-	-	-
^{13}CN	**(0.02)**	**(0.02)**	**(0.01)**	**(0.01)**	0.03	0.03	0.03
$C^{18}O$	0.11	0.09	0.13	0.18	1.09	0.74	0.83
^{13}CO	1.10	0.56	1.02	1.18	4.90	3.74	4.53
$C^{17}O$	**(0.04)**	0.08	**(0.02)**	0.12	0.10	0.14	0.14
CN	12.64	9.14	19.91	7.35	4.40	5.94	7.08

Values in boldface are upper limit estimates. For more details, please check the text.

Table 5.13: Total Column Densities (cm^{-2}): Comparison between M 82 and IC 342.

Line	M 82				IC 342		
	Position A	Position B	Position C	Position D	Position A	Position B	Position C
$H^{13}CN$	$\mathbf{(4.05\times 10^{12})}$	$\mathbf{(1.35\times 10^{12})}$	$\mathbf{(1.74\times 10^{12})}$	$\mathbf{(1.52\times 10^{12})}$	$(1.21\pm0.08)\times10^{13}$	$(8.85\pm0.60)\times10^{12}$	$(6.04\pm0.37)\times10^{12}$
$H^{13}CO^+$	$(8.91\pm0.28)\times10^{12}$	$(4.08\pm0.16)\times10^{12}$	$(6.98\pm0.53)\times10^{12}$	$(4.58\pm0.34)\times10^{12}$	$(3.04\pm0.20)\times10^{12}$	$(3.60\pm0.16)\times10^{12}$	$(3.70\pm0.15)\times10^{12}$
SiO	$\mathbf{(3.82\times 10^{12})}$	$\mathbf{(1.13\times 10^{12})}$	$\mathbf{(1.72\times 10^{12})}$	$\mathbf{(1.29\times 10^{12})}$	$(1.44\pm0.06)\times10^{13}$	$(5.18\pm0.26)\times10^{12}$	$(2.31\pm0.31)\times10^{12}$
$HN^{13}C$	$\mathbf{(3.99\times 10^{12})}$	$\mathbf{(9.68\times 10^{11})}$	$\mathbf{(1.63\times 10^{12})}$	$\mathbf{(1.57\times 10^{12})}$	$(4.04\pm0.42)\times10^{12}$	$(2.84\pm0.38)\times10^{12}$	$(4.02\pm0.34)\times10^{12}$
CCH	$(3.33\pm0.04)\times10^{15}$	$(1.92\pm0.02)\times10^{15}$	$(2.57\pm0.05)\times10^{15}$	$(2.85\pm0.06)\times10^{15}$	$(7.57\pm0.12)\times10^{14}$	$(7.45\pm0.11)\times10^{14}$	$(8.07\pm0.09)\times10^{14}$
HNCO	$\mathbf{(6.99\times 10^{12})}$	$\mathbf{(8.55\times 10^{12})}$	$\mathbf{(2.82\times 10^{12})}$	$\mathbf{(2.43\times\times 10^{12})}$	$(1.45\pm0.02)\times10^{14}$	$(5.27\pm0.27)\times10^{13}$	$(3.58\pm0.23)\times10^{13}$
HCN	$(1.99\pm0.03)\times10^{14}$	$(1.67\pm0.03)\times10^{14}$	$(2.11\pm0.05)\times10^{14}$	$(2.33\pm0.07)\times10^{14}$	$(1.44\pm0.03)\times10^{14}$	$(1.47\pm0.02)\times10^{14}$	$(1.48\pm0.02)\times10^{14}$
HCO^+	$(1.85\pm0.04)\times10^{14}$	$(1.40\pm0.07)\times10^{14}$	$(1.83\pm0.04)\times10^{14}$	$(1.98\pm0.08)\times10^{14}$	$(5.81\pm0.10)\times10^{13}$	$(6.78\pm0.13)\times10^{13}$	$(7.30\pm0.11)\times10^{13}$
HNC	$(9.57\pm0.18)\times10^{13}$	$(6.15\pm0.07)\times10^{13}$	$(8.93\pm0.40)\times10^{13}$	$(6.92\pm0.32)\times10^{13}$	$(3.29\pm0.06)\times10^{13}$	$(4.59\pm0.06)\times10^{13}$	$(3.15\pm0.06)\times10^{13}$
HC_3N	$(3.12\pm0.23)\times10^{13}$	$(1.03\pm0.11)\times10^{13}$	$(1.83\pm0.16)\times10^{13}$	$(7.26\pm1.31)\times10^{12}$	$(3.16\pm0.12)\times10^{13}$	$(1.24\pm0.04)\times10^{13}$	$(4.20\pm0.41)\times10^{12}$
CH_3CN	$\mathbf{(1.24\times 10^{12})}$	$\mathbf{(5.84\times 10^{11})}$	$\mathbf{(6.73\times 10^{11})}$	$\mathbf{(4.43\times 10^{11})}$	$(3.74\pm0.32)\times10^{12}$	$(2.19\pm0.22)\times10^{12}$	$(9.62\pm2.15)\times10^{11}$
N_2H^+	$(7.28\pm0.48)\times10^{12}$	$(4.51\pm0.27)\times10^{12}$	$(2.04\pm0.36)\times10^{12}$	$(7.43\pm0.39)\times10^{12}$	$(8.41\pm0.32)\times10^{12}$	$(1.14\pm0.04)\times10^{13}$	$(2.36\pm0.21)\times10^{12}$
$C^{34}S$	$(5.30\pm0.90)\times10^{12}$	$(1.59\pm0.30)\times10^{12}$	$(1.24\pm0.52)\times10^{12}$	$(7.28\pm1.12)\times10^{12}$	$(1.27\pm0.09)\times10^{13}$	$(9.27\pm0.98)\times10^{12}$	$(2.99\pm0.57)\times10^{12}$
CH_3OH	$\mathbf{(3.51\times 10^{12})}$	$\mathbf{(2.11\times 10^{12})}$	$\mathbf{(1.40\times 10^{12})}$	$\mathbf{(1.02\times 10^{12})}$	$(5.70\pm0.15)\times10^{13}$	$(2.14\pm0.10)\times10^{14}$	$(6.21\pm0.70)\times10^{13}$
CS	$(3.24\pm0.13)\times10^{14}$	$(1.26\pm0.03)\times10^{14}$	$(1.23\pm0.06)\times10^{14}$	$(1.69\pm0.05)\times10^{14}$	$(1.05\pm0.01)\times10^{14}$	$(8.97\pm0.17)\times10^{13}$	$(5.86\pm0.15)\times10^{13}$
SO	$(3.57\pm0.32)\times10^{13}$	$(8.89\pm2.22)\times10^{12}$	$(9.44\pm3.18)\times10^{12}$	$(1.32\pm0.29)\times10^{13}$	$(3.84\pm0.35)\times10^{13}$	$(2.00\pm0.21)\times10^{13}$	$(1.52\pm0.27)\times10^{13}$
CH_3CCH	$(1.47\pm0.03)\times10^{15}$	$(1.14\pm0.09)\times10^{15}$	$(4.20\pm0.70)\times10^{14}$	$(5.22\pm0.36)\times10^{14}$	$(8.05\pm0.84)\times10^{12}$	$(7.10\pm0.74)\times10^{13}$	$(6.47\pm0.86)\times10^{13}$
^{13}CN	$\mathbf{(6.53\times 10^{12})}$	$\mathbf{(4.90\times 10^{12})}$	$\mathbf{(3.53\times 10^{12})}$	$\mathbf{(2.18\times 10^{12})}$	$(8.71\pm1.56)\times10^{12}$	$(1.10\pm0.13)\times10^{13}$	$(1.91\pm1.25)\times10^{12}$
$C^{18}O$	$(1.32\pm0.24)\times10^{15}$	$(1.27\pm0.20)\times10^{15}$	$(1.81\pm0.12)\times10^{15}$	$(2.59\pm0.24)\times10^{15}$	$(1.74\pm0.05)\times10^{16}$	$(1.21\pm0.05)\times10^{16}$	$(1.33\pm0.04)\times10^{16}$
^{13}CO	$(1.58\pm0.07)\times10^{16}$	$(7.93\pm0.53)\times10^{15}$	$(1.25\pm0.11)\times10^{16}$	$(1.61\pm0.09)\times10^{16}$	$(8.15\pm0.24)\times10^{16}$	$(6.24\pm0.18)\times10^{16}$	$(7.55\pm0.10)\times10^{16}$
$C^{17}O$	$\mathbf{(3.23\times\times 10^{14})}$	$(7.59\pm0.15)\times10^{14}$	$\mathbf{(1.36\times 10^{14})}$	$(9.51\pm2.74)\times10^{14}$	$(1.56\pm0.06)\times10^{15}$	$(2.08\pm0.16)\times10^{15}$	$(2.07\pm0.16)\times10^{15}$
CN	$(1\pm0.02)\times10^{15}$	$(9.64\pm1.53)\times10^{14}$	$(1.04\pm0.06)\times10^{15}$	$(5.89\pm0.12)\times10^{14}$	$(3.57\pm0.10)\times10^{14}$	$(4.74\pm0.14)\times10^{14}$	$(5.20\pm0.09)\times10^{14}$

Values in boldface are upper limit estimates. For more details, please check the text.

The values in boldface in Table. 5.12 and 5.13 are upper limit estimates with 3σ significance. The upper limits for the flux were obtained from the rms of the channels where the line would be if it were detected and the supposed width of the line, usually estimated from lines with similar frequency. The upper limits of the column densities were estimated by assuming that the conversion factor from flux to column density of these lines are the same in IC 342 and M 82.
From the column density presented in Table 5.13, one can calculate relevant column densities ratios (abundances ratios) for each region in the two galaxies (For more information about how the column densities are calculated, see Chapter 4, Section 4.4). These abundance ratios are presented in Table 5.14. These ratios were selected as they might give more insights about the chemical and physical properties of the emission regions in the galaxies. More details about these ratios, their implications, and their interpretation will be discussed at length in Chapter 6.

Table 5.14: Column Density Ratios: Comparison between M 82 and IC 342

Ratio	M 82				IC 342		
	Position A	Position B	Position C	Position D	Position A	Position B	Position C
$\frac{\mathrm{HCO^+(1-0)}}{\mathrm{H^{13}CO^+(1-0)}}$	20.76	34.31	26.22	43.23	19.11	18.83	19.73
$\frac{\mathrm{HCN(1-0)}}{\mathrm{H^{13}CN(1-0)}}$	-	-	-	-	11.90	16.61	24.50
$\frac{\mathrm{C^{18}O(1-0)}}{\mathrm{C^{17}O(1-0)}}$	-	1.32	-	2.72	11.15	5.82	6.43
$\frac{\mathrm{HCO^+(1-0)}}{\mathrm{HNC(1-0)}}$	1.90	2.27	2.04	2.86	1.75	1.47	2.33
$\frac{\mathrm{HCO^+(1-0)}}{\mathrm{HCN(1-0)}}$	0.93	0.84	0.87	0.85	0.40	0.46	0.49
$\frac{\mathrm{HNC(1-0)}}{\mathrm{HCN(1-0)}}$	0.48	0.37	0.42	0.30	0.23	0.31	0.23
$\frac{\mathrm{CN(1-0)}}{\mathrm{HCN(1-0)}}$	5.03	4.55	4.93	2.53	2.48	3.22	3.51
$\frac{\mathrm{CS(2-1)}}{\mathrm{HCN(1-0)}}$	1.63	0.75	0.58	0.73	0.73	0.61	0.40
$\frac{\mathrm{HNCO}}{\mathrm{CS(2-1)}}$	-	-	-	-	1.38	0.64	0.61
$\frac{\mathrm{HC_3N}}{\mathrm{CN(1-0)}}$	0.03	0.01	0.02	0.01	0.08	0.03	0.01
$\frac{\mathrm{SO(2-1)}}{\mathrm{CS(2-1)}}$	0.11	0.07	0.07	0.08	0.37	0.22	0.26
$\frac{\mathrm{CS(2-1)}}{\mathrm{C^{34}S(2-1)}}$	61.13	79.25	99.19	23.21	8.27	9.68	19.60

5.3 Relative Abundances

In order to make molecular abundances comparison possible, one usually uses the fractional abundance of a molecular species relative to H_2 (see eq. 2.16 in Chapter 2 Section2.2). The column densities of H_2 in M 82 and IC 342 have values of $\sim 10^{22}\,\mathrm{cm}^{-2}$ (e.g. Meier and Turner 2005 and Martín et al. 2010). However, these values are averaged values over the central regions of the galaxies, covering ~ 250 pc and ~ 80 pc in M 82 and IC 342 respectively. In this study, the observed regions (positions) have a size of ~ 30 pc. Therefore, one cannot use the column densities of H_2 estimated in previous studies. However, one can use the column densities of $C^{18}O$ obtained from this study. The column density of $C^{18}O$ is often used to estimate the column density of H_2, as its transitions are optically thin (Wilson et al. 2012). Therefore, in this study, the fractional abundances of the molecular species relative to $C^{18}O$ (see Table. 5.15) will be used to compare the abundances of these molecules between M 82 and IC 342. The boldface values in Table. 5.15 are upper limit estimates.

Table 5.15: Comparison of M 82 and IC 342 fractional abundances relative to $C^{18}O$

Line	M 82				IC 342		
	Position A	Position B	Position C	Position D	Position A	Position B	Position C
$H^{13}CN$	($\mathbf{3.07}\times10^{-3}$)	($\mathbf{1.06}\times10^{-3}$)	($\mathbf{9.61}\times10^{-4}$)	($\mathbf{5.87}\times10^{-4}$)	6.95×10^{-4}	7.31×10^{-4}	4.54×10^{-4}
$H^{13}CO^+$	6.75×10^{-3}	3.21×10^{-3}	3.86×10^{-3}	1.77×10^{-3}	1.75×10^{-4}	2.98×10^{-4}	2.78×10^{-4}
SiO	($\mathbf{2.89}\times10^{-3}$)	($\mathbf{8.90}\times10^{-3}$)	($\mathbf{9.50}\times10^{-4}$)	($\mathbf{4.98}\times10^{-4}$)	8.28×10^{-4}	4.28×10^{-4}	1.74×10^{-4}
$HN^{13}C$	($\mathbf{3.02}\times10^{-3}$)	($\mathbf{7.62}\times10^{-4}$)	($\mathbf{9.01}\times10^{-4}$)	($\mathbf{6.06}\times10^{-4}$)	2.32×10^{-4}	2.35×10^{-4}	3.02×10^{-4}
CCH	2.52	1.51	1.42	1.10	4.35×10^{-2}	6.16×10^{-2}	6.07×10^{-2}
HNCO	($\mathbf{5.30}\times10^{-3}$)	($\mathbf{6.73}\times10^{-3}$)	($\mathbf{1.56}\times10^{-3}$)	($\mathbf{9.38}\times10^{-4}$)	8.33×10^{-3}	4.36×10^{-3}	2.69×10^{-3}
HCN	1.51×10^{-1}	1.31×10^{-1}	1.17×10^{-1}	9.0×10^{-2}	8.28×10^{-3}	1.21×10^{-2}	1.11×10^{-2}
HCO^+	1.40×10^{-1}	1.10×10^{-1}	1.017×10^{-1}	7.64×10^{-2}	3.34×10^{-3}	5.60×10^{-3}	5.49×10^{-3}
HNC	7.25×10^{-2}	4.84×10^{-2}	4.93×10^{-2}	2.67×10^{-2}	1.89×10^{-3}	3.79×10^{-3}	2.37×10^{-3}
HC_3N	2.36×10^{-2}	8.11×10^{-3}	1.01×10^{-2}	2.80×10^{-3}	1.82×10^{-3}	1.02×10^{-3}	3.16×10^{-4}
CH_3CN	($\mathbf{9.39}\times10^{-4}$)	($\mathbf{4.60}\times10^{-4}$)	($\mathbf{3.72}\times10^{-4}$)	($\mathbf{1.71}\times10^{-4}$)	2.15×10^{-4}	1.81×10^{-4}	7.23×10^{-5}
N_2H^+	5.52×10^{-3}	3.55×10^{-3}	1.13×10^{-3}	2.87×10^{-3}	4.83×10^{-4}	9.42×10^{-4}	1.77×10^{-4}
$C^{34}S$	4.02×10^{-3}	1.25×10^{-3}	6.85×10^{-4}	2.81×10^{-3}	7.30×10^{-4}	7.66×10^{-4}	2.25×10^{-4}
CH_3OH	($\mathbf{2.66}\times10^{-3}$)	($\mathbf{1.66}\times10^{-3}$)	($\mathbf{7.73}\times10^{-4}$)	($\mathbf{3.94}\times10^{-4}$)	3.28×10^{-3}	1.77×10^{-2}	4.67×10^{-3}
CS	2.45×10^{-1}	9.92×10^{-2}	6.80×10^{-2}	6.53×10^{-2}	6.03×10^{-3}	7.41×10^{-3}	4.41×10^{-3}
SO	2.70×10^{-2}	7.00×10^{-3}	5.22×10^{-3}	5.10×10^{-3}	2.21×10^{-3}	1.65×10^{-3}	1.14×10^{-3}
CH_3CCH	1.11	8.98×10^{-1}	2.32×10^{-1}	2.02×10^{-1}	4.63×10^{-4}	5.87×10^{-3}	4.86×10^{-3}
^{13}CN	($\mathbf{4.95}\times10^{-3}$)	($\mathbf{3.86}\times10^{-3}$)	($\mathbf{1.95}\times10^{-3}$)	($\mathbf{8.42}\times10^{-4}$)	5.01×10^{-4}	9.12×10^{-4}	1.44×10^{-4}
$C^{18}O$	1	1	1	1	1	1	1
^{13}CO	12.0	6.24	6.91	6.22	4.68	5.16	5.68
$C^{17}O$	($\mathbf{2.45}\times10^{-1}$)	5.98×10^{-1}	($\mathbf{1.78}\times10^{-1}$)	3.67×10^{-1}	8.97×10^{-2}	1.72×10^{-1}	1.56×10^{-1}
CN	7.58×10^{-1}	7.59×10^{-1}	5.75×10^{-1}	3.27×10^{-1}	2.05×10^{-2}	3.92×10^{-2}	3.91×10^{-2}

Values in boldface are upper limit estimates. For more details, please check the text.

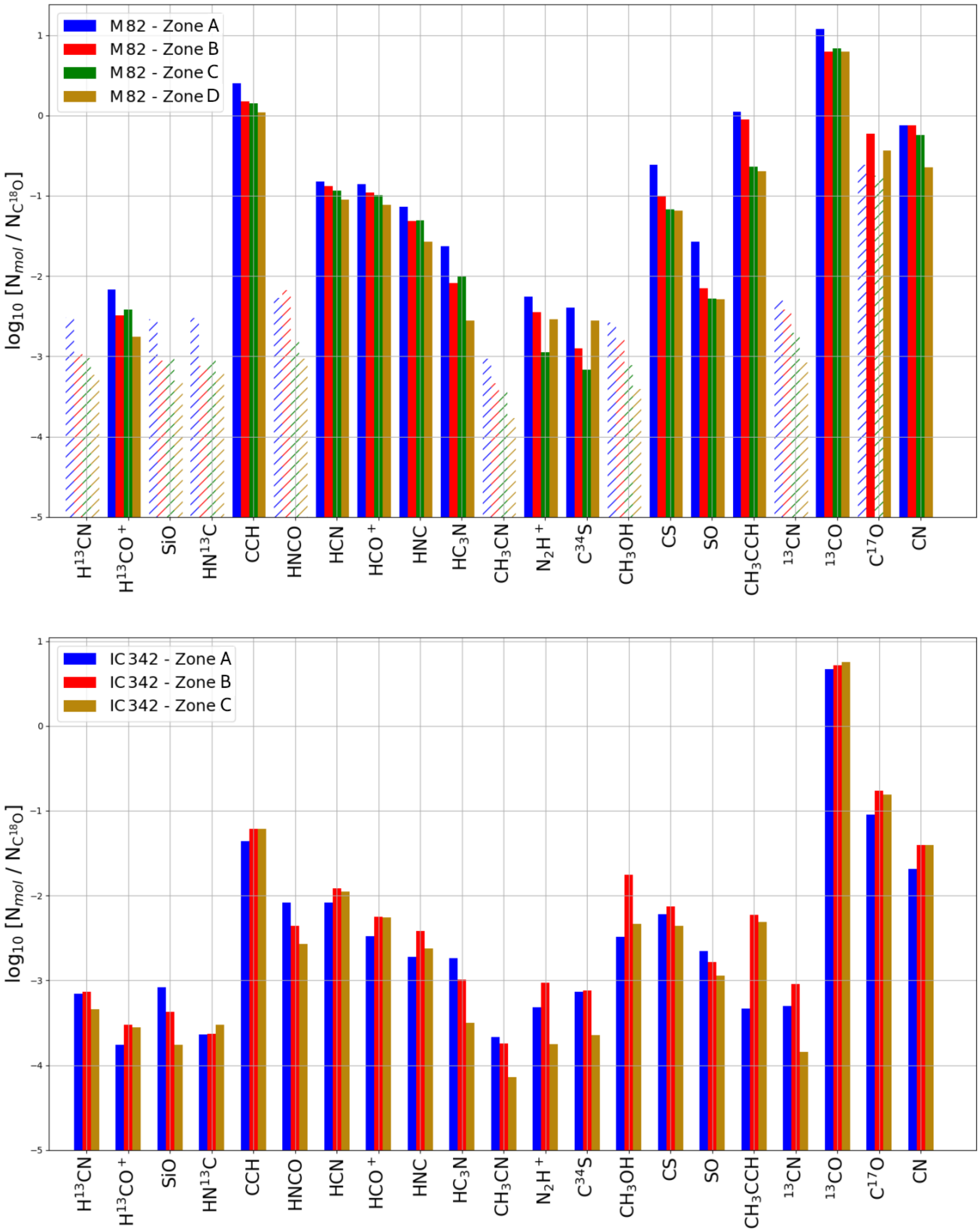

Figure 5.6: Top panel: Comparison of the fractional abundances relative to $C^{18}O$ in M 82. The hashed lines are upper limit estimates with 3σ significance level. Bottom panel: Comparison of the fractional abundances relative to $C^{18}O$ in IC 342

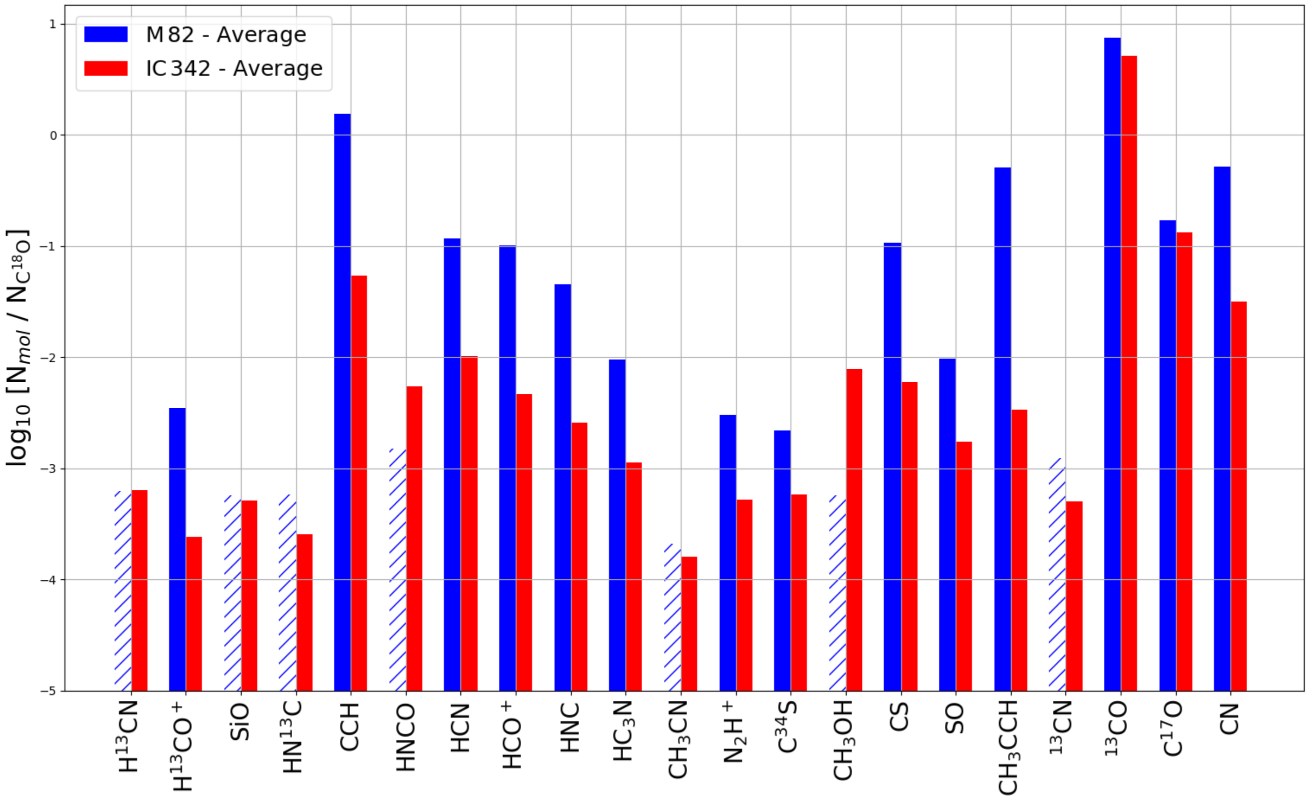

Figure 5.7: Comparison of the average fractional abundances relative to $C^{18}O$ in M 82 and IC 342. The hashed lines are upper limit estimates with 3σ significance level.

5.4 Comparison with Chemical Models

The column densities obtained for each zone in M 82 and IC 342 were compared with the chemical models presented in Viti (2017). These chemical models cover broad range of gas densities (10^4- $10^6\,\mathrm{cm^{-3}}$), temperatures (50 - 200 K), with the cosmic ray ionisation field ζ varying between 1 and $10^5\,\zeta_0$ ($\zeta_0 = 5 \times 10^{-17}\,\mathrm{s^{-1}}$ is the standard local value for the cosmic ray ionisation field), a radiation field χ ranging between 1 and 500 χ_0 ($\chi_0 = 2.74 \times 10^{-3}\,\mathrm{erg\,s^{-1}\,cm^{-2}}$ is the standard local value for the radiation field), and a visual extinction A_v ranging between 1 and 50 mag. The models were produced using the publicly available UCL_CHEM gas-grain time dependent chemical code[1] (see Holdship et al. 2017). The code assumes a large velocity gradient and non-LTE radiative transfer. Some initial parameters were given: the H_2 formation rate was set at $10^{-16}\,\mathrm{cm^3\,s^{-1}}$, the abundance of C relative to H was set to $\frac{\mathrm{C}}{\mathrm{H}} = 1.8 \times 10^{-4}$, the abundance of O was set to $\frac{\mathrm{O}}{\mathrm{H}} = 3 \times 10^{-4}$, that of Mg was set at $\frac{\mathrm{Mg}}{\mathrm{H}} = 5.1 \times 10^{-6}$, and finally the abundance of electrons was set at $\frac{\mathrm{e}}{\mathrm{H_{tot}}} = 7.5 \times 10^{-2}$ (Viti, priv. comm.).

The parameters used for the chemical modelling were selected based on their influence on the column density of molecular species. For instance, the visual extinction is directly correlated to the column density of hydrogen, while the radiation and the cosmic-ray ionisation fields affect the chemistry of the molecular cloud, and differ in starburst galaxies from those in AGN-dominated environments. The model starts from a diffuse and atomic gas with a density of $10\,\mathrm{cm^{-3}}$, and

---

[1] The code can be downloaded at https://uclchem.github.io/

shows the evolution of the molecular abundances as a function of time.

The time-dependency of the model offers an important insight on the chemical evolution of the molecular cloud with respect to time, as such time-dependent evolution is difficult to observe (Viti 2017). In some models, chemical equilibrium was reached within a million years, while in others, changes in the chemistry between 10^6 and 10^7 years were noticeable. For instance, in models with high cosmic ray ionisation rates, the chemical equilibrium was reached in early times. However, in models with high radiation fields and with the visual extinction values considered for the models, chemical equilibrium was not reached. Therefore, the column densities of some molecular line species (for example, HCN, and CS) are highly time dependent. Some species such as CH_3OH and HNCO were destroyed before the chemical equilibrium was reached.

Viti (2017) presents 67 models. In some of these models (models 65, 66, and 67), shocks with a velocity of $40\,\mathrm{km\,s^{-1}}$ are simulated. Viti (2017) also compared the survey results of M 82 using the IRAM 30-m telescope presented by Aladro et al. (2011a) to the chemical models and stated that no single model was able to explain the column densities, intensities, or line ratios for all the molecular species observed. Considering that the spatial resolution obtained by Aladro et al. (2011a) was 150-350 kpc, the small-scale components and substructures of the molecular gas of M 82 remained unresolved. Viti (2017) concludes that a single chemical model cannot describe the chemistry of a large-scale molecular gas, especially if it includes substructures with different chemistries, and that single-dish observations with low spatial resolutions are not optimal for a comparison with chemical models.

In this interferometric study, the integrated intensities, column densities and abundance ratios of different molecular species in each individual zone of M 82 and IC 342 are compared with the online available tables published by Viti (2017). In the online-available tables, Viti (2017) presented the integrated intensities, column densities of nine molecules: HCN, HNC, HCO^+, CS, CO, SO, SiO, HNCO, and CH_3OH, and the abundance ratios of $\frac{\mathrm{HCN}}{\mathrm{HCO^+}}$. The comparison was made for these molecules, except for CO, which is not observed in this study. A match is considered when the difference between the observed and predicted values for each molecular species is within a 25 % margin of the predicted value. The models with the highest number of matches are then the models that best describe the observed data.

The column densities of the molecular species observed in this study are similar across the different zones of each galaxy, showing thus a lack of strong chemical diversity between the different zones. This is why the same model can be a match for all the zones of a galaxy. The comparison showed that the chemistry in the different zones of M 82 and IC 342 is best described by models 13, 19, 36, and 39 of Viti (2017). The parameters of these models are presented in Table. 5.16.

Table 5.16: The parameters of the chemical models as presented in Viti 2017

Model	$\zeta^{(a)}$	$\chi^{(b)}$	T (K)	$n_{\mathrm{H}}(\mathrm{cm}^{-3})$	A_v (mag)
13	10	1	100	10^5	10
19	1	10	100	10^4	50
36	5000	1	100	10^4	50
39	10^5	1	100	10^5	50

(a) ζ is given as a factor of $\zeta_0 = 5 \times 10^{-17}\,\mathrm{s^{-1}}$

(b) χ is given as a factor of $\chi_0 = 2.74 \times 10^{-3}\,\mathrm{erg\,s^{-1}\,cm^{-2}}$

In order to take a deeper look into these models and find the best match out of these four models, Viti (priv. comm.) provided the estimated fractional abundances relative to hydrogen for each matched model. In each model, the fractional abundances of around 250 molecules and atoms were estimated, at a time $t = 10^7$ years. The fractional abundances in the models of Viti (2017) are calculated relative to H. In this study, the fractional abundances were calculated relative to $C^{18}O$. Therefore a comparison of fractional abundances might be erroneous. It is then better to compare the column densities of the models with the column densities derived in this work. In order to obtain the column densities predicted by the model, the fractional abundance was multiplied by $2 \times 10^{21}\,\mathrm{cm^{-2}} \times A_v$ ($\frac{N_\mathrm{H}}{A_v} \backsimeq 2 \times 10^{21}\,\mathrm{cm^{-2}\,mag^{-1}}$, Zhu et al. 2017).

From the 250 molecular and atomic species in the models, only 14 molecules were observed in this study: CCH, CN, HCN, HNC, HCO^+, N_2H^+, CH_3OH, CH_3CCH, CH_3CN, CS, SiO, SO, HC_3N, and HNCO. In Figs. 5.8 - 5.11, the column densities of the 14 molecules observed in this study are compared to their predicted column densities in the models (toward M 82, only upper limits of CH_3OH, CH_3CN, SiO, and HNCO are shown). As seen in the figures below, a single model does not match the column densities of all molecular species. The best matched molecular species are HCN, HNC, HCO^+, and N_2H^+, and to a lesser extent, CS, and CN.

In M 82, where 10 molecular species (out of the 250 species presented in the chemical model of Viti 2017) were observed (CCH, CN, HCN, HNC, HCO^+, N_2H^+, CH_3CCH, CS, SO, and HC_3N), the best matched model is Model 36, where the column densities of 8 out of 10 molecular species were a match. For the CH_3OH, CH_3CN, SiO, and HNCO only the upper limits were estimated. For CH_3OH, CH_3CN, and HNCO, the upper limits are higher than the predicted column densities of the model. Therefore, it could not be determined, for those species, if they match the prediction of the chemical models. However, for SiO, the upper limits are lower than the values predicted by the model, and thus a match can be ruled out. In IC 342, only 9 out of the 14 observed molecular species were a match in Model 36.

Table 5.17 shows the molecular species whose column densities matched the predicted value of the model. One can see that Model 36 is the best match for both M 82 and IC 342. The second best match is Model 39. These models are characterised by a high cosmic-ray ionisation rate ($5000\zeta_0$ for Model 36, and $10^5\zeta_0$ for Model 39). This would indicate that both M 82 and IC 342 have a strong cosmic-ray ionisation rate, ranging between $\zeta = 2.5 \times 10^{-13}\,\mathrm{s^{-1}}$ (Model 36) and $\zeta = 5 \times 10^{-12}\,\mathrm{s^{-1}}$ (Model 39). The radiation field is similar to that in the Milky Way ($\chi = 2.74 \times 10^{-3}\,\mathrm{erg\,s^{-1}\,cm^{-2}}$) (Model 36 and 39), a temperature of 100 K (Model 36 and 39), a gas density between 10^4 (Model 36) and $10^5\,\mathrm{cm^3}$ (Model 39), and finally a visual extinction of 50 mag (Model 36 and 39).

Table 5.17: Molecular species and chemical models matches

Model	M 82 Matches	M 82 total$^{(a)}$	IC 342 Matches	IC 342 total$^{(b)}$
13	HCN, HNC, HCO^+, N_2H^+, CS	5	HCN, HNC, HCO^+, N_2H^+, CS	5
19	HCN, HNC, HCO^+, N_2H^+	4	HCN, HNC, HCO^+, N_2H^+	4
36	CCH, CN, HCN, HNC, HCO^+, N_2H^+, CS, SO	8	CCH, CN, HCN, HNC, HCO^+, N_2H^+, CS, SiO, SO	9
39	CN, HCN, HNC, HCO^+, N_2H^+, CS, SO	7	CCH, CN, HCN, HNC, HCO^+, N_2H^+, SiO, SO	8

(a) Match out of the 10 molecular species observed in M 82: CCH, CN, HCN, HNC, HCO^+, N_2H^+, CH_3CCH, CS, SiO, SO, and HC_3N. For CH_3OH, CH_3CN, and HNCO a match could not be confirmed.
(b) Match out of the 14 molecular species observed in IC 342: CCH, CN, HCN, HNC, HCO^+, N_2H^+, CH_3OH, CH_3CCH, CH_3CN, CS, SiO, SO, HC_3N, and HNCO.

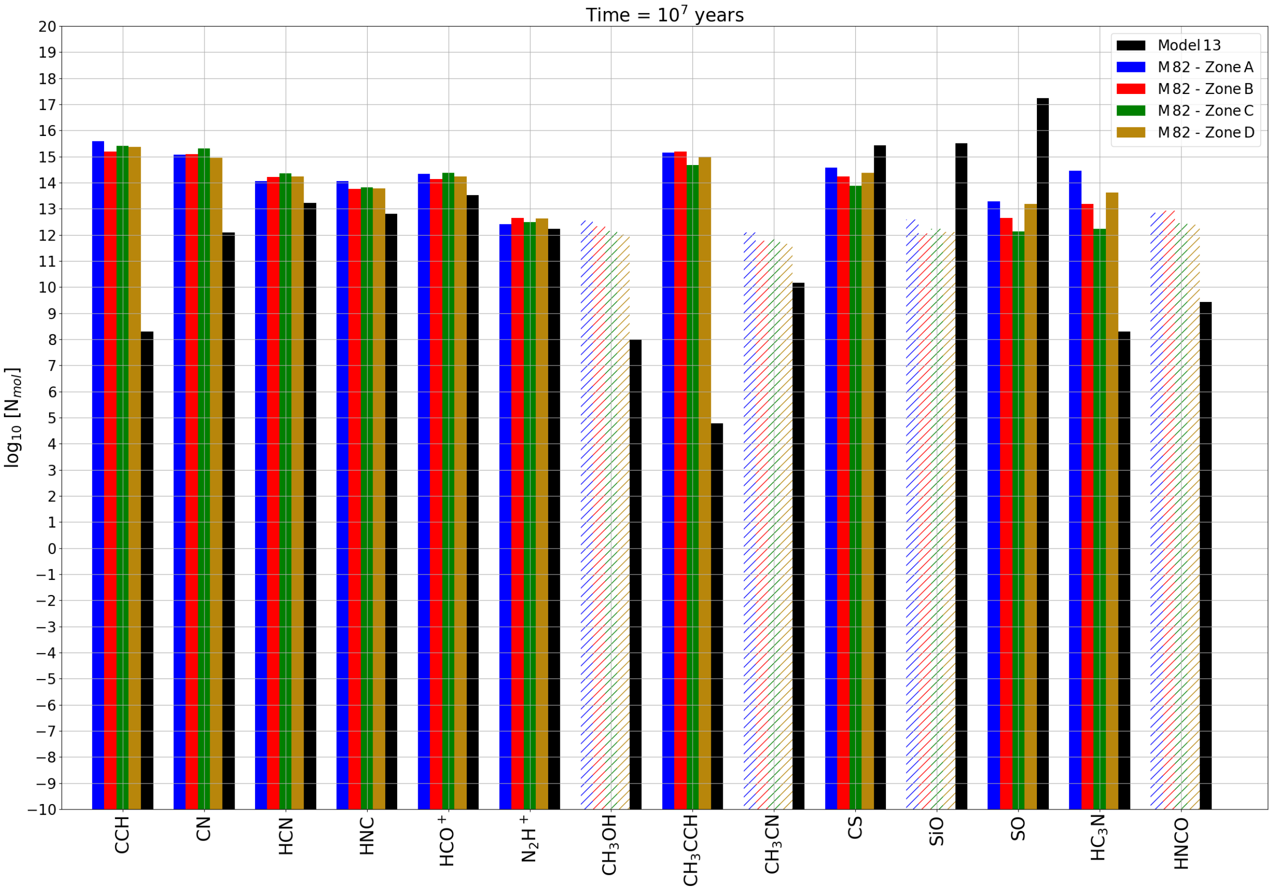

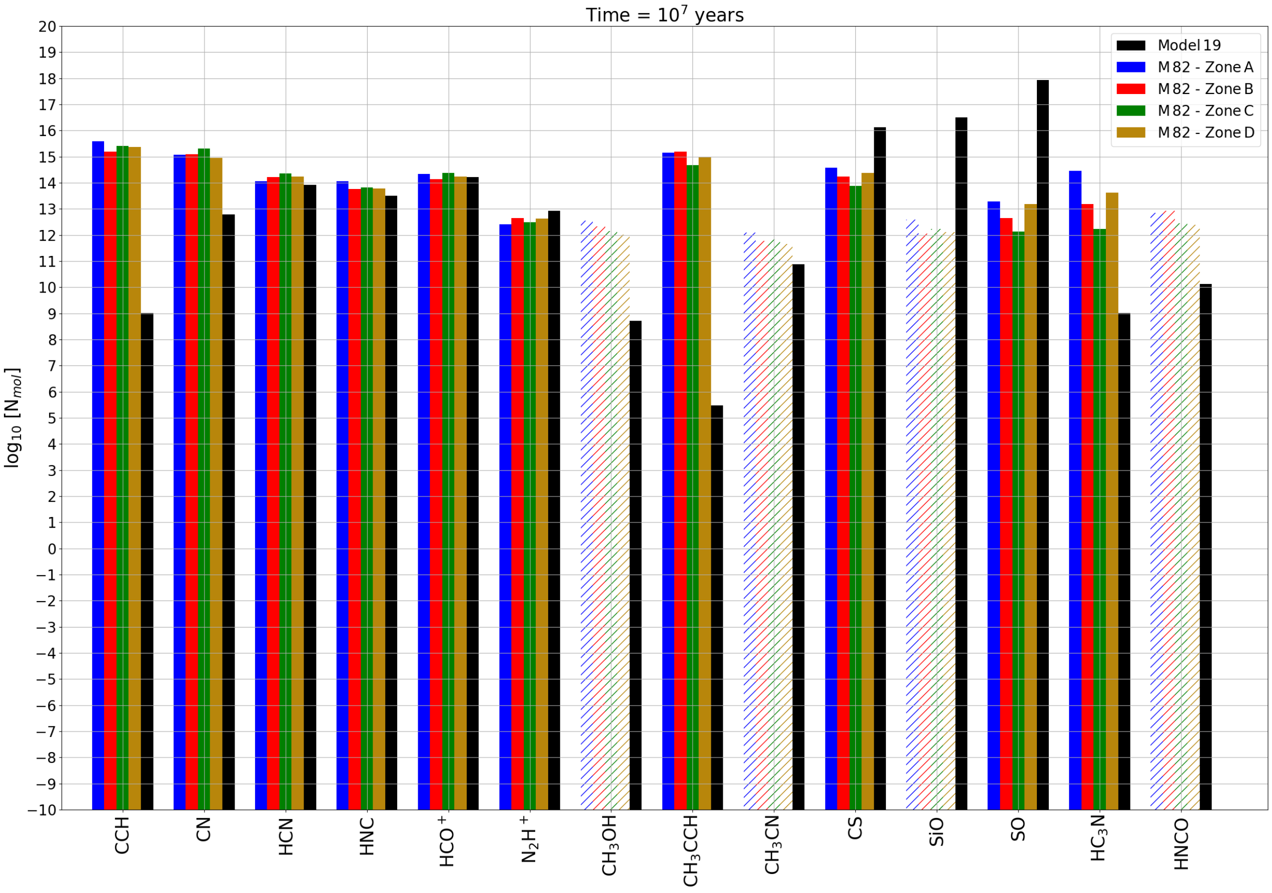

Figure 5.8: Column Densities of the 14 molecular species in M 82 compared with the chemical model 13 and 19. The hashed lines are upper limit estimates of the observed column densities with 3σ significance level.

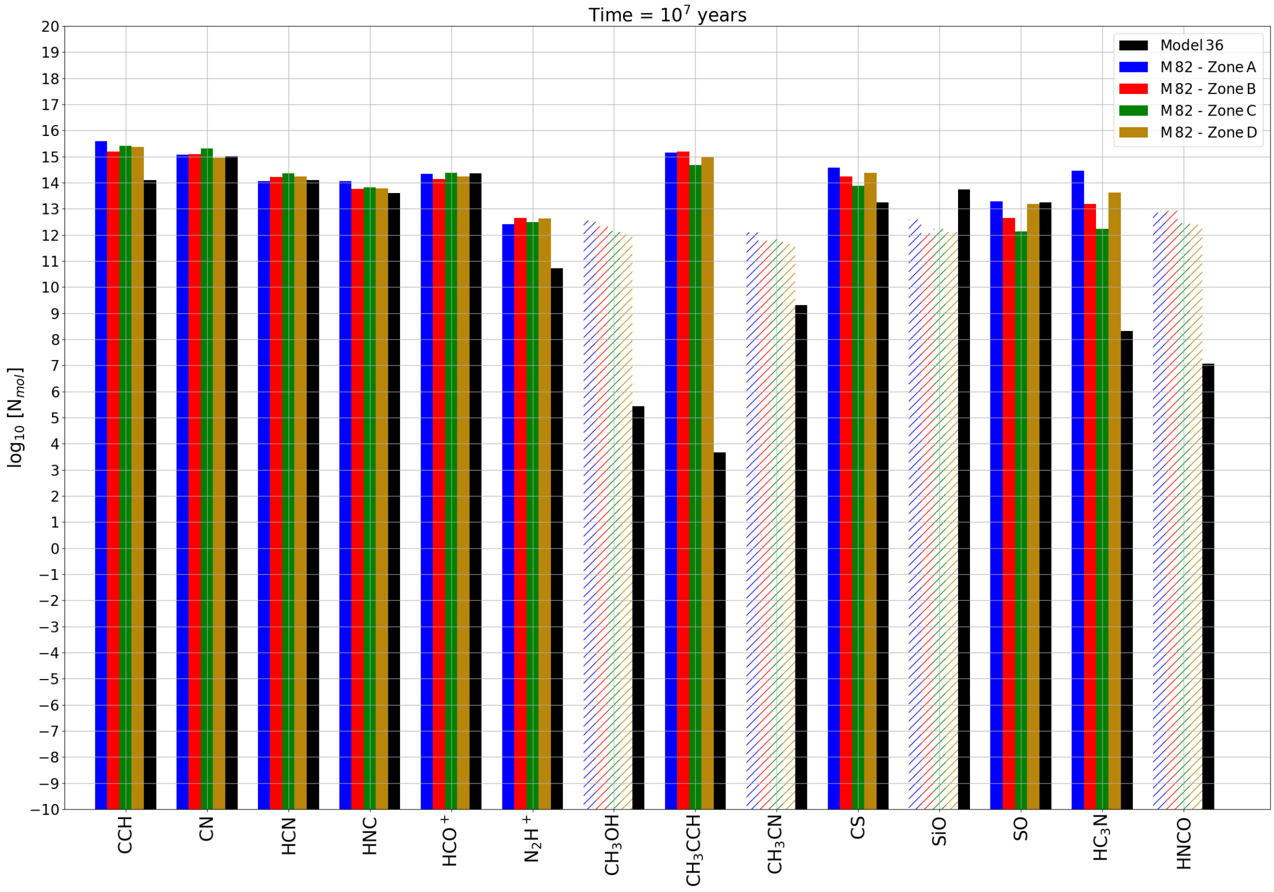

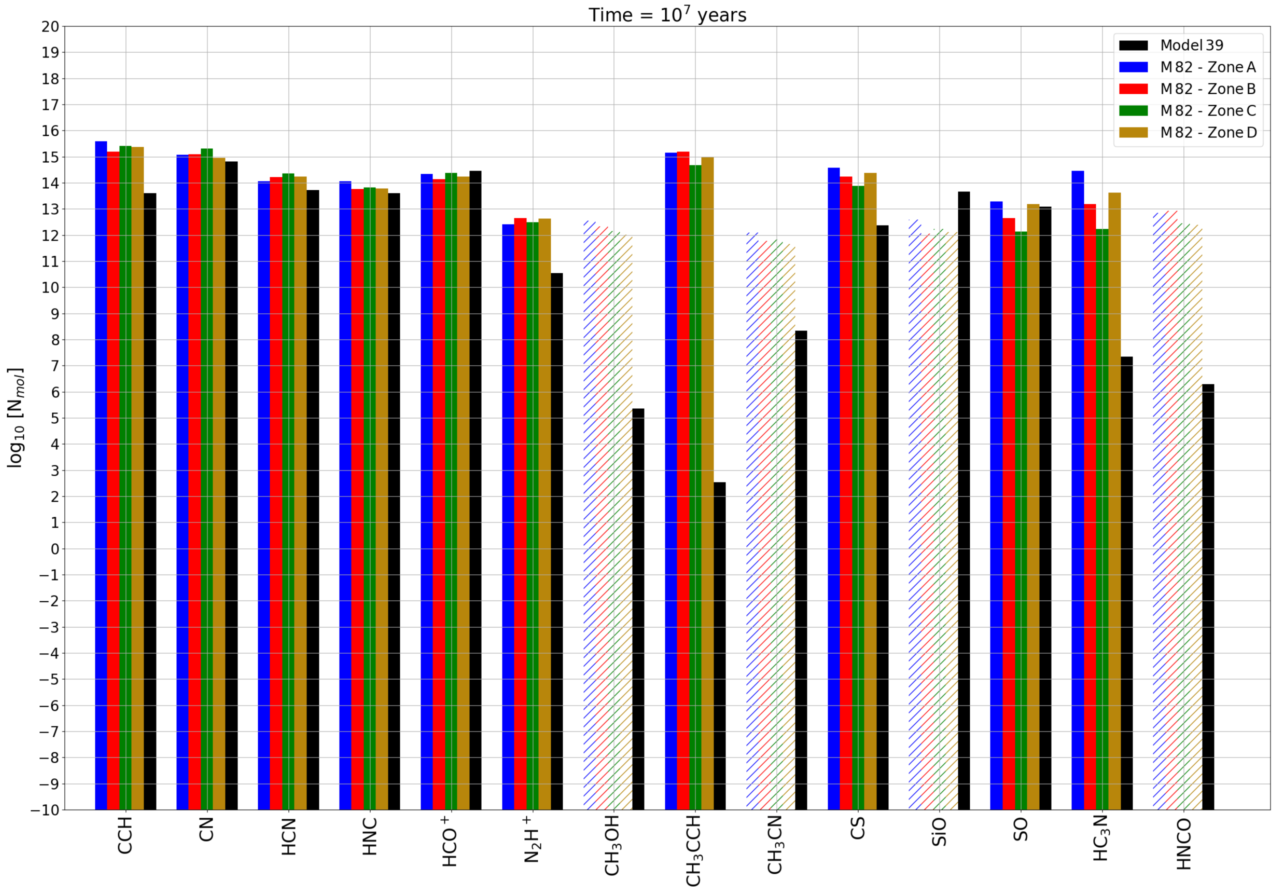

Figure 5.9: Column Densities of the 14 molecular species in M 82 compared with the chemical model 36 and 39. The hashed lines are upper limit estimates of the observed column densities with 3σ significance level.

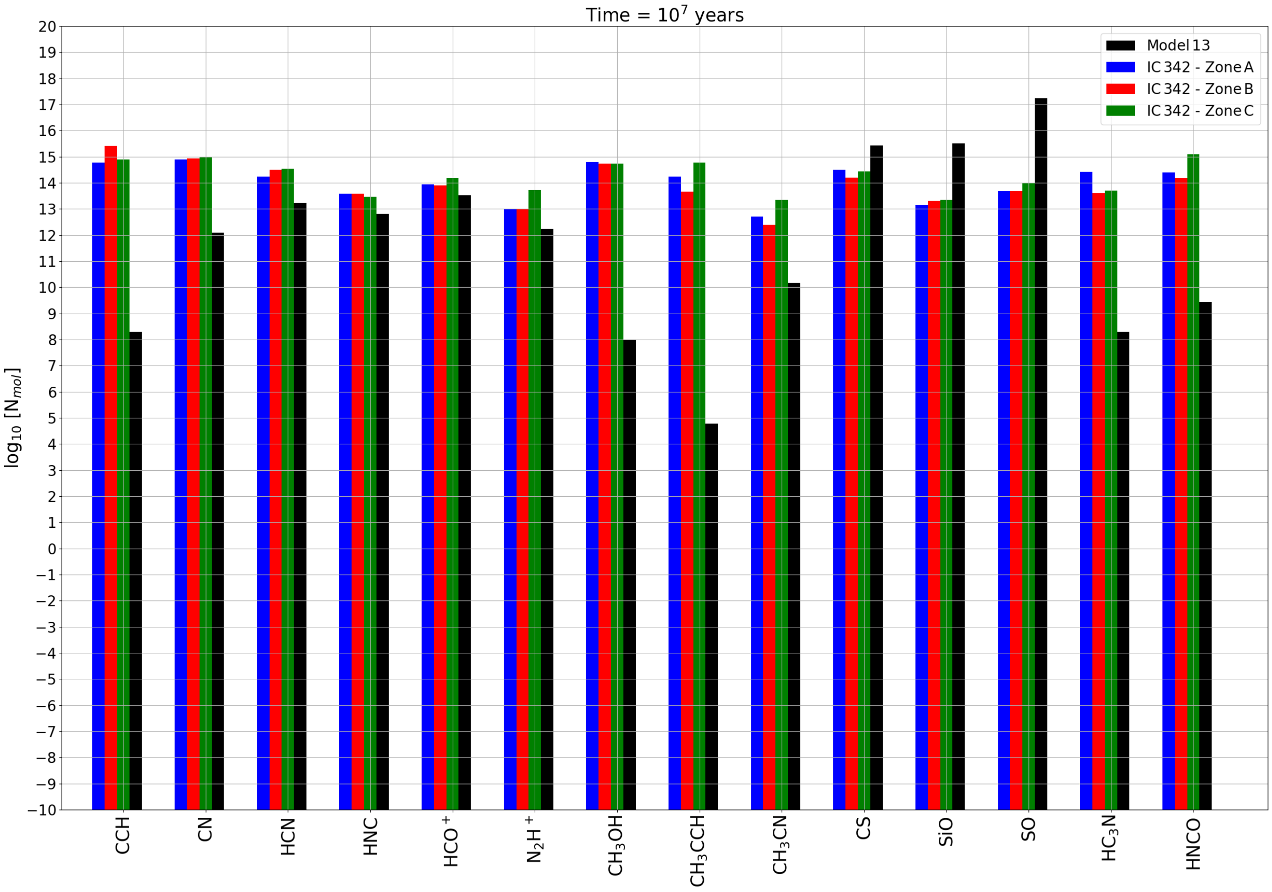

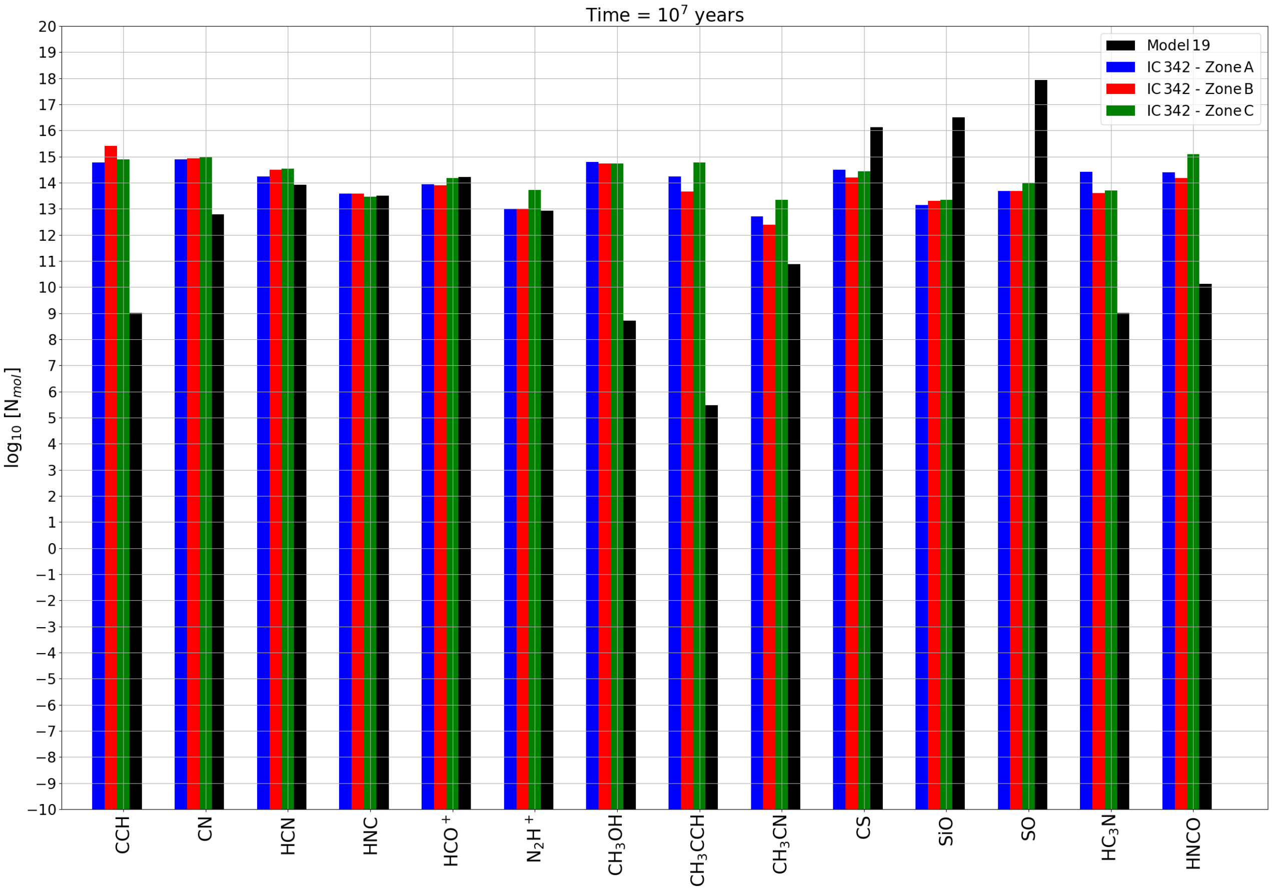

Figure 5.10: Column Densities of the 14 molecular species in IC 342 compared with the chemical model 13 and 19.

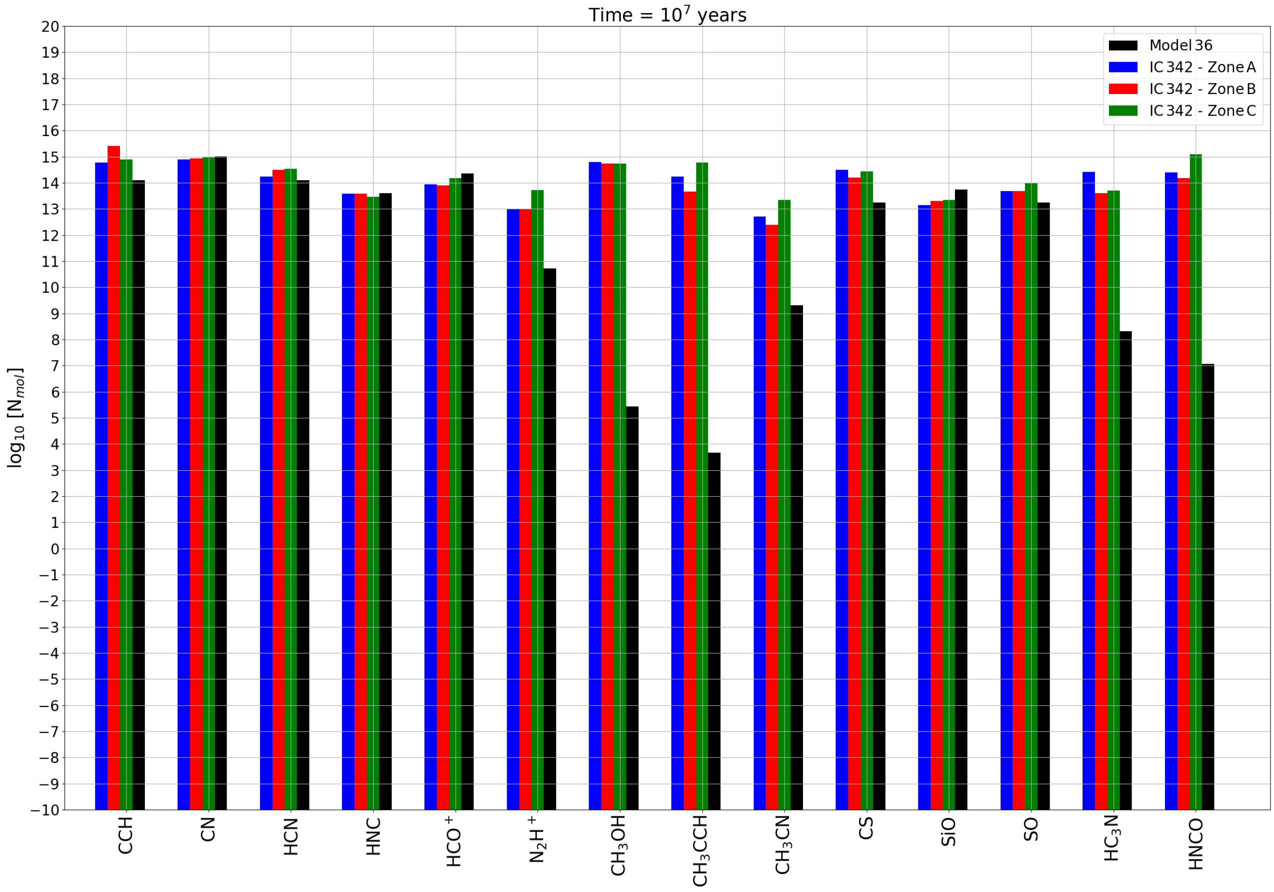

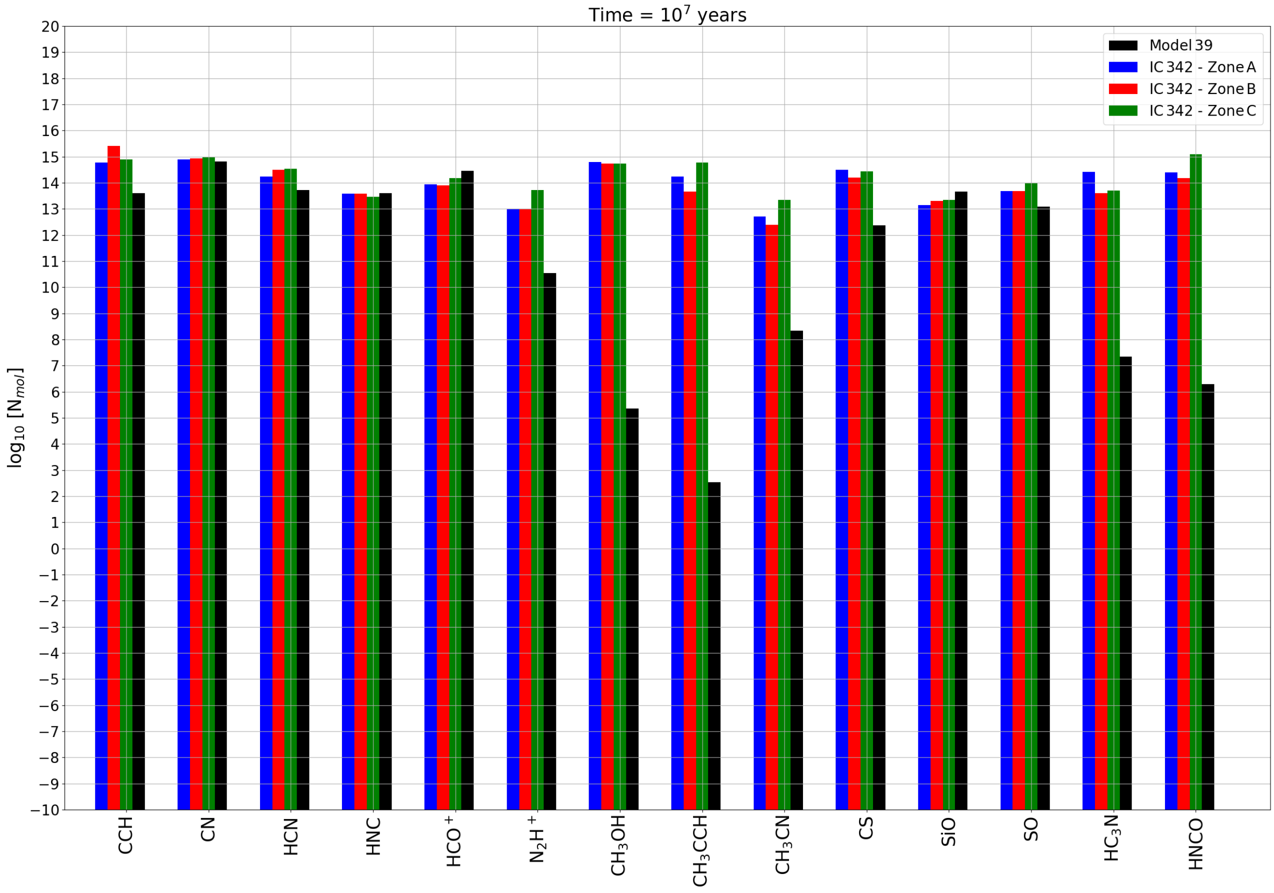

Figure 5.11: Column Densities of the 14 molecular species in IC 342 compared with the chemical model 36 and 39.

5.5 Comparison of spatial and velocity distribution

After finalising the inventory of the emission lines detected in this survey, one images the lines, and their moments. The imaging of the lines, and their different moments are presented in Appendix C. An example of these images was presented in Chapter 4, Section 4.2, in Figure 4.6.

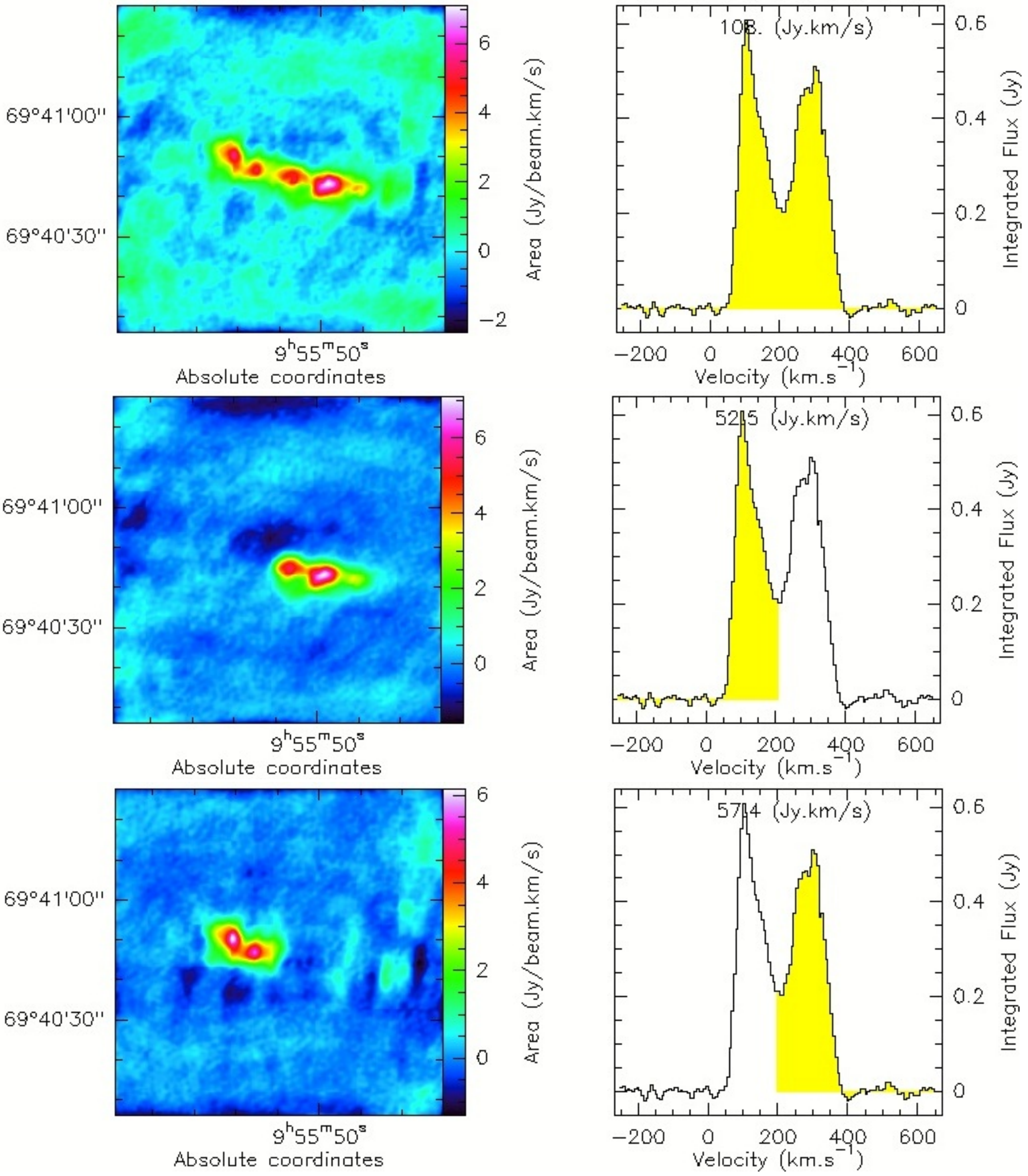

Figure 5.12: Top panel: Line distribution of $\mathrm{HCN}(1-0)$ at 88.632 GHz in M 82. Middle panel: $\mathrm{HCN}(1-0)$ at 88.632 GHz in M 82, showing that the emission region responsible for the lower velocity peak is the western region of the galaxy. Bottom panel: $\mathrm{HCN}(1-0)$ at 88.632 GHz in M 82, showing that the emission region responsible for the higher velocity peak is the eastern region of the galaxy. The regions seen in the left panel correspond to the velocity range seen in yellow in the right panel.

Many of the line emission spectra showed a double peak feature when averaged over the entire CMZ. In some cases, this double peak feature is simply due to velocity components. The spectrum of HCN for instance, exhibits a double peak emission as seen in Fig. 5.12 showing two velocity components. The top panel of the figure presents the line emission of HCN (1-0) at 88.632 GHz across the galaxy to the left, with the spectrum of the line emission to the right. This double peak feature is caused by the radial velocity distribution of the inclined galaxy M 82. The left peak of the emission line is emitted from the eastern region of the galaxy, while the right peak is coming from the western part of the M 82. The large velocity gradient that is observed in M 82, going from 0 to 200 km s^{-1} in one region, and from 200 to 400 km s^{-1} in another, will cause such a feature in the emission line (bottom panel of Fig. 5.12). This feature is not observed in the HCN emission line in IC 342, where the velocity gradients are much smaller than in M 82, since it is seen face on (see Fig. 5.13).

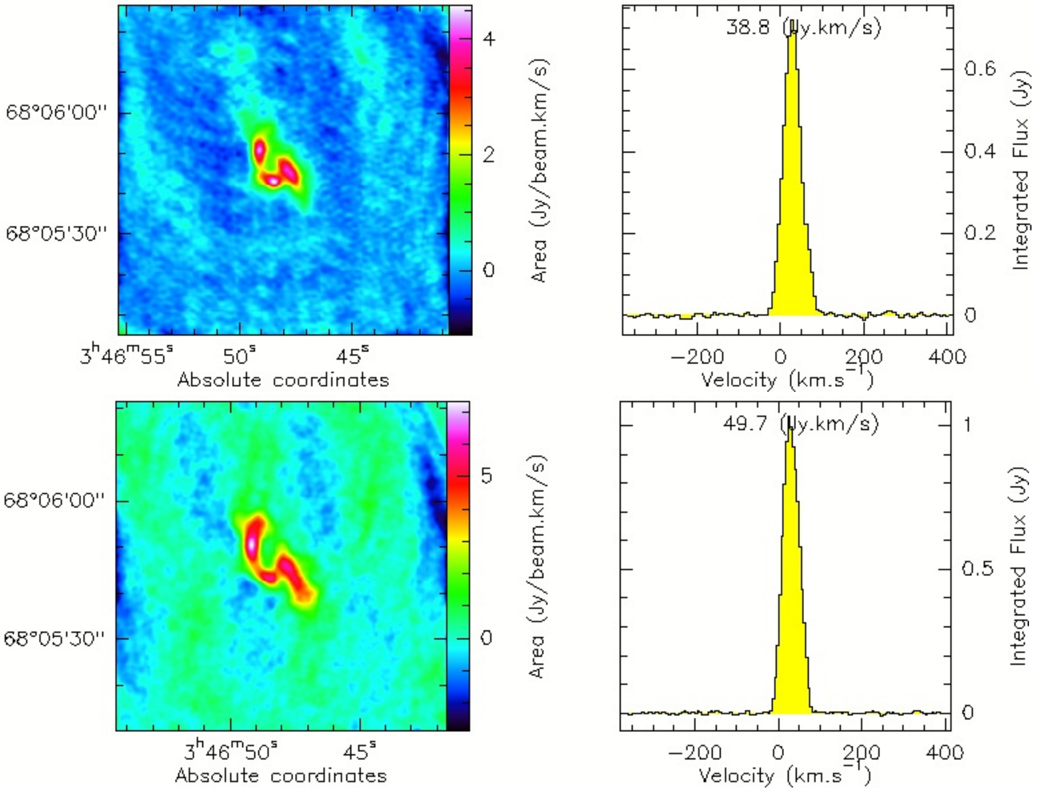

Figure 5.13: Top panel: Line flux distribution of $\mathrm{HCN}(1-0)$ at 88.632 GHz (left) and its line spectrum (right) in IC 342. Bottom panel: Line flux distribution of $^{13}\mathrm{CO}(1-0)$ at 110.201 GHz (left) and its line spectrum (right) in IC 342.

5.5.1 Flux Distribution

From the line imaging in Section 5.5, one can image the flux, velocity, and line width distribution, as described in Chapter 4, Section 4.2. Figures 5.14, 5.15, and 5.16 show the flux distribution (moment zero) of the different emission lines detected in M 82. The flux distributions of some lines such as, CCH (1-0), HCN (1-0), HCO$^+$ (1-0), HNC (1-0), CH$_3$CCH ($6_k - 5_k$), ^{13}CO (1-0), and CN (1-0) cover all four emission regions of M 82, despite noticeable changes in the emission flux from region to region, and from line to line, with extended emission that is connecting the four regions. However, some lines seem to be emitted from only a few regions within M 82.

For instance, CS shows a strong emission from region A but a much weaker emission in regions B, C, and D. The weak emission of N_2H^+ originates mainly from regions A, B, and D. Other weaker lines, such as HC_3N (12-11) at 109.174 GHz, are mainly emitted in region A with some contribution from region C. In general, region A seems to be the most prominent molecular line emission region in M 82.

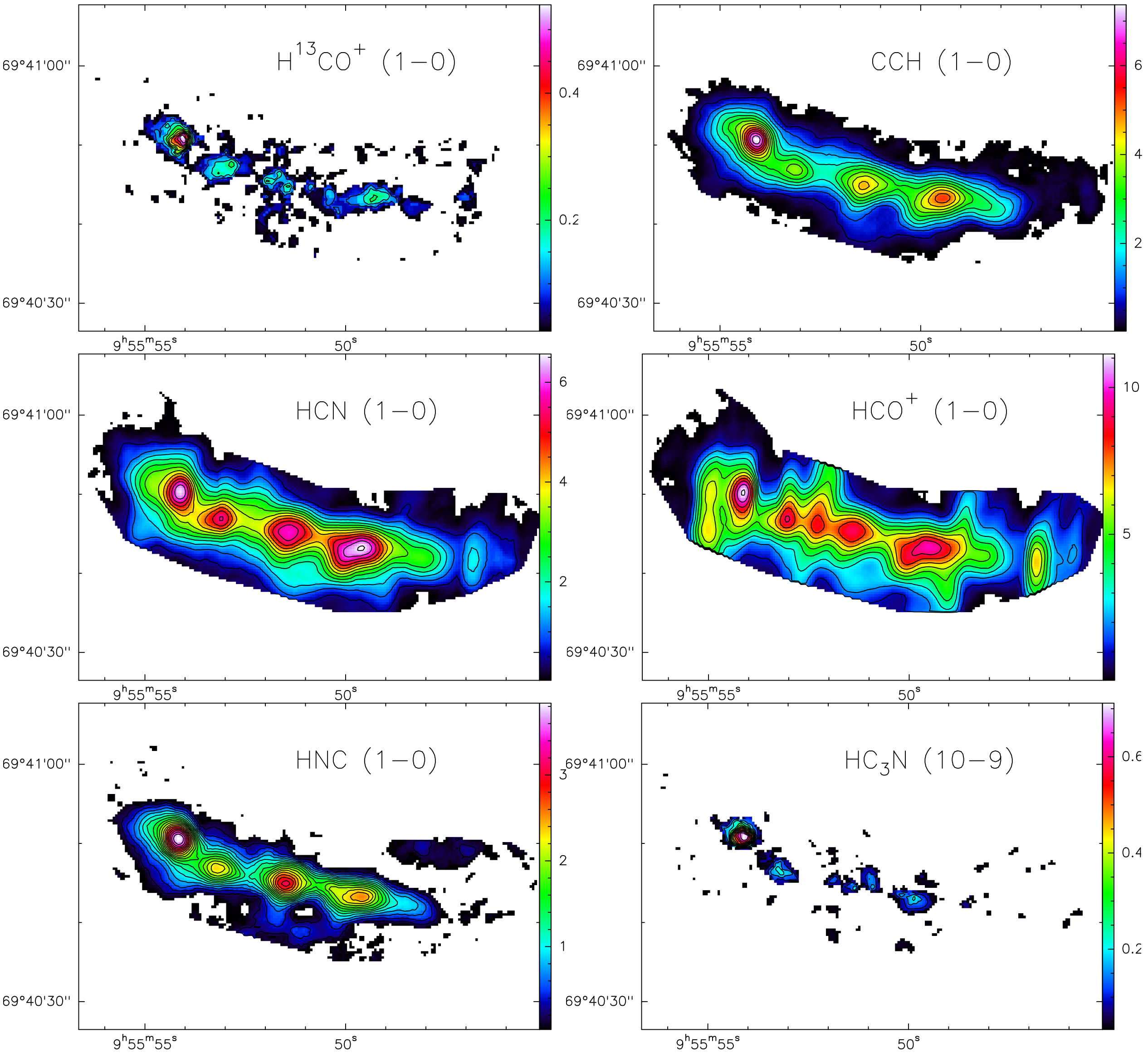

Figure 5.14: M 82: Flux distribution map of $\mathrm{H^{13}CO^+}(1-0)$ at 86.754 GHz (top left) (contour levels from 0.05 to 0.55 $\mathrm{Jy\,beam^{-1}\,km\,s^{-1}}$ by steps of 0.05 $\mathrm{Jy\,beam^{-1}\,km\,s^{-1}}$), $\mathrm{C_2H}(1-0)$ at 87.317 GHz (top right) (contour levels from 0.5 to 7.5 $\mathrm{Jy\,beam^{-1}\,km\,s^{-1}}$ by steps of 0.5 $\mathrm{Jy\,beam^{-1}\,km\,s^{-1}}$), $\mathrm{HCN}(1-0)$ at 88.632 GHz (middle left) (contour levels from 0.5 to 6.5 $\mathrm{Jy\,beam^{-1}\,km\,s^{-1}}$ by steps of 0.5 $\mathrm{Jy\,beam^{-1}\,km\,s^{-1}}$), $\mathrm{HCO^+}(1-0)$ at 89.189 GHz (middle right) (contour levels from 1 to 11 $\mathrm{Jy\,beam^{-1}\,km\,s^{-1}}$ by steps of 1 $\mathrm{Jy\,beam^{-1}\,km\,s^{-1}}$), $\mathrm{HNC}(1-0)$ at 90.664 GHz (bottom left) (contour levels from 0.2 to 3.8 $\mathrm{Jy\,beam^{-1}\,km\,s^{-1}}$ by steps of 0.2 $\mathrm{Jy\,beam^{-1}\,km\,s^{-1}}$), and $\mathrm{HC_3N}(10-9)$ at 90.979 GHz (bottom right) (contour levels from 0.05 to 0.7 $\mathrm{Jy\,beam^{-1}\,km\,s^{-1}}$ by steps of 0.05 $\mathrm{Jy\,beam^{-1}\,km\,s^{-1}}$)

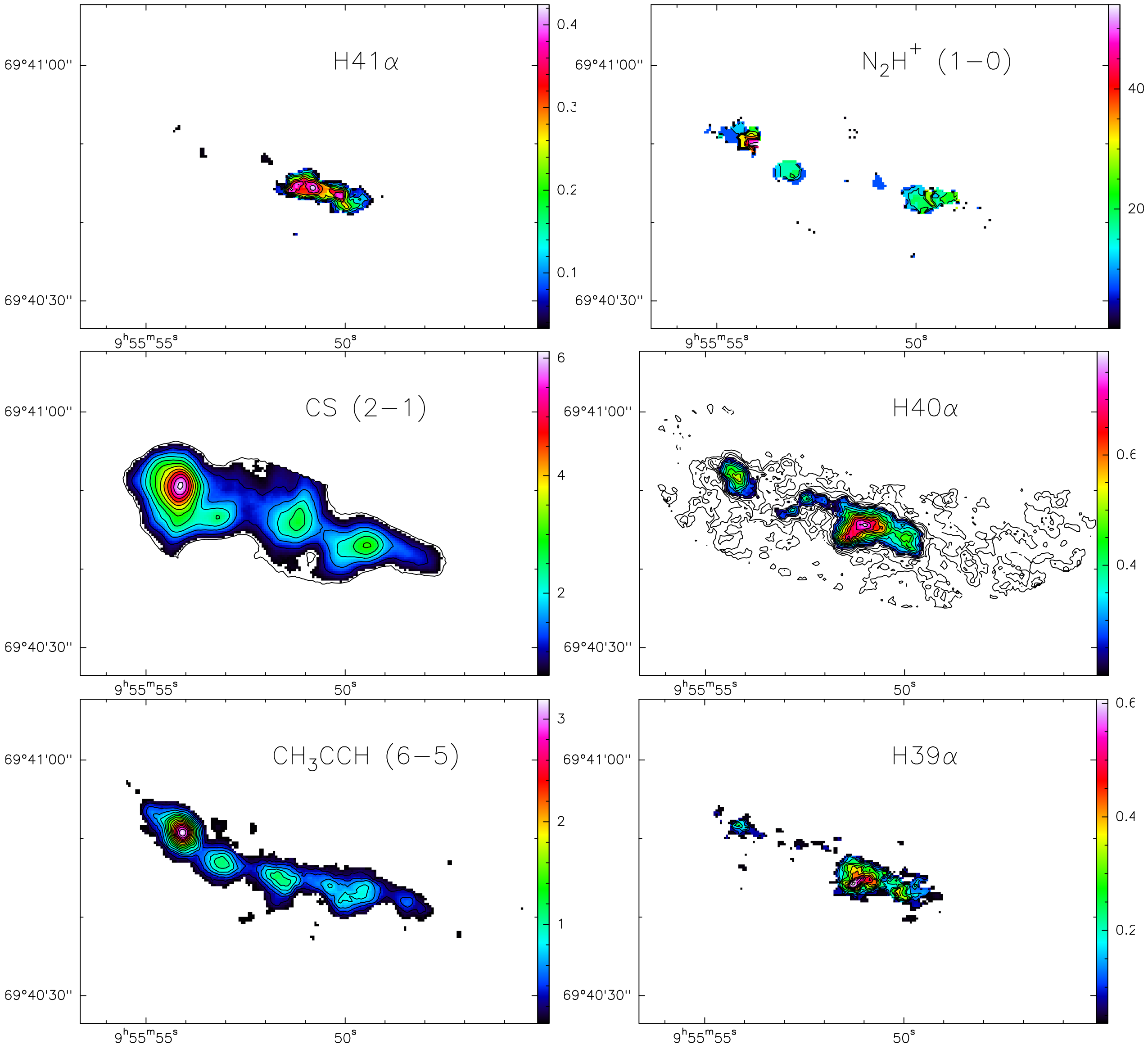

Figure 5.15: M 82: Flux distribution map of H41α at 92.034 GHz (top left) (contour levels from 0.05 to 0.4 Jy beam^{-1} km s^{-1} by steps of 0.05 Jy beam^{-1} km s^{-1}), N$_2$H$^+$($1-0$) at 93.174 GHz (top right) (contour levels from 0.05 to 0.45 Jy beam^{-1} km s^{-1} by steps of 0.05 Jy beam^{-1} km s^{-1}), CS($2-1$) at 97.981 GHz (middle left) (contour levels from 0.5 to 6.0 Jy beam^{-1} km s^{-1} by steps of 0.5 Jy beam^{-1} km s^{-1}), H40α at 99.023 GHz (middle right) (contour levels from 0.05 to 0.8 Jy beam^{-1} km s^{-1} by steps of 0.05 Jy beam^{-1} km s^{-1}), CH$_3$CCH(6_k-5_k) at 102.548 GHz (bottom left) (contour levels from 0.2 to 3.2 Jy beam^{-1} km s^{-1} by steps of 0.2 Jy beam^{-1} km s^{-1}), H39α at 106.737 GHz (bottom right) (contour levels from 0.05 to 0.6 Jy beam^{-1} km s^{-1} by steps of 0.05 Jy beam^{-1} km s^{-1})

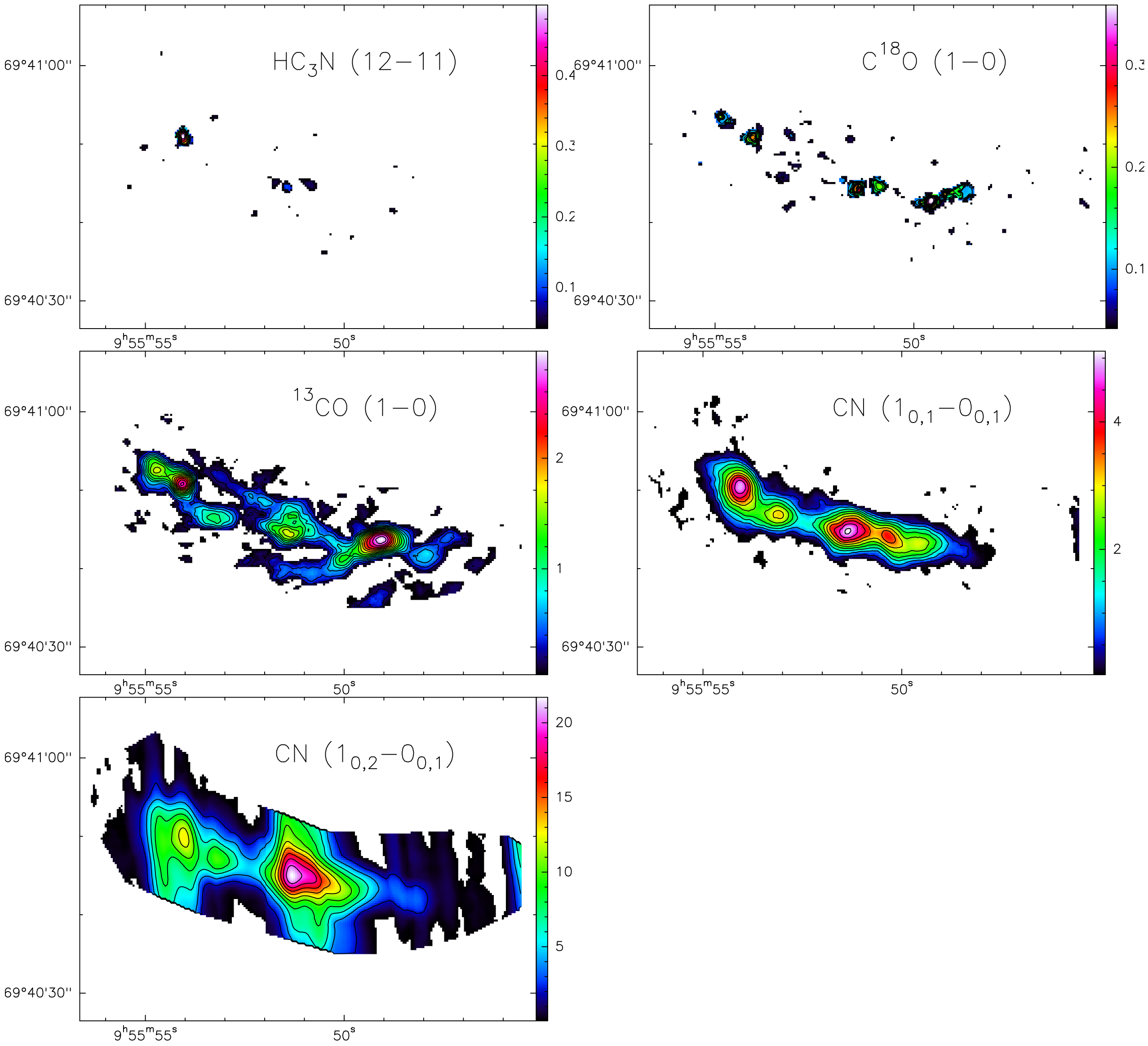

Figure 5.16: M 82: Flux distribution map of $HC_3N(12-11)$ at 109.174 GHz (top left) (contour levels from 0.05 to 0.5 Jy beam^{-1} km s^{-1} by steps of 0.05 Jy beam^{-1} km s^{-1}), $C^{18}O(1-0)$ at 109.782 GHz (top right) (contour levels from 0.02 to 0.36 Jy beam^{-1} km s^{-1} by steps of 0.02 Jy beam^{-1} km s^{-1}), $^{13}CO(1-0)$ at 110.201 GHz (middle left) (contour levels from 0.2 to 3 Jy beam^{-1} km s^{-1} by steps of 0.2 Jy beam^{-1} km s^{-1}), $CN(1_{0,1}-0_{0,1})$ at 113.191 GHz (middle right) (contour levels from 0.5 to 5 Jy beam^{-1} km s^{-1} by steps of 0.5 Jy beam^{-1} km s^{-1}), and $CN(1_{0,2}-0_{0,1})$ at 113.491 GHz (bottom left) (contour levels from 2 to 22 Jy beam^{-1} km s^{-1} by steps of 2 Jy beam^{-1} km s^{-1})

However, in IC 342, all three emission regions seem to be contributing significantly to the flux of most of the emission lines, with the exception of $C^{34}S$, SO, and HC_3N (11-10) at 100.076 GHz, that seem to be emitted mainly from regions A and B, and $C^{17}O$, that is mostly originating from regions A and C. The flux distributions of the lines observed in IC 342 are presented in Fig. 5.17, 5.18, 5.19, 5.20, and 5.21. Even though most of the line emissions are originating from the three regions of IC 342, some lines exhibit a more continuous and extended distribution such as CCH, HNCO, HCN, HCO^+, CS, $C^{18}O$, ^{13}CO, and CN, while others show a more concentrated and local emission regions such as $HN^{13}C$, HC_3N, SO, CH_3OH, and $C^{17}O$.

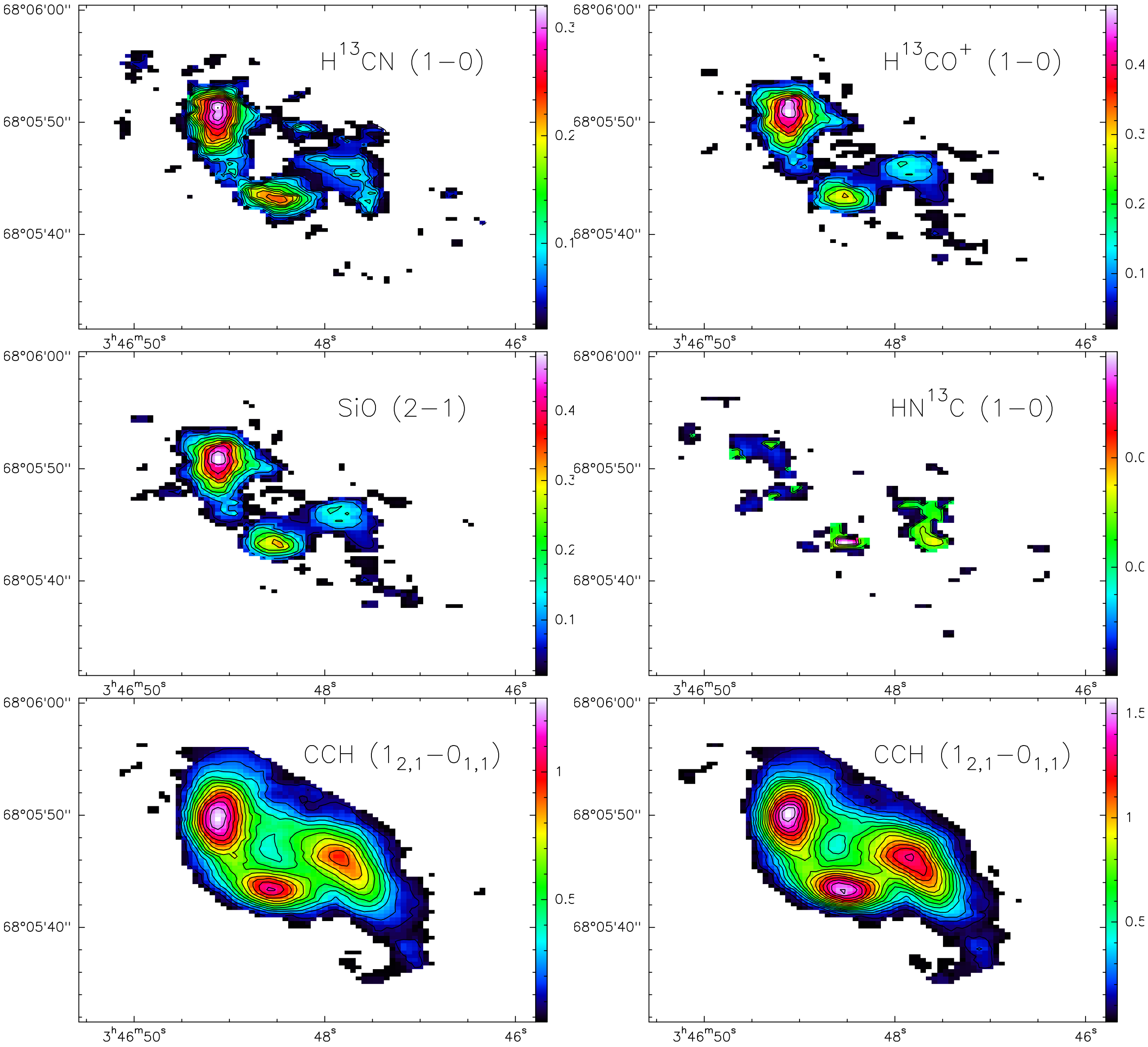

Figure 5.17: IC 342: Flux distribution map of H^{13}CN$(1-0)$ at 86.340 GHz (top left) (contour levels from 0.02 to 0.32 Jy beam^{-1} km s^{-1} by steps of 0.02 Jy beam^{-1} km s^{-1}), H^{13}CO$^{+}(1-0)$ at 86.754 GHz (top right) (contour levels from 0.05 to 0.5 Jy beam^{-1} km s^{-1} by steps of 0.05 Jy beam^{-1} km s^{-1}), SiO$(2-1)$ at 86.846 GHz (middle left), HN^{13}C$(1-0)$ at 87.090 GHz (middle right) (contour levels from 0.05 to 0.5 Jy beam^{-1} km s^{-1} by steps of 0.05 Jy beam^{-1} km s^{-1}), C$_2$H$(1-0)$ at 87.284 GHz (bottom left) (contour levels from 0.1 to 1.3 Jy beam^{-1} km s^{-1} by steps of 0.1 Jy beam^{-1} km s^{-1}), and C$_2$H$(1-0)$ at 87.402 GHz (bottom right) (contour levels from 0.1 to 1.6 Jy beam^{-1} km s^{-1} by steps of 0.1 Jy beam^{-1} km s^{-1}).

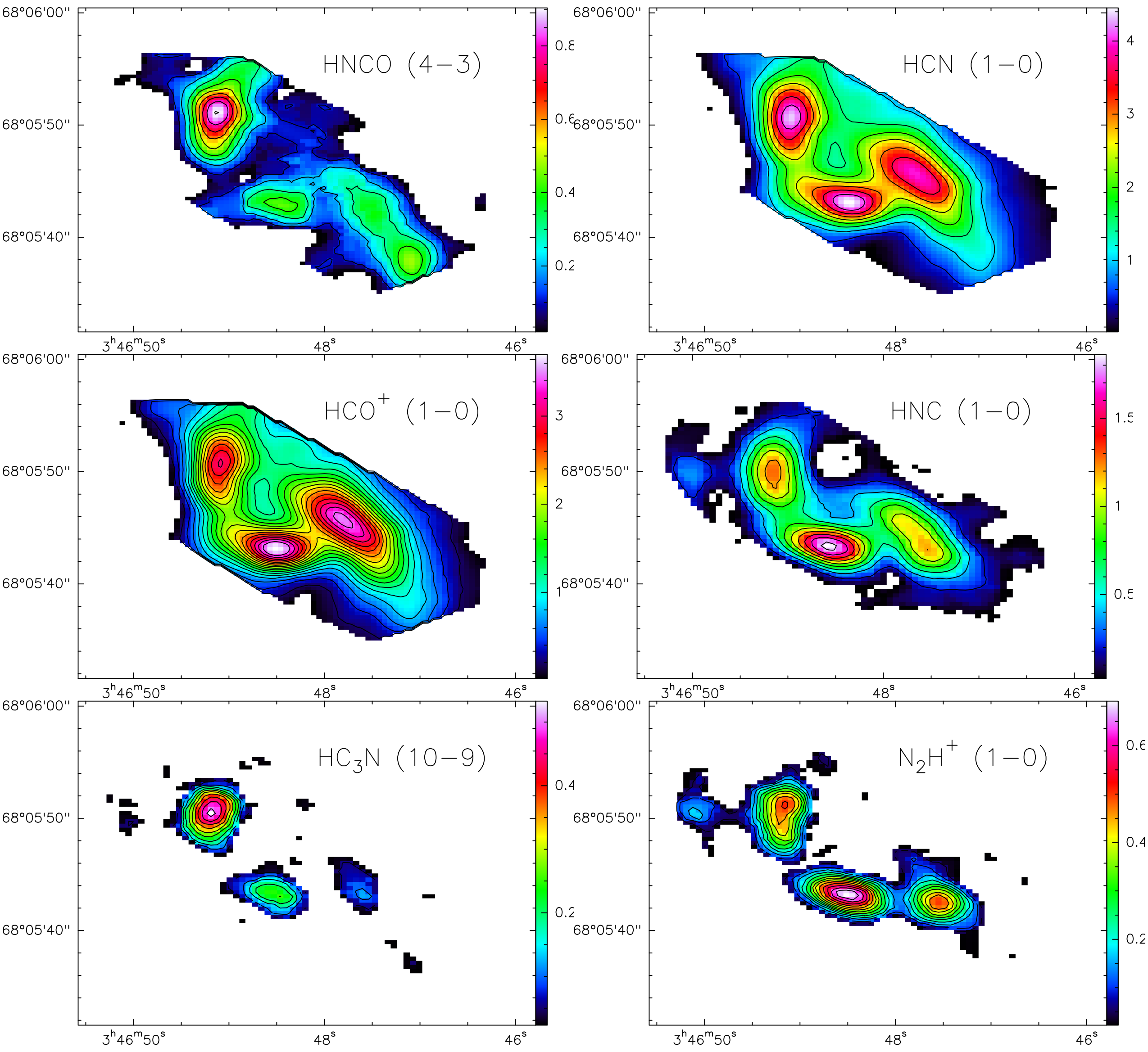

Figure 5.18: IC 342: Flux distribution map of $\mathrm{HNCO}(4_{0,4}-3_{0,3})$ at 87.925 GHz (top left) (contour levels from 0.1 to 0.9 $\mathrm{Jy\,beam^{-1}\,km\,s^{-1}}$ by steps of 0.1 $\mathrm{Jy\,beam^{-1}\,km\,s^{-1}}$), $\mathrm{HCN}(1-0)$ at 88.631 GHz (top right) (contour levels from 0.5 to 4.5 $\mathrm{Jy\,beam^{-1}\,km\,s^{-1}}$ by steps of 0.5 $\mathrm{Jy\,beam^{-1}\,km\,s^{-1}}$), $\mathrm{HCO^+}(1-0)$ at 89.188 GHz (middle left) (contour levels from 0.2 to 3.6 $\mathrm{Jy\,beam^{-1}\,km\,s^{-1}}$ by steps of 0.2 $\mathrm{Jy\,beam^{-1}\,km\,s^{-1}}$), $\mathrm{HNC}(1-0)$ at 90.663 GHz (middle right) (contour levels from 0.2 to 1.8 $\mathrm{Jy\,beam^{-1}\,km\,s^{-1}}$ by steps of 0.2 $\mathrm{Jy\,beam^{-1}\,km\,s^{-1}}$), $\mathrm{HC_3N}(10-9)$ at 90.978 GHz (bottom left), $\mathrm{N_2H^+}(1-0)$ at 93.173 GHz (bottom right) (contour levels from 0.05 to 0.55 $\mathrm{Jy\,beam^{-1}\,km\,s^{-1}}$ by steps of 0.05 $\mathrm{Jy\,beam^{-1}\,km\,s^{-1}}$)

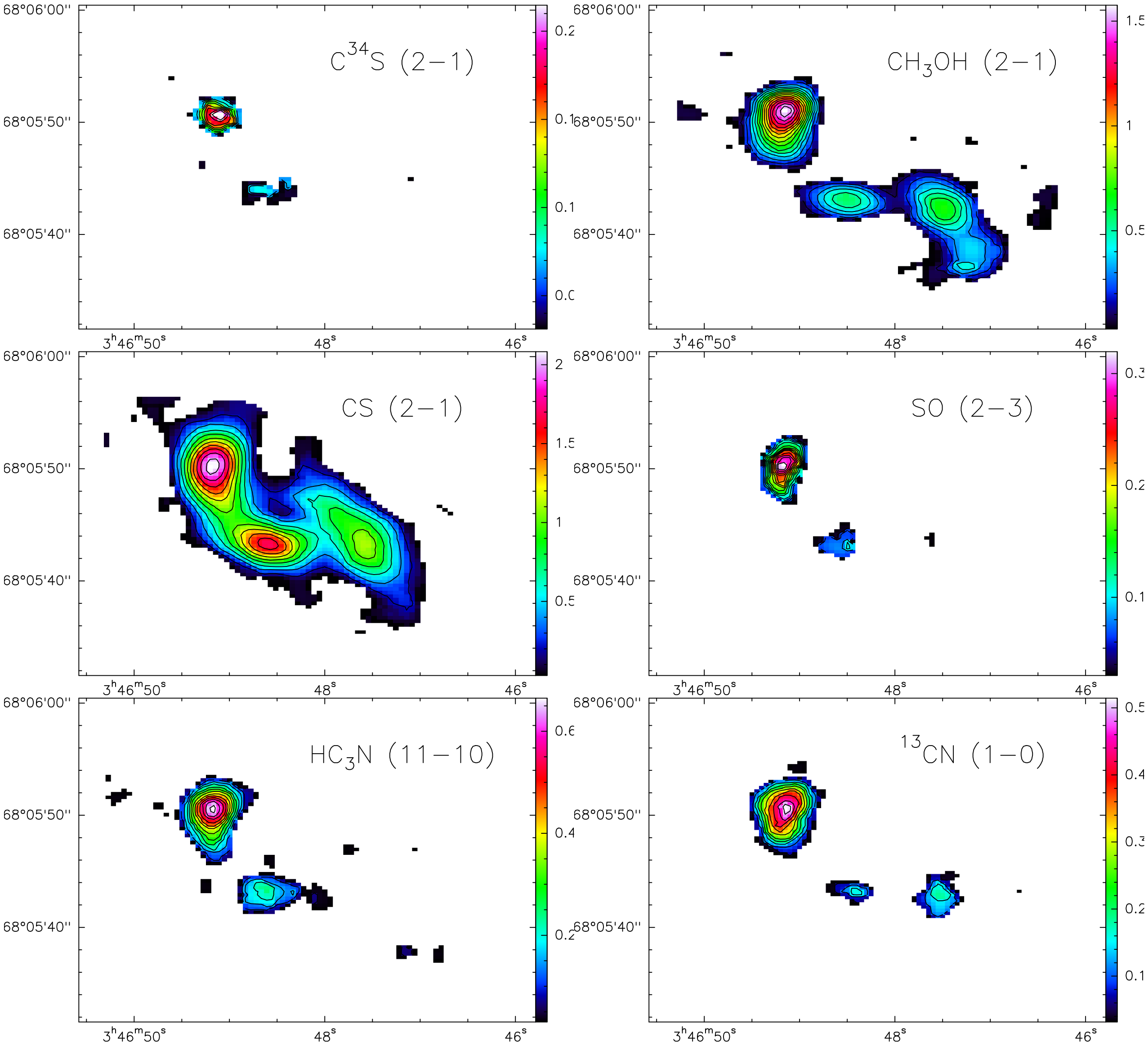

Figure 5.19: IC 342: Flux distribution map of C^{34}S$(2-1)$ at 96.413 GHz (top left) (contour levels from 0.02 to 0.22 Jy beam^{-1} km s^{-1} by steps of 0.02 Jy beam^{-1} km s^{-1}), CH$_3$OH$(2_k - 1_k)$ at 96.744 GHz (top right) (contour levels from 0.1 to 1.6 Jy beam^{-1} km s^{-1} by steps of 0.1 Jy beam^{-1} km s^{-1}), CS$(2-1)$ at 97.973 GHz (middle left) (contour levels from 0.2 to 2 Jy beam^{-1} km s^{-1} by steps of 0.2 Jy beam^{-1} km s^{-1}), SO$(2_1 - 3_2)$ at 99.299 GHz (middle right) (contour levels from 0.02 to 0.32 Jy beam^{-1} km s^{-1} by steps of 0.02 Jy beam^{-1} km s^{-1}), HC$_3$N$(11-10)$ at 100.076 GHz (bottom left) (contour levels from 0.05 to 0.65 Jy beam^{-1} km s^{-1} by steps of 0.05 Jy beam^{-1} km s^{-1}), ^{13}CN at 108.780 GHz (bottom right) (contour levels from 0.05 to 0.5 Jy beam^{-1} km s^{-1} by steps of 0.05 Jy beam^{-1} km s^{-1})

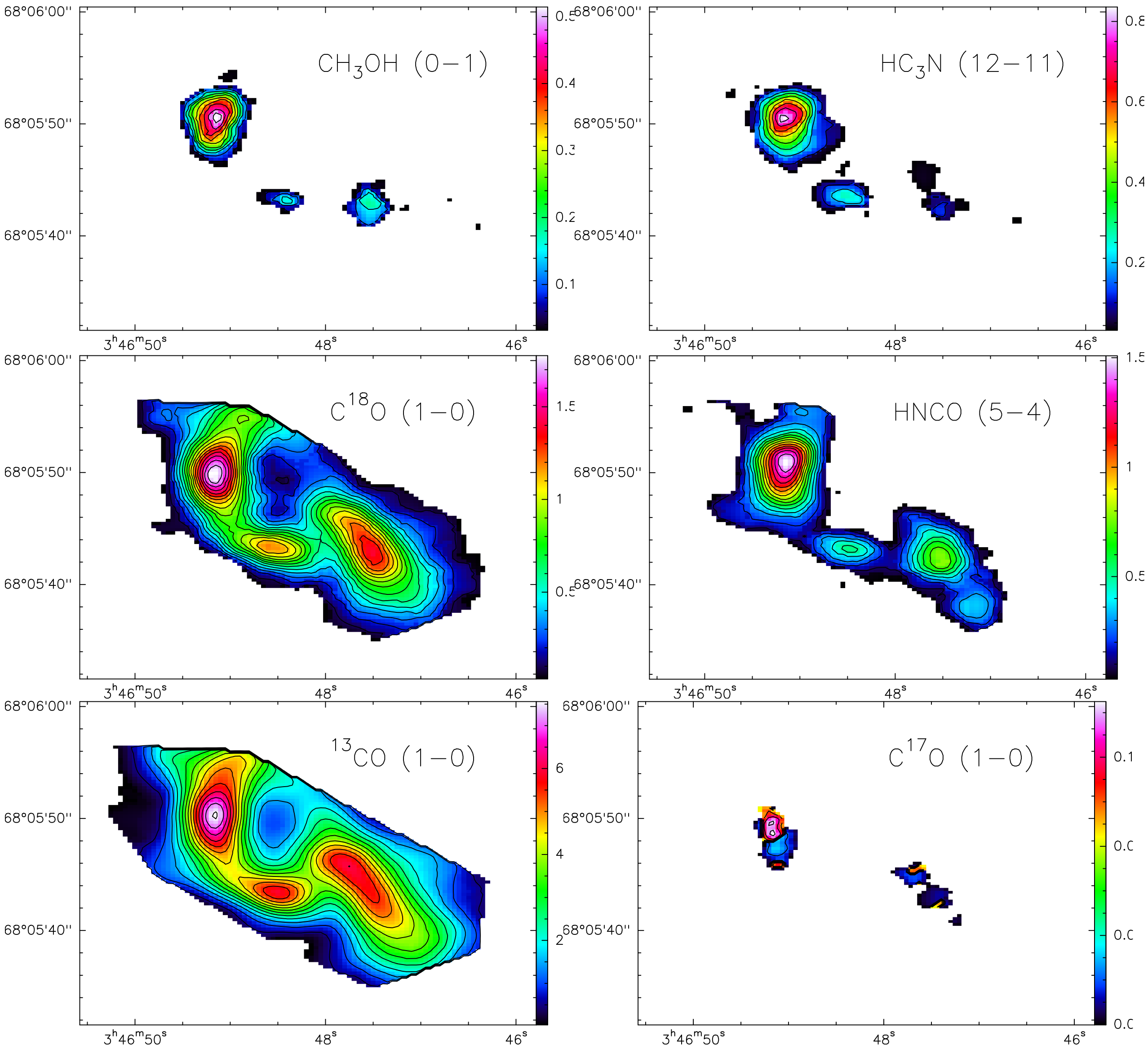

Figure 5.20: IC 342: Flux distribution map of , $CH_3OH(0_0, 1_{-1})$ at 108.894 GHz (top left) (contour levels from 0.05 to 0.5 Jy beam^{-1} km s^{-1} by steps of 0.05 Jy beam^{-1} km s^{-1}), $HC_3N(12-11)$ at 109.173 GHz (top right) (contour levels from 0.1 to 0.8 Jy beam^{-1} km s^{-1} by steps of 0.1 Jy beam^{-1} km s^{-1}), $C^{18}O(1-0)$ at 109.782 GHz (middle left) (contour levels from 0.1 to 1.8 Jy beam^{-1} km s^{-1} by steps of 0.1 Jy beam^{-1} km s^{-1}), $HNCO(5_{0,5} - 4_{0,4})$ at 109.905 GHz (middle right) (contour levels from 0.1 to 1.5 Jy beam^{-1} km s^{-1} by steps of 0.1 Jy beam^{-1} km s^{-1}), $^{13}CO(1-0)$ at 110.201 GHz (bottom left) (contour levels from 0.5 to 7.5 Jy beam^{-1} km s^{-1} by steps of 0.5 Jy beam^{-1} km s^{-1}), $C^{17}O(1-0)$ at 112.358 GHz (bottom right) (contour levels from 0.01 to 0.11 Jy beam^{-1} km s^{-1} by steps of 0.01 Jy beam^{-1} km s^{-1})

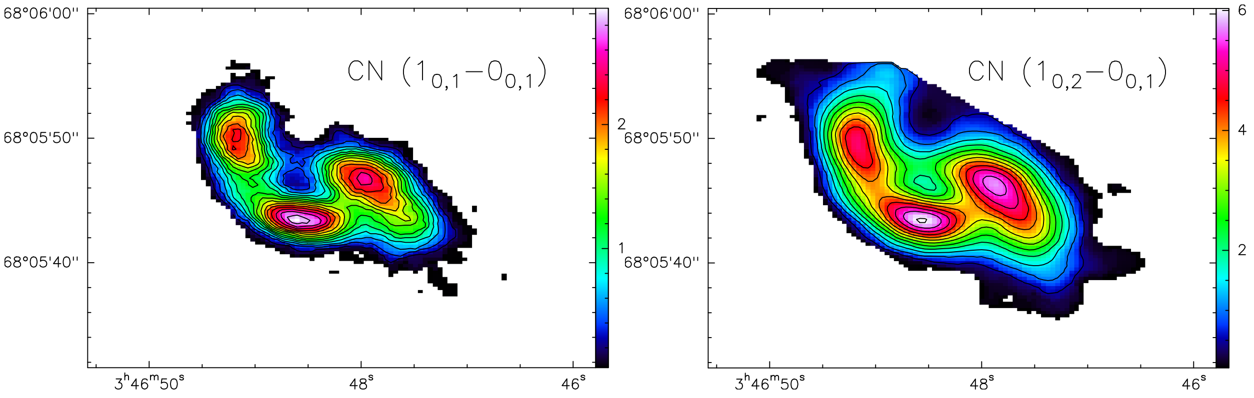

Figure 5.21: IC 342: Flux distribution map of $\mathrm{CN}(1_{0,1}-0_{0,1})$ at 113.190 GHz (left) (contour levels from 0.2 to 3 Jy beam^{-1} km s^{-1} by steps of 0.2 Jy beam^{-1} km s^{-1}), $\mathrm{CN}(1_{0,2}-0_{0,1})$ at 113.490 GHz (right) (contour levels from 0.5 to 6 Jy beam^{-1} km s^{-1} by steps of 0.5 Jy beam^{-1} km s^{-1})

5.5.2 Distribution of Radial Velocity and Line Width

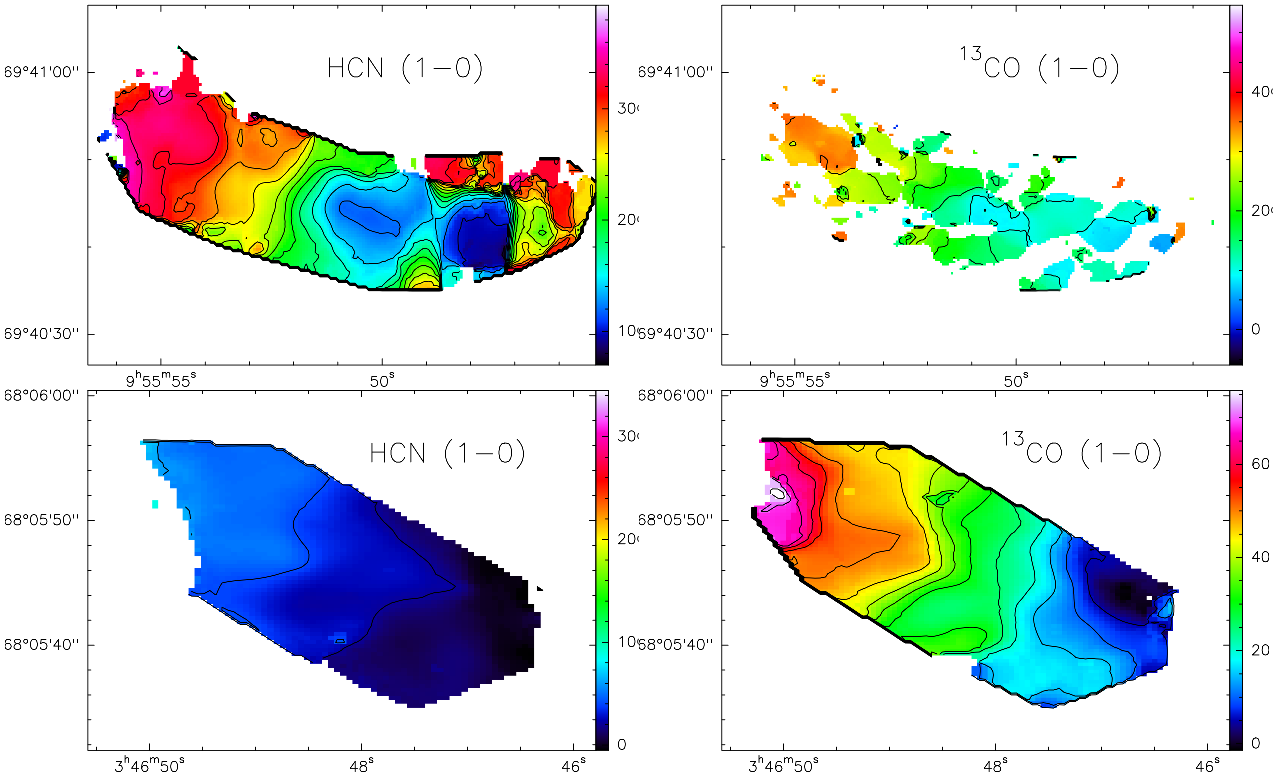

Figure 5.22: Top panel, M 82: Radial velocity distribution maps of $\mathrm{HCN}(1-0)$ at 88.632 GHz (top left) (contour levels from 200 to 600 km s^{-1} by steps of 100 km s^{-1}), and of $^{13}\mathrm{CO}(1-0)$ at 110.201 GHz (top right) (contour levels from -50 to 550 km s^{-1} by steps of 50 km s^{-1}), Bottom panel, IC 342: Velocity distribution map of $\mathrm{HCN}(1-0)$ at 88.632 GHz (bottom left) (contour levels from 20 to 340 km s^{-1} by steps of 20 km s^{-1}), and of $^{13}\mathrm{CO}(1-0)$ at 110.201 GHz (bottom right) (contour levels from 5 to 75 km s^{-1} by steps of 5 km s^{-1})

Moments one and two depict the radial velocity and width distributions of emission lines, respectively. In Fig. 5.22, the moment one of two lines (HCN, and ^{13}CO) is shown for both M 82 and IC 342. In M 82, there is a strong velocity gradient, where the radial velocity of the line in the eastern part of the galaxy is around 300 km s^{-1}, while on the western side is around 100 km s^{-1}. This gradient is not as pronounced in IC 342, which is seen face-on, where the velocity ranges between 30 and 40 km s^{-1}. The line width, and velocity distributions of each molecular line observed in M 82 and IC 342 are presented in Appendix *C*.

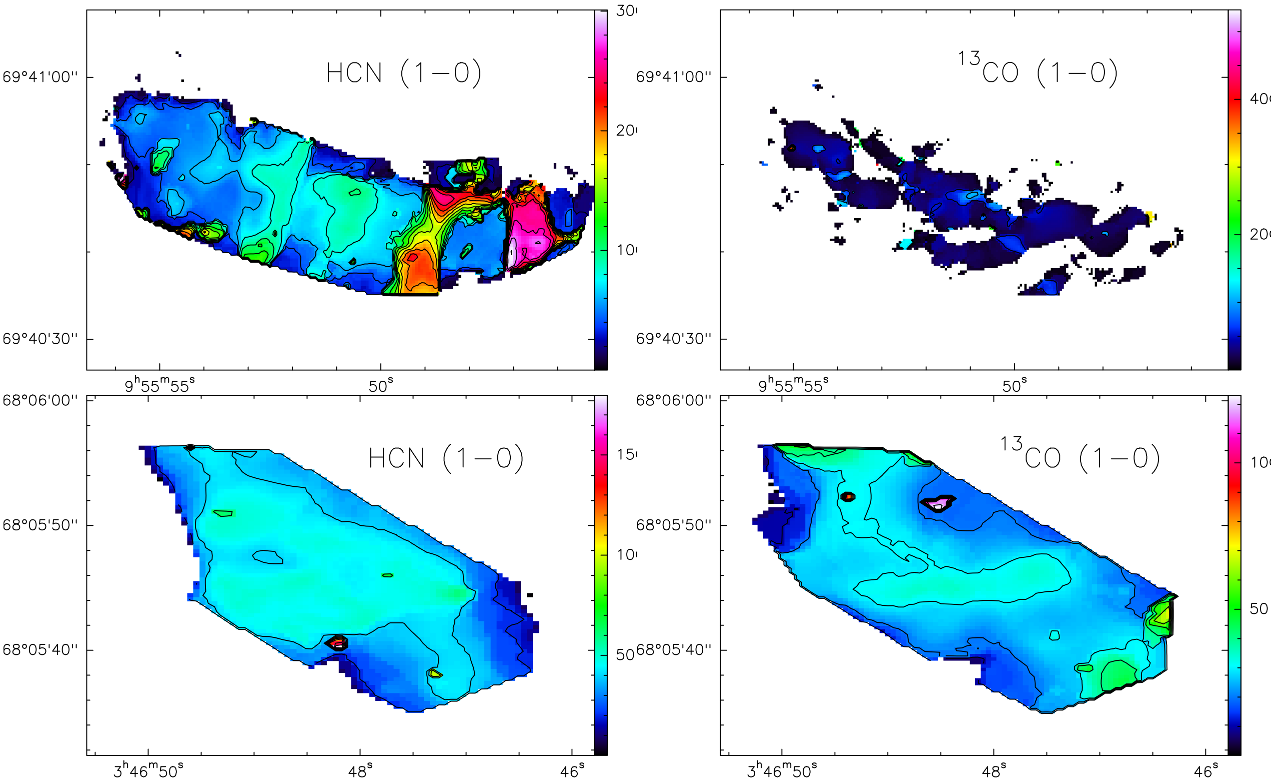

Figure 5.23: Top panel, M 82: Width distribution map of $\mathrm{HCN}(1-0)$ at 88.632 GHz (top left) (contour levels from 20 to 300 $\mathrm{km\,s^{-1}}$ by steps of 20 $\mathrm{km\,s^{-1}}$), and of $^{13}\mathrm{CO}(7-0)$ at 110.201 GHz (top right) (contour levels from 50 to 550 $\mathrm{km\,s^{-1}}$ by steps of 50 $\mathrm{km\,s^{-1}}$). Bottom panel, IC 342: Line width distribution map of $\mathrm{HCN}(1-0)$ at 88.632 GHz (bottom left) (contour levels from 20 to 180 $\mathrm{km\,s^{-1}}$ by steps of 10 $\mathrm{km\,s^{-1}}$), and of $^{13}\mathrm{CO}(7-0)$ at 110.201 GHz (bottom right) (contour levels from 10 to 120 $\mathrm{km\,s^{-1}}$ by steps of 10 $\mathrm{km\,s^{-1}}$)

5.5.3 Flux Distribution Comparison

From the intensity distributions maps, one can compare the different distributions of the lines by plotting the flux distribution of a line over that of another. For this purpose, the flux distribution of HCN (1-0) has been used as a reference, since it is a line of strong and extended emission with a distribution that covers all regions of the two studied galaxies.

Figures 5.24, and 5.25 show the results of the flux distribution comparison for emission lines in M 82. From these figures, one can see that some lines, such as CCH, HCO^{+}, and CN follow the distribution of HCN very closely, with an extended emission similar to that of HCN. Other lines, such as HNC, CS, $\mathrm{H}40\alpha$, and ^{13}CO, even though they follow the HCN distribution to a certain extent, they exhibit differences in their distribution.

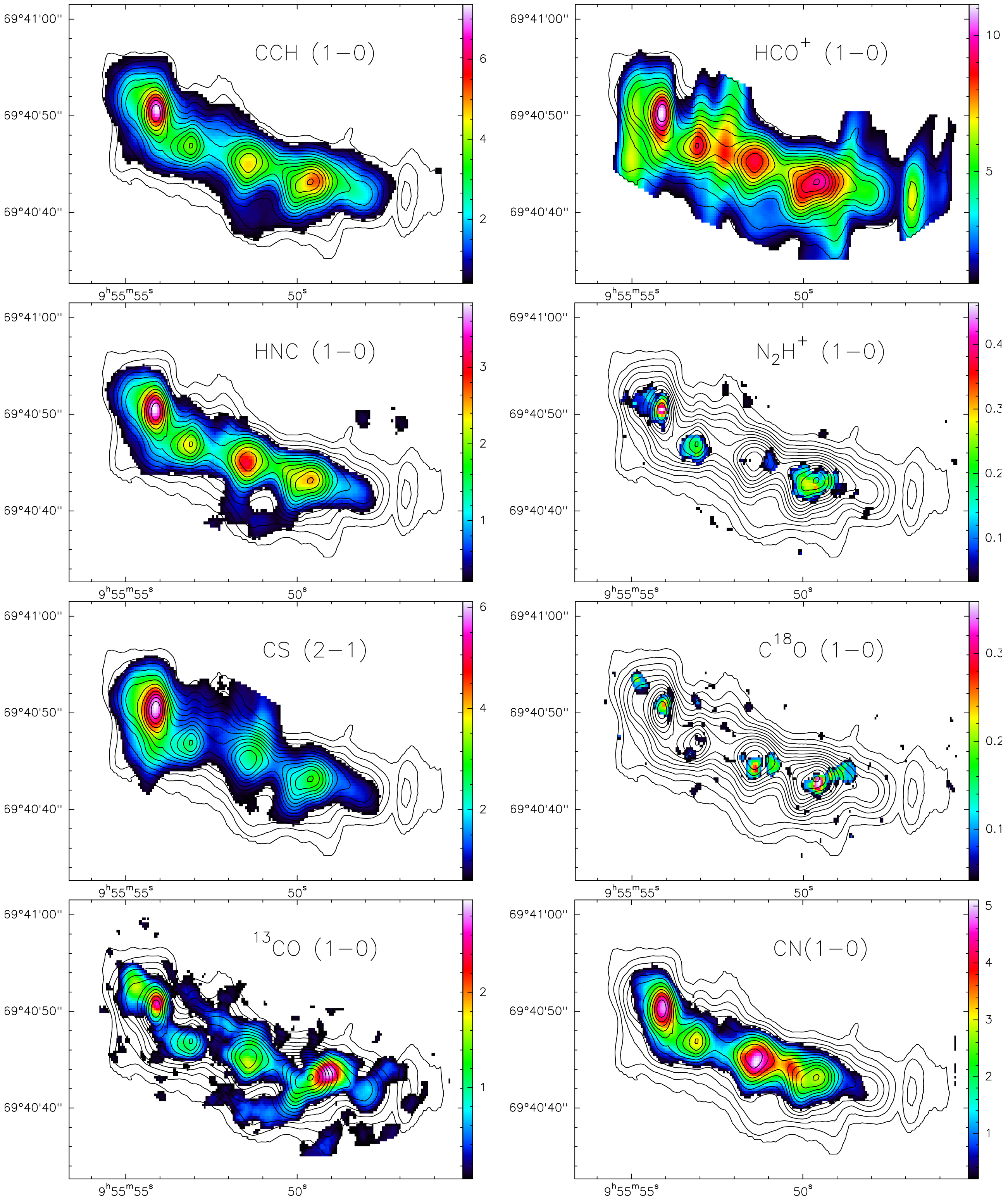

Figure 5.24: The flux distribution of different molecules (in colours) compared with the flux distribution of HCN(1-0) at 88.632 GHz (in contours of 0.5 to 6.5 Jy $\mathrm{beam}^{-1}\,\mathrm{km\,s}^{-1}$ by steps of 0.5 Jy $\mathrm{beam}^{-1}\,\mathrm{km\,s}^{-1}$) in M 82

For instance, the flux peaks of ^{13}CO seem to be slightly shifted from the flux peaks of HCN. Lines such as N_2H^+, C^{18}O, H41α , H40α and H39α have a more localised emission that does not extend across the galaxy. This localised emission originates from certain regions of the galaxy only.

On the other hand, Fig. 5.26, and 5.27 show the results of the comparison of the flux distributions for emission lines in IC 342. Similarly to the results in M 82, some lines follow the distribution of HCN very closely, such as SiO, CCH, HCO$^+$, C^{18}O, ^{13}CO, and CN. However, even though these lines follow the HCN distribution, they still show slight shifts in the location of the peak emission. Other lines show even more significant shifts with respect to the location of the peak emission compared to HCN, such as HNCO, N_2H^+, and CH_3OH. Other lines such HNC, and CS show weaker and less extended emission than HCN, albeit similar distributions.

There are important differences in the distributions of some lines between the two galaxies. For instance, while N_2H^+ and C^{18}O have a localised and relatively weak emission in M 82, their emission is well extended and strong in IC 342. On the other hand, while HNC and CS follow the HCN distribution with a similar extent and flux in M 82, they have a much weaker and less extended emission compared to HCN in IC 342.

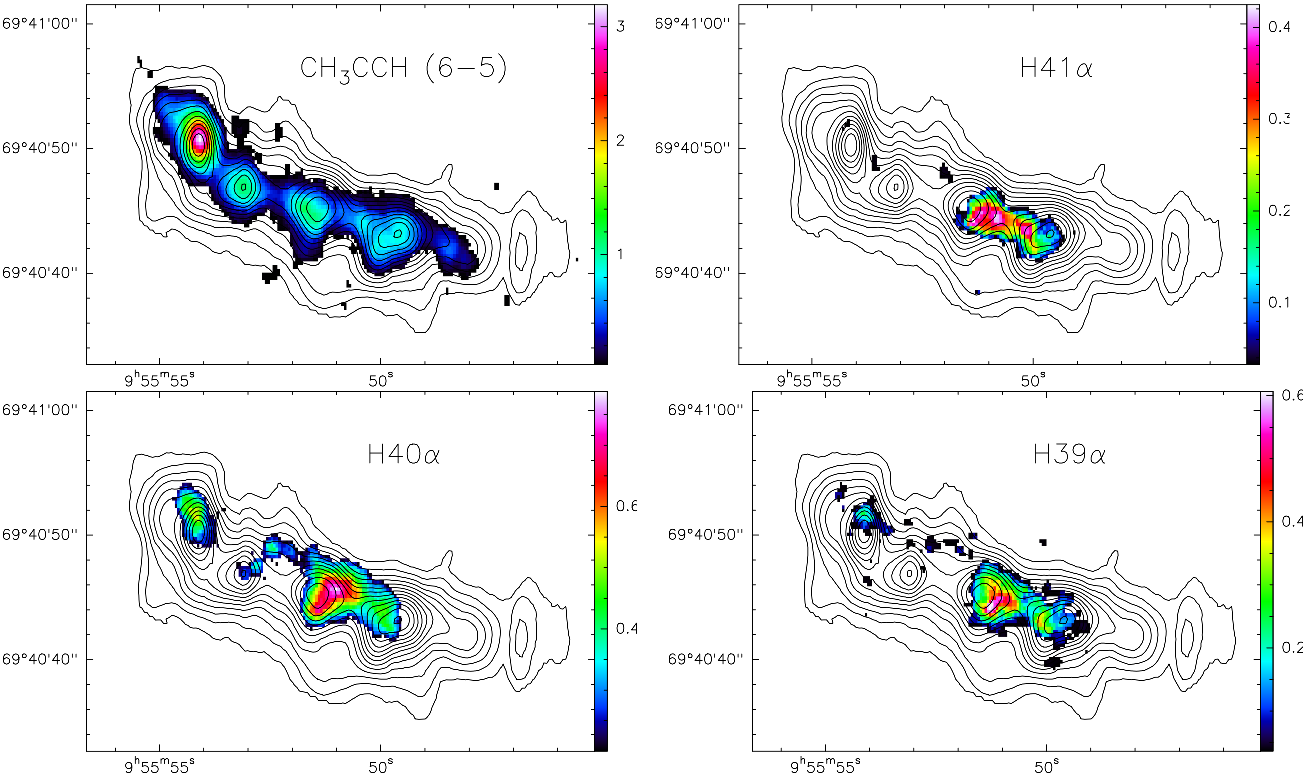

Figure 5.25: Same as in Fig. 5.24.

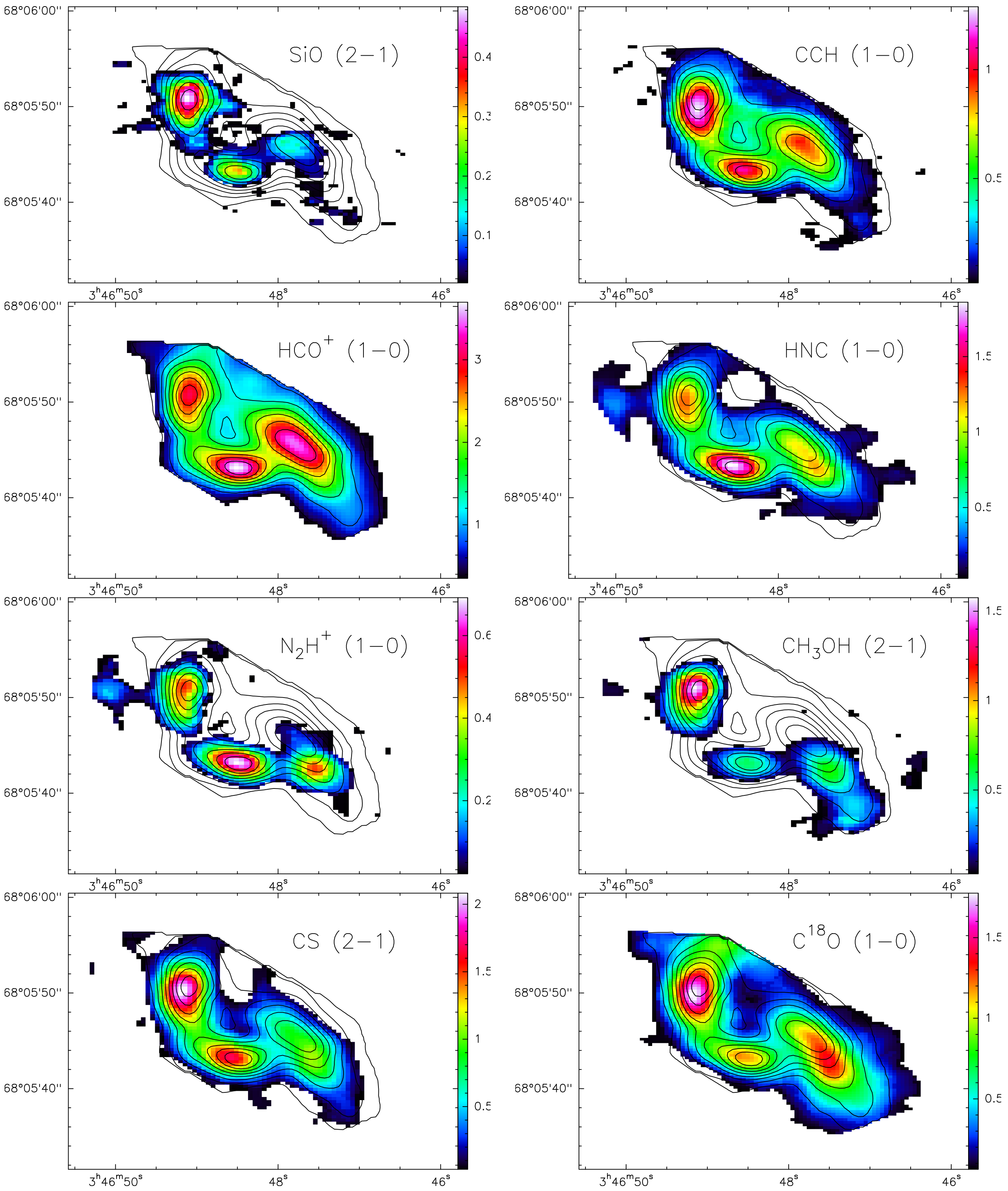

Figure 5.26: The flux distribution of different molecules (in colours) compared with the flux distribution of HCN(1-0) at 88.632 GHz (in contours of 0.5 to 4.5 Jy $\mathrm{beam}^{-1}\,\mathrm{km\,s}^{-1}$ by steps of 0.5 Jy $\mathrm{beam}^{-1}\,\mathrm{km\,s}^{-1}$) in IC 342

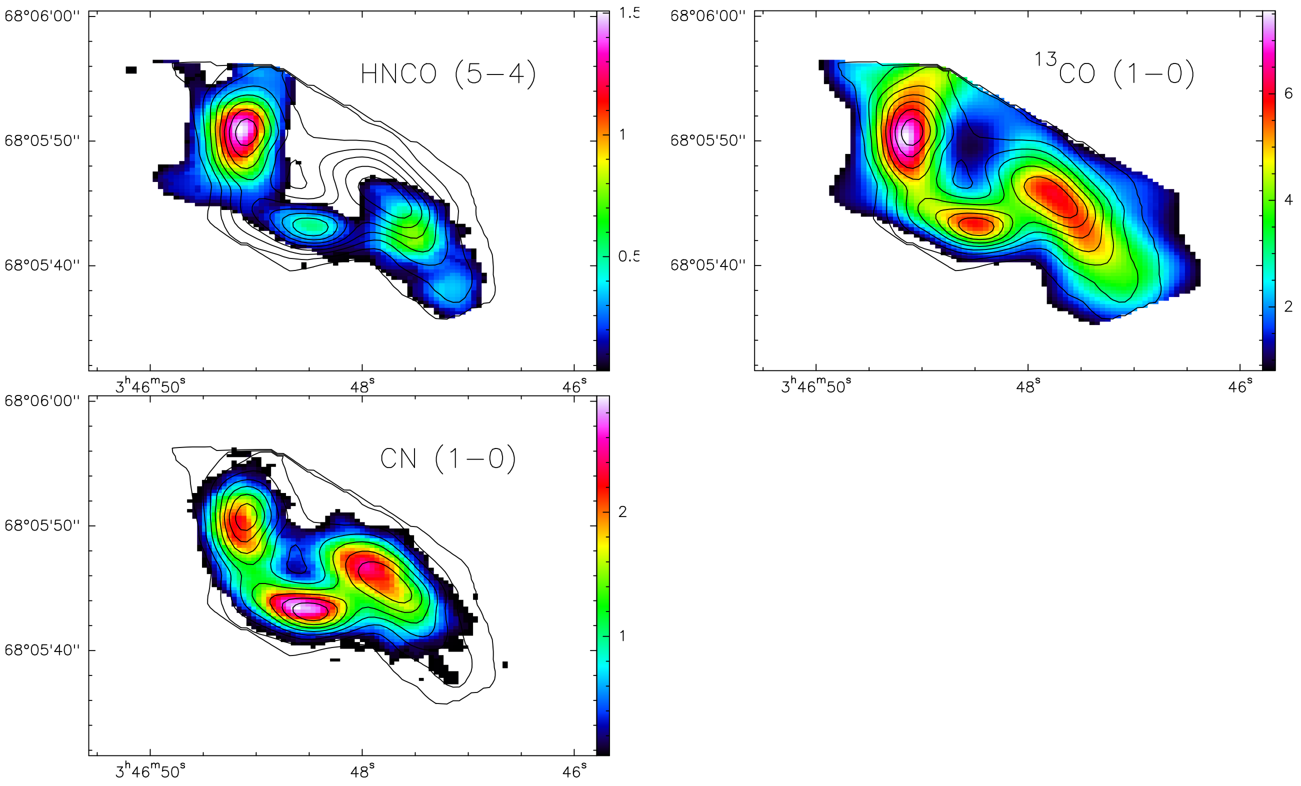

Figure 5.27: Same as in Fig. 5.26

5.6 PCA Results

5.6.1 M 82

For the PCA application on the data obtained for M 82, seven lines have been chosen, namely: CCH (1-0), HCN(1-0), HCO$^+$(1-0), HNC(1-0), CS(2-1), ^{13}CO(1-0), and CN($1_{0,1}$-$0_{0,1}$). The lines have been selected based on their flux density (a low signal-to-noise ratio can cause problems in the application of PCA), distributions, and the characteristic gas they trace. For instance, HCN, HCO$^+$, and HNC have been characterised as tracers of dense cold gas (Aalto et al. 2002; Meier and Turner 2005), while CS, CN and CCH are often described as tracers of UV-dominated regions (Aalto et al. 2002).

A correlation matrix has been produced, to quantify the correlations between the difference molecules. In Table 5.18, one can see that HCN and HCO$^+$ have the strongest correlation, followed by HCN and CCH. On the other hand, ^{13}CO shows relatively weak correlations with all the other molecules, while HNC is strongly correlated with all of them.

The seven lines used for the analysis can be described by seven components. Table 5.19 presents the loadings and variance of each component. These values are better represented by plotting the loadings of each component against those of another as seen in Fig. 5.28. The first plot at the top left in the figure shows the loadings of the first principal component plotted against the loadings of the second principal component. All the molecules have positive principal component loadings, indicating a correlation between the molecules at least at first approximation. Nevertheless, ^{13}CO shows already a significantly lower correlation than all the others with HCN.

However, ^{13}CO and CN have positive second PC loadings, while the other have negative loadings, indicating slight differences in emission regions between ^{13}CO and CN, and the other molecules. The variances of the PCs give an indicator to how different the components are from each other. One notices that the biggest difference is between the first and the second PC, where the first PC has a variance of around 75%, while the second PC has a variance of around 10%. The other PCs show similar variances ranging from around 0.5 to 6%, which indicates minimal differences to their contributions to the flux.

Table 5.18: Correlation matrix for M 82

	CCH	CN	CS	HCN	HCO^+	HNC	^{13}CO
CCH	1						
CN	0.82	1					
CS	0.75	0.73	1				
HCN	0.92	0.86	0.69	1			
HCO^+	0.82	0.77	0.61	0.93	1		
HNC	0.88	0.77	0.73	0.83	0.73	1	
^{13}CO	0.49	0.58	0.43	0.52	0.48	0.46	1

Table 5.19: Loadings of PCA on M 82

	Variance of PC	CCH	CN	CS	HCN	HCO+	HNC	13CO
PC 1	75.73%	0.41	0.40	0.35	0.42	0.39	0.39	0.27
PC 2	9.78%	-0.18	0.08	-0.14	-0.11	-0.10	-0.19	0.94
PC 3	6.36%	0.03	-0.04	-0.78	0.32	0.52	-0.12	-0.04
PC 4	3.57%	-0.27	0.36	0.35	0.09	0.34	-0.73	-0.13
PC 5	2.66%	0.07	-0.82	0.35	0.04	0.40	-0.11	0.16
PC 6	1.43%	-0.74	0.08	0.06	-0.21	0.39	0.49	-0.02
PC 7	0.48%	0.41	0.16	-0.06	-0.81	0.38	-0.04	-0.01

For a better understanding of the principal component analysis, one needs to interpret the principal component loading plots hand in hand with the maps of the principal components. The maps represent the scores of the principal components in a manner that visualises the contribution of these scores to the total emission of the lines. Figure 5.29 shows the maps of the different components from M 82. The map of the first PC (the scores of the PCs are plotted, showing the distribution of the variables against the principal components) at the left of Figure 5.29, resembles strongly the flux map of M 82. This indicates that the correlation between the molecules seen in the loadings of the first PC is due to the fact that all selected molecular lines are being emitted from similar regions in M 82, with most of the emission originating from the four "red" regions seen in the first PC map. However, the map of the second PC shows mainly two different regions, highlighting differences in the emission morphology of some molecules. From the scores of the second PC (bottom plot in Fig. 5.28), one can see that the ^{13}CO and CN emission lines have positive scores. Therefore, one can conclude that they are mainly emitted from the two "red" regions seen in the map of the second PC, while the other molecules are mainly emitted from the "blue" regions where the PC scores are negative.

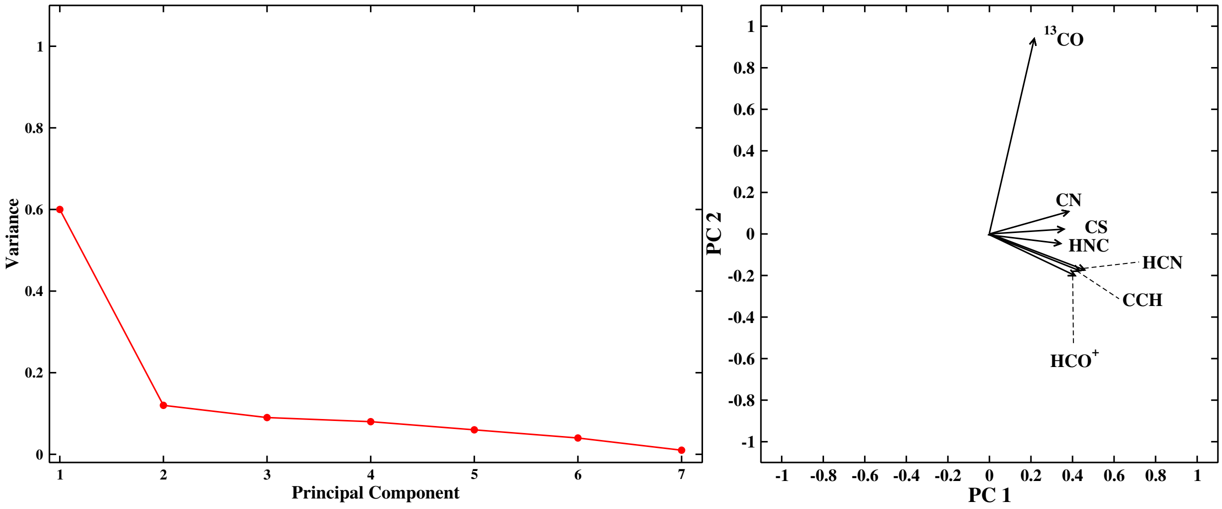

Figure 5.28: Left: Variance of the principal components of IC 342. Right: Plot of the principal component loadings for M 82.

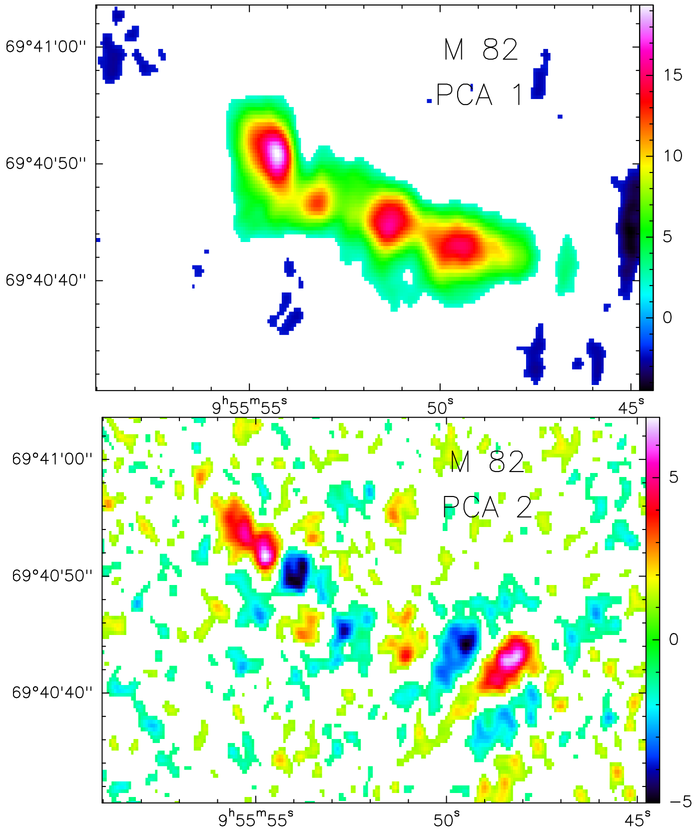

Figure 5.29: Maps of the first principal component of M 82 (top), and the second principal component (bottom).

5.6.2 IC 342

For the PC application to the data collected for IC 342, five lines were selected, namely: HCN(1-0), HCO$^+$(1-0), C^{18}O(1-0), HNCO($5_{0,5}$-$4_{0,4}$), and ^{13}CO(1-0). These lines have been chosen based on their flux and distribution. Specifically, HNCO has been chosen because it is a good shock tracer (Martín et al. 2009), while $C^{18}O$ has been used as H_2 column density tracer (Dahmen et al. 1998).

The correlation matrix 5.20 obtained from the PC analysis shows a strong correlation between HCN and HCO^+(HCN and HCO^+ have the strongest correlation coefficient with 0.99), as well as between ^{13}CO and $C^{18}O$ (with a correlation coefficient of 0.92). Moreover, ^{13}CO and $C^{18}O$ correlate well with all molecules, with the weakest correlation being with HNCO (correlation coefficient of 0.60 with ^{13}CO and of 0.72 with $C^{18}O$). The weakest correlation is between HNCO and HCN (0.45), and HCO^+ (0.42).

Table 5.20: Correlation matrix for IC 342

	^{13}CO	HNCO	HCN	HCO^+	$C^{18}O$
^{13}CO	1				
HNCO	0.60	1			
HCN	0.85	0.45	1		
HCO^+	0.85	0.42	0.99	1	
$C^{18}O$	0.92	0.72	0.83	0.83	1

Table 5.21: Loadings of PCA on IC 342

	Variance of PC	HCN	HCO+	13CO	HNCO	C18O
PC 1	80.62%	0.47	0.46	0.47	0.34	0.48
PC 2	14.67%	-0.36	-0.39	-0.02	0.83	0.16
PC 3	3.37%	-0.40	-0.33	0.71	-0.37	0.29
PC 4	1.25%	-0.08	-0.05	-0.52	-0.23	0.81
PC 5	0.08%	0.70	-0.72	0.02	-0.04	0.03

From the five lines used as input, one gets five components. The loadings and the variance of each component are presented in Table 5.21. Most of the variance is contained in the first PC, which shows a variance of around 81%, while the second PC has a variance of around 15%, showing a strong difference between the first and the second component. The other PCs have variabilities ranging from 0.08% up to 3%, suggesting that the contribution of these components to the flux is minimal.

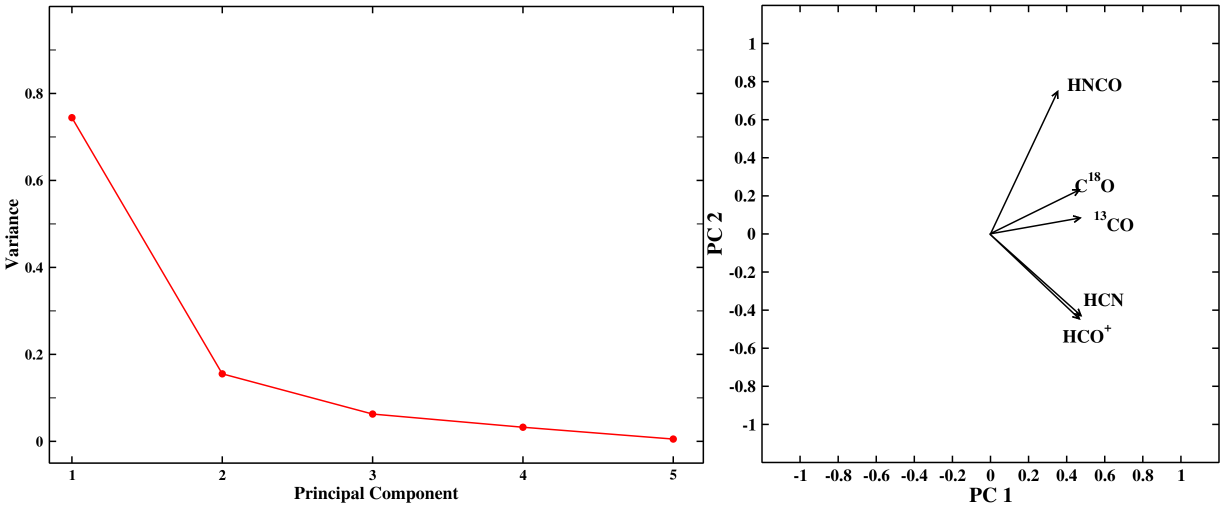

Figure 5.30: Left: Variance of the principal components of IC 342. Right: Plot of the principal component loadings for IC 342.

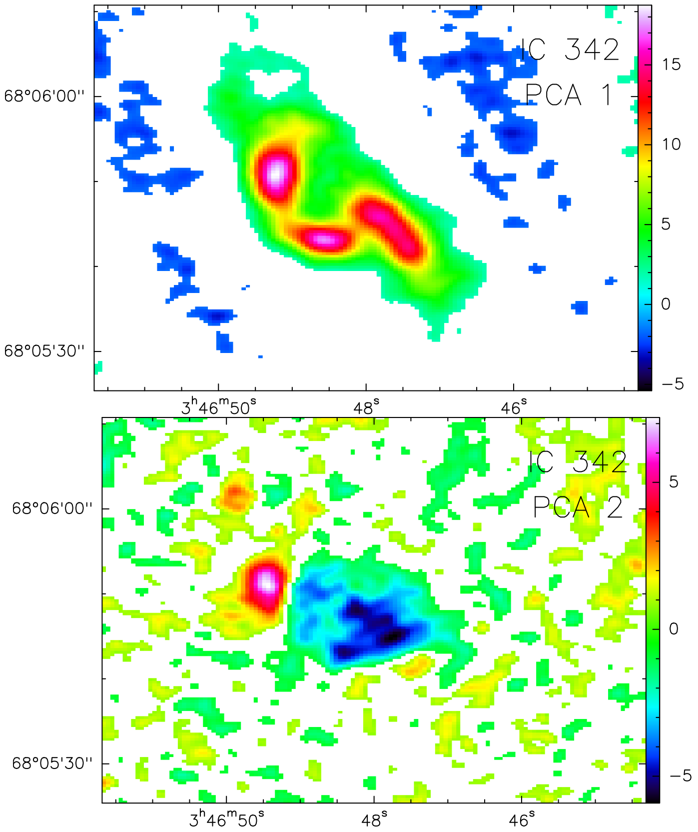

Figure 5.31: Maps of the first principal component of IC 342 (top), and the second principal component (bottom).

In the left plot of Figure 5.30, the loadings of the first PC are plotted against the loadings of the second PC. This plot shows that the loadings of the first PC for all selected molecules are positive, indicating a positive correlation between all the molecules. This correlation is due to the fact that all the molecules were emitted from the same regions, with concentrations in the “red” regions seen in the top plot of Figure 5.31 (in this figure, the scores of the first PC are plotted, showing the distribution of the variables against that principal component). However, one can see that HCN, HCO^+, and ^{13}CO have negative loadings for the second PC, while the other two molecules show positive loadings for the second PC. This highlights a difference between HCN, HCO^+ and ^{13}CO, with respect to the other molecules. This difference is clearly seen in the right plot of Fig. 5.30 and in the bottom plot of Fig. 5.31 (this figure maps the scores of the second PC), where one clearly sees that HCN, and HCO^+ behave differently than HNCO.

Chapter 6

Discussion

The results of the analyses performed on the data are discussed in this chapter and interpreted in the context of the chemical evolution of the sources. Furthermore, the results from this work are related to previous studies. The chemical composition of the central molecular zones (CMZs) in M 82 and IC 342 will be discussed, as well as the distribution of the different molecules in those galaxies, and their abundances relative to $C^{18}O$. Unless mentioned otherwise, all molecular lines are assumed to be optically thin. Spatial correlations among molecules will be discussed and related to possible chemical properties in the respective regions of the galaxies. The discussion will address the gas distribution, known tracers of PDRs, XDRs, shocks, as well as dense, cold, and warm gas. The conditions under which certain complex molecules can form will be investigated. Column density ratios (abundance ratios) will be used as a tool to shed light on the state of the chemical evolution of the galaxies. Finally, the significant differences in the star formation rate in the two galaxies will be discussed, taking into account their chemical properties.

6.1 Chemical Modelling

The column densities obtained in this study were compared with the chemical models presented by Viti (2017). The details of the models and the comparison are explained in Chapter 5 Section 5.4. The chemistry in M 82 and IC 342 can be best described by Model 36 of Viti (2017) (see Table 5.16), which predicts a cosmic-ray ionisation rate of $\zeta = 2.5 \times 10^{-13}\,\mathrm{s}^{-1}$, a radiation field is similar to that in the Milky Way ($\chi = 2.74 \times 10^{-3}\,\mathrm{erg\,s^{-1}\,cm^{-2}}$), a temperature of 100 K, a gas density of $10^4\,\mathrm{cm}^3$, and finally a visual extinction in the clouds of 50 mag.
For M 82, the cosmic-ray ionisation rate has been previously estimated to be $\zeta_{\mathrm{M\,82}} \sim 5 \times 10^{-15}\,\mathrm{s}^{-1}$ in a region of $15''$ or $\sim\ 290\,\mathrm{pc}$ (van der Tak et al. 2008) and $\zeta_{\mathrm{M\,82}} \sim 5 \times 10^{-15}$ from observations at 100 MeV (Paglione and Abrahams 2012), and the density of the molecular gas in M 82 was estimated to be between 10^3 and $10^5\,\mathrm{cm}^{-3}$ (Loenen et al. 2010), which is consistent with the model's prediction. The radiation field in M 82 was however estimated to be between $\chi_{\mathrm{M\,82}} = 1.6 \times 10^{-1}\,\mathrm{erg\,s^{-1}\,cm^{-2}}$ and $8.9 \times 10^{-1}\,\mathrm{erg\,s^{-1}\,cm^{-2}}$ (Loenen et al. 2010), which is two orders of magnitude higher than the value estimated in the model. Since M 82 is a known starburst galaxy, it is expected to have a stronger UV-radiation field than that in the Milky Way, however, the higher radiation rate can be diminished by high extinction. Kamenetzky et al. (2012) found evidence of two gas components with a region of $3\,\mathrm{kpc} \times 3\,\mathrm{kpc}$ one with a temperature of 30 K, and the other with a temperature of 500 K, traced by high $J-$transitions of CO. Therefore, it is plausible that the temperature predicted by the chemical model might described a

warm gas component found within the central few hundred pc of M 82. Moreover, the visual extinction in multiple clouds in M 82 was estimated to be >20 mag, based on the observed column density of N_2H^+, with some clouds having a visual extinction $> 50\,\mathrm{mag}$ (Ginard et al. 2015). In general terms, Model 36 seems to be a good match for the properties of M 82.

Meier and Turner (2005) stated that the bright emission of N_2H^+ in the nucleus of IC 342 can be explained by cosmic-ray ionisation rate higher than the standard local values, $\zeta_{\mathrm{IC\,342}} > 10^{-17}\mathrm{s}^{-1}$. This is consistent with the prediction of the model of Viti (2017), but it is unclear if the cosmic-ray ionisation rate of IC 342 is in fact three orders of magnitude stronger than in the Milky Way. From NH_3 observations, kinetic temperatures between $\sim 30\,\mathrm{K}$ and 500 K were estimated (Mauersberger et al. 2003; Lebrón et al. 2011). Moreover, Bayet et al. (2006) estimated a radiation field $\chi_{\mathrm{IC\,342}} = 23\,\mathrm{erg\,s^{-1}\,cm^{-2}}$ which is much higher than the model's prediction, and the estimated value for M 82. The gas density of IC 342 was estimated to be $1.5 \times 10^5\,\mathrm{cm^{-3}}$ (Bayet et al. 2006), and it is one order of magnitude larger than the model's prediction. In this work, the column density of $C^{18}O$ is estimated. From these values, one can estimate the column density of H_2 by assuming that $\frac{N(\mathrm{H_2})}{N(\mathrm{C^{18}O})} = 2.5 \times 10^6$ (Dahmen et al. 1998). Therefore, the column densities of H_2 estimated from the column densities of $C^{18}O$ in this work are $N(\mathrm{H_2}) \sim 3.5 \times 10^{22}\,\mathrm{cm^{-2}}$. This corresponds to a visual extinction of $A_v \sim 35\,\mathrm{mag}$ (assuming that $N(\mathrm{H_2}) = 10^{20}\,\mathrm{cm^{-2}}$ corresponds to a visual extinction $A_v = 0.1\,\mathrm{mag}$, Wilson et al. 2012). Therefore, Model 36 is a good description of the physical properties of the molecular clouds in IC 342.

A single model did not match the column density of all molecular species in both M 82 and IC 324. As seen in in Chapter 5 Section 5.4, the best matched molecules are HCN, HNC, HCO^+, and N_2H^+, while CH_3CCH, CH_3OH and HNCO were significantly underestimated by all the matched models for both galaxies. There are two main reasons why these molecules could be underestimated. Either the chemical equations used for the formation and destruction of these molecules cannot, on their own, determine the abundances of these molecules. Or, these molecules are destroyed before chemical equilibrium is reached, as is the case for CH_3OH and HNCO (Viti 2017). In other words, the abundances of these molecules are better described at a time before or after chemical equilibrium is reached. This points to the fact that molecular species can be tracing different chemical conditions that co-exist in the same molecular cloud.

While the chemical models assume large velocity gradients and non-LTE conditions, in this study, the calculations of the column densities were done under LTE-assumptions. Moreover, the models have predicted the abundances of around 250 molecules, out of which only 14 were observed in this study and compared with the predictions. Therefore, caution is required when comparing the results of this study with the predictions of the chemical models, and one needs a wider range of molecular species observed at the same spatial resolution (Viti 2017).

6.2 Chemical Composition Of The CMZs of M 82 and IC 342

6.2.1 The Hα Recombination Lines

The spectral analysis shows, despite the many similarities in the chemical composition and physical conditions of M 82 and IC 342, many significant differences. For instance, in M 82, three Hα radio recombination lines were detected in this work (H41α, H40α, H39α), while more Hα radio recombination lines were detected in Aladro et al. (2011a, 2015). However, no such Hα recombination lines were detected in IC 342. The Hα recombination lines are tracers of ionised hydrogen, as these lines are emitted when a free electron recombines with a proton to form a neutral hydrogen atom (for more details check Chapter 2.1.1). H II regions have typical electron temperatures of almost $10^4\,\mathrm{K}$ (Draine 2011). Such high temperatures are due to UV-radiation from young hot massive stars, and supernova explosions. Massive stars emit strong enough UV radiation and winds, to ionise the regions around it. Therefore, Hα recombination lines are tracing the regions of recent massive star formation. The Hα recombination lines show a weak emission in regions A and B of M 82, but a strong peak and extended emission in regions C, and D (see Fig. 5.15, and 5.25). Compared with molecular emission over M 82, the Hα recombination lines show a clustered emission in the south-western part of the M 82, while PDR and dense gas tracers such as CH_3CCH (see Section 6.2.5) and CN (see Section 6.2.8) are spread over the four emission regions A, B, C, and D of the galaxy. The high density PDR tracer CS (see Section 6.2.10) shows an emission peak in region A, with a weaker emission in regions B, C, and D. This indicates that, while dense gas and PDRs are present in all regions (A, B, C, and D) of the galaxy, younger massive stars (traced by the Hα recombination lines) seem to be clustered around certain regions, particularly at the south-western part of the galaxy (regions C and D). Such clusters were also found by O'Connell and Mangano (1978); Barker et al. (2008); Divakara Mayya and Carrasco (2009). This confirms that M 82 is dominated by starburst activity, while no such activity is seen in IC 342.

6.2.2 HNCO and SiO

On the other hand, in this work, a number of molecules such as HNCO, and SiO were observed in IC 342 but not in M 82. Studies such as Hüttemeister et al. (1997) and Martín et al. (2006a) show that while HNCO is abundant in IC 342, it is not in M 82. Similarly Aladro et al. (2015) detected (with a $23'' - 28''$ beam) only faint emission of HNCO, and SiO in M 82 (with abundances relative to $C^{18}O$ if 10^{-3} and 1.7×10^{-4}, respectively). The presence of HNCO (see Table. 5.13) in IC 342 as detected in the study presented here, indicates that the molecular gas in IC 342 is dominated by shock, that allow such molecules to form. For instance, HNCO is formed on the grain mantles through low velocity shocks (shock velocity $\sim 10\,\mathrm{km\,s^{-1}}$, Holdship et al. 2017) and is enhanced in high-velocity gas (Zinchenko et al. 2000; Martín et al. 2009). These shocks can also prevent efficient star formation from taking place (e.g. Huettemeister et al. 1998; Dekel and Birnboim 2006). The faint emission of shock tracers in M 82 detected by some studies (e.g. Martín et al. 2006a, 2009; Aladro et al. 2011a, 2015) can be relics from the interaction with M 81 (Yun et al. 1993, 1994) that triggered the burst of star formation by introducing new material and gas into the ISM of M 82, allowing for a large reservoir of gas for the ongoing starburst (de Grijs et al. 2001, 2005). However, an alternative explanation (which may be the more likely one) is, that the strong UV-radiation due to massive stars in M 82 is dissociating such complex molecules, and therefore, the hot gas in M 82 is destroying molecules such as HNCO (Martín et al. 2009). HNCO is formed through a two-step process in which NCO is first formed from reactions between CN and O_2, then NCO and H_2 can react to form HNCO (Turner et al. 1999). It is suggested, that if O_2 is destroyed by strong UV radiation and powerful shocks (shocks with velocity > $30\,\mathrm{km\,s^{-1}}$), then HNCO would also be destroyed by PDR regions and strong shocks (Zinchenko et al. 2000). The line emission of HNCO as observed in the study presented here covers all the regions of IC 342 indicating an extended emission. This suggests the presence of mild shocks (shock velocity $\sim 10\,\mathrm{km\,s^{-1}}$, Holdship et al. 2017) across all the different regions of IC 342.

SiO is the only silicon-bearing molecule detected in this study. It is observed in IC 342 ($(2.31 - 14.4) \times 10^{12}\,\mathrm{cm^{-2}}$, see Table. 5.13), with an abundance of (1.7-8.3)$\times 10^{-4}$ relative to $C^{18}O$ (see Table. 5.15), but not in M 82. Aladro et al. (2015) detected faint SiO emission ($4.4 \times 10^{12}\,\mathrm{cm^{-2}}$, and an abundance of 1.7×10^{-4} relative to $C^{18}O$) in M 82 using the IRAM

30-m telescope. Formation conditions for SiO are still unclear. However, one possible formation process is through silicon reactions with OH or O_2, even though these temperature-dependent reactions are not sufficient to explain the SiO abundances observed in galaxies (Turner 1998a). An alternative explanation is that SiO is formed due to the destruction of grains in violent shocks and in high-temperature gas (Ziurys et al. 1989). SiO is, therefore, a signpost of violent, shocked gas (shocks with velocity > $30\,\mathrm{km\,s^{-1}}$, Mauersberger and Henkel 1991). In IC 342, SiO abundances then trace shocked gas, and its absence (or faint emission) in M 82 is indicative of a more quiescent gas in the galaxy, where violent shocks are absent.

6.2.3 CH_3OH

Similarly, Mauersberger and Henkel (1993) and Martín et al. (2006a) reported low abundances of CH_3OH in M 82. Methanol (CH_3OH) is formed through one of the following two processes. The first is through a photo-dissociative recombination of $CH_3OH_2^+$, that is formed through a radiative association of CH_3^+ with water molecules (H_2O) (Turner 1998b). However, this process is thought to be too slow to allow for the observed abundances of methanol (Meier and Turner 2005, and references therein). The second process involves the hydrogenation of CO on grain surfaces, which requires high temperatures ($\sim 90\,\mathrm{K}$) (Meier and Turner 2005). This and subsequent evaporation (e.g. as a consequence of mild shocks) make methanol a warm molecular gas tracer (Meier and Turner 2005). In this study, methanol was detected in IC 342 but not in M 82. CH_3OH in IC 342 is mainly detected towards the peaks of the emission regions (A, B, and C) with very little extended emission. These column densities indicate the presence of warm dense gas and mild shocks, concentrated in the different emission regions of IC 342. Mild shocks disrupt the grain mantles, allowing for the formation of methanol without destroying the molecules (Bergin et al. 1998; Meier and Turner 2005), while shocks from massive stellar outflows are not strong enough to influence the chemistry of the surrounding ISM in IC 342, and therefore, large-scale shocks, such as orbital shocks and cloud-cloud collisions, may be responsible for the methanol abundance in IC 342 (Meier and Turner 2005).

6.2.4 CH_3CN

CH_3CN traces hot gas in star-forming regions, but is observed as well in cold dark clouds in cool quiescent objects (Turner et al. 1999). In M 82, the source-averaged CH_3CN column densities determined by Mauersberger et al. (1991) and Aladro et al. (2015) are significantly lower than the column densities of other molecules detected in these studies. Chemical modelling shows that the abundance of CH_3CN depends on the abundance ratio of $\frac{C}{O}$, where the CH_3CN abundance increases significantly when C and O have similar abundances (this is also the case for many other molecules such as HCN, HNC, HC_3N, CCH, and CH_3CCH) (Turner et al. 1999). CH_3CN is frequently observed in hot cores (eg. Zhang et al. 1998; Remijan et al. 2004; Mendoza et al. 2018). Its detection in IC 342 indicates the presence of a hot dense gas component in the galaxy. There are some indications that CH_3CN can be produced from CH_3OH (Mendoza et al. 2018), suggesting that the hot gas in IC 342 has been present for a long enough time to allow for the production of CH_3CN from CH_3OH that traces colder gas.

6.2.5 CH_3CCH

CH_3CCH is the only complex organic molecule with high abundance relative to $C^{18}O$ in M 82 and it is even largely more abundant (relatively to $C^{18}O$) in M 82 than it is in IC 342. This is similar to the results of the single dish observation of M 82 and IC 342 done by Aladro et al. (2011b). The formation processes for CH_3CCH are still unclear. Complex molecules may be formed on dust grains, and dissociated in the gas phase by UV-radiation. Therefore, complex molecules show low abundances in starburst galaxies and photo-dissociation regions (PDRs) where, in general, dust evaporation is important. However, CH_3CCH is very abundant in starburst galaxies, and observed to be boosted in PDR regions (eg. Aladro et al. 2011b, 2013 and Aladro et al. 2015). The high relative abundance of CH_3CCH (compared to the relative abundance of other complex molecules) observed in M 82 and other starburst galaxies (eg. M 83, NGC 253, and Arp 220 (Aladro et al. 2015)) suggests that CH_3CCH is formed through gas phase neutral-neutral and ion-neutral reactions, rather than from ice grain mantles (Aladro et al. 2011b). Since CH_3CCH is, most likely, not formed on dust grains but rather in the gas phase, it will not be destroyed by UV-radiation that is causing dust evaporation. The question of how CH_3CCH escapes UV-dissociation in the gas phase, is still open. Moreover, since other complex molecules that are formed on dust grains are dissociated in the gas phase, they provide seed ions and molecules, that allow the formation of CH_3CCH in the gas phase, from neutral-neutral and ion-neutral reactions. Therefore, the abundance of CH_3CCH is strongly correlated with the abundance of ions (Herbst and Leung 1989). In galaxies such as M 82, where the strong UV radiation would dissociate complex molecules, CH_3CCH could be formed through ions and molecules resulting from the dissociation, and CH_3CCH would then escape destruction through photo-dissociation in M 82 (Aladro et al. 2011b). More chemical modelling and studies are needed to shed more light on the formation of CH_3CCH.

The high column density of CH_3CCH (see Table. 5.13) detected toward M 82 in this study, is consistent with previous results from Aladro et al. (2015). Since M 82 is dominated by strong UV radiation as indicated by the Hα recombination lines and the different PDR tracers (HCN, HCO^+, ...), this strong UV field will dissociate enough complex molecules to allow for the high abundance of CH_3CCH relative to $C^{18}O$. This high abundance suggests than that the complex molecules in M 82, such as HNCO, CH_3CN, and CH_3OH are not destroyed through shocks, but rather through the strong UV-field from young massive stars and the photo-dissociation regions in M 82. Therefore, the high abundance of CH_3CCH in M 82 could be another indicator of a PDR-dominated gas.

6.2.6 HCN and HNC

In thermodynamical equilibrium, HCN formation is favoured over that of HNC (Meier and Turner 2005). This is due to the fact that C has four valence electrons while N has five. Thus, the charge distribution and electronegativity is different between C and N, and therefore, their binding with hydrogen is also different. In order to form HCN, carbon will form a triple bond with nitrogen and a simple bond with hydrogen. Bonding its four electrons with four bonds, it has thus a formal charge of 0, while nitrogen bonds three of its electrons with three electrons of carbon, leaving two electrons on its outer electron orbit. On the other hand, in order to form HNC, nitrogen will bond one electron with hydrogen and three with carbon. Thus nitrogen has bonded four out of its five electrons, and now has a formal charge of +1, while carbon now has five electrons, bonding three of them with nitrogen, and thus carbon now has a formal charge of -1 (Fig. 6.1). Since the formal charges of the atoms in HNC are different from zero, HNC is less

stable than HCN, whose atoms all have a formal charge of zero.
However, in dark clouds, the abundance ratio of $\frac{\mathrm{HNC}}{\mathrm{HCN}}$ is relatively high (close to 1 Harju 1989), with the ratio reaching 3 in some cold dark clouds in the Milky Way (Hirota et al. 1998). Even in hot regions where HCN is significantly more abundant, HNC is still detected (eg. Schilke et al. 1992; Turner et al. 1997). Baan et al. (2008) proposed that an abundance ratio of $\frac{\mathrm{HNC}}{\mathrm{HCN}} > 1$ is indicative of an X-ray dominated region, while $\frac{\mathrm{HNC}}{\mathrm{HCN}} < 1$ is tracing a PDR. Theoretical and chemical modelling suggest that HNC is as likely to be formed as HCN under a variety of different conditions (Lee et al. 1996). Schilke et al. (1992) suggested that the abundances of both HCN and HNC are density and temperature dependent: at low densities and low temperatures, HCN and HNC have the same probability of forming. Since the results of this study show that HCN is more abundant than HNC, the gas in M 82 and in IC 342 is assumed to be, at least partially, dense and warm, where HCN is more likely to form than HNC (Schilke et al. 1992).
The dependence of the abundance ratio of $\frac{\mathrm{HNC}}{\mathrm{HCN}}$ on temperature is still in question, however. Since HCN is found to be more abundant in warm regions, it is proposed that HNC molecules are destroyed in a high temperature environment (Meier and Turner 2005; Baan et al. 2008). HCN is collisionally excited, and is used to trace dense (density$>10^4 - 10^5\,\mathrm{cm}^{-3}$) molecular gas (eg. Solomon et al. 1992; Helfer and Blitz 1993; Curran et al. 2000; Aalto et al. 2002). However, if HNC is originating from a gas with such densities, it can still have significant abundances even in a warm molecular medium, since reactions with HCNH^{+} will form HCN and HNC with equal probabilities (Aalto et al. 2002). It has also been proposed that HCN is enhanced in regions with strong X-ray emission (Lepp and Dalgarno 1996; Kohno et al. 1996, 2001; Imanishi et al. 2004, 2007). HNC bright sources are mostly AGN, however, in some Seyfert galaxies, the HNC emission is faint (Aalto et al. 2002).

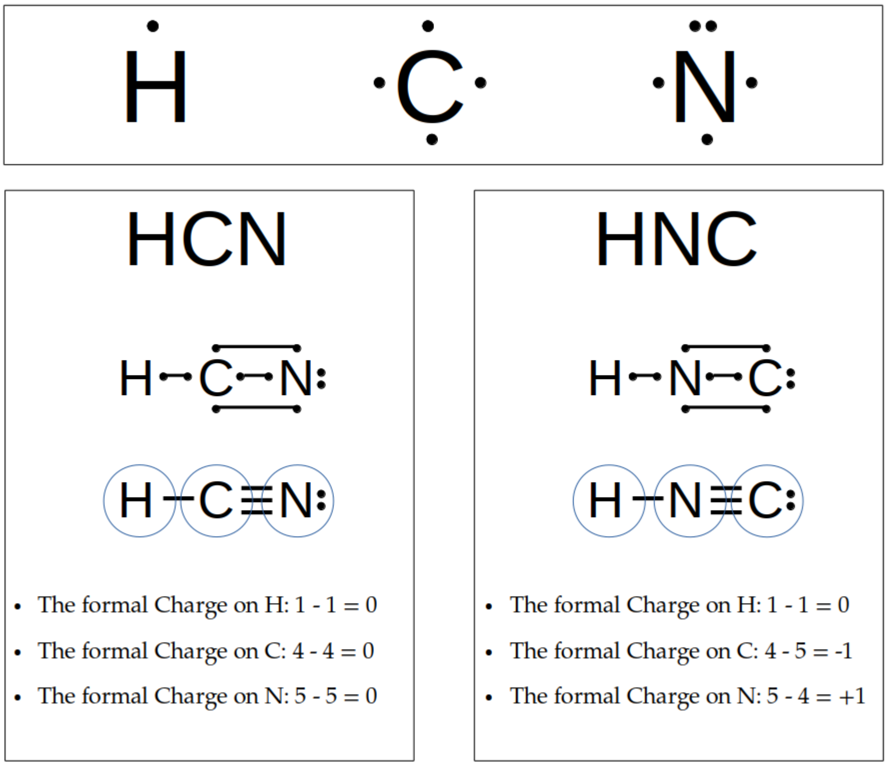

- The formal Charge on H: 1 - 1 = 0
- The formal Charge on C: 4 - 4 = 0
- The formal Charge on N: 5 - 5 = 0

- The formal Charge on H: 1 - 1 = 0
- The formal Charge on C: 4 - 5 = -1
- The formal Charge on N: 5 - 4 = +1

Figure 6.1: Lewis Dots Structure of HCN and HNC

Downes et al. (1992) suggested that the morphology of HNC follows closely the morphology of HCN . This similarity between the morphologies of HCN and HNC are also observed in this work as seen in Fig. 5.25 and 5.27. Aalto et al. (2002) challenged the assumption that HNC is a reliable cold gas tracer, but suggested that it can trace a fraction of the cold gas. Furthermore, the $\frac{\mathrm{HNC}}{\mathrm{HCN}}$ ratio between 0.30 and 0.48 in M 82 and between 0.23 and 0.31 in IC 342 (as seen in Table. 5.14) suggests that HCN and HNC are tracing warm environments in these galaxies (Irvine et al. 1987).

The abundance of HNC in M 82 relative to $C^{18}O$ is on average one order of magnitude lower than the abundance of HCN relative to $C^{18}O$ and that of $\mathrm{HCO^+}$ (see Table. 5.15), which is typical for star forming regions (Hüttemeister et al. 1995). HNC is more abundant in M 82 than it is in IC 342 (see Table. 5.15). This slight difference in abundance can be due to shocks destroying HNC in IC 342 (Schilke et al. 1992), but favouring SiO formation (see Section 6.2.2).

Moreover, Meier and Turner (2005) found an abundance ratio of $\frac{\mathrm{HNC}}{\mathrm{HCN}} \sim 0.45 - 0.8$ in IC 342, which could be interpreted as an indication for a dense cold gas. However, they found that HCN and HNC distributions follow closely the distribution of CO that traces warm gas, leading to the conclusion that the $\frac{\mathrm{HNC}}{\mathrm{HCN}}$ ratio can be temperature independent (Meier and Turner 2005). Figures 5.17, 5.19, and 5.20 show that HNC is characterised by a similar distribution as those of $\mathrm{HC_3N}$, $\mathrm{N_2H^+}$, and HNCO, indicating a possible correlation between HNC and nitrogen abundances. Similar results, with similar distributions of $\mathrm{NH_3}$ were found in Meier and Turner (2005).

6.2.7 $\mathrm{HCO^+}$

The molecule $\mathrm{HCO^+}$, i.e. protonated CO, is thought to be a good tracer of cosmic ray and UV dominated regions in dense gas (eg. Hüttemeister et al. 1995). Moreover, $\mathrm{HCO^+}$ is thought to be enhanced in regions with young supernova remnants, massive star formation regions, and shocked and dense environments, even though HCN may be a more reliable dense gas tracer than $\mathrm{HCO^+}$ (Dickinson et al. 1980; Wootten 1981; Baan et al. 2008). The abundance ratio of $\frac{\mathrm{HCO^+}}{\mathrm{HCN}}$ is often used as a tracer for X-ray dominated regions (XDR) (Baan et al. 2008), and/or for AGN activity (Kohno et al. 2001; Imanishi et al. 2004, 2007). Baan et al. (2008) suggests that the ratios of $\frac{\mathrm{HCO^+}}{\mathrm{HCN}} < 1$ and $\frac{\mathrm{HCO^+}}{\mathrm{HNC}} < 1$ are typical of PDR regions, while $\frac{\mathrm{HCO^+}}{\mathrm{HCN}} > 1$ and $\frac{\mathrm{HCO^+}}{\mathrm{HNC}} > 1$ are tracing XDRs. However, a ratio of $\frac{\mathrm{HCO^+}}{\mathrm{HCN}} < 0.5$ is suggestive of AGN activity if this AGN is dominating the galaxy, and indeed, many AGNs have been observed with such a low ratio (Kohno et al. 2001; Imanishi et al. 2004, 2007; Krips et al. 2008).

Nevertheless, the dichotomies are strongly debated: It has been suggested that, the variations in the abundances ratio of $\frac{\mathrm{HCO^+}}{\mathrm{HCN}}$ and $\frac{\mathrm{HCO^+}}{\mathrm{HNC}}$ depend strongly on the variation in densities (the ratio would decrease for higher densities), and not on the variations in the UV-field radiation or the cosmic-ray ionisation rate (Loenen et al. 2008 and Bayet et al. 2009). ALMA observations showed a ratio of $\frac{\mathrm{HCO^+}}{\mathrm{HCN}} \sim 0.77$ in the nuclear torus of NGC 1068, a galaxy with an AGN (García-Burillo et al. 2014; Viti et al. 2014). This ratio also seems to be strongly time dependent in dense gas and XDRs (Bayet et al. 2008; Meijerink et al. 2013). Results from Martín et al. (2015) could not corroborate the suggestion that HCN is enhanced in XDRs, and thus cast doubt on the effectiveness of using the abundance ratio of $\frac{\mathrm{HCO^+}}{\mathrm{HCN}}$ to identify AGNs. Moreover, $\mathrm{HCO^+}$ is found to be enhanced in XDRs and cosmic-ray dominated regions, as well as in star forming regions, making $\mathrm{HCO^+}$ a tracer for massive star formation (Meijerink and Spaans 2005; Bayet et al. 2008, 2011; Martín et al. 2015). Viti (2017) performed chemical modelling of the ISM, and showed that a ratio of $\frac{\mathrm{HCO^+}}{\mathrm{HCN}} < 0.5$ is not unique to AGN dominated galaxies, but can also be found in starburst dominated galaxies.

In the study presented here, the abundance of $\mathrm{HCO^+}$ relative to $C^{18}O$ in IC 342 is lower than its abundance in M 82 (see Table. 5.15), compatible with strong massive star formation in M 82, but not in IC 342. Moreover, the $\frac{\mathrm{HCO^+}}{\mathrm{HCN}}$ ratio is found to be ~ 0.9 in M 82, but between 0.4 and 0.5 in IC 342 (Table. 5.14). This might be indicative of a strong PDR in M 82, and an AGN activity in IC 342. However, one must proceed with caution with this interpretation, because, even though the PDR dominance is confirmed in M 82, there are no clear indications of AGN activity in IC 342 despite the existence of multi-wavelength data studies (eg. Mak et al. 2008; Rigopoulou et al. 2013; Nakajima et al. 2018). Another explanation for the $\frac{\mathrm{HCO^+}}{\mathrm{HCN}}$ ratio, is that M 82 is a small galaxy with sub-solar metallicities (Nagao et al. 2011), where nitrogen is likely under-abundant, thus reducing the abundance of HCN. Furthermore, dust may also be under-abundant, therefore, radiation can better penetrate the dense gas and create $\mathrm{HCO^+}$ in larger volumes.

6.2.8 CN

The PDR and dense gas tracer CN is observed to be one order to magnitude more abundant in M 82 than it is in IC 342 (see Table. 5.15). $\frac{\mathrm{CN}}{\mathrm{HCN}}$ abundances ratios are between 2.5 and 5.0 toward the four regions with strong emission in M 82 (see Fig. 5.1 and Table. 5.14). This is consistent with the ratio found by Fuente et al. (2005), and is indicative of strong and dense PDR regions in M 82 (Fuente et al. 2005). However, in IC 342, the ratio is between 2.5 and 3.5, suggesting a less dominant PDR presence in this galaxy. Baan et al. (2008) suggested that if $\frac{\mathrm{CN}}{\mathrm{HCN}} \gg 1$,then the environment is most likely an X-ray dominated region (XDR). The ratios found in this study, albeit being greater than one, are not large enough to indicate such an XDR. However, results from Aalto et al. (2002) where CN emission was not detected in many galaxies known to contain an AGN where the X-ray ionisation rate is high, cast doubt on the assumption that CN is enhanced in X-ray dominated regions (Krolik and Kallman 1983; Baan et al. 2008). Many models indicate that CN is a product of photo-dissociated HCN, and is also enhanced in strong UV fields through reactions of $\mathrm{C_2}$ and N, or CH and N, to form CN (Greaves and Church 1996; Rodríguez-Franco et al. 1998; Aalto et al. 2002). Aalto et al. (2002) also indicated that CN has greater abundances than HCN in many starbursts that they observed, suggesting that the $\frac{\mathrm{CN}}{\mathrm{HCN}}$ abundance ratio can be used as a PDR tracer. From this ratio, the results of this study confirms that M 82 is a strong starburst galaxy, while IC 342, is dominated by a more quiescent molecular interstellar medium.

6.2.9 CCH

Another difference in the chemical compositions between M 82 and IC 342 highlighted by this work, is the abundance of CCH. Ethynyl (CCH) is formed either through the photodissociation of $\mathrm{C_2H_2}$, or through the dissociative recombination of $\mathrm{C_2H_2}^+$ or $\mathrm{C_2H_3}^+$ with an electron (Meier and Turner 2005 and references therein). Therefore, CCH traces diffuse PDR regions, where $\mathrm{C^+}$ and UV-photons are abundant. However, CCH is also destroyed in strong UV fields (Li et al. 2012). Therefore, it has been suggested that CCH can trace star formation in deeply embedded environments, as well as different stages of starbursts (Li et al. 2012; Martín et al. 2015). CCH is detected in extended and diffuse gas where the UV radiation is just strong enough to enhance it (Li et al. 2012; Martín et al. 2015). It is important to study CCH closely, as its optical depth declines in more evolved starbursts as it gets destroyed by strong UV-radiation, and by detecting this molecule and comparing the intensities of its different hyperfine structure components that one observes in the 3-mm range, one can precisely calculate its optical depth and therefore determine the starburst stage (Li et al. 2012). Moreover, the intensity of CCH correlates well

with the intensities of HC_3N and HNC in regions of massive star formation, with CCH tracing, extended diffuse gas.
CCH is two orders of magnitude more abundant in M 82 than it is in IC 342 (see Table. 5.15), indicating once more the presence of strong PDRs in M 82 with an extended component, and weaker, less intense PDRs in IC 342.

6.2.10 CS and $C^{34}S$

In regions dominated by UV-radiation, CS is formed through dissociative recombination of HCS^+ ($HCS^+ + \bar{e} \longrightarrow CS + H$), and it would be destroyed by "photodissociation and charge transfer with H^+" (Goicoechea et al. 2006). If the gas is shielded from UV-radiation, CS will then be formed through dissociative recombination of OCS^+ ($OCS^+ + \bar{e} \longrightarrow CS + O$), and through reactions between C and SO (Goicoechea et al. 2006). In such a shielded gas, ion-molecular reactions with HCO^+ and with H_3O^+ will destroy CS, but will form HCS^+ , which in turn can form CS (Goicoechea et al. 2006). CS is mainly seen as a probe of high density PDRs (eg. Martín et al. 2009, 2015).
The high density ($n_{H_2} > 10^4 cm^{-3}$) tracer CS is found to have a higher abundance in M 82 (by an order of magnitude) than in IC 342 (see Table. 5.15) in this study. However, the column density of CS in IC 342 is still substantial.
The abundances of CS (relative to $C^{18}O$) in this study indicate the existence of high density gas in both M 82 and IC 342. In order to determine whether a region is dominated by photo-dissociation or by shocks, Martín et al. (2009) proposed comparing the column density of CS to that of HNCO to distinguish between PDRs and shock dominated regions, since HNCO is formed though shocks and is destroyed in PDRs, while CS is enhanced in PDR through reactions with S^+. If the column density ratio $\frac{HNCO}{CS} > 1$, it indicates that, since HNCO is more abundant than CS, the region is dominated by shocks, and if on the other hand, $\frac{HNCO}{CS} < 1$, then CS is more abundant than HNCO, and therefore, the region is dominated by photo-dissociation. Since HNCO is not detected in M 82 in this work, the high abundance of CS is suggestive of strong PDRs. In IC 342 however, the abundance ratio of $\frac{HNCO}{CS}$ is between 0.61 and 1.38 (Table. 5.14), indicating the presence of both PDRs and shock dominated regions. Izumi et al. (2013) proposed the use of $\frac{CS}{HCN}$ to distinguish between AGN and starburst dominated galaxies, suggesting that this ratio would be lower in AGNs and higher in PDRs. These differences can be due to a strong enhancement of CS in high density PDRs, while it would be underproduced in AGNs (Aladro et al. 2011b; Martín et al. 2015). In this study, the abundance ratio $\frac{CS}{HCN}$ is between 0.6 and 1.6 for M 82 and between 0.4 and 0.7 in IC 342 (Table. 5.14). Even though the $\frac{CS}{HCN}$ abundance ratio is lower in IC 342 than it is in M 82, the differences are not large enough to conclude that IC 342 is dominated by an AGN, for which there exists also otherwise no clear evidence. The conservative conclusion would be that photo-dissociation by radiation is stronger in M 82 than they are in IC 342.
The isotopic ratio of $\frac{CS}{C^{34}S}$ can be used to put limits on the isotopic ratio of $\frac{^{32}S}{^{34}S}$ (eg. Mauersberger and Henkel 1989; Chin et al. 1996). In this study, IC 342 shows a $\frac{CS}{C^{34}S}$ abundance ratio between 8 and 20 (Table. 5.14), which is similar to the results from previous interferometric observations targeting IC 342 (Meier and Turner 2005). On the other hand, M 82 shows a ratio between 23 and 100 (Table. 5.14), suggesting a strong under-abundance of $C^{34}S$ relative to its isotope CS in the galaxy. Aladro et al. (2015) presented an abundance ratio of $\frac{CS}{C^{34}S} \sim 17$ toward M 82. This strong difference in the abundance ratios could be due to different amount of missing flux between CS and $C^{34}S$, which were observed in different configurations. In both galaxies, CS is

more abundant (relative to $C^{18}O$) than $C^{34}S$ (see Table. 5.15 and Fig. 5.6, and 5.7). This overabundance of CS compared to $C^{34}S$ reflects on one hand the elemental $\frac{^{32}S}{^{34}S}$ ratio, but could also be enhanced through the presence of strong PDRs, followed by isotopologue selective photodissociation (less shielding of $C^{34}S$ against UV-photons) that are selectively dissociating $C^{34}S$ in M 82. Note that Wang et al. (2004) and Martín et al. (2005) proposed $\frac{\mathrm{CS}}{\mathrm{C^{34}S}}$ ratios between 8 and 13 for some starburst galaxies. However, IC 342 is not a starburst galaxy, and the significantly higher ratios in M 82 are more suggestive of a strong PDR dominated interstellar medium. In the Galactic Centre of the Milky Way, an intensity ratio of $\frac{\mathrm{CS(2-1)}}{\mathrm{C^{34}S(2-1)}} \sim 12$ has been determined (Lis et al. 2001). However, since it is not entirely clear whether the main isotopic CS line is optically thin or thick, this ratio is then only a lower limit for the abundance ratio of $\frac{\mathrm{CS}}{\mathrm{C^{34}S}}$ in the Milky Way.

6.2.11 SO

The sulfur-bearing molecule SO is formed through neutral-neutral reactions between S and OH, and is considered chemically a late-time species (Meier and Turner 2005). In early times, C is more abundant as it has not been turned to CO yet, and thus SO is more likely to turn into CS, since it is destroyed through reactions with C^+ and C in environments where C and C^+ are abundant (Meier and Turner 2005). Therefore, the abundance ratio $\frac{\mathrm{SO}}{\mathrm{CS}}$ can be used to determine the evolutionary stage of a molecular cloud, where a ratio $\frac{\mathrm{SO}}{\mathrm{CS}} \ll 1$ indicates early-times where atomic C is highly abundant compared to O, and a ratio of $\frac{\mathrm{SO}}{\mathrm{CS}} \gg 1$ indicates late-time chemistry (eg. Bergin et al. 1997; Nilsson et al. 2000). This would imply that, since column density ratios are between 0.07 and 0.11 for M 82 and between 0.01 and 0.08 in IC 342 (Table. 5.14), early-chemistry is dominant in both M 82 and IC 342. Both CS and SO are more abundant in M 82 than they are in IC 342 (see Table. 5.15). The low $\frac{\mathrm{SO}}{\mathrm{CS}}$ ratios are due to a relative under-abundance of SO compared to CS in both galaxies. The under-abundance of SO can be explained in terms of its destruction in favour of CS in C rich environments in both galaxies, and it is clearly not due to early-stage chemistry in M 82, but due to the presence of strong PDRs that are dissociating complex molecules, providing the dense gas with enough C and C^+ atoms to favour the formation of CS.

6.2.12 N_2H^+

The nitrogen-rich molecule N_2H^+ is a dense quiescent gas tracer in the Milky Way and it is found to be more abundant in regions with high cosmic-ray ionisation rate, and with high N_2, while it is less abundant in hot cores, outflows, and PDR regions (Meier and Turner 2005 and references therein). N_2H^+ is only formed through the reaction between N_2 and H_3^+ and therefore it is a tracer of N_2 (Womack et al. 1992; Turner 1995a; Benson et al. 1998; Meier and Turner 2005). In diffuse gas, N_2H^+ is destroyed through dissociative recombination with electrons, and in dark clouds through ion-neutral reactions with CO and O (Meier and Turner 2005).
In this study, N_2H^+ is one order of magnitude more abundant in M 82 than it is in IC 342 (see Table. 5.15). Meier and Turner 2005 explained the N_2H^+ column density in IC 342 through a high cosmic-ray ionisation rate that they estimated to be $\zeta_{\mathrm{IC\,342}} > 10^{-17}\mathrm{s}^{-1}$. This could be consistent with the values of cosmic ray ionisation rates found for the two galaxies in this work, based on the models of Viti (2017), where the estimated model for IC 342 predicts a cosmic ray ionisation rate of around $\zeta = 2.5 \times 10^{-13}\,\mathrm{s}^{-1}$ (see Section 6.1). Another explanation could be the rich variety of nitrogen-bearing molecules in IC 342 that is corroborated by the presence of HC_3N, HNCO, and NH_3 (NH_3 is mainly observed at $\lambda \sim 1.3\,\mathrm{cm}$ and is thus not part of this

work) that have been detected in IC 342 in this work and in previous studies (eg. Meier and Turner 2005).

The column density of N_2H^+ estimated in this work, when compared with the chemical models of Viti (2017), point to a model where the cosmic ray ionisation rate in M 82 is $\zeta = 2.5 \times 10^{-13}\,\mathrm{s}^{-1}$, which is compatible with the observations that estimates a cosmic-ray ionisation rate that vary between $\zeta_{\mathrm{M\,82}} \sim 10^{-17}$ and $10^{-12}\,\mathrm{s}^{-1}$ (Farquhar et al. 1994; Seaquist and Frayer 2000; van der Tak et al. 2008 and Paglione and Abrahams 2012).

In M 82, the abundances of N_2H^+ cannot be explained through strong cosmic-ray ionisation rates alone, but possibly through a combination of UV-radiations and cosmic-ray ionisation (Ginard et al. 2015). However, there is a strong correlation between the abundance of N_2H^+ and the visual extinction of clouds in the V-band (A_ν), where the abundance of N_2H^+ is negligible in clouds with $A_\nu < 10\,\mathrm{mag}$, but increases significantly in clouds where $A_\nu > 20\,\mathrm{mag}$ (Ginard et al. 2015). The chemical models estimated a visual extinction of ~ 50 mag in the M 82, which can also explain the column densities of N_2H^+ observed in this work. This correlation indicates that dense gas with high column densities is present in M 82 clouds, providing a strong gas reservoir that could fuel future star formation (Ginard et al. 2015). This assumption is corroborated by the high CS abundance relative to SO in M 82. N_2H^+ is also used as tracer of quiescent gas (Mauersberger and Henkel 1991). Its presence in IC 342 with abundances similar to that of SiO (see Table. 5.15) is indicative of the co-existence of quiescent and shocked gas in IC 342, as it is the case with NGC 253 and in the Milky Way (Mauersberger and Henkel 1991).

6.2.13 HC_3N

The formation of HC_3N (a typical species of early chemistry) is still unclear. However, the most likely formation process is through neutral-neutral reaction between C_2H_2 and CN, and it is destroyed in PDR dominated regions and through reactions with C^+ (Turner et al. 1998; Meier and Turner 2005 and references therein). Therefore, one expects that the morphology of HC_3N follows the morphology of CCH and CN. This is generally the case for IC 342 in this study, even though CCH and CN are more extended in the galaxy than HC_3N, that seems to be concentrated in regions A, B, and C with no extended emission (see Figs. 5.18, 5.19, and 5.20). This less extended morphology could be attributed to the existence of PDRs in IC 342 that might destroy HC_3N. It could also be, that HC_3N has a weaker emission than other molecules, and therefore only the peaks of the emission is detected in this study. This is more relevant in M 82 where the distribution of HC_3N is concentrated in small regions across the galaxy with no extended emission (see Fig. 5.14, and 5.16), despite the fact that the abundance HC_3N relative to $C^{18}O$ is one order of magnitude higher in M 82 than it is in IC 342 (see Table. 5.15).

Aladro et al. (2011b) assumed that CS and HC_3N have similar excitation temperatures and are therefore tracing the same dense gas in M 82 and IC 342. Mauersberger et al. (1990) suggested that HC_3N is a good dense gas tracer. Rodríguez-Franco et al. (1998) and Aalto et al. (2002) observed that HC_3N shows low abundances in PDRs with an abundance ratio of $\frac{HC_3N}{CN} \sim 10^{-3}$, but high abundances in hot and dense cores. In this study, the column density ratio of $\frac{HC_3N}{CN}$ is around 10^{-2} for both M 82 (the value is consistent with the results of Aladro et al. 2015) and IC 342 (Table. 5.14). The value of this ratio might differ from the typical PDR value of $\frac{HC_3N}{CN} \sim 10^{-3}$ (Aalto et al. 2002). However, this does not exclude the possibility of PDRs in M 82 and IC 342.

6.2.14 $C^{17}O$ and $C^{18}O$

The relative abundances of $\mathrm{C^{17}O}$ and $\mathrm{C^{18}O}$ gives insight on the $\frac{^{17}\mathrm{O}}{^{18}\mathrm{O}}$ ratio, and hence, on the dominant mass of stars forming in a given galaxy. During the helium-burning phase in massive stars, the isotope $^{16}\mathrm{O}$ is produced from $^{12}\mathrm{C}$, and $^{18}\mathrm{O}$ is produced from $^{14}\mathrm{N}$ (which is synthesised from $^{12}\mathrm{C}$ in the CN-cycle and from $^{16}\mathrm{O}$ in the ON-cycle), while $^{17}\mathrm{O}$ is produced in intermediate-mass stars during the hydrogen-burning phase in the ON-cycle (Heikkila et al. 1998). Hence, the abundance of $^{18}\mathrm{O}$ is dependent on the abundance of $^{12}\mathrm{C}$ and the abundance of $^{17}\mathrm{O}$ depends on the abundance of $^{16}\mathrm{O}$. A low ratio would indicate that massive stars did not influence the metallicity of the surrounding ISM as much (Heikkila et al. 1998). In the study presented here, the $\frac{^{18}\mathrm{O}}{^{17}\mathrm{O}}$ ratio is between 12 and 25 for IC 342, which is consistent with the limit given by Sage et al. (1991), which states that the ratio should be $\frac{^{18}\mathrm{O}}{^{17}\mathrm{O}} \gtrsim 5$. The Solar System value of the $\frac{^{18}\mathrm{O}}{^{17}\mathrm{O}}$ ratio is 5.5 (Muller et al. 2006), and the typical value for an ISM in the Milky Way is 3-5 (eg.Wouterloot et al. 2005). The values of the $\frac{^{18}\mathrm{O}}{^{17}\mathrm{O}}$ ratio found in this study toward IC 342, are similar to the value of 12 found toward PKS 1830-211, a relatively young galaxy with a redshift of $\mathrm{z} = 0.89$, with a population of young massive stars (Muller et al. 2006). Toward M 82, the $\frac{^{18}\mathrm{O}}{^{17}\mathrm{O}}$ ratio in this study presented here, is between 1 and 3, which is much lower than the value of 8.3 ± 1.3 estimated by Sage et al. (1991) and the value of 16.31 found by Aladro et al. (2015). The values found toward M 82 in this study, are similar to the value of 1.6 found toward the Large Magellanic Cloud (LMC) (Heikkila et al. 1998). The discrepancy between the values found in this work, and those found in previous studies can be attributed to the low signal-to-noise, and/or low sensitivity of the single-dish data. Martín et al. (2019b) reported similar discrepancies between the values of the abundance $\frac{^{18}\mathrm{O}}{^{17}\mathrm{O}}$ obtained from single-dish data, and those obtained from interferometric observations toward NGC 253.

In M 82, $\mathrm{C^{17}O}$ has slightly higher abundances relative to $\mathrm{C^{18}O}$ than in IC 342 (see Table. 5.15). This would indicate that massive stars are effective in influencing the ISM in both IC 342 and M 82. An explanation for the under-abundance of $\mathrm{C^{17}O}$ relative to $\mathrm{C^{18}O}$, is that $\mathrm{C^{17}O}$ (that has a lower optical depth than $\mathrm{C^{18}O}$) is selectively photo-dissociated by UV-radiation, in favour of $\mathrm{C^{18}O}$ that is better self-shielded from that radiation at high $\mathrm{H_2}$ column densities, making it more overabundant relative to $\mathrm{C^{17}O}$ (the column density of $\mathrm{H_2}$ would have to be 3 to 4 times higher in order to shield $\mathrm{C^{17}O}$, Ladd 2004). However $\mathrm{C^{18}O}$ self-shielding is significant at high $\mathrm{H_2}$ column densities ($> 10^{21}\,\mathrm{cm^{-2}}$), and high $A_v > 13\,\mathrm{mag}$ (Wouterloot et al. 2005). At such conditions, UV-radiation would not be able to affect the $\frac{^{18}\mathrm{O}}{^{17}\mathrm{O}}$, as $\mathrm{C^{17}O}$ would also be shielded (Wouterloot et al. 2005). Another, more plausible, explanation, is that, since $^{18}\mathrm{O}$ is formed in massive stars (that evolve faster than low mass stars) will be released into the ISM faster than $^{17}\mathrm{O}$ that are mainly produced in low- and intermediate-mass stars (Martín et al. 2019b). The under-abundance of $\mathrm{C^{17}O}$ relative to $\mathrm{C^{18}O}$ in M 82 and IC 342 (see Table. 5.15) can be explained by the strong formation of massive stars in this galaxy.

6.2.15 ^{13}CO and Other ^{13}C-bearing Molecules

The isotopologue $^{13}\mathrm{CO}$ is detected in both M 82 and IC 342 with high abundances relative to $\mathrm{C^{18}O}$ (see Table. 5.15). The $^{13}\mathrm{C}$ isotope is a secondary product from $^{12}\mathrm{C}$ which is produced during the helium burning of massive stars (Meyer 1994; Wilson and Rood 1994). Specifically, both $^{13}\mathrm{C}$ and $^{18}\mathrm{O}$ are mainly produced in low-metallicity fast-rotating massive and intermediate-mass stars (Martín et al. 2019b and reference therein). Therefore, the high abundances of $^{13}\mathrm{CO}$ relative to $\mathrm{C^{18}O}$ observed in this study are the result of high abundances of $^{12}\mathrm{C}$ produced in massive stars, that are formed in both M 82 and IC 342 (In this study, $^{13}\mathrm{CO}$ is assumed to be optically thin). The abundance ratio of $\frac{^{12}\mathrm{C}}{^{13}\mathrm{C}}$ is then an important diagnostic tool that determines the contribution of massive stars to the ISM, as ^{12}C is produced during the nucleosynthesis of massive stars, and ^{13}C is produced in the CNO burning of intermediate-mass stars. Sage et al. (1991) predicted a relation between the $\frac{^{12}\mathrm{C}}{^{13}\mathrm{C}}$ ratio and the $\frac{^{18}\mathrm{O}}{^{17}\mathrm{O}}$ ratio, where if the former is low, so is the latter. In this study, two ^{13}C-bearing molecules were detected in M 82, namely H^{13}CO^{+} and ^{13}CO. The abundance ratio of $\frac{^{13}\mathrm{CO}}{\mathrm{C}^{18}\mathrm{O}}$ has a value of $6.22 - 12.0$ in M 82, and $4.7 - 5.7$ in IC 342 (see Table. 5.15). These results are consistent with the values presented in Sage et al. (1991), and previous single-dish observations of Aladro et al. (2015). However, in IC 342, five ^{13}C-bearing molecules were detected: H^{13}CN, H^{13}CO^{+},HN^{13}C, ^{13}CO, and ^{13}CN, with ^{13}CO having the highest abundance of the five molecules relative to C^{18}O, while the others have relatively low abundances relative to C^{18}O (see Table. 5.15). The carbon isotope ratio is $\frac{^{12}\mathrm{C}}{^{13}\mathrm{C}} \gg 20$ in starburst dominated galaxies (Martín et al. 2010). In this study, the abundance ratio of $\frac{^{12}\mathrm{C}}{^{13}\mathrm{C}}$ is derived from the $\frac{\mathrm{HCO}^{+}}{\mathrm{H}^{13}\mathrm{CO}^{+}}$ column density ratio for M 82, and from $\frac{\mathrm{HCO}^{+}}{\mathrm{H}^{13}\mathrm{CO}^{+}}$ and $\frac{\mathrm{HCN}}{\mathrm{H}^{13}\mathrm{CN}}$ in IC 342, assuming that the main isotope lines are optically thin. In M 82, the abundance ratio is between 21 and 43. However, since the optical depth of HCO^{+} is unknown, the ratio derived for M 82 is a lower limit. In IC 342 is between 12 and 20, with one ratio reaching 25. These ratios corroborate once again, that M 82 is dominated by a starburst involving the formation of massive stars, while the stellar population in the centre of IC 342 have been produced in a much more quiescent stage.

6.3 Chemical Distribution and Correlations

The chemical compositions of M 82 and IC 342 has been extensively studied (eg. Mauersberger and Henkel 1991; Sage et al. 1991; Mauersberger et al. 2003; Aladro et al. 2011b, 2015; Ginard et al. 2015). However, few studies have focused on the distributions of the molecules detected in these galaxies (eg. Meier and Turner 2005 fr IC 342). Spatially resolving the chemistry of a galaxy gives insight on the different mechanisms and physical processes that take place, as it reveals the regions where each process is taking place. In order to study the chemical distribution of these galaxies, the intensity distribution of the lines have been plotted (see Chapter 5 Section5.5). Moreover, a Principal Component Analysis (PCA) has been applied on selected lines in order to reveal possible correlations between the molecules, and to uncover differences in the chemistry of distinct regions (see Chapter 5 Section5.6).

6.3.1 Line Intensity Distribution

M 82

In M 82, four distinct emission regions were identified, where most of the line emission originates (see Fig. 5.1). The emission extends to cover 175×350 pc ($10'' \times 20''$) in M 82. The four emission regions and the selected positions for this study are presented in Table. 5.1, and Table. 5.2. With the exception of a few molecules, the intensity of most molecular lines (CCH, HCN, HCO^{+}, HNC, ^{13}CO, and CN) covers all four regions, and includes extended emission also between these regions (see Figs. 5.14, 5.15, and 5.16). These lines indicate the presence of a dense warm gas, with a particularly extended component traced by CCH. However, the intensity distribution of CS, for instance, seems to be concentrated in the north-eastern region (Region A) of M 82, revealing a high density PDR in this region. The isotopologue H^{13}CO^{+} is distributed across the four regions, but shows a more concentrated distribution in the inner parts of these regions, without any extension beyond the four distinct separate regions. This morphology could be due to the fact, that only the peak emission of the weak H^{13}CO^{+} is detected in this study, due to the limited sensitivity of the interferometer. The flux distribution of CH$_3$CCH hints at the regions where the photo-dissociation is most effective. This distribution extends over the four regions, but is mostly concentrated in the northeastern region of the galaxy (Region A). The flux distributions of $C^{18}O$ (Region A, B, C, and D), and the $H\alpha$ recombination lines (mostly in Region C and D) reveal the formation regions of massive stars that are influencing significantly the chemistry of the ISM. On the other hand, the concentrated distribution of NH_2^+ hints at the regions where cosmic-ray ionisation rate is influencing the chemistry, and where the molecular column densities are exceptionally large. These regions traced by NH_2^+ host quiescent gas, that can act like a reservoir for future star formation. In general, the molecular gas in M 82 seems to be mostly chemically homogeneous showing little diversity, with some regions highlighted due to strong PDRs, and/or cosmic-ray affecting the chemistry. This homogeneity is due to a strong PDR presence across the four different regions from the late-type starburst galaxy.

IC 342

Despite differences in the chemical composition between M 82 and IC 342, the distribution of the various molecular species seem to extend over all main regions of the galaxies. The emission extends to cover 80×480 pc ($5'' \times 30''$) in IC 342. The three emission regions and the selected positions for this study are presented in Table. 5.1, and Table. 5.2. In IC 342, CCH, HNCO, HCN, HCO^+, HNC, CS, $C^{18}O$, ^{13}CO, and CN show an extended and strong emission across the three main emission regions (see Figs. 5.17, 5.18, 5.19, 5.20, and 5.21). These molecules are tracing dense gas, with an extended component and are highlighting the regions where massive stars have contributed to the ISM. The HNCO intensity is extended over the three main emission regions in IC 342, and indicates a dominant shock chemistry across the galaxy. This distribution is much more extended than the distribution of other shock tracers such as SiO, HNCO and CH_3OH that cover Region A, and parts of Region B and C of the galaxy, possibly highlighting the regions where shocks are more pronounced. The distributions of HC_3N, HNC, HNCO, and NH_2^+ are similar, highlighting regions with high nitrogen abundance. HC_3N is tracing dense gas in the galaxy, while NH_2^+ highlights regions with strong stellar feedback, a gas reservoir for future star formation, and regions affected by cosmic-rays. The main difference in the intensity distribution between the two galaxies is highlighted by the intensity distribution of $C^{18}O$, which is extended across the emission regions of IC 342 and concentrated in small regions across M 82. Since $C^{18}O$ is a column density tracer, this difference in the distribution indicates that the molecular gas in M 82 resides in well shielded pockets, while in IC 342 such gas is more extended.

6.3.2 Principal Component Analysis

Now that the intensity distribution of the molecular lines has been analysed and the chemistry assigned to physical regions, one can check for correlations or differences between the detected molecules. For this purpose, a Principal Component Analysis (PCA) has been applied, and the results are presented in Chapter 5 Section5.6.

M 82

Seven molecular lines (CCH, HCN, HCO^+, HNC, CS, ^{13}CO, and CN) were selected for the PCA application in M 82. The correlation matrix (see Table 5.18) shows a strong correlation between all molecules except ^{13}CO. The highest correlation coefficient is 0.93 between HCN and HCO^+, followed by a correlation coefficient of 0.92 between HCN and CCH. This correlation indicates that the dense gas tracers HCN, HCO^+, HNC, CS, and CN are very well correlated with CCH, a PDR tracer of extended gas, and thus, that the dense gas and the extended gas co-exist in M 82.

However, the weak correlation between ^{13}CO and the other dense gas tracer molecules, indicates the presence of a lower density molecular gas component that has not been dissociated yet by the strong radiation field in M 82.

The scores of the principal components were plotted in Fig. 5.28, with the tomographs plotted in Fig. 5.29. From the score plots, all molecules have positive scores projected on the first principal component (PC). This is also seen in the map of the first PC. The first PC map looks very similar to the intensity distribution of the molecules tracing the dense gas. This indicates, that on larger scales, the gas in M 82 is mostly homogeneous, where the dense and the extended components of the gas co-exist. However, the second PC scores of ^{13}CO and CN are positive, while the scores of the other molecules are negative. This highlights slight differences between the two groups of molecules. This is reflected in the map of the second PC, in the regions depicted in red and yellow (^{13}CO, and CN), and the blue regions correspond to molecules with negative scores (CCH, HCN, $\mathrm{HCO^+}$, HNC, and CS). These differences highlight regions where each group of molecules is more dominant: ^{13}CO and CN (persumably representing less dense environments) are more dominant in the red and yellow regions (coinciding with Region A and C), while CCH, HCN, $\mathrm{HCO^+}$, HNC, and CS are more dominant in the blue regions. The other PCs (3, 4, 5, 6, and 7) are highlighting further differences in the chemistry of M 82. However, due to their low variance (see Table 5.19), these differences are negligible.

IC 342

For the PCA application in IC 342, five lines were selected (HCN, $\mathrm{HCO^+}$, $\mathrm{C^{18}O}$, HNCO, and ^{13}CO). As seen in the correlation matrix (Table. 5.20), all molecules (with the exception of HNCO) are well correlated with each other. The highest correlation coefficient is 0.99 correlating HCN and $\mathrm{HCO^+}$. The second highest correlation coefficient is 0.92 between ^{13}CO and $\mathrm{C^{18}O}$. HNCO is well correlated with $\mathrm{C^{18}O}$ (0.72) showing that shocks are present across IC 342. This correlation is seen again between ^{13}CO and HNCO (0.60). These correlations might imply that the shocks are caused by winds from massive stellar outflows.

In Fig. 5.30, the scores of the PCs are plotted, and the tomographs are presented in Fig. 5.31. The scores of the first PCs are all positive for all molecules, indicating a first-order correlation between all molecular lines. The map of the first PC shows similarities with the intensity distribution of HCN and most other gas dense tracers. However, the strong differences in the second PC scores show significant differences in the chemistry in the galaxy. The scores of the second PC of HCN, $\mathrm{HCO^+}$, and ^{13}CO are negative, while they are positive for HNCO, and $\mathrm{C^{18}O}$. These scores are reflected in the map of the second PC where the blue region in the centre of IC 342 corresponds to HCN, $\mathrm{HCO^+}$, and ^{13}CO, while the red and yellow regions surrounding the centre correspond to HNCO, and $\mathrm{C^{18}O}$. This shows that the dense hot gas, traced by HCN and $\mathrm{HCO^+}$ is concentrated in the centre of IC 342, while the shocks, and the regions affected by massive stars are mostly distributed at the edge of the galaxy. This result is consistent with the interferometric results presented by Meier and Turner (2005), who also applied PCA, and found a significant correlation between HNCO and $\mathrm{C^{18}O}$, and argued that the shock regions are related to the spiral arms of the galaxy. The data presented here has better angular resolution than the data used by Meier and Turner (2005), allowing for a better spatial distribution imaging and analysis.

Chapter 7

Summary and Outlook

This study focuses on the central molecular zones of two nearby galaxies, M 82 and IC 342. Using data from the Plateau de Bure Interferometer (PdBI) (now known as NOrthern Extended Millimetre Array (NOEMA)) with six antennas in different configurations, the innermost 50 to 200 pc of M 82 and IC 342 were targeted, with a resolution of $2.9''$ and $2.7''$, respectively, covering the 3-mm range from 85.7 to 115.1 GHz. The molecular survey was performed, with the goal to create an unbiased spatially resolved inventory of the molecular content in the CMZ of these two galaxies, and to assign chemical properties to physical regions within these galaxies. Another objective of this thesis is to relate the chemistries to the strong difference in star formation rate between M 82 and IC 342, despite the fact that these galaxies share many similarities.

Four main emission regions were identified in M 82 (Region A, B, C, and D), and three were identified in IC 342 (Region A, B, and C). Images of the molecular line emission, the distribution of their flux density, velocity and width, and the emission spectra from different regions in the galaxy are presented. The obtained spectra were identified, and physical properties such as flux density and column density were extracted. The estimated column densities were compared with the column densities predicted by chemical models. Finally, a principal component analysis (PCA) has been applied on the data in order to uncover correlation between the different molecules, as well as highlight the differences in their spatial distribution.

The results of these analyses can be summarised as follow:

- In M 82, 15 molecular species with different transitions, in addition to three radio Hα recombination lines have been identified, while 22 molecular species have been identified in IC 342.

- The detection of H41α, H40α, and H39α radio recombination lines in M 82, indicates the presence of hot ionised gas in the CMZs of the galaxy (with temperature reaching $\sim 10^4$ K), and traces regions of massive star formation. These lines were not detected in IC 342. They were mainly detected in the south-western regions (C, and D) in M 82, while other PDRs and dense gas tracers where detected in all regions (A, B, C, and D) in the galaxy. This indicates that while star formation is taking place in all regions of the galaxy (as traced by CCH, CH_3CCH, and CN), the young massive stars are mostly formed in regions C and D.

- In M 82, as well as in IC 342, the abundances of the molecules relative to $C^{18}O$ are fairly similar within the different regions of each galaxy, indicating a certain homogeneity in the chemical composition in each galaxy.

- A number of molecules were detected in both galaxies: HCN, HNC, HCO^+, CN, CCH, $H^{13}CO^+$, HC_3N, N_2H^+, CS, CH_3CCH, $C^{18}O$, $C^{17}O$, ^{13}CO.

- However, despite the many similarities in the chemical composition of these two galaxies, there are many differences:

  - Shock tracers like SiO, HNCO, and CH_3OH were detected in IC 342, with an extended flux distribution covering the different regions in the galaxy. This indicates that the gas in IC 342 is heated through mild shocks (traced by HNCO) and violent shocks (traced by SiO). Complex molecules such as CH_3OH, and CH_3CN detected in IC 342 indicate the presence of hot gas. The absence of shock tracers and complex molecules in M 82 is indicative of a strong photo-dissociation radiation which destroys complex molecules.

  - The abundance of CCH relative to $C^{18}O$ in M 82 is two orders of magnitude higher than in IC 342. Its presence in M 82 indicates the presence of strong PDRs with an extended diffuse component of the ISM gas in the galaxy. The lower abundances of CCH suggest the existence of weak and less intense PDRs in IC 342.

  - The high abundance of CH_3CCH and the absence of other complex molecules in M 82 suggest that the chemistry of CH_3CCH is fundamentally different from that of e.g. CH_3CN, and CH_3OH, and possibly related to strong UV-radiation from PDRs. More observations and chemical modelling are required to shed more light on the formation and destruction of CH_3CCH. The much lower abundance of this molecule in IC 342 may be due to the absence of strong photo-dissociation radiation the galaxy. This conclusion is corroborated by the abundance of HNCO and the low abundance of CCH in IC 342, as HNCO is destroyed in the presence of PDRs.

  - The isotopic ratio $\frac{^{18}\mathrm{O}}{^{17}\mathrm{O}}$ derived from $\mathrm{C}^{18}\mathrm{O}$ and $\mathrm{C}^{17}\mathrm{O}$ is between 1 and 3 toward M 82, and between 12 and 25 toward IC 342 (the standard value in the Galactic ISM is 3-5). The abundances of $\mathrm{C}^{17}\mathrm{O}$ and the strong presence of $C^{18}O$ in both galaxies indicate that young massive and intermediate-mass stars have greatly influenced the ISM in this galaxy.

  - The isotopic ratio $\frac{^{12}\mathrm{C}}{^{13}\mathrm{C}}$ derived from ^{13}C-bearing molecules highlighted once more the presence of strong starburst and massive stars in M 82. The ratios found toward IC 342 indicated the presence of intermediate-mass stars.

- Chemical modelling showed that the Model 36 of Viti (2017) best describes the chemistry in M 82 and IC 342. This model indicates that the cosmic-ray ionisation rate in those two galaxies is significantly stronger than it is in the Milky Way, and that the UV-radiation field in these galaxies is very similar to that in the Galaxy. However, a strong UV-radiation field can be diminished by a high visual extinction. The model also showed that M 82 and IC 342 has a dense hot gas with a strong visual extinction ($A_v \sim 50\,\mathrm{mag}$).

- The molecular flux distribution showed that in M 82, the chemistry is mostly homogeneous, showing little diversity between the different regions. Regions traced by the Hα recombination lines highlighted the regions where massive stars are greatly influencing the ISM, and NH_2^+ traces regions where ISM is influenced by comic rays, and quiescent dense gas, that can act as fuel for future star formation. Tracers of dense gas are detected toward all regions of M 82.

- The molecular flux distributions in IC 342 also show a homogeneous chemistry in the different regions of the galaxy. The similar intensity distribution of SiO and HNCO indicated the dominance of shocks across the different regions observed in this galaxy. CH_3OH exhibits a more concentrated distribution highlighting the regions where shocks are more pronounced. The similar distributions of NH_2^+, HC_3N, HNC, and HNCO highlighted the regions where nitrogen is efficiently transformed into molecules.

- The PCA showed strong correlation between tracers of dense gas (HCN, HCO^+, HNC, CS, CN) and tracers of extended diffuse gas (CCH) in M 82. This correlation suggests that the dense component and the extended component of the ISM in M 82 co-exist, even at a high angular resolution. The weak correlation between ^{13}CO and the other molecules can be explained if ^{13}CO traces a diffuse molecular component with a low density while the other molecules trace mainly denser gas.

- The application of PCA in IC 342 shows a strong correlation between the shock tracer HNCO and both $C^{18}O$ and ^{13}CO. These strong correlations indicate that shocks are dominating and are spread across IC 342, and that these shocks are most likely due to winds from massive stars. Moreover, the second PC scores showed a concentration of dense and warm gas (traced by HCN, and HCO^+) in the centre of IC 342, while shocks (traced by HNCO) are mostly dominating the outer regions of the galaxy.

In conclusion, the gas in M 82 is dominated by strong PDRs, heating the dense gas that is still present in the galaxy. This dense gas can act as fuel for future star formation. However, this new generation of star formation can be halted, if the dense gas is continuously being heated by massive stars and PDR regions. On the other hand, the dense gas in IC 342 that is mostly concentrated in the central regions, is heated through mild and violent shocks, possibly preventing an efficient star formation.

Despite the high spatial resolution of the data, molecular lines such as SiO, and HNCO have escaped detection in M 82 due to their low abundance in the central molecular zones of this galaxy, and the limited sensitivity of the PdBI interferometer data used in this study. Molecular surveys targeting the CMZs in M 82 and IC 342 with higher spatial resolution and better sensitivity would offer more details on the molecular line intensity distribution, and the correlation between these molecules. Performing a molecular survey similar to the one presented in this study towards known AGN such as IC 5063 and 4C 12.50. In these two galaxies, the AGN activity seems to influence the surrounding ISM within few kpc of the nucleus (Dasyra et al. 2015, 2016; Oosterloo et al. 2017; Fotopoulou et al. 2019). Such a molecular survey can shed light on the influence of the AGN activity on the chemical composition of the surrounding molecular gas.

Chapter 8

Bibliography

Aalto, S. (2015). Astrochemistry and star formation in nearby galaxies: from galaxy disks to hot nuclei. In *EAS Publications Series*, volume 75 of *EAS Publications Series*, pages 73–80.

Aalto, S., Polatidis, A. G., and Hüttemeister, S., e. a. (2002). CN and HNC line emission in IR luminous galaxies. *Astronomy and Astrophysics*, 381:783–794.

Ables, H. D. (1971). Optical study of nearby galaxies. *Publications of the U.S. Naval Observatory Second Series*, 20.

Adande, G. R. and Ziurys, L. M. (2012). Millimeter-wave Observations of CN and HNC and Their ^{15}N Isotopologues: A New Evaluation of the ^{14}N/^{15}N Ratio across the Galaxy. *Astrophysical Journal*, 744(2):194.

Aladro, R., Martín, S., and Martín-Pintado, J., e. a. (2011a). λ = 1.3 mm and 2 mm molecular line survey towards M 82. *Astronomy and Astrophysics*, 535:A84.

Aladro, R., Martín, S., and Riquelme, e. a. (2015). Lambda = 3 mm line survey of nearby active galaxies. *Astronomy and Astrophysics*, 579:A101.

Aladro, R., Martín-Pintado, J., and Martín, S., e. a. (2011b). CS, HC_3N, and CH_3CCH multi-line analyses toward starburst galaxies. The evolution of cloud structures in the central regions of galaxies. *Astronomy and Astrophysics*, 525:A89.

Aladro, R., Viti, S., and Bayet, E., e. a. (2013). A λ = 3 mm molecular line survey of NGC 1068. Chemical signatures of an AGN environment. *Astronomy and Astrophysics*, 549:A39.

Allen, M. L. and Kronberg, P. P. (1998). Radio Spectra of Selected Compact Sources in the Nucleus of M82. *Astrophysical Journal*, 502:218–228.

Ansdell, M., Williams, J. P., and van der Marel, N., e. a. (2016). ALMA Survey of Lupus Protoplanetary Disks. I. Dust and Gas Masses. *Astrophysical Journal*, 828(1):46.

Ao, Y., Henkel, C., and Menten, K. M., e. a. (2013). The thermal state of molecular clouds in the Galactic center: evidence for non-photon-driven heating. *Astronomy and Astrophysics*, 550:A135.

Appleton, P. N., Davies, R. D., and Stephenson, R. J. (1981). The neutral hydrogen content of the M81/M82 group of galaxies. - I. The observations. *Monthly Notices of the RAS*, 195:327–352.

Avison, A. and George, S. J. (2012). A graphical tool for demonstrating the techniques of radio interferometry. *European Journal of Physics*, 34(1):7–17.

Baan, W. A., Henkel, C., and Loenen, A. F., e. a. (2008). Dense gas in luminous infrared galaxies. *Astronomy and Astrophysics*, 477:747–762.

Bachetti, M., Harrison, F. A., and Walton, D. J., e. a. (2014). An ultraluminous X-ray source powered by an accreting neutron star. *Nature*, 514:202–204.

Bally, J., Stark, A. A., and Wilson, Robert W., e. a. (1988). Galactic Center Molecular Clouds. II. Distribution and Kinematics. *Astrophysical Journal*, 324:223.

Balser, D. S., Wenger, T. V., and Goss, W. M., e. a. (2017). JVLA Observations of IC 342: Probing Star Formation in the Nucleus. *Astrophysical Journal*, 844:73.

Barker, S., de Grijs, R., and Cerviño, M. (2008). Star cluster versus field star formation in the nucleus of the prototype starburst galaxy M 82. *Astronomy and Astrophysics*, 484:711–720.

Bate, M. R. (2000). Recent Advances in Binary Star Formation Using SPH. *ArXiv Astrophysics e-prints*.

Bayet, E., Gerin, M., and Phillips, T. G., e. a. (2006). A survey of submillimeter C and CO lines in nearby galaxies. *Astronomy and Astrophysics*, 460(2):467–485.

Bayet, E., Viti, S., and Williams, D. A., e. a. (2008). Molecular Tracers of High-Mass Star Formation in External Galaxies. *Astrophysical Journal*, 676:978–990.

Bayet, E., Viti, S., and Williams, D. A., e. a. (2009). Molecular Tracers of Pdr-Dominated Galaxies. *Astrophysical Journal*, 696(2):1466–1477.

Bayet, E., Williams, D. A., and Hartquist, T. W., e. a. (2011). Chemistry in cosmic ray dominated regions. *Monthly Notices of the RAS*, 414:1583–1591.

Beck, R. (2015). Magnetic fields in the nearby spiral galaxy IC 342: A multi-frequency radio polarization study. *Astronomy and Astrophysics*, 578:A93.

Beirão, P., Armus, L., and Lehnert, M. D., e. a. (2015). Spatially resolved Spitzer-IRS spectral maps of the superwind in M82. *Monthly Notices of the RAS*, 451:2640–2655.

Belloche, A., Müller, H. S. P., and Menten, K. M., e. a. (2013). Complex organic molecules in the interstellar medium: IRAM 30 m line survey of Sagittarius B2(N) and (M). *Astronomy and Astrophysics*, 559:A47.

Benson, P. J., Caselli, P., and Myers, P. C. (1998). Dense Cores in Dark Clouds. XI. A Survey for N_2H^+, C_3H_2, and CCS. *Astrophysical Journal*, 506(2):743–757.

Bergin, E. A., Goldsmith, P. F., and Snell, R. L., e. a. (1997). The Chemical Composition and Evolution of Giant Molecular Cloud Cores: A Comparison of Observation and Theory. *Astrophysical Journal*, 482:285–297.

Bergin, E. A., Melnick, G. J., and Neufeld, D. A. (1998). The Postshock Chemical Lifetimes of Outflow Tracers and a Possible New Mechanism to Produce Water Ice Mantles. *Astrophysical Journal*, 499:777–792.

Boker, T., Forster-Schreiber, N. M., and Genzel, R. (1997). Near-Infrared Imaging Spectroscopy of IC 342: Evolution of a Bar-Driven Central Starburst. *Astronomical Journal*, 114:1883.

Böker, T., van der Marel, R. P., and Vacca, W. D. (1999). CO Band Head Spectroscopy of IC 342: Mass and Age of the Nuclear Star Cluster. *Astronomical Journal*, 118:831–842.

Bregman, J. N., Cox, C. V., and Tomisaka, K. (1993). X-Ray Emission from the Starburst Galaxy IC 342. *Astrophysical Journal*, 415:L79.

Brouillet, N., Baudry, A., and Combes, F., e. a. (1991). M81 - CO content and interaction with its companion galaxies. *Astronomy and Astrophysics*, 242:35–48.

Brunthaler, A., Martí-Vidal, I., and Menten, K. M., e. a. (2010). VLBI observations of SN 2008iz. I. Expansion velocity and limits on anisotropic expansion. *Astronomy and Astrophysics*, 516:A27.

Brunthaler, A., Menten, K. M., and Reid, M. J., e. a. (2009). Discovery of a bright radio transient in M 82: a new radio supernova? *Astronomy and Astrophysics*, 499:L17–L20.

Buat, V. (2015). How to measure star formation rates in galaxies? In Biernacka, M., Bajan, K., Stachowski, G., and Flin, P., editors, *Introduction to Cosmology*, pages 134–141.

Caldwell, S. and Chang, P. (2018). The accelerating pace of star formation. *Monthly Notices of the RAS*, 474:4818–4823.

Carruthers, G. R. (1970). Rocket Observation of Interstellar Molecular Hydrogen. *Astrophysical Journal, Letters*, 161:L81.

Chiang, Y.-K. and Kong, A. K. H. (2011). The long-term variability of the X-ray sources in M82. *Monthly Notices of the RAS*, 414:1329–1338.

Chin, Y.-N., Henkel, C., and Whiteoak, J. B., e. a. (1996). Interstellar sulfur isotopes and stellar oxygen burning. *Astronomy and Astrophysics*, 305:960.

Chlewicki, G. and Mayo Greenberg, J. (1984). General constraints on the average scattering characteristics of interstellar grains in the ultraviolet. *Monthly Notices of the RAS*, 210:791–801.

Combes, F. (1991). Distribution of CO in the Milky Way. *Annual Review of Astron and Astrophys*, 29:195–237.

Crosthwaite, L. P., Turner, J. L., and Ho, P. T. P. (2000). Structure in the Neutral Hydrogen Disk of the Spiral Galaxy IC 342. *Astronomical Journal*, 119:1720–1736.

Curran, S. J., Aalto, S., and Booth, R. S. (2000). Dense molecular gas in Seyfert galaxies. *Astronomy and Astrophysics, Supplement*, 141:193–209.

Cyganowski, C. J., Brogan, C. L., and Hunter, T. R., e. a. (2017). Simultaneous low- and high-mass star formation in a massive protocluster: ALMA observations of G11.92-0.61. *Monthly Notices of the RAS*, 468:3694–3708.

Dahmen, G., Huttemeister, S., and Wilson, T. L., e. a. (1998). Molecular gas in the Galactic center region. II. Gas mass and N_, = H_2/I_(̂12)CO conversion based on a C(̂18)O(J = 1 -> 0) survey. *Astronomy and Astrophysics*, 331:959–976.

Dame, T. M., Hartmann, D., and Thaddeus, P. (2001). The Milky Way in Molecular Clouds: A New Complete CO Survey. *Astrophysical Journal*, 547(2):792–813.

Dasyra, K. M., Bostrom, A. C., Combes, F., and Vlahakis, N. (2015). A Radio Jet Drives a Molecular and Atomic Gas Outflow in Multiple Regions within One Square Kiloparsec of the Nucleus of the nearby Galaxy IC5063. *Astrophysical Journal*, 815(1):34.

Dasyra, K. M., Combes, F., Oosterloo, T., Oonk, J. B. R., Morganti, R., Salomé, P., and Vlahakis, N. (2016). ALMA reveals optically thin, highly excited CO gas in the jet-driven winds of the galaxy IC 5063. *Astronomy and Astrophysics*, 595:L7.

de Grijs, R., O'Connell, R. W., and Becker, G. D., e. a. (2000). Supernova Remnants in the Fossil Starburst in M82. *Astronomical Journal*, 119:681–687.

de Grijs, R., O'Connell, R. W., and Gallagher, III, J. S. (2001). The Fossil Starburst in M82. *Astronomical Journal*, 121:768–792.

de Grijs, R., Parmentier, G., and Lamers, H. J. G. L. M. (2005). The initial mass distribution of the M82 star cluster system. *Monthly Notices of the RAS*, 364:1054–1062.

de Vaucouleurs, G., de Vaucouleurs, A., and Corwin, Jr., H. G. (1976). *Second reference catalogue of bright galaxies. Containing information on 4,364 galaxies with references to papers published between 1964 and 1975.*

de Vaucouleurs, G., de Vaucouleurs, A., and Corwin, Jr., H. G. e. a. (1991). *Third Reference Catalogue of Bright Galaxies. Volume I: Explanations and references. Volume II: Data for galaxies between* 0^h *and* 12^h*. Volume III: Data for galaxies between* 12^h *and* 24^h*.*

de Vicente, P., Martin-Pintado, J., and Wilson, T. L. (1996). A Hot Ring in the SGR B2 Molecular Cloud. In Gredel, R., editor, *The Galactic Center*, volume 102 of *Astronomical Society of the Pacific Conference Series*, page 64.

Dekel, A. and Birnboim, Y. (2006). Galaxy bimodality due to cold flows and shock heating. *Monthly Notices of the RAS*, 368(1):2–20.

Dickinson, D. F., Rodriguez Kuiper, E. N., and Dinger, A. S. C., e. a. (1980). Shock enhancement of HCO/+/. *Astrophysical Journal, Letters*, 237:L43–L45.

Divakara Mayya, Y. and Carrasco, L. (2009). M82 as a Galaxy: Morphology and Stellar Content of the Disk and Halo. *arXiv e-prints*.

Downes, D., Radford, S. J. E., and Guilloteau, S., e. a. (1992). HCN in the center of the galaxy IC 342. *Astronomy and Astrophysics*, 262:424–432.

Draine, B. T. (2011). *Physics of the Interstellar and Intergalactic Medium*.

Draine, B. T. and McKee, C. F. (1993). Theory of interstellar shocks. *Annual Review of Astronomy and Astrophysics*, 31:373–432.

Eckart, A. and Genzel, R. (1997). Stellar proper motions in the central 0.1 PC of the Galaxy. *Monthy Notices of the RAS*, 284:576–598.

Event Horizon Telescope Collaboration, Akiyama, K., Alberdi, A., and Alef, Walter, e. a. (2019). First M87 Event Horizon Telescope Results. I. The Shadow of the Supermassive Black Hole. *Astrophysical Journal, Letters*, 875(1):L1.

Farquhar, P. R. A., Millar, T. J., and Herbst, E. (1994). The effect of varying cosmic ray ionization rates on dark cloud chemistry. *Monthly Notices of the RAS*, 269:641–648.

Favre, C., Ceccarelli, C., and Lefloch, B., e. a. (2016). Complex organic molecules toward low-mass and high-mass star forming regions. In Reylé, C., Richard, J., Cambrésy, L., Deleuil, M., Pécontal, E., Tresse, L., and Vauglin, I., editors, *SF2A-2016: Proceedings of the Annual meeting of the French Society of Astronomy and Astrophysics*, pages 321–325.

Federman, S. R., Glassgold, A. E., and Kwan, J. (1979). Atomic to molecular hydrogen transition in interstellar clouds. *Astrophysical Journal*, 227:466–473.

Ferrière, K., Gillard, W., and Jean, P. (2007). Spatial distribution of interstellar gas in the innermost 3 kpc of our galaxy. *Astronomy and Astrophysics*, 467(2):611–627.

Ferrière, K. M. (2001). The interstellar environment of our galaxy. *Reviews of Modern Physics*, 73(4):1031–1066.

Fossey, S. J., Cooke, B., and Pollack, G., e. a. (2014). Supernova 2014J in M82 = Psn J09554214+6940260. *Central Bureau Electronic Telegrams*, 3792.

Fotopoulou, C. M., Dasyra, K. M., Combes, F., Salomé, P., and Papachristou, M. (2019). Complex molecular gas kinematics in the inner 5 kpc of 4C12.50 as seen by ALMA. *Astronomy and Astrophysics*, 629:A30.

Fuente, A., García-Burillo, S., and Gerin, M., e. a. (2005). Photon-dominated Chemistry in the Nucleus of M82: Widespread HOC^+ Emission in the Inner 650 Parsec Disk. *Astrophysical Journal, Letters*, 619:L155–L158.

Fuente, A., García-Burillo, S., and Usero, A., e. a. (2008). On the chemistry and distribution of HOC^+ in M 82. More evidence for extensive PDRs. *Astronomy and Astrophysics*, 492:675–684.

Gaffney, N. I., Lester, D. F., and Telesco, C. M. (1993). The stellar velocity dispersion in the nucleus of M82. *Astrophysical Journal, Letters*, 407:L57–L60.

García-Burillo, S., Combes, F., and Usero, A., e. a. (2014). Molecular line emission in NGC 1068 imaged with ALMA. I. An AGN-driven outflow in the dense molecular gas. *Astronomy and Astrophysics*, 567:A125.

García-Burillo, S., Martín-Pintado, J., and Fuente, A., e. a. (2001). SiO Chimneys and Supershells in M82. *Astrophysical Journal, Letters*, 563:L27–L30.

Gerhard, O. (2002). The Galactic Bar. In Da Costa, G. S., Sadler, E. M., and Jerjen, H., editors, *The Dynamics, Structure, History of Galaxies: A Workshop in Honour of Professor Ken Freeman*, volume 273 of *Astronomical Society of the Pacific Conference Series*, page 73.

Ghez, A. M., Klein, B. L., and Morris, M., e. a. (1998). High Proper-Motion Stars in the Vicinity of Sagittarius A*: Evidence for a Supermassive Black Hole at the Center of Our Galaxy. *Astrophysical Journal*, 509:678–686.

Ghez, A. M., Salim, S., and Weinberg, N. N., e. a. (2008). Measuring Distance and Properties of the Milky Way's Central Supermassive Black Hole with Stellar Orbits. *Astrophysical Journal*, 689:1044–1062.

Ginard, D., Fuente, A., and García-Burillo, S., e. a. (2015). Chemical footprint of star formation feedback in M 82 on scales of ˜100 pc. *Astronomy and Astrophysics*, 578:A49.

Goicoechea, J. R., Pety, J., and Cuadrado, Sara, e. a. (2016). Compression and ablation of the photo-irradiated molecular cloud the Orion Bar. *Nature*, 537(7619):207–209.

Goicoechea, J. R., Pety, J., and Gerin, M., e. a. (2006). Low sulfur depletion in the Horsehead PDR. *Astronomy and Astrophysics*, 456:565–580.

Gottesman, S. T. and Weliachew, L. (1977). A high angular resolution study of the neutral hydrogen in the IRR II galaxy M82. *Astrophysical Journal*, 211:47–61.

Götz, M., Downes, D., and Greve, A., e. a. (1990). Structure of the disk of M82. *Astronomy and Astrophysics*, 240:52–69.

Greaves, J. S. and Church, S. E. (1996). Photodissociation and the CN:HCN ratio: observations of a 'Third Bar' in OMC1. *Monthly Notices of the RAS*, 283:1179–1183.

Greco, J. P., Martini, P., and Thompson, T. A. (2012). Measurement of the Mass and Stellar Population Distribution in M82 with the LBT. *Astrophysical Journal*, 757:24.

Gurzadyan, V. G., De Paolis, F., and Nucita, A. A., e. a. (2015). Planck view of the M 82 galaxy. *Astronomy and Astrophysics*, 582:A77.

Harju, J. (1989). HCN and HNC observations towards dark clouds. *Astronomy and Astrophysics*, 219:293–302.

Heikkila, A., Johansson, L. E. B., and Olofsson, H. (1998). The Cˆ18O/Cˆ17O ratio in the Large Magellanic Cloud. *Astronomy and Astrophysics*, 332:493–502.

Helfer, T. T. and Blitz, L. (1993). Dense Gas in the Bulges of External Galaxies. *Astrophysical Journal*, 419:86.

Henkel, C., Chin, Y.-N., and Mauersberger, R., e. a. (1998). Dense gas in nearby galaxies. XI. Interstellar ˆ12C/ˆ13C ratios in the central regions of M82 and IC342. *Astronomy and Astrophysics*, 329:443–450.

Herbst, E. and Leung, C. M. (1989). Gas Phase Production of Complex Hydrocarbons, Cyanopolyynes, and Related Compounds in Dense Interstellar Clouds. *Astrophysical Journal, Supplement*, 69:271.

Heyer, M. and Dame, T. M. (2015). Molecular Clouds in the Milky Way. *Annual Review of Astron and Astrophys*, 53:583–629.

Heyminck, S., Graf, U. U., and Güsten, R., e. a. (2012). GREAT: the SOFIA high-frequency heterodyne instrument. *Astronomy and Astrophysics*, 542:L1.

Hirota, T., Yamamoto, S., and Mikami, H., e. a. (1998). Abundances of HCN and HNC in Dark Cloud Cores. *Astrophysical Journal*, 503:717–728.

Ho, L. C., Filippenko, A. V., and Sargent, W. L. W. (1997). A Search for “Dwarf” Seyfert Nuclei. III. Spectroscopic Parameters and Properties of the Host Galaxies. *Astrophysical Journal, Supplement*, 112:315–390.

Hodge, P. W. and Kennicutt, Jr., R. C. (1983). An atlas of H II regions in 125 galaxies. *Astronomical Journal*, 88:296–328.

Högbom, J. A. (1974). Aperture Synthesis with a Non-Regular Distribution of Interferometer Baselines. *Astronomy and Astrophysics, Supplement*, 15:417.

Holdship, J., Viti, S., and Jiménez-Serra, I., e. a. (2017). UCLCHEM: A Gas-grain Chemical Code for Clouds, Cores, and C-Shocks. *Astronomical Journal*, 154:38.

Hollenbach, D. and McKee, C. F. (1989). Molecule Formation and Infrared Emission in Fast Interstellar Shocks. III. Results for J Shocks in Molecular Clouds. *Astrophysical Journal*, 342:306.

Hollenbach, D. J. and Tielens, A. G. G. M. (1997). Dense Photodissociation Regions (PDRs). *Annual Review of Astron and Astrophys*, 35:179–216.

Hollenbach, D. J., Werner, M. W., and Salpeter, E. E. (1971). Molecular Hydrogen in H i Regions. *Astrophysical Journal*, 163:165.

Hubble, E. P. (1936). *Realm of the Nebulae*.

Huettemeister, S., Dahmen, G., Mauersberger, R., Henkel, C., Wilson, T. L., and Martin-Pintado, J. (1998). Molecular gas in the Galactic center region. III. Probing shocks in molecular cores. *Astronomy and Astrophysics*, 334:646–658.

Hüttemeister, S., Henkel, C., and Mauersberger, R., e. a. (1995). Dense gas in nearby galaxies. IX. A survey for HNC. *Astronomy and Astrophysics*, 295:571.

Hüttemeister, S., Mauersberger, R., and Henkel, C. (1997). Dense gas in nearby galaxies. X. H_2_CO and CH_3_OH: molecular abundances and physical conditions. *Astronomy and Astrophysics*, 326:59–68.

Hutton, S., Ferreras, I., and Wu, K., e. a. (2014). A panchromatic analysis of starburst galaxy M82: probing the dust properties. *Monthly Notices of the RAS*, 440:150–160.

Ichikawa, T., van Driel, W., and Aoki, T., e. a. (1994). The peculiar dust distribution of M82. *Astrophysical Journal*, 433:645–647.

Ichikawa, T., Yanagisawa, K., and Itoh, N., e. a. (1995). Near-Infrared Wide-Field Surface Photometry of M82. *Astronomical Journal*, 109:2038.

Imanishi, M., Nakanishi, K., and Kuno, N., e. a. (2004). Near-Infrared and Millimeter Constraints on the Nuclear Energy Source of the Infrared-luminous Galaxy NGC 4418. *Astronomical Journal*, 128:2037–2047.

Imanishi, M., Nakanishi, K., and Tamura, Y., e. a. (2007). Millimeter Interferometric HCN(1-0) and HCO^+(1-0) Observations of Luminous Infrared Galaxies. *Astronomical Journal*, 134:2366–2384.

Irvine, W. M., Goldsmith, P. F., and Hjalmarson, A. (1987). Chemical abundances in molecular clouds. In Hollenbach, D. J. and Thronson, Jr., H. A., editors, *Interstellar Processes*, volume 134 of *Astrophysics and Space Science Library*, pages 561–609.

Ishizuki, S., Kawabe, R., and Ishiguro, M., e. a. (1990). A molecular gas bar fuelling starburst activity in galaxy IC342. *Nature*, 344:224–226.

Izumi, T., Kohno, K., and Aalto, S., e. a. (2016). Submillimeter-HCN Diagram for Energy Diagnostics in the Centers of Galaxies. *Astrophysical Journal*, 818:42.

Izumi, T., Kohno, K., and Martín, S., e. a. (2013). Submillimeter ALMA Observations of the Dense Gas in the Low-Luminosity Type-1 Active Nucleus of NGC 1097. *Publications of the ASJ*, 65:100.

Jarrett, T. H., Chester, T., and Cutri, R., e. a. (2003). The 2MASS Large Galaxy Atlas. *Astronomical Journal*, 125:525–554.

Jiménez-Serra, I., Caselli, P., and Martín-Pintado, J., e. a. (2008). Parametrization of C-shocks. Evolution of the sputtering of grains. *Astronomy and Astrophysics*, 482(2):549–559.

Jolliffe, I. T. (2002). *Principal component analysis*. Principal Component Analysis (Second Edition.), New York, NY: Springer New York.

Jones, P. A., Burton, M. G., and Cunningham, M. R., e. a. (2013). Spectral imaging of the central molecular zone in multiple 7-mm molecular lines. *Monthly Notices of the RAS*, 433:221–234.

Kaaret, P., Prestwich, A. H., and Zezas, A., e. a. (2001). Chandra High-Resolution Camera observations of the luminous X-ray source in the starburst galaxy M82. *Monthly Notices of the RAS*, 321:L29–L32.

Kafle, P. R., Sharma, S., and Lewis, G. F., e. a. (2014). On the Shoulders of Giants: Properties of the Stellar Halo and the Milky Way Mass Distribution. *Astrophysical Journal*, 794:59.

Kamenetzky, J., Glenn, J., and Rangwala, N., e. a. (2012). Herschel-SPIRE Imaging Spectroscopy of Molecular Gas in M82. *Astrophyscial Journal*, 753(1):70.

Karachentsev, I. D. (2005). The Local Group and Other Neighboring Galaxy Groups. *Astronomical Journal*, 129:178–188.

Karachentsev, I. D. and Kashibadze, O. G. (2006). Masses of the local group and of the M81 group estimated from distortions in the local velocity field. *Astrophysics*, 49:3–18.

Karachentsev, I. D. and Tikhonov, N. A. (1993). Photometric distances to the nearby galaxies IC 10, IC 342, and UGCA 86, visible through the Milky Way. *Astronomy and Astrophysics, Supplement*, 100:227–235.

Klessen, R. S. (2011). Star Formation in Molecular Clouds. In Charbonnel, C. and Montmerle, T., editors, *EAS Publications Series*, volume 51 of *EAS Publications Series*, pages 133–167.

Knapp, G. R., Leighton, R. B., and Wannier, P. G., e. a. (1980). Detection of the CO J = 2-1 line in M82 and IC 342. *Astrophysical Journal*, 240:60–64.

Kohno, K., Kawabe, R., and Tosaki, T., e. a. (1996). Aperture Synthesis CO and HCN Observationsof M51: Dense Molecular Disk around a Low-Luminosity Active Galactic Nucleus. *Astrophysical Journal, Letters*, 461:L29.

Kohno, K., Matsushita, S., and Vila-Vilaró, B., e. a. (2001). Dense Molecular Gas and Star Formation in Nearby Seyfert Galaxies. In Knapen, J. H., Beckman, J. E., Shlosman, I., and Mahoney, T. J., editors, *The Central Kiloparsec of Starbursts and AGN: The La Palma Connection*, volume 249 of *Astronomical Society of the Pacific Conference Series*, page 672.

Kong, A. K. H. (2003). XMM-Newton observation of the X-ray point source population of the starburst galaxy IC 342. *Monthly Notices of the RAS*, 346:265–272.

Krips, M., Neri, R., and García-Burillo, S., e. a. (2008). A Multi-Transition HCN and HCO^+ Study of 12 Nearby Active Galaxies: Active Galactic Nucleus versus Starburst Environments. *Astrophysical Journal*, 677:262–275.

Krolik, J. H. and Kallman, T. R. (1983). X-ray ionization and the Orion molecular cloud. *Astrophysical Journal*, 267:610–624.

Kubota, A., Done, C., and Makishima, K. (2002). Another interpretation of the power-law-type spectrum of an ultraluminous compact X-ray source in IC 342. *Monthly Notices of the RAS*, 337:L11–L15.

Ladd, E. F. (2004). On the Relative Abundance of $C^{18}O$ and $C^{17}O$ in the Taurus Molecular Cloud. *Astrophysical Journal*, 610:320–328.

Larson, R. B. (1996). Star Formation and Galactic Evolution. In Kunth, D., Guiderdoni, B., Heydari-Malayeri, M., and Thuan, T. X., editors, *The Interplay Between Massive Star Formation, the ISM and Galaxy Evolution*, page 3.

Lebrón, M., Mangum, J. G., and Mauersberger, R., e. a. (2011). Dense gas in nearby galaxies. XVII. The distribution of ammonia in NGC 253, Maffei 2, and IC 342. *Astronomy and Astrophysics*, 534:A56.

Lee, E. J., Chang, P., and Murray, N. (2015). Time-varying Dynamical Star Formation Rate. *Astrophysical Journal*, 800:49.

Lee, H.-H., Bettens, R. P. A., and Herbst, E. (1996). Fractional abundances of molecules in dense interstellar clouds: A compendium of recent model results. *Astronomy and Astrophysics, Supplement*, 119:111–114.

Lepp, S. and Dalgarno, A. (1996). X-ray-induced chemistry of interstellar clouds. *Astronomy and Astrophysics*, 306:L21–L24.

Leurini, S., Schisano, E., and Pillai, T., e. a. (2019). Characterising the high-mass star forming filament G351.776-0.527 with Herschel and APEX dust continuum and gas observations. *Astronomy and Astrophysics*, 621:A130.

Li, A. and Greenberg, J. M. (1997). A unified model of interstellar dust. *Astronomy and Astrophysics*, 323:566–584.

Li, J., Wang, J., and Gu, Q., e. a. (2012). Large-scale Kinematics, Astrochemistry, and Magnetic Field Studies of Massive Star-forming Regions through HC_3N, HNC, and C_2H Mappings. *Astrophysical Journal*, 745:47.

Lis, D. C., Serabyn, E., and Zylka, R., e. a. (2001). Quiescent Giant Molecular Cloud Cores in the Galactic Center. *Astrophysical Journal*, 550(2):761–777.

Liu, T., Kim, K.-T., and Juvela, Mika, e. a. (2018). The TOP-SCOPE Survey of Planck Galactic Cold Clumps: Survey Overview and Results of an Exemplar Source, PGCC G26.53+0.17. *Astrophysical Journal, Supplement*, 234(2):28.

Lo, N., Cunningham, M. R., and Jones, P. A., e. a. (2009). Molecular line mapping of the giant molecular cloud associated with RCW 106 - III. Multimolecular line mapping. *Monthly Notices of the RAS*, 395:1021–1042.

Loenen, A. F., Spaans, M., and Baan, W. A., e. a. (2008). Mechanical feedback in the molecular ISM of luminous IR galaxies. *Astronomy and Astrophysics*, 488:L5–L8.

Loenen, A. F., van der Werf, P. P., and Güsten, R., e. a. (2010). Excitation of the molecular gas in the nuclear region of M 82. *Astronomy and Astrophysics*, 521:L2.

Loiseau, N., Nakai, N., and Sofue, Y., e. a. (1990). (C-12)O (J = 2-1) mapping of M 82. *Astronomy and Astrophysics*, 228:331–340.

Lomax, O., Whitworth, A. P., and Hubber, D. A., e. a. (2015). Simulations of star formation in Ophiuchus - II. Multiplicity. *Monthly Notices of the RAS*, 447(2):1550–1564.

López-Corredoira, M., Allende Prieto, C., and Garzón, F., e. a. (2018). Disk stars in the Milky Way detected beyond 25 kpc from its center. *Astronomy and Astrophysics*, 612:L8.

Lovas, F. J. (1992). Recommended Rest Frequencies for Observed Interstellar Molecular Microwave Transitions–1991 Revision. *Journal of Physical and Chemical Reference Data*, 21:181–272.

Lovas, F. J. (2004). NIST Recommended Rest Frequencies for Observed Interstellar Molecular Microwave Transitions-2002 Revision. *Journal of Physical and Chemical Reference Data*, 33:177–355.

Lynds, C. R. and Sandage, A. R. (1963). Evidence for an Explosion in the Center of the Galaxy M82. *Astrophysical Journal*, 137:1005.

Mak, D. S. Y., Pun, C. S. J., and Kong, A. K. H. (2008). High-Resolution X-Ray Imaging of the Center of IC 342. *Astrophysical Journal*, 686:995–1006.

Mak, D. S. Y., Pun, C. S. J., and Kong, A. K. H. (2011). Long-term X-ray Variability Study of IC342 from XMM-Newton Observations. *Astrophysical Journal*, 728:10.

Mao, R.-Q., Schulz, A., and Henkel, Christian, e. a. (2010). An Extragalactic ^{12}CO J = 3-2 Survey with the Heinrich Hertz Telescope. *Astrophysical Journal*, 724:1336–1356.

Martin, R. N. and Ho, P. T. P. (1986). Hot Gas in the Nucleus of IC 342. *Astrophysical Journal*, 308:L7.

Martín, S., Aladro, R., and Martín-Pintado, J., e. a. (2010). A large ^{12}C/^{13}C isotopic ratio in M 82 and NGC 253. *Astronomy and Astrophysics*, 522:A62.

Martín, S., Kohno, K., and Izumi, T., e. a. (2015). Multimolecule ALMA observations toward the Seyfert 1 galaxy NGC 1097. *Astronomy and Astrophysics*, 573:A116.

Martín, S., Martín-Pintado, J., and Blanco-Sánchez, C., e. a. (2019a). Spectral Line Identification and Modelling (SLIM) in the MAdrid Data CUBe Analysis (MADCUBA) package: An interactive software for data cube analysis. *arXiv e-prints*, page arXiv:1909.02147.

Martín, S., Martín-Pintado, J., and Mauersberger, R., e. a. (2005). Sulfur Chemistry and Isotopic Ratios in the Starburst Galaxy NGC 253. *Astrophysical Journal*, 620:210–216.

Martín, S., Martín-Pintado, J., and Mauersberger, R. (2006a). Methanol detection in M 82. *Astronomy and Astrophysics*, 450:L13–L16.

Martín, S., Martín-Pintado, J., and Mauersberger, R. (2009). HNCO Abundances in Galaxies: Tracing the Evolutionary State of Starbursts. *Astrophysical Journal*, 694:610–617.

Martín, S., Mauersberger, R., and Martín-Pintado, J., e. a. (2006b). A 2 Millimeter Spectral Line Survey of the Starburst Galaxy NGC 253. *Astrophysical Journal, Supplement*, 164:450–476.

Martín, S., Muller, S., and Henkel, C., e. a. (2019b). Spatially resolved carbon and oxygen isotopic ratios in NGC 253 using optically thin tracers. *Astronomy and Astrophysics*, 624:A125.

Matsumoto, H. and Tsuru, T. G. (1999a). X-Ray Evidence of an AGN in M82. *Publications of the Astronomical Society of Japan*, 51:321–331.

Matsumoto, H. and Tsuru, T. G. (1999b). Erratum: X-Ray Evidence of an AGN in M82. *Publications of the Astronomical Society of Japan*, 51:567–567.

Mauersberger, R. and Henkel, C. (1989). Dense gas in nearby galaxies. I - Distribution, kinematics and multilevel studies of CS. *Astronomy and Astrophysics*, 223:79–88.

Mauersberger, R. and Henkel, C. (1991). Dense gas in nearby galaxies. IV - The detection of N2H(+), SiO, H(C-13)O(+), H(C-13)N, and HN(C-13). *Astronomy and Astrophysics*, 245:457–466.

Mauersberger, R. and Henkel, C. (1993). Dense Gas in Galactic Nuclei. In Klare, G., editor, *Reviews in Modern Astronomy*, volume 6 of *Reviews in Modern Astronomy*, pages 69–102.

Mauersberger, R., Henkel, C., and Sage, L. J. (1990). Dense gas in nearby galaxies. III - HC3N as an extragalactic density probe. *Astronomy and Astrophysics*, 236:63–68.

Mauersberger, R., Henkel, C., and Walmsley, C. M., e. a. (1991). Dense gas in nearby galaxies. V - Multilevel studies of CH3CCH and CH3CN. *Astronomy and Astrophysics*, 247:307–314.

Mauersberger, R., Henkel, C., and Walsh, W., e. a. (1999). Dense gas in nearby galaxies . XII. A survey for CO J=3-2 emission. *Astronomy and Astrophysics*, 341:256–263.

Mauersberger, R., Henkel, C., and Weiß, A., e. a. (2003). Dense gas in nearby galaxies. XV. Hot ammonia in NGC 253, Maffei 2 and IC 342. *Astronomy and Astrophysics*, 403:561–571.

Mauersberger, R., Henkel, C., and Wilson, T. L., e. a. (1986). Hot ammonia in the Galaxy. *Astronomy and Astrophysics*, 162:199–210.

Mayya, Y. D., Carrasco, L., and Luna, A. (2005). The Discovery of Spiral Arms in the Starburst Galaxy M82. *Astrophysical Journal, Letters*, 628:L33–L36.

McCall, M. L. (1989). H II Regions, Extinction, and IC 342: A New View of the Galactic Neighborhood. *Astronomical Journal*, 97:1341.

McDonald, A. R., Muxlow, T. W. B., and Wills, K. A., e. a. (2002). A parsec-scale study of the 5/15-GHz spectral indices of the compact radio sources in M82. *Monthly Notices of the RAS*, 334:912–924.

McGinn, M. T., Sellgren, K., and Becklin, E. E., e. a. (1989). Stellar Kinematics in the Galactic Center. *Astrophysical Journal*, 338:824.

McKeith, C. D., Greve, A., and Downes, D., e. a. (1995). The outflow in the halo of M 82. *Astronomy and Astrophysics*, 293:703–709.

McMillan, P. J. (2017). The mass distribution and gravitational potential of the Milky Way. *Monthly Notices of the RAS*, 465:76–94.

Meier, D. S. (2014). The nucleus of IC 342 as a potential twin of the Galactic center. In Sjouwerman, L. O., Lang, C. C., and Ott, J., editors, *The Galactic Center: Feeding and Feedback in a Normal Galactic Nucleus*, volume 303 of *IAU Symposium*, pages 66–68.

Meier, D. S. and Turner, J. L. (2005). Spatially Resolved Chemistry in Nearby Galaxies. I. The Center of IC 342. *Astrophysical Journal*, 618:259–280.

Meier, D. S., Turner, J. L., and Hurt, R. L. (2000). Molecular Gas Properties of the Starburst Nucleus of IC 342: High-Resolution ^{13}CO (2-1) Imaging. *Astrophysical Journal*, 531:200–209.

Meijerink, R. and Spaans, M. (2005). Diagnostics of irradiated gas in galaxy nuclei. I. A far-ultraviolet and X-ray dominated region code. *Astronomy and Astrophysics*, 436:397–409.

Meijerink, R., Spaans, M., and Kamp, I., e. a. (2013). Tracing the Physical Conditions in Active Galactic Nuclei with Time-Dependent Chemistry. *Journal of Physical Chemistry A*, 117:9593–9604.

Mendoza, E., Bronfman, L., and Duronea, N. U., e. a. (2018). G331.512-0.103: An Interstellar Laboratory for Molecular Synthesis. I. The Ortho-to-para Ratios for CH_3OH and CH_3CN. *Astrophysical Journal*, 853:152.

Meyer, B. S. (1994). The r-, s-, and p-Processes in Nucleosynthesis. *Annual Review of Astron and Astrophys*, 32:153–190.

Montero-Castaño, M., Herrnstein, R. M., and Ho, P. T. P. (2006). Hot Molecular Gas in the Nuclear Region of IC 342. *Astrophysical Journal*, 646:919–928.

Morris, M. and Serabyn, E. (1996). The Galactic Center Environment. *Annual Review of Astron and Astrophys*, 34:645–702.

Mühle, S., Seaquist, E. R., and Henkel, C. (2007). Formaldehyde as a Tracer of Extragalactic Molecular Gas. I. Para-H_2CO Emission from M82. *Astrophysical Journal*, 671(2):1579–1590.

Müller, H. S. P., Schlöder, F., and Stutzki, J., e. a. (2005). The Cologne Database for Molecular Spectroscopy, CDMS: a useful tool for astronomers and spectroscopists. *Journal of Molecular Structure*, 742:215–227.

Müller, H. S. P., Thorwirth, S., and Roth, D. A., e. a. (2001). The Cologne Database for Molecular Spectroscopy, CDMS. *Astronomy and Astrophysics*, 370:L49–L52.

Muller, S., Guélin, M., and Dumke, M., e. a. (2006). Probing isotopic ratios at z = 0.89: molecular line absorption in front of the quasar PKS 1830-211. *Astronomy and Astrophysics*, 458(2):417–426.

Nagao, T., Maiolino, R., and Marconi, A., e. a. (2011). Metallicity diagnostics with infrared fine-structure lines. *Astronomy and Astrophysics*, 526:A149.

Nakajima, T., Takano, S., and Kohno, e. a. (2018). A molecular line survey toward the nearby galaxies NGC 1068, NGC 253, and IC 342 at 3 mm with the Nobeyama 45 m radio telescope: Impact of an AGN on 1 kpc scale molecular abundances. *Publications of the Astronomical Society of Japan*, 70:7.

Nakanishi, H. and Sofue, Y. (2003). Three-Dimensional Distribution of the ISM in the Milky Way Galaxy: I. The H I Disk. *Publications of the Astronomical Society of Japan*, 55:191–202.

Neininger, N., Guelin, M., and Klein, U., e. a. (1998). (13) CO at the centre of M 82. *Astronomy and Astrophysics*, 339:737–744.

Newton, K. (1980). Neutral hydrogen in IC 342. II - The detailed structure. *Monthly Notices of the RAS*, 191:615–630.

Nilsson, A., Hjalmarson, Å., and Bergman, P., e. a. (2000). SO and CS observations of molecular clouds. II. Analysis and modelling of the abundance ratios - probing O_2/CO with SO/CS? *Astronomy and Astrophysics*, 358:257–275.

O'Connell, R. W. (2002). Super Star Clusters in M82. In Geisler, D. P., Grebel, E. K., and Minniti, D., editors, *Extragalactic Star Clusters*, volume 207 of *IAU Symposium*, page 383.

O'Connell, R. W. and Mangano, J. J. (1978). The central regions of M82. *Astrophysical Journal*, 221:62–65.

Ohyama, Y., Taniguchi, Y., and Iye, M., e. a. (2002). Decomposition of the Superwind in M 82. *Publications of the ASJ*, 54:891–898.

Oosterloo, T., Raymond Oonk, J. B., Morganti, R., Combes, F., Dasyra, K., Salomé, P., Vlahakis, N., and Tadhunter, C. (2017). Properties of the molecular gas in the fast outflow in the Seyfert galaxy IC 5063. *Astronomy and Astrophysics*, 608:A38.

Ortiz, R. and Lepine, J. R. D. (1993). A model of the galaxy for predicting star counts in the infrared. *Astronomy and Astrophysics*, 279:90–106.

Paglione, T. A. D. and Abrahams, R. D. (2012). Properties of nearby Starburst Galaxies Based on their Diffuse Gamma-Ray Emission. *Astrophysical Journal*, 755(2):106.

Palla, F. and Stahler, S. W. (2002). Star Formation in Space and Time: Taurus-Auriga. *Astrophysical Journal*, 581:1194–1203.

Pan, H.-A., Kuno, N., and Hirota, A. (2014). Environmental dependence of star formation law in the disk and center of IC 342. *Publications of the Astronomical Society of Japan*, 66:27.

Pasham, D. R., Strohmayer, T. E., and Mushotzky, R. F. (2014). A 400-solar-mass black hole in the galaxy M82. *Nature*, 513:74–76.

Pfeffer, D. N., Kovetz, E. D., and Kamionkowski, M. (2017). Ultrahigh-energy cosmic ray hotspots from tidal disruption events. *Monthly Notices of the RAS*, 466:2922–2926.

Pickett, H. M., Poynter, R. L., and Cohen, E. A., e. a. (1998). Submillimeter, millimeter and microwave spectral line catalog. *Journal of Quantitiative Spectroscopy and Radiative Transfer*, 60:883–890.

Reina, C. and Tarenghi, M. (1973). X-ray Absorption and Optical Extinction in Interstellar Space. *Astronomy and Astrophysics*, 26:257.

Remijan, A., Sutton, E. C., and Snyder, L. E., e. a. (2004). High-Resolution Observations of Methyl Cyanide (CH_3CN) toward the Hot Core Regions W51e1/e2. *Astrophysical Journal*, 606:917–928.

Riaz, R., Bovino, S., and Vanaverbeke, S., e. a. (2018). The formation of protostellar binaries in primordial minihaloes. *Monthly Notices of the RAS*, 479(1):667–686.

Rigopoulou, D., Hurley, P. D., and Swinyard, B. M., e. a. (2013). Herschel-SPIRE Fourier transform spectroscopy of the nearby spiral galaxy IC 342. *Monthly Notices of the RAS*, 434:2051–2059.

Riquelme, D., Amo-Baladrón, M. A., and Martín-Pintado, J., e. a. (2018). Footpoints of the giant molecular loops in the Galactic center region. *Astronomy and Astrophysics*, 613:A42.

Riquelme, D., Bronfman, L., and Mauersberger, R., e. a. (2010). A survey of the Galactic center region in HCO^+, $H^{13}CO^+$, and SiO. *Astronomy and Astrophysics*, 523:A45.

Robitaille, T. P. and Whitney, B. A. (2010). The Galactic star formation rate as seen by the Spitzer Space Telescope. *Highlights of Astronomy*, 15:799–799.

Rodríguez-Franco, A., Martin-Pintado, J., and Fuente, A. (1998). CN emission in Orion. The high density interface between the H II region and the molecular cloud. *Astronomy and Astrophysics*, 329:1097–1110.

Röllig, T. L., Becklin, E. E., and Evans, N. J., e. a. (2009). The Science Vision for the Stratospheric Observatory for Infrared Astronomy (SOFIA). *ArXiv e-prints*.

Sage, L. J., Mauersberger, R., and Henkel, C. (1991). Extragalactic O-18/O-17 ratios and star formation - High-mass stars preferred in starburst systems? *Astronomy and Astrophysics*, 249:31–35.

Sage, L. J. and Solomon, P. M. (1991). Star formation and the molecular content of IC 342. *Astrophysical Journal*, 380:392–402.

Saha, A., Claver, J., and Hoessel, J. G. (2002). Cepheids and Long-Period Variables in IC 342. *Astronomical Journal*, 124:839–861.

Sakamoto, K., Okumura, S. K., and Ishizuki, S., e. a. (1999). Bar-driven Transport of Molecular Gas to Galactic Centers and Its Consequences. *Astrophysical Journal*, 525:691–701.

Salak, D., Nakai, N., and Miyamoto, Y., e. a. (2013). Large-Field CO(J = 1-0) Observations of the Starburst Galaxy M 82. *Publications of the ASJ*, 65:66.

Sandage, A. and Brucato, R. (1979). The Las Campanas survey of bright southern galaxies. II - New classifications for 153 systems. *Astronomical Journal*, 84:472–496.

Sandage, A. and Tammann, G. A. (1974). Steps toward the Hubble constant. IV - Distances to 39 galaxies in the general field leading to a calibration of the galaxy luminosity classes and a first hint of the value of H sub 0. *Astrophysical Journal*, 194:559–568.

Satyapal, S., Watson, D. M., and Pipher, J. L., e. a. (1997). The Intrinsic Properties of the Stellar Clusters in the M82 Starburst Complex: Propagating Star Formation? *Astrophysical Journal*, 483:148–160.

Schilke, P., Walmsley, C. M., and Pineau Des Forets, G., e. a. (1992). A study of HCN, HNC and their isotopomers in OMC-1. I - Abundances and chemistry. *Astronomy and Astrophysics*, 256:595–612.

Schinnerer, E., Böker, T., and Meier, D. S. (2003). Molecular Gas and the Nuclear Star Cluster in IC 342: Sufficient Inflow for Recurring Star Formation Events? *Astrophysical Journal*, 591:L115–L118.

Schulz, A., Güsten, R., and Köster, B., e. a. (2001). The nucleus of the nearby galaxy IC 342. *Astronomy and Astrophysics*, 371:25–36.

Scoville, N., Lee, N., and Vanden Bout, P., e. a. (2017). Evolution of Interstellar Medium, Star Formation, and Accretion at High Redshift. *Astrophysical Journal*, 837:150.

Seaquist, E. R. and Frayer, D. T. (2000). The Distribution of HCO^+ J=4-3 and HCN J=4-3 in the Nuclear Region of M82. *Astrophysical Journal*, 540(2):765–770.

Seaquist, E. R., Frayer, D. T., and Frail, D. A. (1997). OH Satellite Line Masers and an Active Galactic Nucleus Candidate in M82. *Astrophysical Journal*, 487:L131–L134.

Shen, J. and Lo, K. Y. (1995). Locations of strabursts in M82. *Astrophysical Journal, Letters*, 445:L99–L103.

Shopbell, P. L. and Bland-Hawthorn, J. (1998). The Asymmetric Wind in M82. *Astrophysical Journal*, 493:129–153.

Sigalotti, L. D. G., Cruz, F., and Gabbasov, Ruslan, e. a. (2018). From Large-scale to Protostellar Disk Fragmentation into Close Binary Stars. *Astrophysical Journals*, 857(1):40.

Snell, R., Kurtz, S., and Marr, J. (2019). *Fundamentals of Radio Astronomy: Astrophysics*. Series in Astronomy and Astrophysics. CRC Press.

Sodroski, T. J., Odegard, N., and Dwek, E., e. a. (1995). The Ratio of H 2 Column Density to 12CO Intensity in the Vicinity of the Galactic Center. *Astrophysical Journal*, 452:262.

Sofue, Y., Tomita, A., and Tutui, Y., e. a. (1998a). Nuclear-to-Disk Rotation Curves of Galaxies in the Hα and [N $\{$II$\}$] Emission Lines. *Publications of the ASJ*, 50:427–463.

Sokolovsky, K. V., Voytsik, P. A., and Alakoz, Alexei V., e. a. (2014). RadioAstron Space-VLBI observation of SN2014J and the possible AGN in M82. *The Astronomer's Telegram*, 6197:1.

Solomon, P. M., Downes, D., and Radford, S. J. E. (1992). Dense molecular gas and starbursts in ultraluminous galaxies. *Astrophysical Journal, Letters*, 387:L55–L59.

Spaans, M. and Meijerink, R. (2007). CO^+ in M82: A Consequence of Irradiation by X-Rays. *Astrophysical Journal*, 664:L23–L26.

Stecher, T. P. and Williams, D. A. (1967). Photodestruction of Hydrogen Molecules in H I Regions. *Astrophysical Journal*, 149:L29.

Steppe, H., Mauersberger, R., and Schulz, A., e. a. (1990). First sub-mm spectral line observations with the IRAM 30-m telescope - A CO (J = 3-2) map of IC 342. *Astronomy and Astrophysics*, 233:410–416.

Stoyan, R., Binnewies, S., and Friedrich, S., e. a. (2008). *Atlas of the Messier Objects: Highlights of the Deep Sky*.

Telesco, C. M., Campins, H., and Joy, M., e. a. (1991). Infrared mapping of M82 - A starburst in an edge-on barred galaxy. *Astrophysical Journal*, 369:135–146.

Temi, P., Marcum, P. M., and Young, E., e. a. (2014). The SOFIA Observatory at the Start of Routine Science Operations: Mission Capabilities and Performance. *Astrophysical Journal, Supplement*, 212:24.

Tielens, A. G. G. M. (2005). *The Physics and Chemistry of the Interstellar Medium*.

Tikhonov, N. A. and Galazutdinova, O. A. (2010). Distance to the galaxy IC 342. *Astronomy Letters*, 36:167–174.

Turner, B. E. (1989). A molecular line survey of Sagittarius B2 and Orion-KL from 70 to 115 GHz. I - The observational data. *Astrophysical Journal, Supplement*, 70:539–622.

Turner, B. E. (1995a). The Physics and Chemistry of Small Molecular Clouds in the Galactic Plane. III. NH 3. *Astrophysical Journal*, 444:708.

Turner, B. E. (1998a). The Physics and Chemistry of Small Translucent Molecular Clouds. X. SiO. *Astrophysical Journal*, 495:804–820.

Turner, B. E. (1998b). The Physics and Chemistry of Small Translucent Molecular Clouds. XI. Methanol. *Astrophysical Journal*, 501:731–748.

Turner, B. E., Lee, H.-H., and Herbst, E. (1998). The Physics and Chemistry of Small Translucent Molecular Clouds. IX. Acetylenic Chemistry. *Astrophysical Journal, Supplement*, 115:91–118.

Turner, B. E., Pirogov, L., and Minh, Y. C. (1997). The Physics and Chemistry of Small Translucent Molecular Clouds. VIII. HCN and HNC. *Astrophysical Journal*, 483:235–261.

Turner, B. E., Terzieva, R., and Herbst, E. (1999). The Physics and Chemistry of Small Translucent Molecular Clouds. XII. More Complex Species Explainable by Gas-Phase Processes. *Astrophysical Journal*, 518:699–732.

Turner, J. L. and Hurt, R. L. (1992). 13CO in IC 342: Evidence for a Spiral Density Wave in the Nucleus. *Astrophysical Journal*, 384:72.

Ungerechts, H., Bergin, E. A., and Goldsmith, P. F., e. a. (1997). Chemical and Physical Gradients along the OMC-1 Ridge. *Astrophysical Journal*, 482:245–266.

Usero, A., García-Burillo, S., and Martín-Pintado, J., e. a. (2006). Large-scale molecular shocks in galaxies: the SiO interferometer map of IC 342. *Astronomy and Astrophysics*, 448:457–470.

van der Plas, G., Ménard, F., and Gonzalez, J. F., e. a. (2019). ALMA study of the HD 100453 AB system and the tidal interaction of the companion with the disk. *Astronomy and Astrophysics*, 624:A33.

van der Tak, F. F. S., Aalto, S., and Meijerink, R. (2008). Detection of extragalactic H_3Oˆ+. *Astronomy and Astrophysics*, 477:L5–L8.

van der Wiel, M. H. D., van der Tak, F. F. S., and Ossenkopf, V., e. a. (2009). Chemical stratification in the Orion Bar: JCMT Spectral Legacy Survey observations. *Astronomy and Astrophysics*, 498:161–165.

Viti, S. (2017). Molecular transitions as probes of the physical conditions of extragalactic environments. *Astronomy and Astrophysics*, 607:A118.

Viti, S., García-Burillo, S., and Fuente, A., e. a. (2014). Molecular line emission in NGC 1068 imaged with ALMA. II. The chemistry of the dense molecular gas. *Astronomy and Astrophysics*, 570:A28.

Walter, F., Weiss, A., and Scoville, N. (2001). OVRO Observations of Molecular Streamers around M 82. In *American Astronomical Society Meeting Abstracts*, volume 33 of *Bulletin of the American Astronomical Society*, page 1372.

Walter, F., Weiss, A., and Scoville, N. (2002). Molecular Gas in M82: Resolving the Outflow and Streamers. *Astrophysical Journal, Letters*, 580:L21–L25.

Wang, M., Henkel, C., and Chin, Y.-N., e. a. (2004). Dense gas in nearby galaxies. XVI. The nuclear starburst environment in NGC 4945. *Astronomy and Astrophysics*, 422:883–905.

Weiß, A., Neininger, N., and Henkel, C., e. a. (2001). First Detection of Ammonia in M82. *Astrophysical Journal*, 554(2):L143–L146.

White, G. J., Ellison, B., and Claude, S., e. a. (1994). CO and CI maps of the starburst galaxy M 82. *Astronomy and Astrophysics*, 284:L23–L26.

Williams, D. A. and Viti, S. (2005). Meeting Report: Recent advances in star-formation studies. *Astronomy and Geophysics*, 46(1):1.30–1.31.

Wills, K. A., Das, M., and Pedlar, A., e. a. (2000). Modelling the bar in the centre of the starburst galaxy M82. *Monthly Notices of the RAS*, 316:33–48.

Wills, K. A., Pedlar, A., and Muxlow, T. W. B., e. a. (1997). Low-frequency observations of supernova remnants in M82. *Monthly Notices of the RAS*, 291:517.

Wills, K. A., Pedlar, A., and Muxlow, T. W. B., e. a. (1999). A possible active galactic nucleus in M82? *Monthly Notices of the RAS*, 305:680–684.

Wilson, T. L., Rohlfs, K., and Huttemeister, S. (2012). *Tools of Radio Astronomy, 5th edition*.

Wilson, T. L. and Rood, R. (1994). Abundances in the Interstellar Medium. *Annual Review of Astron and Astrophys*, 32:191–226.

Womack, M., Ziurys, L. M., and Wyckoff, S. (1992). Estimates of N 2 Abundances in Dense Molecular Clouds. *Astrophysical Journal*, 393:188.

Wootten, A. (1981). A dense molecular cloud impacted by the W28 supernova remnant. *Astrophysical Journal*, 245:105–114.

Wouterloot, J. G. A., Brand, J., and Henkel, C. (2005). The interstellar $C^{18}O/C^{17}O$ ratio in the solar neighbourhood: The ρ Ophiuchus cloud. *Astronomy and Astrophysics*, 430:549–560.

Wu, P.-F., Tully, R. B., and Rizzi, Luca, e. a. (2014). Infrared Tip of the Red Giant Branch and Distances to the Maffei/IC 342 Group. *Astronomical Journal*, 148:7.

Wu, Y.-Z., Zhang, W., and Zhao, Y.-H. (2019). The evolution and dependence of the local mass-metallicity relation. *Monthly Notices of the RAS*, 486(4):5310–5322.

Yuan, J., Li, J.-Z., and Wu, Yuefang, e. a. (2018). High-mass Star Formation through Filamentary Collapse and Clump-fed Accretion in G22. *Astrophysical Journal*, 852(1):12.

Yun, M. S., Ho, P. T. P., and Lo, K. Y. (1993). H I streamers around M82 - Tidally disrupted outer gas disk. *Astrophysical Journal, Letters*, 411:L17–L20.

Yun, M. S., Ho, P. T. P., and Lo, K. Y. (1994). A high-resolution image of atomic hydrogen in the M81 group of galaxies. *Nature*, 372:530–532.

Yusef-Zadeh, F., Cotton, B., and Wardle, M., e. a. (2017). ALMA and VLA Observations: Evidence for Ongoing Low-mass Star Formation near Sgr A. *Monthly Notices of the RAS*, 467:922–927.

Zhang, J. S., Sun, L. L., and Riquelme, D., e. a. (2015). Isotopic Ratios of $^{18}O/^{17}O$ in the Galactic Central Region. *Astrophysical Journal, Supplement*, 219:28.

Zhang, Q., Ho, P. T. P., and Ohashi, N. (1998). Dynamical Collapse in W51 Massive Cores: CS (3-2) and CH_3CN Observations. *Astrophysical Journal*, 494:636–656.

Zhu, H., Tian, W., Li, A., and Zhang, M. (2017). The gas-to-extinction ratio and the gas distribution in the Galaxy. *Monthly Notices of the RAS*, 471(3):3494–3528.

Zhu, Z., Hartmann, L., and Gammie, C. (2010). Long-term Evolution of Protostellar and Protoplanetary Disks. II. Layered Accretion with Infall. *Astrophysical Journal*, 713(2):1143–1158.

Zinchenko, I., Henkel, C., and Mao, R. Q. (2000). HNCO in massive galactic dense cores. *Astronomy and Astrophysics*, 361:1079–1094.

Ziurys, L. M., Friberg, P., and Irvine, W. M. (1989). Interstellar SiO as a Tracer of High-Temperature Chemistry. *Astrophysical Journal*, 343:201.

Appendix A

Continuum Images

A.1 M 82

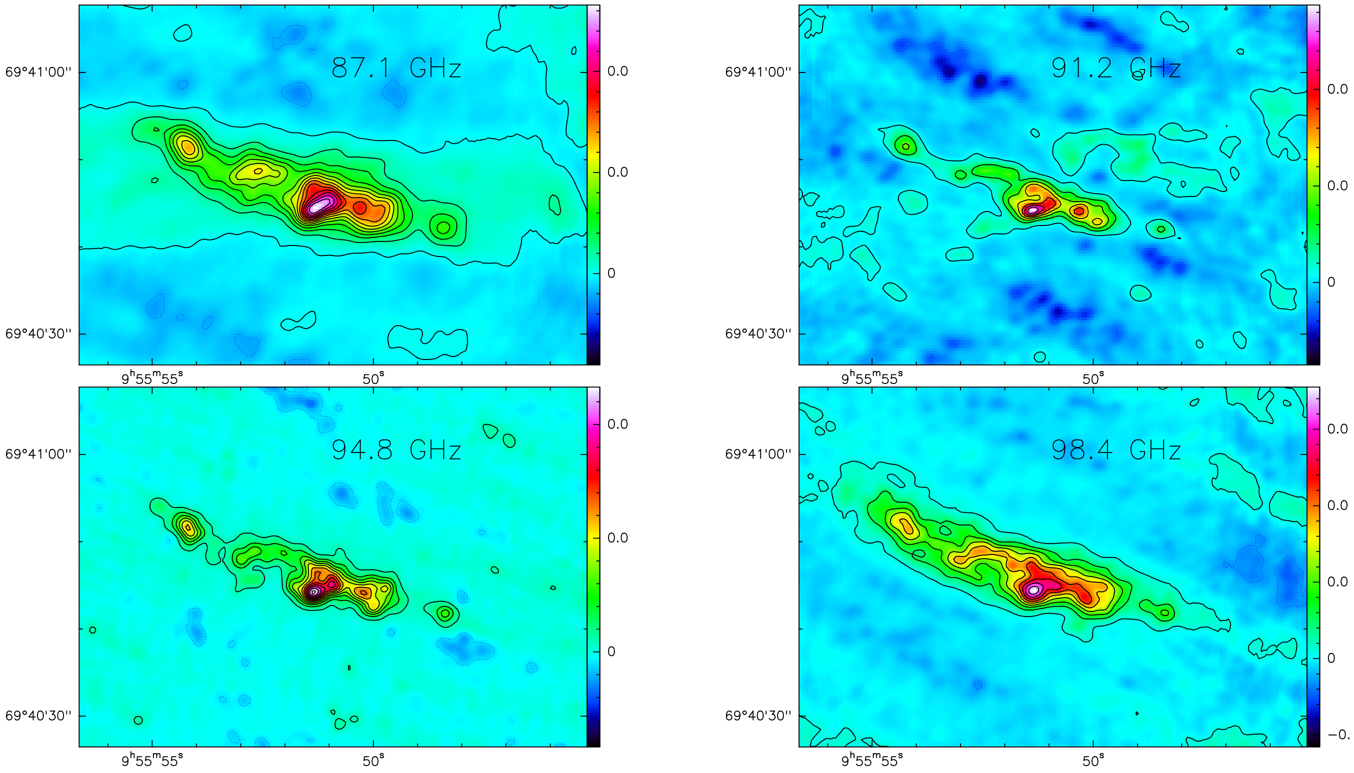

Figure A.1: M 82 continuum at 87.1 GHz (top left) (contour levels from -10 to 26 mJy beam^{-1} km s^{-1} by steps of 2 mJy beam^{-1} km s^{-1}), at 91.2 GHz (top right) (contour levels from -1.5 to 14 mJy beam^{-1} km s^{-1} by steps of 2 mJy beam^{-1} km s^{-1}), at 94.8 GHz (bottom left) (contour levels from -1.5 to 12 mJy beam^{-1} km s^{-1} by steps of 1 mJy beam^{-1} km s^{-1}), at 98.4 GHz (bottom right) (contour levels from -3.5 to 18 mJy beam^{-1} km s^{-1} by steps of 2 mJy beam^{-1} km s^{-1})

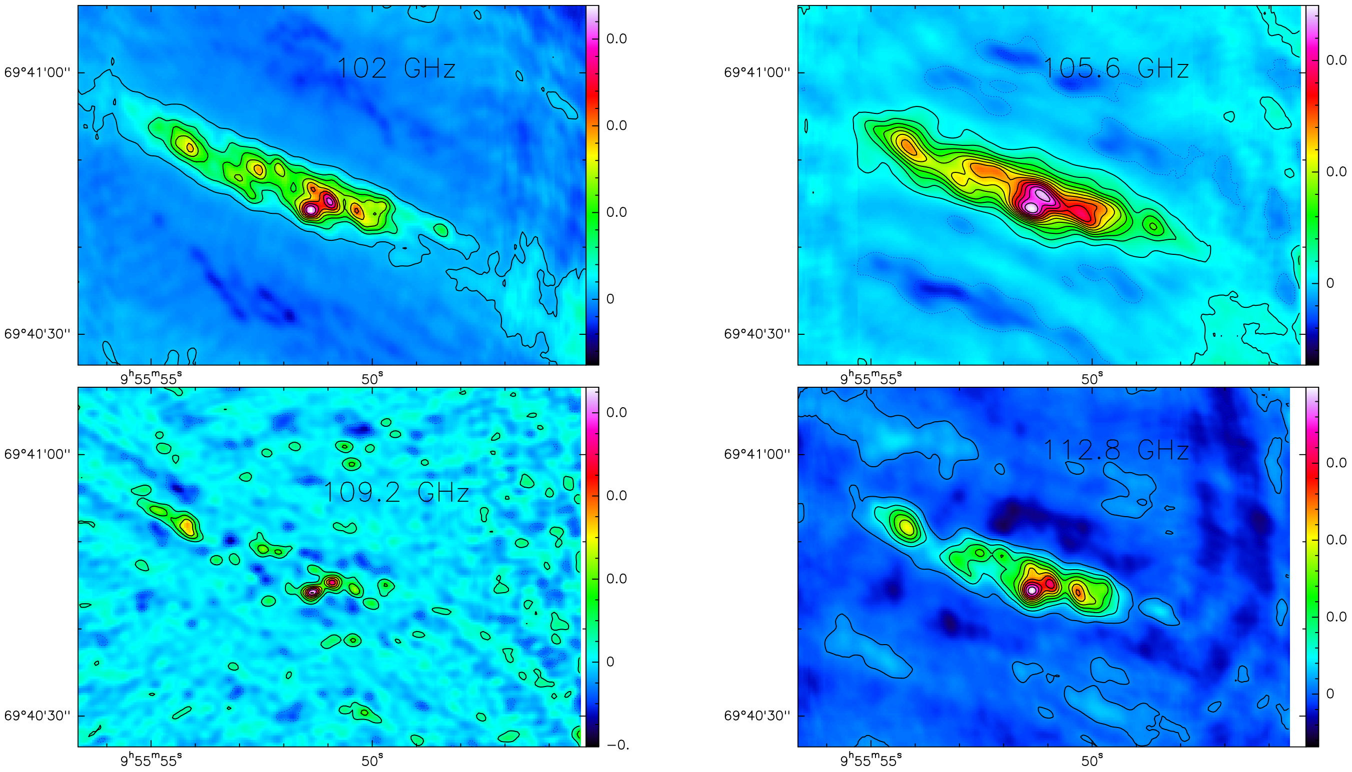

Figure A.2: M 82 continuum at 102 GHz (top left) (contour levels from -4 to 16 mJy beam^{-1} km s^{-1} by steps of 2 mJy beam^{-1} km s^{-1}), at 105.6 GHz (top right) (contour levels from -3 to 24 mJy beam^{-1} km s^{-1} by steps of 2 mJy beam^{-1} km s^{-1}), at 109.2 GHz (bottom left) (contour levels from -0.5 to 7 mJy beam^{-1} km s^{-1} by steps of 1 mJy beam^{-1} km s^{-1}), and at 112.8 GHz (bottom right) (contour levels from -1.5 to 20 mJy beam^{-1} km s^{-1} by steps of 2 mJy beam^{-1} km s^{-1})

A.2 IC 342

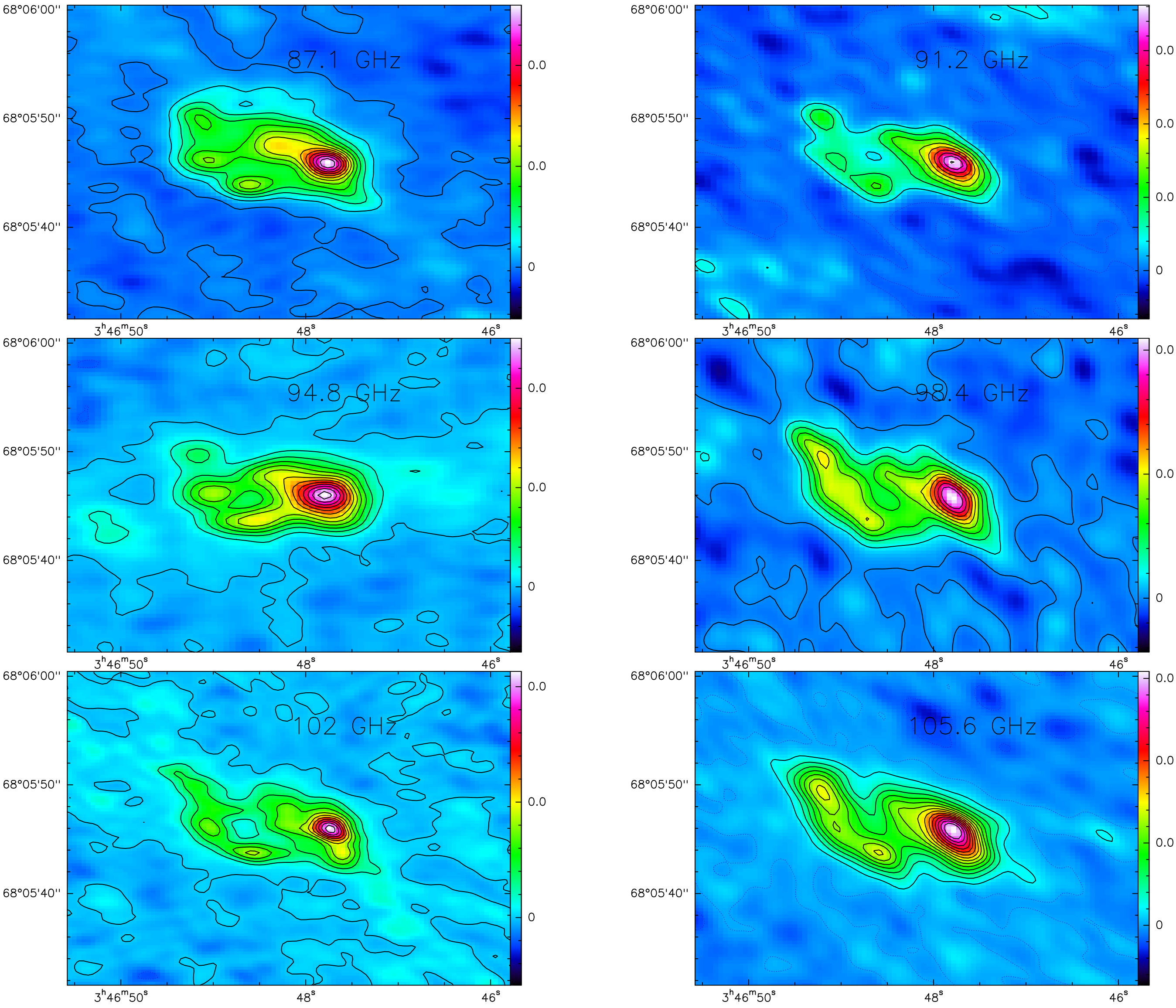

Figure A.3: IC 342 continuum at 87.1 GHz (top left) (contour levels from -0.6 to 2.6 mJy beam^{-1} km s^{-1} by steps of 0.2 mJy beam^{-1} km s^{-1}), at 91.2 GHz (top right) (contour levels from -0.01 to 1.8 mJy beam^{-1} km s^{-1} by steps of 0.2 mJy beam^{-1} km s^{-1}), at 94.8 GHz (middle left) (contour levels from -0.6 to 2.6 mJy beam^{-1} km s^{-1} by steps of 0.2 mJy beam^{-1} km s^{-1}), at 98.4 GHz (middle right) (contour levels from -0.4 to 2 mJy beam^{-1} km s^{-1} by steps of 0.2 mJy beam^{-1} km s^{-1}), at 102 GHz (bottom left) (contour levels from -0.6 to 2.2 mJy beam^{-1} km s^{-1} by steps of 0.2 mJy beam^{-1} km s^{-1}), and at 105.6 GHz (bottom right) (contour levels from -0.8 to 3 mJy beam^{-1} km s^{-1} by steps of 0.2 mJy beam^{-1} km s^{-1})

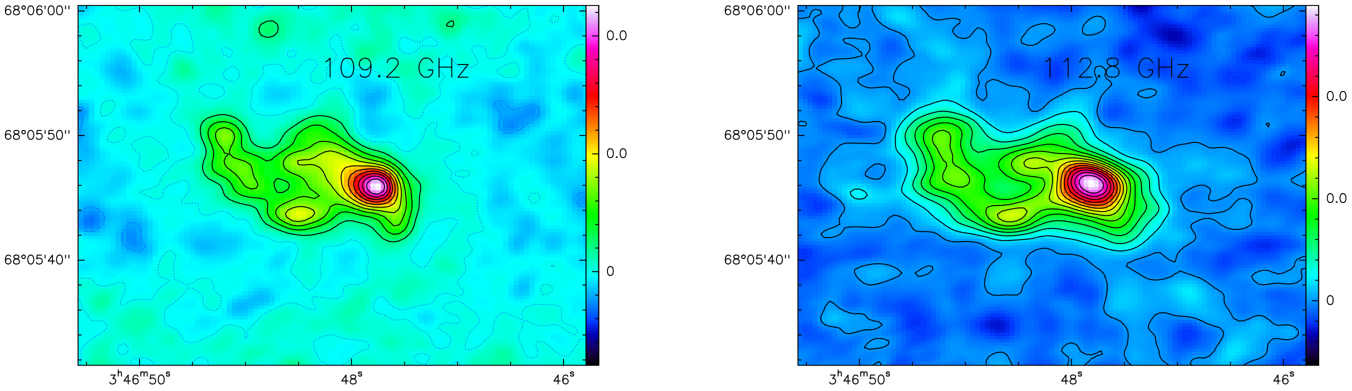

Figure A.4: IC 342 continuum at 109.2 GHz (left) (contour levels from -0.8 to 2.2 $\mathrm{mJy\,beam^{-1}\,km\,s^{-1}}$ by steps of 0.2 $\mathrm{mJy\,beam^{-1}\,km\,s^{-1}}$), and at 112.8 GHz (right) (contour levels from -0.6 to 2.8 $\mathrm{mJy\,beam^{-1}\,km\,s^{-1}}$ by steps of 0.2 $\mathrm{mJy\,beam^{-1}\,km\,s^{-1}}$)

Appendix B

Spectra

B.1 M 82

B.1.1 Complete M 82 spectra

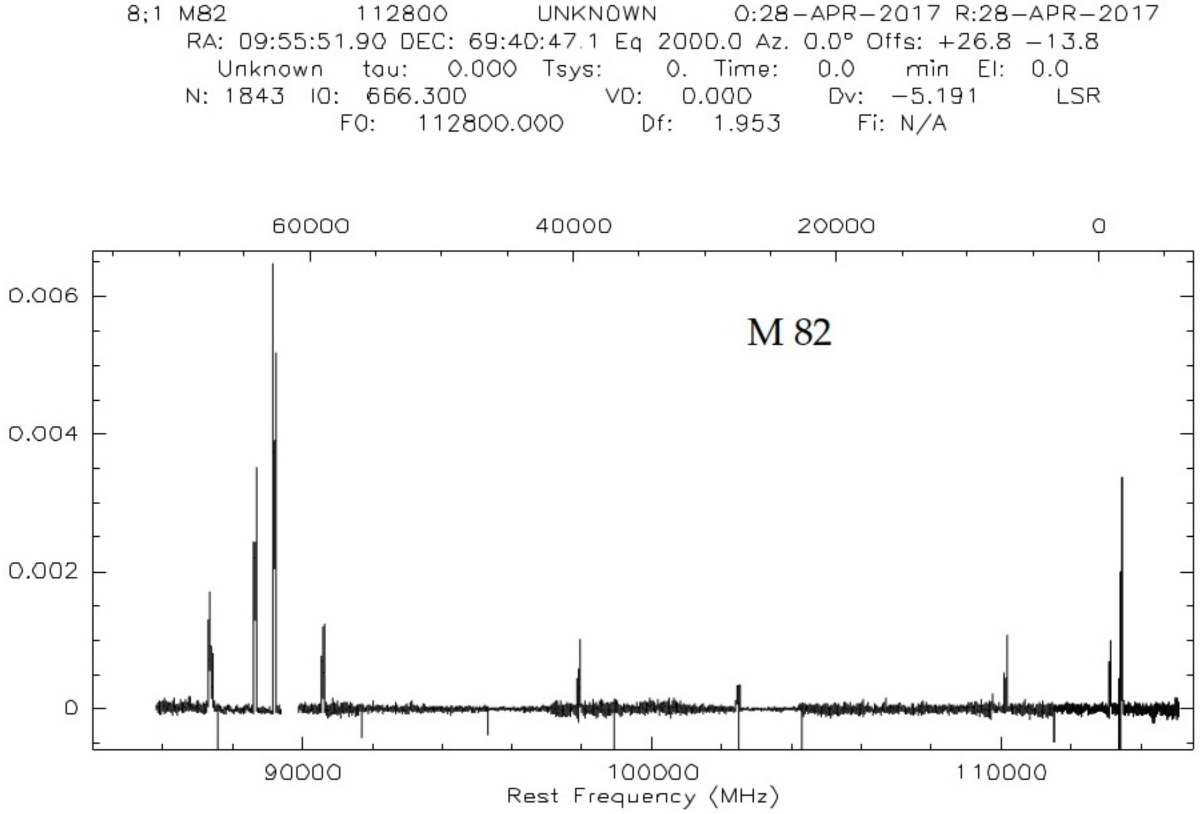

```
8;1 M82          112800       UNKNOWN      0:28-APR-2017 R:28-APR-2017
   RA: 09:55:51.90 DEC: 69:40:47.1 Eq 2000.0 Az. 0.0° Offs: +26.8 -13.8
     Unknown    tau:    0.000  Tsys:      0.  Time:    0.0    min  El:  0.0
   N: 1843  I0:  666.300            V0:    0.000       Dv:  -5.191      LSR
                 F0:   112800.000      Df:    1.953      Fi: N/A
```

Figure B.1: M 82 complete spectrum from 85.7 to 115.1 GHz. The bottom x-axis shows the frequency in MHz and the top x-axis shows the velocity in km s^{-1}. The y-axis shows the flux density in Jy.

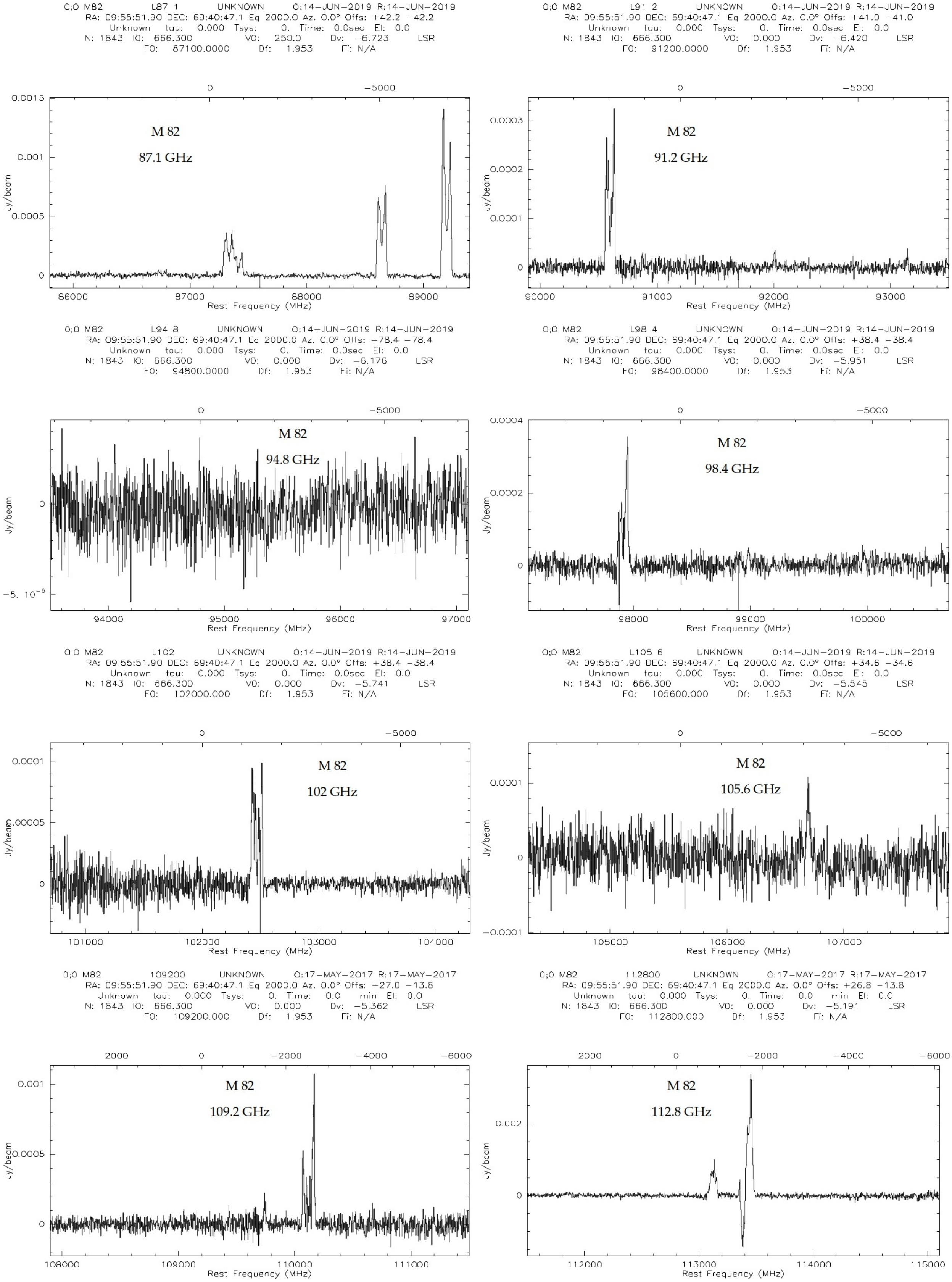

Figure B.2: M 82 spectrum at 87.1, 91.2, 94.8, 98.4, 102, 105.6, 109.2, and 112.8 GHz. The axes are the same as in Fig. B.1.

B.1.2 M 82 spectra in Position A

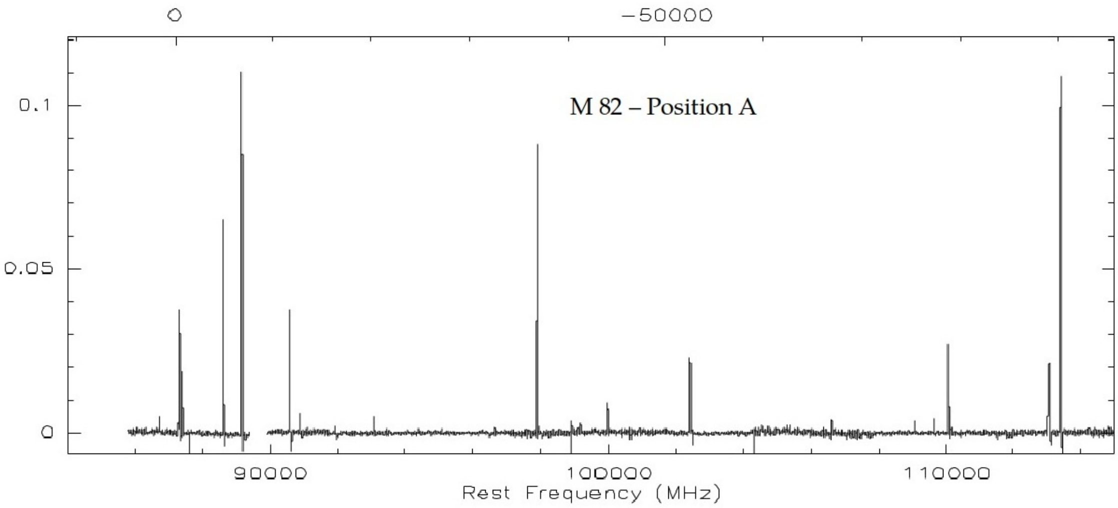

Figure B.3: M 82 complete spectrum in Position A. The axes are the same as in Fig. B.1.

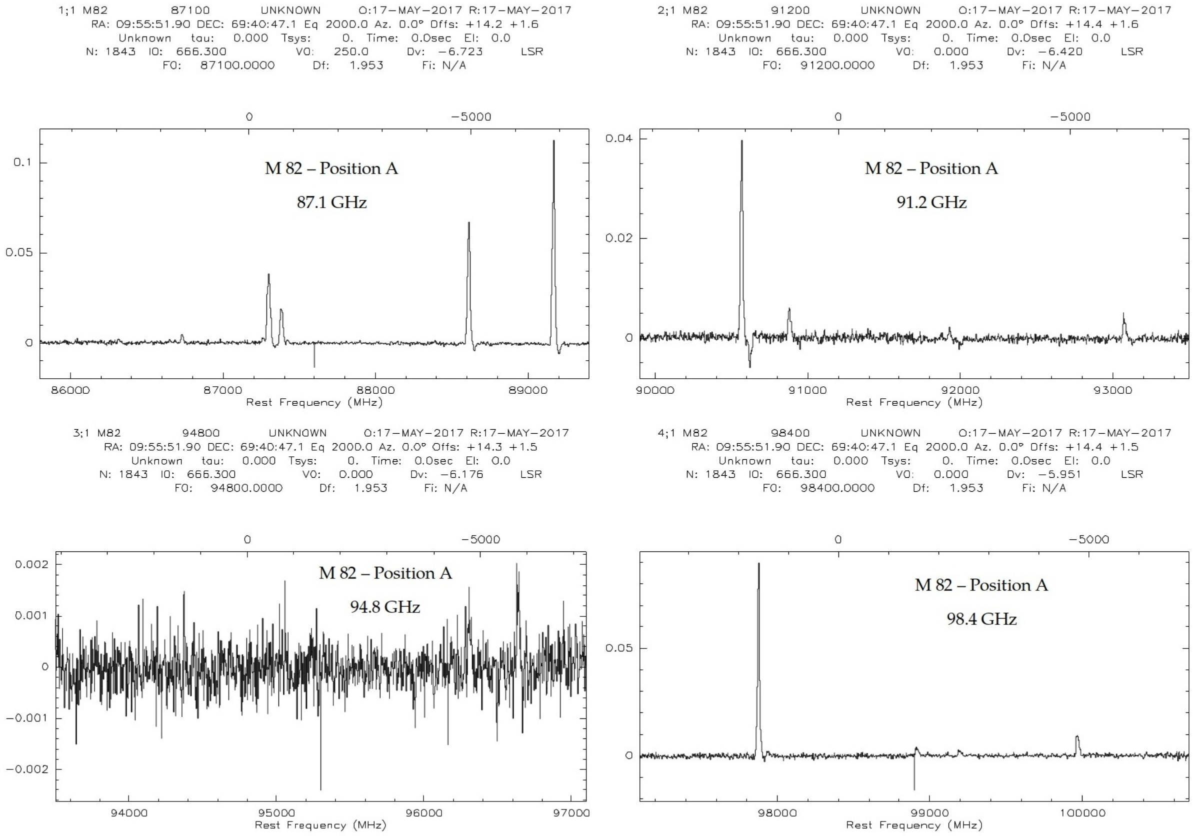

Figure B.4: M 82 spectrum at 87.1, 91.2, 94.8, and 98.4 GHz. The axes are the same as in Fig. B.1.

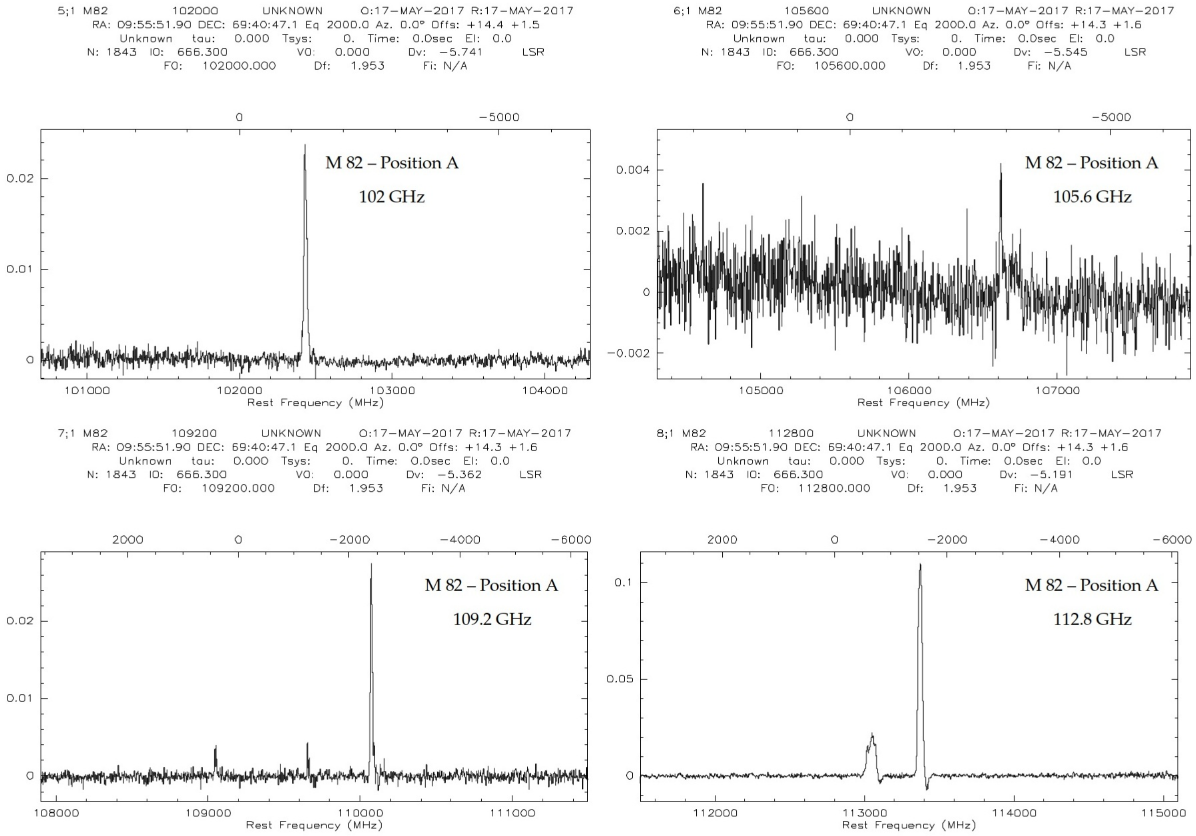

```
5;1 M82          102000        UNKNOWN       O:17-MAY-2017 R:17-MAY-2017
   RA: 09:55:51.90 DEC: 69:40:47.1 Eq 2000.0 Az. 0.0° Offs: +14.4 +1.5
      Unknown    tau:   0.000  Tsys:     0.  Time:  0.0sec  El:  0.0
   N: 1843  I0:  666.300          V0:   0.000      Dv:  -5.741       LSR
             F0:   102000.000       Df:   1.953       Fi: N/A
```

```
6;1 M82          105600        UNKNOWN       O:17-MAY-2017 R:17-MAY-2017
   RA: 09:55:51.90 DEC: 69:40:47.1 Eq 2000.0 Az. 0.0° Offs: +14.3 +1.6
      Unknown    tau:   0.000  Tsys:     0.  Time:  0.0sec  El:  0.0
   N: 1843  I0:  666.300          V0:   0.000      Dv:  -5.545       LSR
             F0:   105600.000       Df:   1.953       Fi: N/A
```

```
7;1 M82          109200        UNKNOWN       O:17-MAY-2017 R:17-MAY-2017
   RA: 09:55:51.90 DEC: 69:40:47.1 Eq 2000.0 Az. 0.0° Offs: +14.3 +1.6
      Unknown    tau:   0.000  Tsys:     0.  Time:  0.0sec  El:  0.0
   N: 1843  I0:  666.300          V0:   0.000      Dv:  -5.362       LSR
             F0:   109200.000       Df:   1.953       Fi: N/A
```

```
8;1 M82          112800        UNKNOWN       O:17-MAY-2017 R:17-MAY-2017
   RA: 09:55:51.90 DEC: 69:40:47.1 Eq 2000.0 Az. 0.0° Offs: +14.3 +1.6
      Unknown    tau:   0.000  Tsys:     0.  Time:  0.0sec  El:  0.0
   N: 1843  I0:  666.300          V0:   0.000      Dv:  -5.191       LSR
             F0:   112800.000       Df:   1.953       Fi: N/A
```

Figure B.5: M 82 spectrum at 102, 105.6, 109.2, and 112.8 GHz. The axes are the same as in Fig. *B*.1.

B.1.3 M 82 spectra in Position B

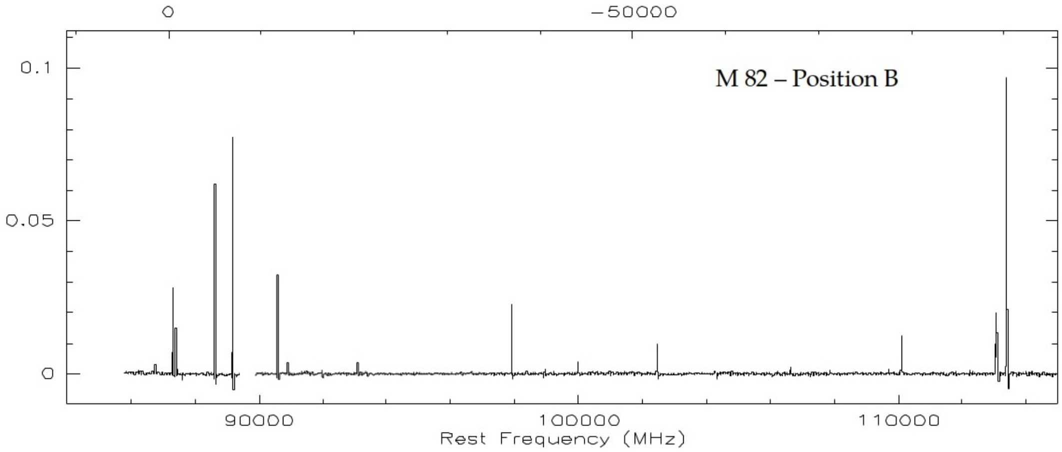

Figure B.6: M 82 complete spectrum in Position B. The axes are the same as in Fig. *B*.1.

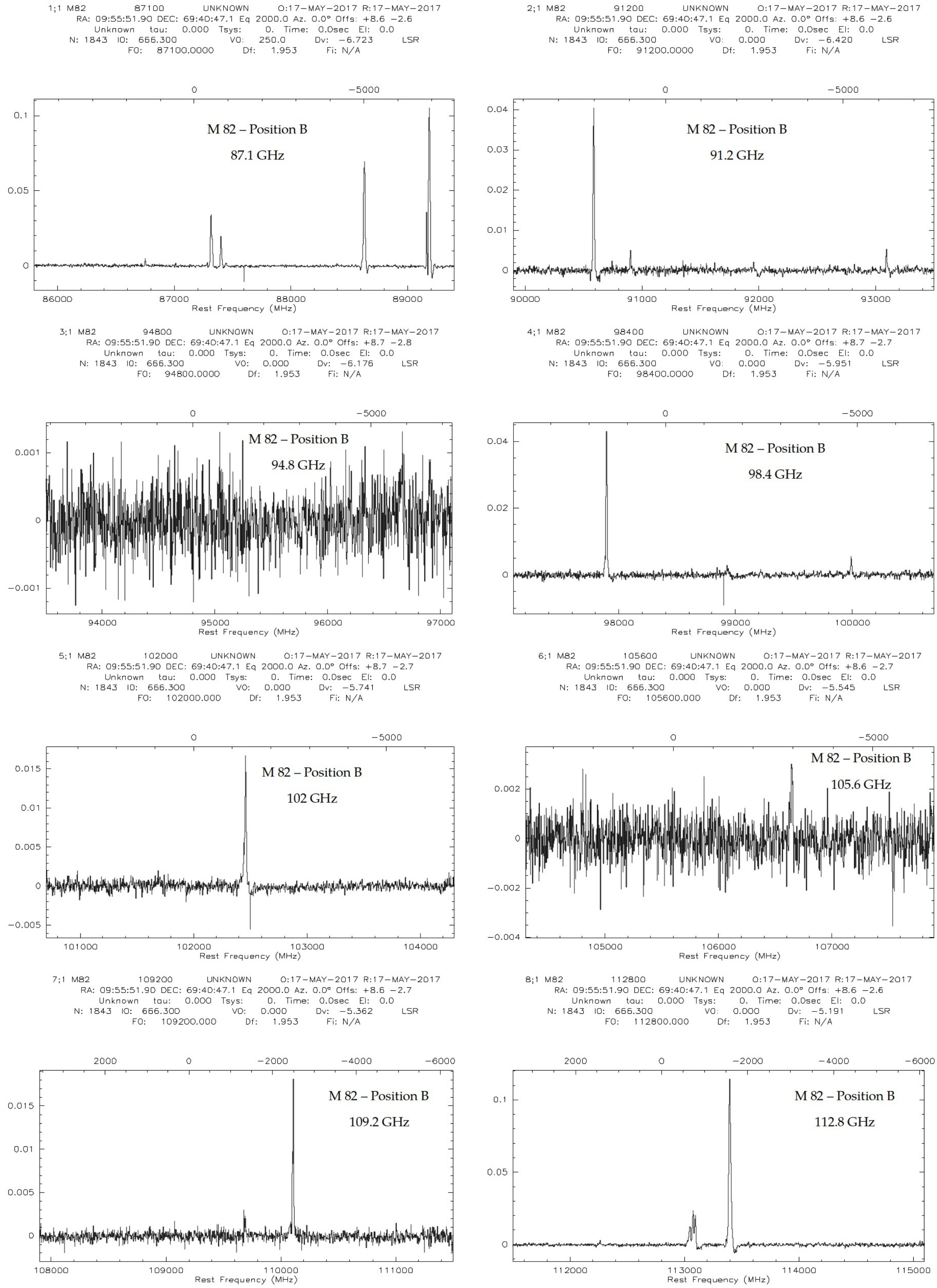

```
1;1 M82          87100        UNKNOWN      O:17-MAY-2017 R:17-MAY-2017
   RA: 09:55:51.90 DEC: 69:40:47.1 Eq 2000.0 Az. 0.0° Offs: +8.6 -2.6
      Unknown   tau:   0.000  Tsys:     0.  Time:  0.0sec  El:  0.0
  N: 1843  I0:  666.300           V0:   250.0      Dv:  -6.723      LSR
             F0:   87100.0000       Df:    1.953       Fi: N/A
```

```
2;1 M82          91200        UNKNOWN      O:17-MAY-2017 R:17-MAY-2017
   RA: 09:55:51.90 DEC: 69:40:47.1 Eq 2000.0 Az. 0.0° Offs: +8.6 -2.6
      Unknown   tau:   0.000  Tsys:     0.  Time:  0.0sec  El:  0.0
  N: 1843  I0:  666.300           V0:   0.000      Dv:  -6.420      LSR
             F0:   91200.0000       Df:    1.953       Fi: N/A
```

```
3;1 M82          94800        UNKNOWN      O:17-MAY-2017 R:17-MAY-2017
   RA: 09:55:51.90 DEC: 69:40:47.1 Eq 2000.0 Az. 0.0° Offs: +8.7 -2.8
      Unknown   tau:   0.000  Tsys:     0.  Time:  0.0sec  El:  0.0
  N: 1843  I0:  666.300           V0:   0.000      Dv:  -6.176      LSR
             F0:   94800.0000       Df:    1.953       Fi: N/A
```

```
4;1 M82          98400        UNKNOWN      O:17-MAY-2017 R:17-MAY-2017
   RA: 09:55:51.90 DEC: 69:40:47.1 Eq 2000.0 Az. 0.0° Offs: +8.7 -2.7
      Unknown   tau:   0.000  Tsys:     0.  Time:  0.0sec  El:  0.0
  N: 1843  I0:  666.300           V0:   0.000      Dv:  -5.951      LSR
             F0:   98400.0000       Df:    1.953       Fi: N/A
```

```
5;1 M82          102000       UNKNOWN      O:17-MAY-2017 R:17-MAY-2017
   RA: 09:55:51.90 DEC: 69:40:47.1 Eq 2000.0 Az. 0.0° Offs: +8.7 -2.7
      Unknown   tau:   0.000  Tsys:     0.  Time:  0.0sec  El:  0.0
  N: 1843  I0:  666.300           V0:   0.000      Dv:  -5.741      LSR
             F0:   102000.000       Df:    1.953       Fi: N/A
```

```
6;1 M82          105600       UNKNOWN      O:17-MAY-2017 R:17-MAY-2017
   RA: 09:55:51.90 DEC: 69:40:47.1 Eq 2000.0 Az. 0.0° Offs: +8.6 -2.7
      Unknown   tau:   0.000  Tsys:     0.  Time:  0.0sec  El:  0.0
  N: 1843  I0:  666.300           V0:   0.000      Dv:  -5.545      LSR
             F0:   105600.000       Df:    1.953       Fi: N/A
```

```
7;1 M82          109200       UNKNOWN      O:17-MAY-2017 R:17-MAY-2017
   RA: 09:55:51.90 DEC: 69:40:47.1 Eq 2000.0 Az. 0.0° Offs: +8.6 -2.7
      Unknown   tau:   0.000  Tsys:     0.  Time:  0.0sec  El:  0.0
  N: 1843  I0:  666.300           V0:   0.000      Dv:  -5.362      LSR
             F0:   109200.000       Df:    1.953       Fi: N/A
```

```
8;1 M82          112800       UNKNOWN      O:17-MAY-2017 R:17-MAY-2017
   RA: 09:55:51.90 DEC: 69:40:47.1 Eq 2000.0 Az. 0.0° Offs: +8.6 -2.6
      Unknown   tau:   0.000  Tsys:     0.  Time:  0.0sec  El:  0.0
  N: 1843  I0:  666.300           V0:   0.000      Dv:  -5.191      LSR
             F0:   112800.000       Df:    1.953       Fi: N/A
```

Figure B.7: M 82 spectrum at 87.1, 91.2, 94.8, 98.4, 102, 105.6, 109.2, and 112.8 GHz. The axes are the same as in Fig. *B*.1.

B.1.4 M 82 spectra in Position C

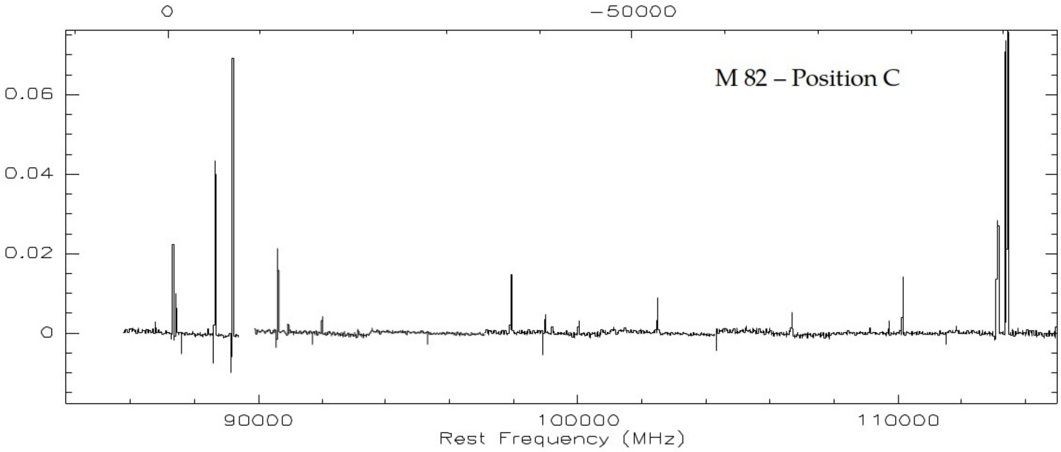

Figure B.8: M 82 complete spectrum in Position C. The axes are the same as in Fig. *B*.1.

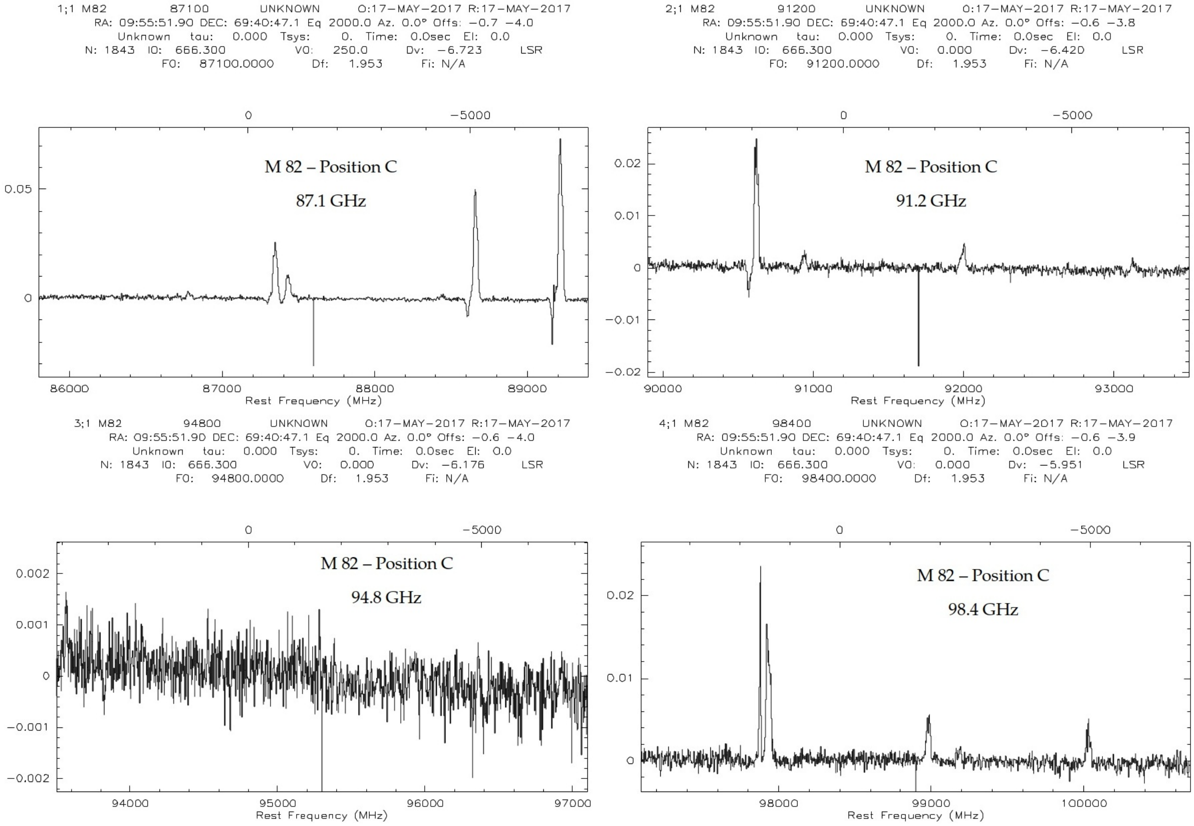

```
1;1 M82          87100        UNKNOWN      O:17-MAY-2017 R:17-MAY-2017
     RA: 09:55:51.90 DEC: 69:40:47.1 Eq 2000.0 Az. 0.0° Offs: -0.7 -4.0
        Unknown   tau:   0.000  Tsys:     0.  Time:  0.0sec  El:  0.0
   N: 1843  I0:  666.300          V0:   250.0      Dv:  -6.723       LSR
              F0:   87100.0000       Df:    1.953       Fi: N/A

2;1 M82          91200        UNKNOWN      O:17-MAY-2017 R:17-MAY-2017
     RA: 09:55:51.90 DEC: 69:40:47.1 Eq 2000.0 Az. 0.0° Offs: -0.6 -3.8
        Unknown   tau:   0.000  Tsys:     0.  Time:  0.0sec  El:  0.0
   N: 1843  I0:  666.300          V0:   0.000      Dv:  -6.420       LSR
              F0:   91200.0000       Df:    1.953       Fi: N/A

3;1 M82          94800        UNKNOWN      O:17-MAY-2017 R:17-MAY-2017
     RA: 09:55:51.90 DEC: 69:40:47.1 Eq 2000.0 Az. 0.0° Offs: -0.6 -4.0
        Unknown   tau:   0.000  Tsys:     0.  Time:  0.0sec  El:  0.0
   N: 1843  I0:  666.300          V0:   0.000      Dv:  -6.176       LSR
              F0:   94800.0000       Df:    1.953       Fi: N/A

4;1 M82          98400        UNKNOWN      O:17-MAY-2017 R:17-MAY-2017
     RA: 09:55:51.90 DEC: 69:40:47.1 Eq 2000.0 Az. 0.0° Offs: -0.6 -3.9
        Unknown   tau:   0.000  Tsys:     0.  Time:  0.0sec  El:  0.0
   N: 1843  I0:  666.300          V0:   0.000      Dv:  -5.951       LSR
              F0:   98400.0000       Df:    1.953       Fi: N/A
```

Figure B.9: M 82 spectrum at 87.1, 91.2, 94.8, and 98.4 GHz. The axes are the same as in Fig. *B*.1.

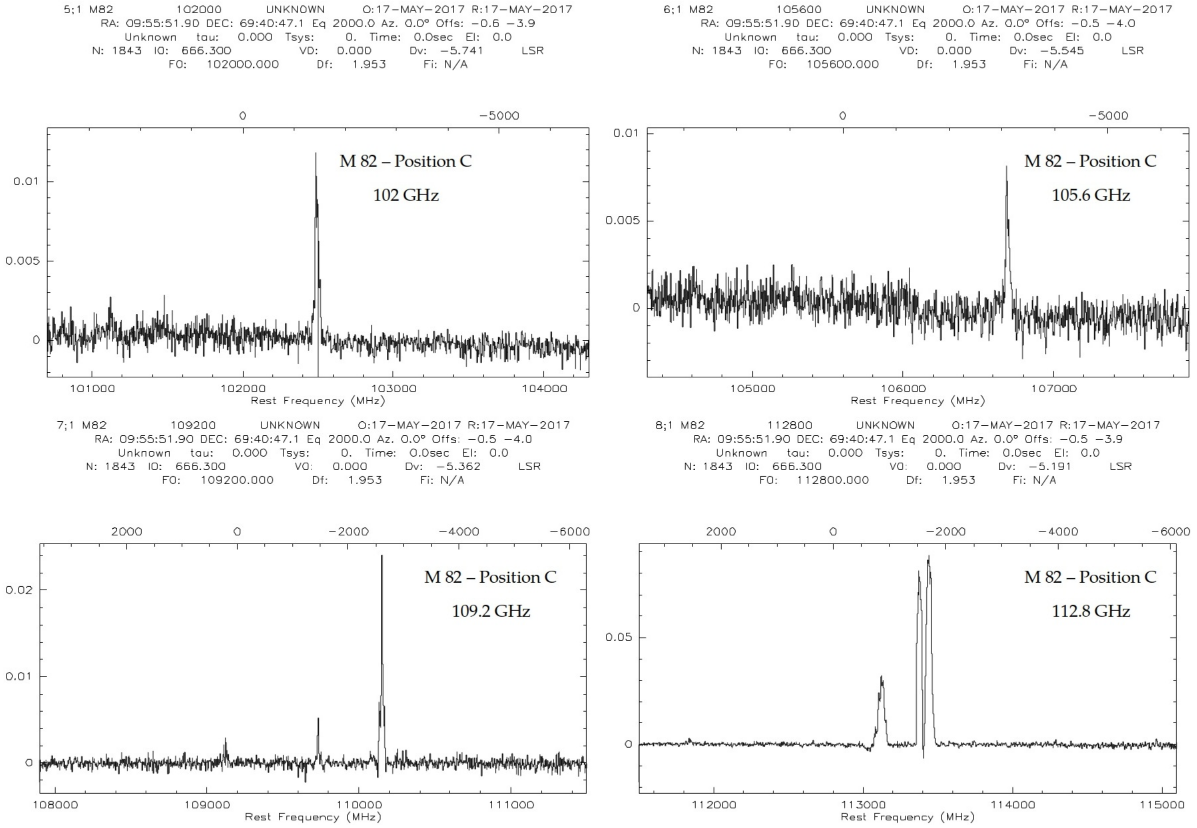

Figure B.10: M 82 spectrum at 102, 105.6, 109.2, and 112.8 GHz. The axes are the same as in Fig. *B*.1.

B.1.5 M 82 spectra in Position D

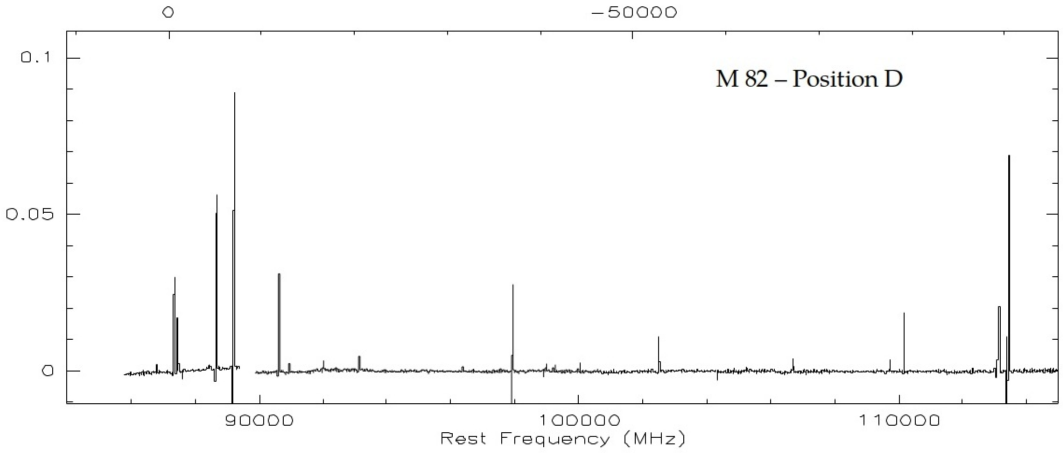

Figure B.11: M 82 complete spectrum in Position D. The axes are the same as in Fig. *B*.1.

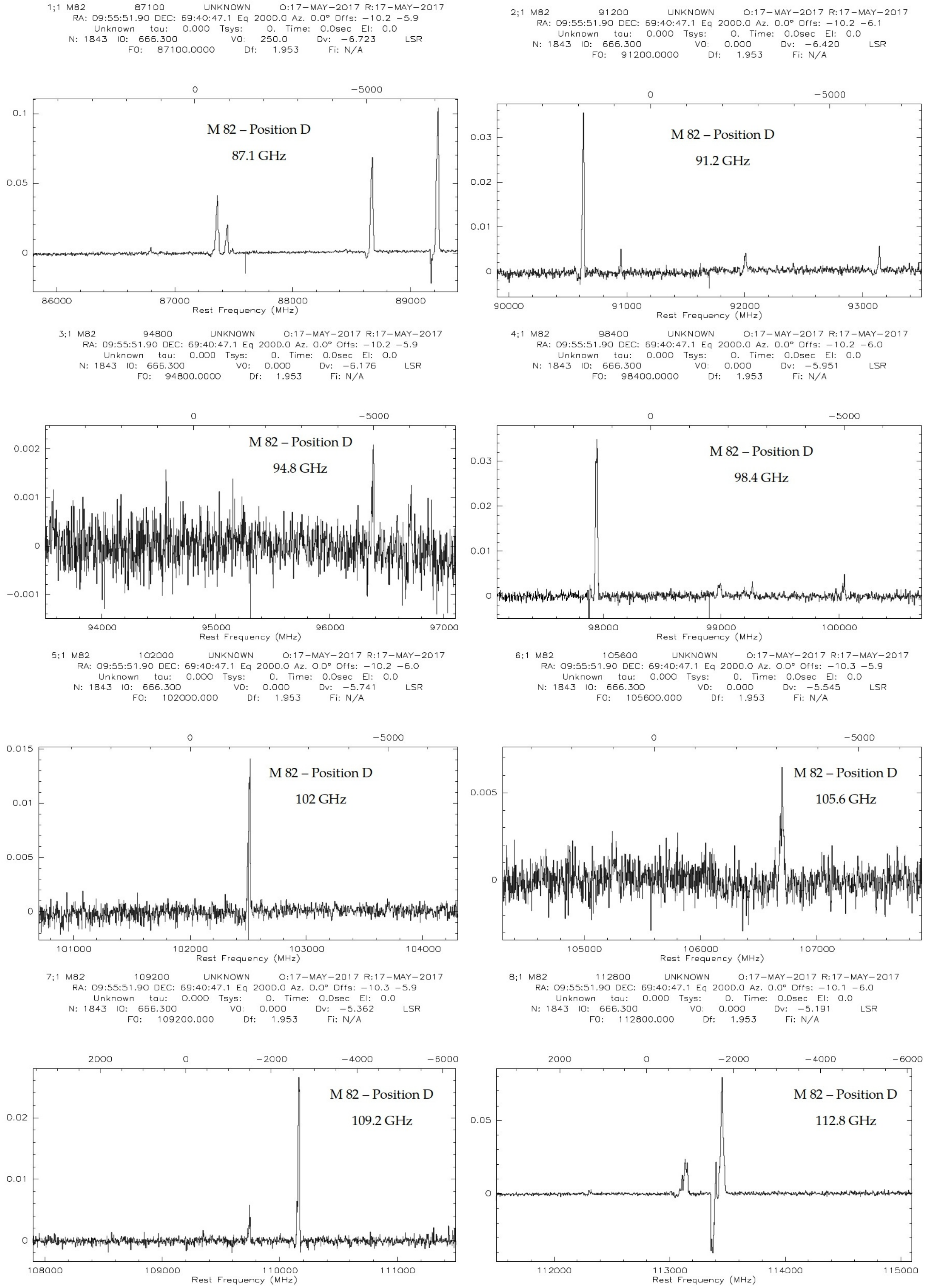

Figure B.12: M 82 spectrum at 87.1, 91.2, 94.8, 98.4, 102, 105.6, 109.2, and 112.8 GHz. The axes are the same as in Fig. B.1.

B.2 IC 342

B.2.1 Complete IC 342 spectra

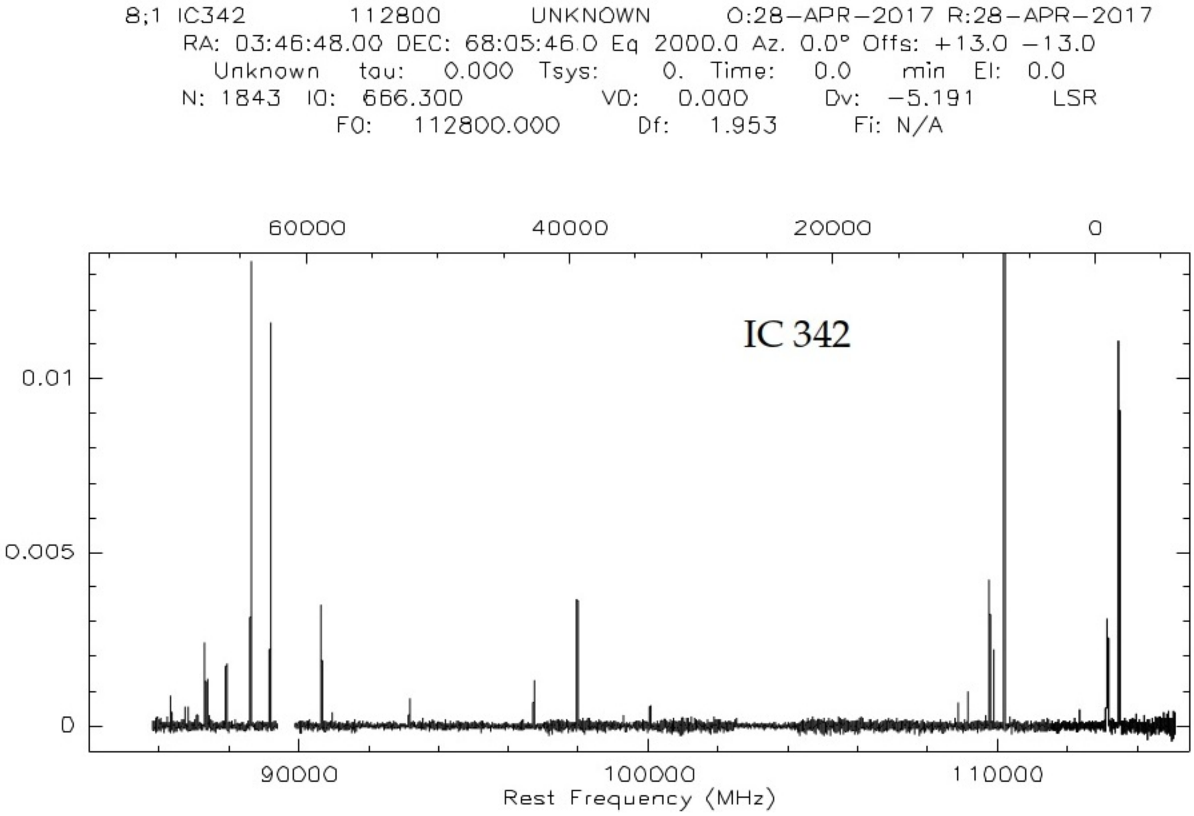

Figure B.13: IC 342 complete spectrum. The axes are the same as in Fig. B.1.

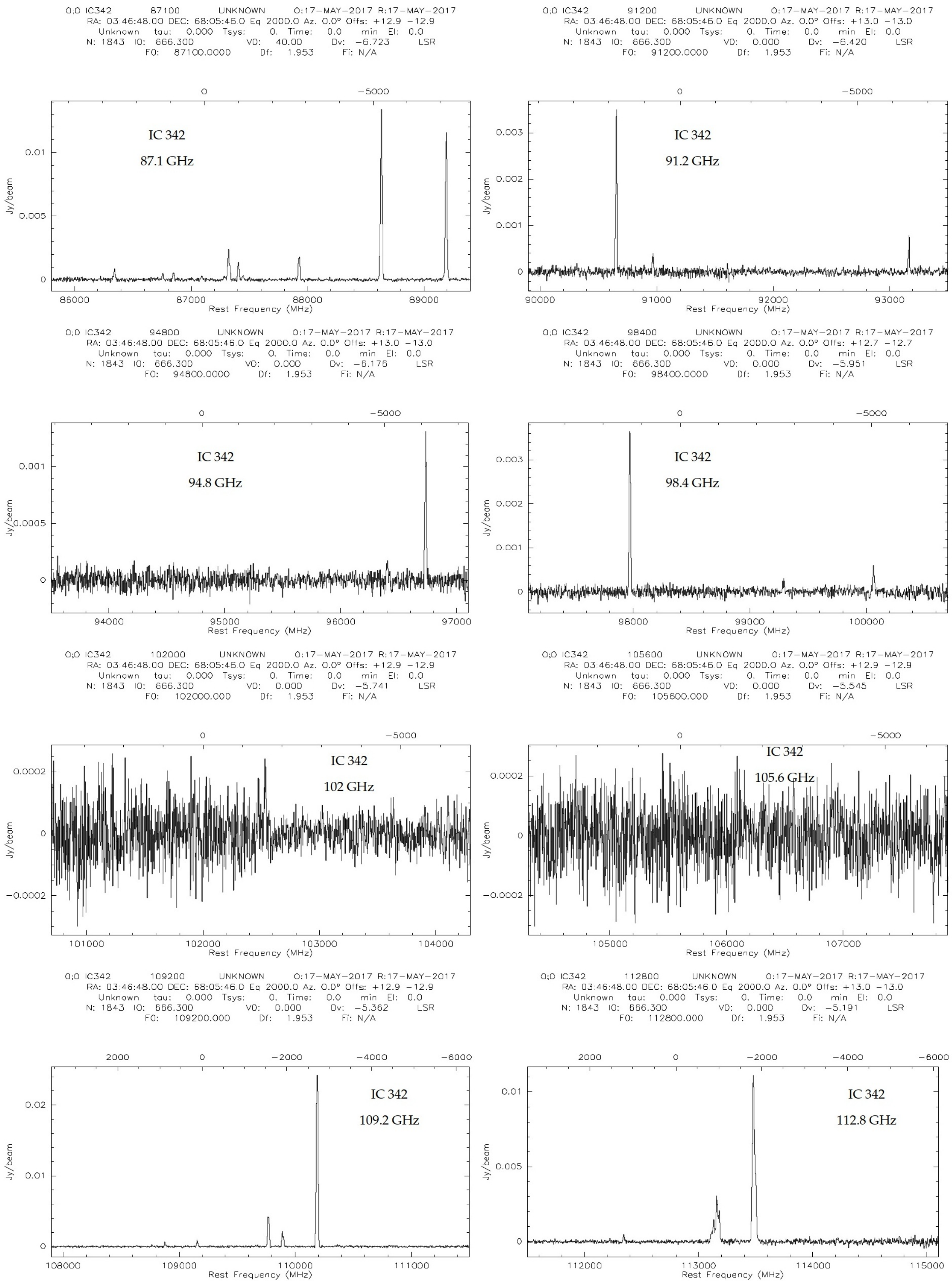

Figure B.14: IC 342 spectrum at 87.1, 91.2, 94.8, 98.4, 102, 105.6, 109.2, and 112.8 GHz. The axes are the same as in Fig. *B*.1.

B.2.2 IC 342 spectra in Position A

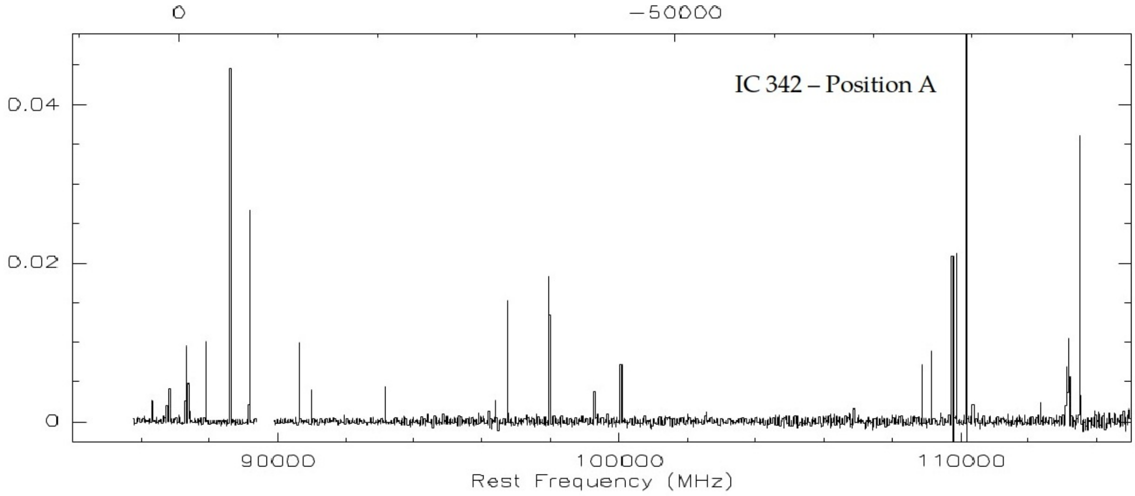

Figure B.15: IC 342 complete spectrum in Position A. The axes are the same as in Fig. *B*.1.

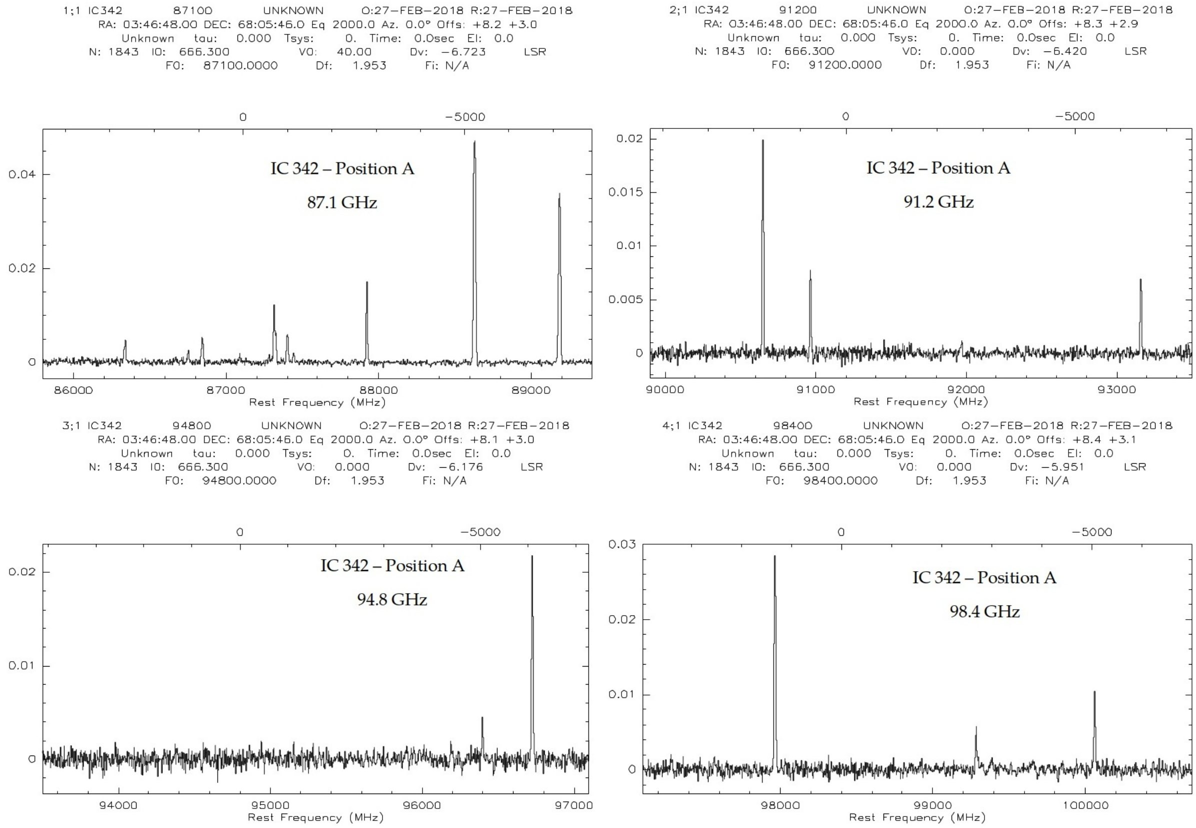

```
1;1 IC342        87100        UNKNOWN       O:27-FEB-2018 R:27-FEB-2018
RA: 03:46:48.00 DEC: 68:05:46.0 Eq 2000.0 Az. 0.0° Offs: +8.2 +3.0
Unknown   tau:   0.000  Tsys:     0.  Time:  0.0sec  El:  0.0
N: 1843  I0:  666.300            V0:   40.00       Dv:  -6.723      LSR
F0:   87100.0000       Df:   1.953       Fi: N/A
```

```
2;1 IC342        91200        UNKNOWN       O:27-FEB-2018 R:27-FEB-2018
RA: 03:46:48.00 DEC: 68:05:46.0 Eq 2000.0 Az. 0.0° Offs: +8.3 +2.9
Unknown   tau:   0.000  Tsys:     0.  Time:  0.0sec  El:  0.0
N: 1843  I0:  666.300            V0:   0.000       Dv:  -6.420      LSR
F0:   91200.0000       Df:   1.953       Fi: N/A
```

```
3;1 IC342        94800        UNKNOWN       O:27-FEB-2018 R:27-FEB-2018
RA: 03:46:48.00 DEC: 68:05:46.0 Eq 2000.0 Az. 0.0° Offs: +8.1 +3.0
Unknown   tau:   0.000  Tsys:     0.  Time:  0.0sec  El:  0.0
N: 1843  I0:  666.300            V0:   0.000       Dv:  -6.176      LSR
F0:   94800.0000       Df:   1.953       Fi: N/A
```

```
4;1 IC342        98400        UNKNOWN       O:27-FEB-2018 R:27-FEB-2018
RA: 03:46:48.00 DEC: 68:05:46.0 Eq 2000.0 Az. 0.0° Offs: +8.4 +3.1
Unknown   tau:   0.000  Tsys:     0.  Time:  0.0sec  El:  0.0
N: 1843  I0:  666.300            V0:   0.000       Dv:  -5.951      LSR
F0:   98400.0000       Df:   1.953       Fi: N/A
```

Figure B.16: IC 342 spectrum at 87.1, 91.2, 94.8, and 98.4 GHz (right). The axes are the same as in Fig. *B*.1.

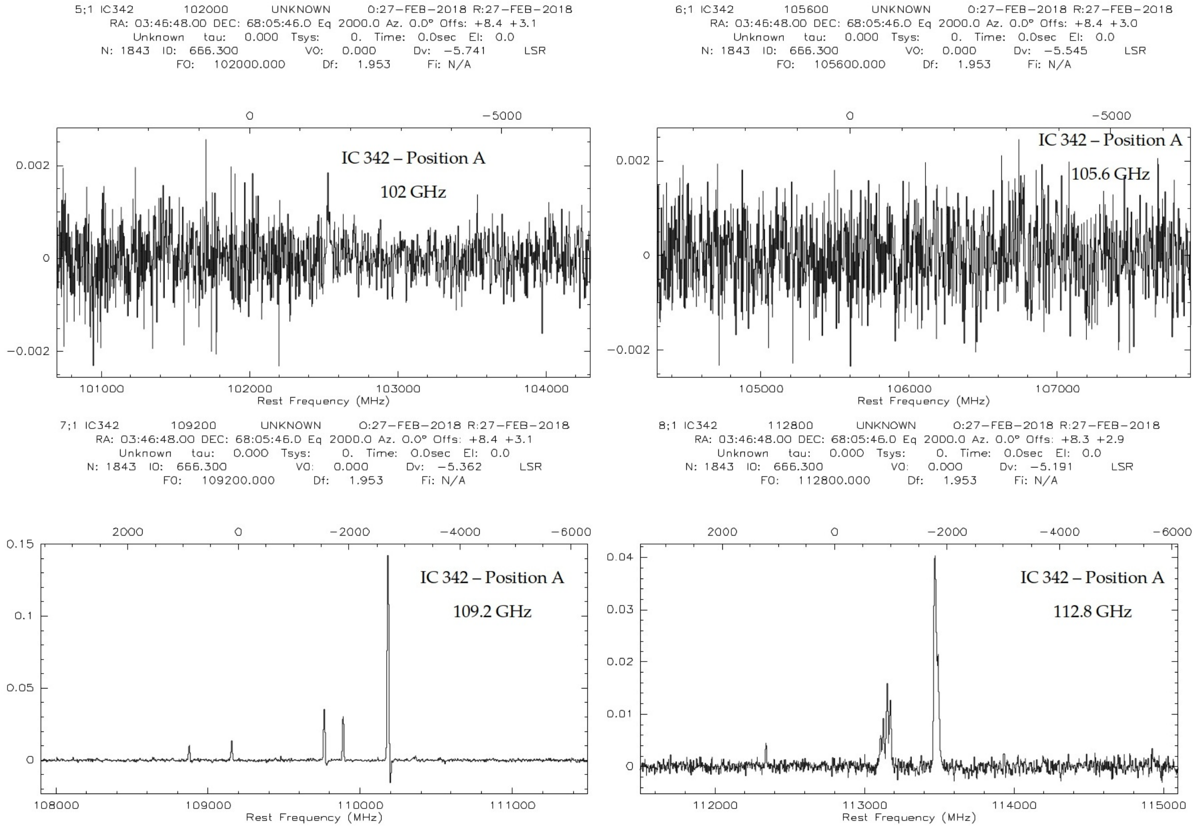

Figure B.17: IC 342 spectrum at 102, 105.6, 109.2, and 112.8 GHz. The axes are the same as in Fig. *B*.1.

B.2.3 IC 342 spectra in Position B

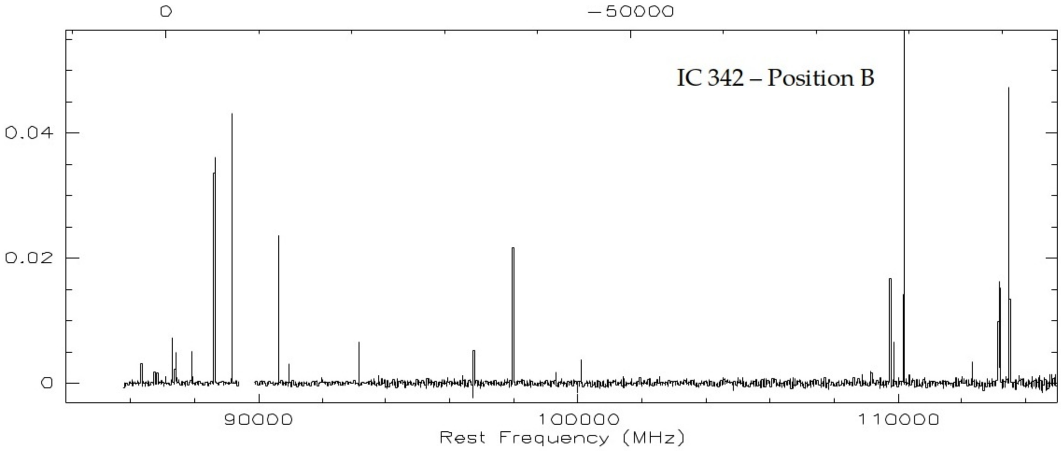

Figure B.18: IC 342 complete spectrum in Position B. The axes are the same as in Fig. *B*.1.

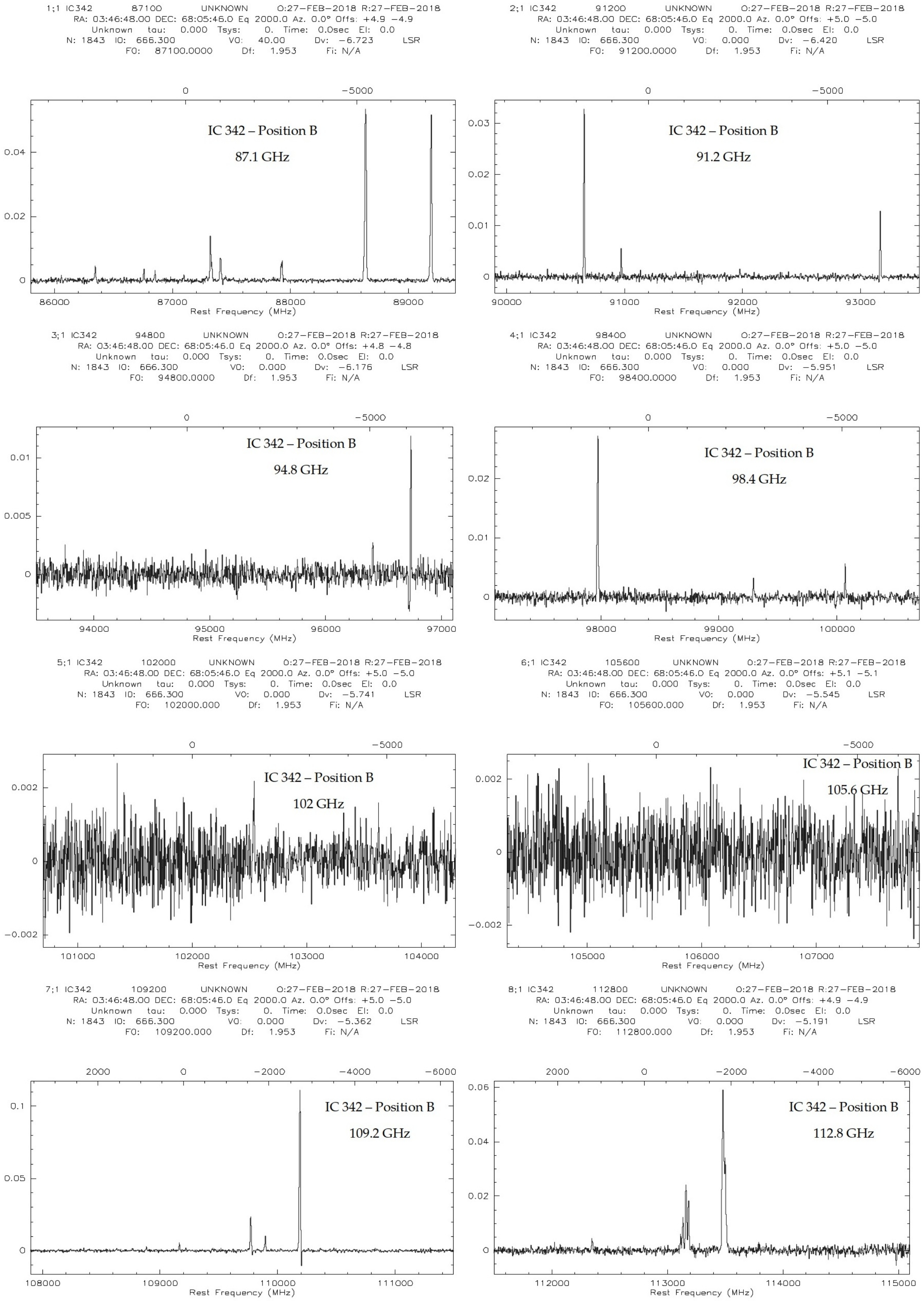

```
1;1 IC342        87100        UNKNOWN      0:27-FEB-2018 R:27-FEB-2018
   RA: 03:46:48.00 DEC: 68:05:46.0 Eq 2000.0 Az. 0.0° Offs: +4.9 -4.9
        Unknown    tau:   0.000  Tsys:      0.  Time:  0.0sec  El:  0.0
   N: 1843  I0:  666.300            V0:   40.00       Dv:  -6.723       LSR
                F0:    87100.0000        Df:    1.953       Fi: N/A
```

```
2;1 IC342        91200        UNKNOWN      0:27-FEB-2018 R:27-FEB-2018
   RA: 03:46:48.00 DEC: 68:05:46.0 Eq 2000.0 Az. 0.0° Offs: +5.0 -5.0
        Unknown    tau:   0.000  Tsys:      0.  Time:  0.0sec  El:  0.0
   N: 1843  I0:  666.300            V0:   0.000       Dv:  -6.420       LSR
                F0:    91200.0000        Df:    1.953       Fi: N/A
```

```
3;1 IC342        94800        UNKNOWN      0:27-FEB-2018 R:27-FEB-2018
   RA: 03:46:48.00 DEC: 68:05:46.0 Eq 2000.0 Az. 0.0° Offs: +4.8 -4.8
        Unknown    tau:   0.000  Tsys:      0.  Time:  0.0sec  El:  0.0
   N: 1843  I0:  666.300            V0:   0.000       Dv:  -6.176       LSR
                F0:    94800.0000        Df:    1.953       Fi: N/A
```

```
4;1 IC342        98400        UNKNOWN      0:27-FEB-2018 R:27-FEB-2018
   RA: 03:46:48.00 DEC: 68:05:46.0 Eq 2000.0 Az. 0.0° Offs: +5.0 -5.0
        Unknown    tau:   0.000  Tsys:      0.  Time:  0.0sec  El:  0.0
   N: 1843  I0:  666.300            V0:   0.000       Dv:  -5.951       LSR
                F0:    98400.0000        Df:    1.953       Fi: N/A
```

```
5;1 IC342        102000       UNKNOWN      0:27-FEB-2018 R:27-FEB-2018
   RA: 03:46:48.00 DEC: 68:05:46.0 Eq 2000.0 Az. 0.0° Offs: +5.0 -5.0
        Unknown    tau:   0.000  Tsys:      0.  Time:  0.0sec  El:  0.0
   N: 1843  I0:  666.300            V0:   0.000       Dv:  -5.741       LSR
                F0:    102000.000        Df:    1.953       Fi: N/A
```

```
6;1 IC342        105600       UNKNOWN      0:27-FEB-2018 R:27-FEB-2018
   RA: 03:46:48.00 DEC: 68:05:46.0 Eq 2000.0 Az. 0.0° Offs: +5.1 -5.1
        Unknown    tau:   0.000  Tsys:      0.  Time:  0.0sec  El:  0.0
   N: 1843  I0:  666.300            V0:   0.000       Dv:  -5.545       LSR
                F0:    105600.000        Df:    1.953       Fi: N/A
```

```
7;1 IC342        109200       UNKNOWN      0:27-FEB-2018 R:27-FEB-2018
   RA: 03:46:48.00 DEC: 68:05:46.0 Eq 2000.0 Az. 0.0° Offs: +5.0 -5.0
        Unknown    tau:   0.000  Tsys:      0.  Time:  0.0sec  El:  0.0
   N: 1843  I0:  666.300            V0:   0.000       Dv:  -5.362       LSR
                F0:    109200.000        Df:    1.953       Fi: N/A
```

```
8;1 IC342        112800       UNKNOWN      0:27-FEB-2018 R:27-FEB-2018
   RA: 03:46:48.00 DEC: 68:05:46.0 Eq 2000.0 Az. 0.0° Offs: +4.9 -4.9
        Unknown    tau:   0.000  Tsys:      0.  Time:  0.0sec  El:  0.0
   N: 1843  I0:  666.300            V0:   0.000       Dv:  -5.191       LSR
                F0:    112800.000        Df:    1.953       Fi: N/A
```

Figure B.19: IC 342 spectrum at 87.1, 91.2, 94.8, 98.4, 102, 105.6, 109.2, 112.8 GHz. The axes are the same as in Fig. *B*.1.

B.2.4 IC 342 spectra in Position C

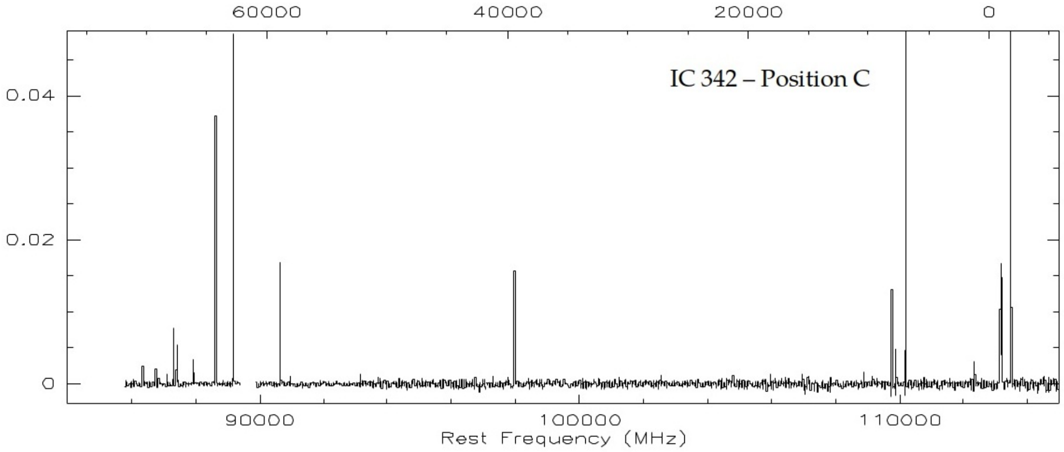

Figure B.20: IC 342 complete spectrum in Position C. The axes are the same as in Fig. *B*.1.

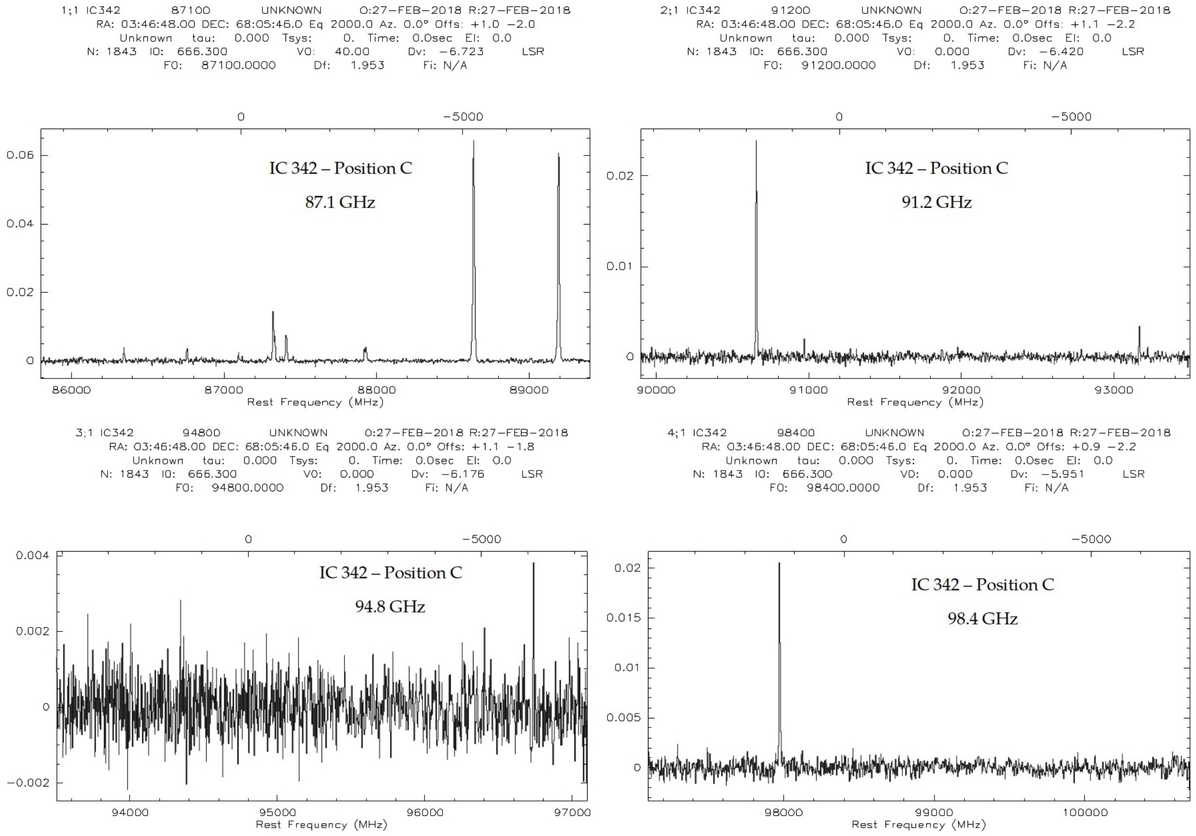

Figure B.21: IC 342 spectrum at 87.1, 91.2, 94.8, and 98.4 GHz. The axes are the same as in Fig. *B*.1.

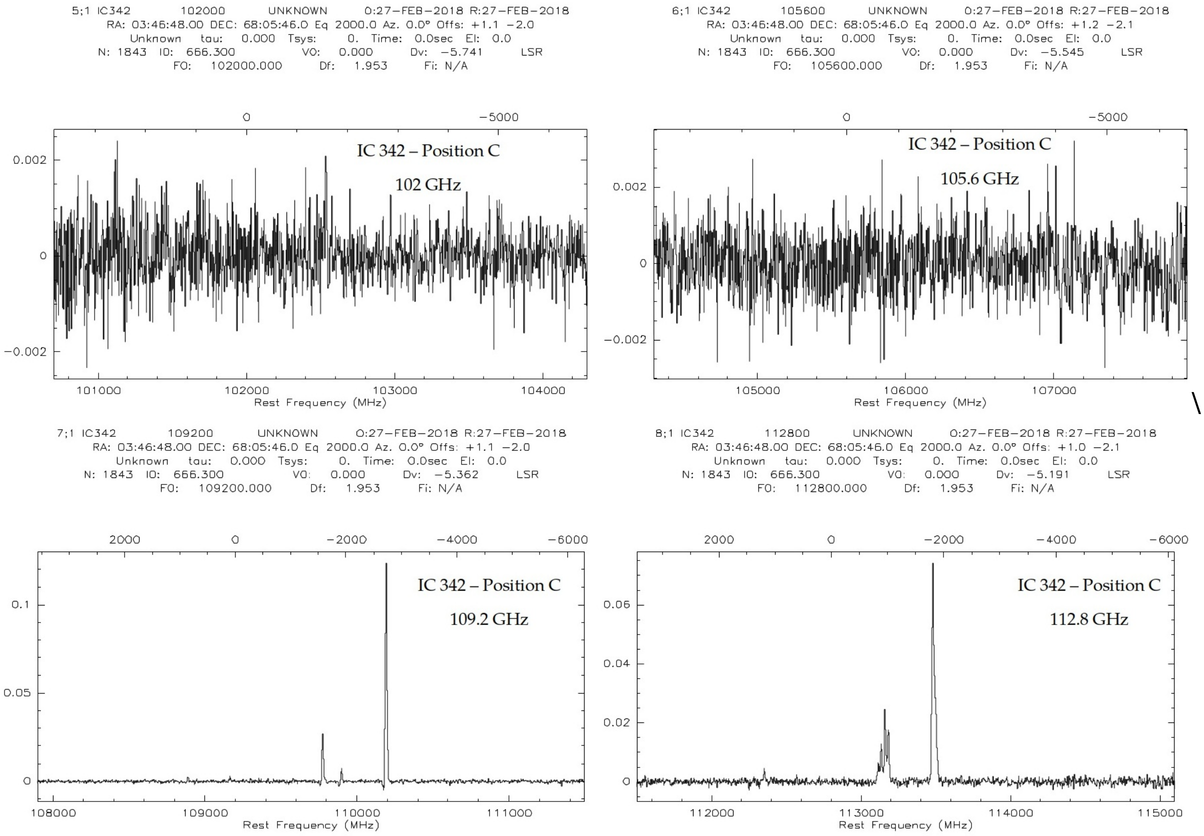

Figure B.22: IC 342 spectrum at 102, 105.6, 109.2, and 112.8 GHz. The axes are the same as in Fig. B.1.

Appendix C

Line Moments

C.1 M 82

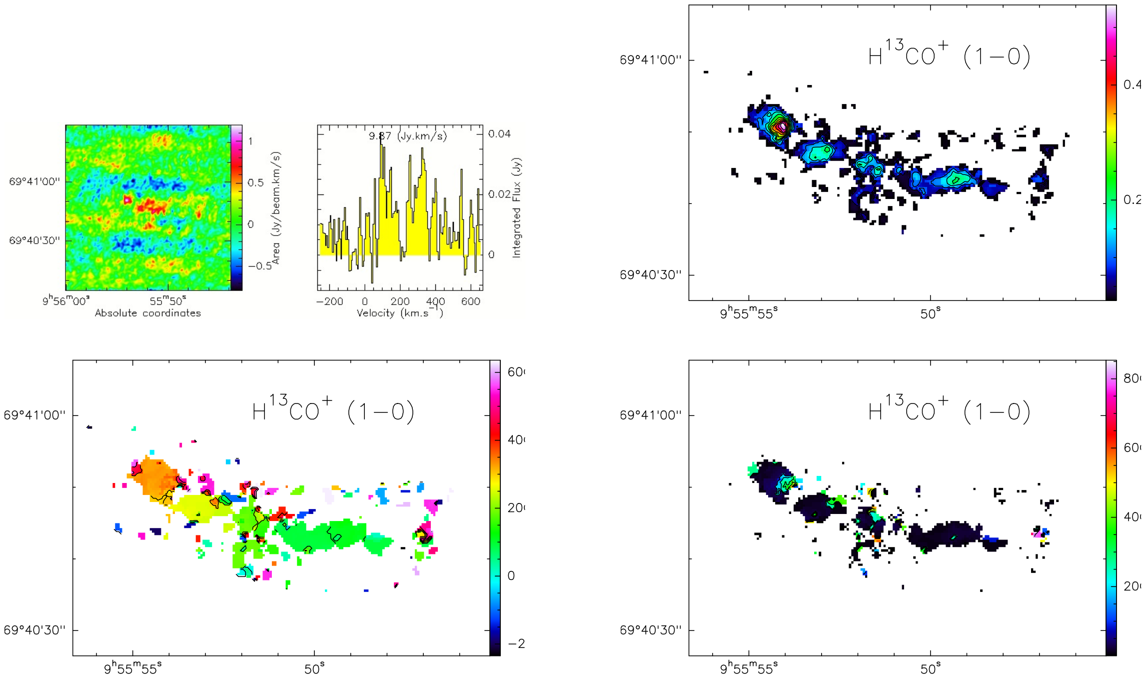

Figure C.1: $H^{13}CO^+$ at 86.754 GHz in M 82. Top left: line image with its spectrum. Top right: line flux distribution (contour levels from 0.05 to 0.55 $\mathrm{Jy\,beam^{-1}\,km\,s^{-1}}$ by steps of 0.05 $\mathrm{Jy\,beam^{-1}\,km\,s^{-1}}$). Bottom left: line velocity distribution (contour levels from -200 to 600 $\mathrm{km\,s^{-1}}$ by steps of 100). Bottom left: line width distribution (contour levels from 100 to 900 $\mathrm{km\,s^{-1}}$ by steps of 100).

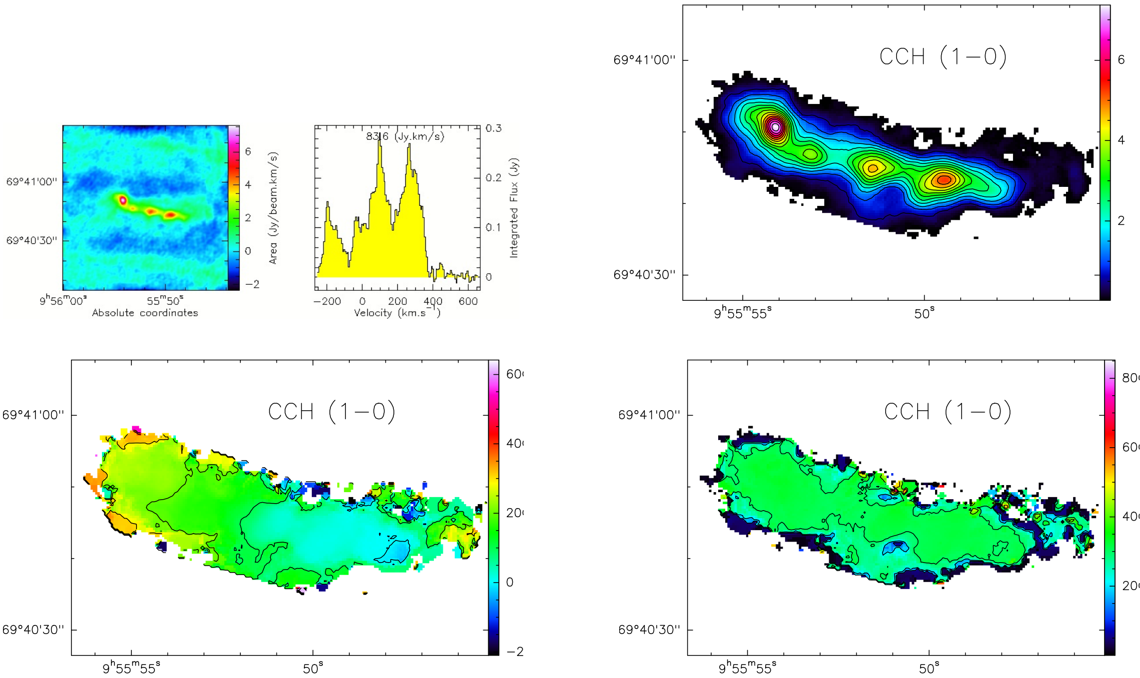

Figure C.2: CCH at 87.317 GHz in M 82 .Top left: line image with its spectrum. Top right: line flux distribution (contour levels from 0.5 to 7.5 Jy beam^{-1} km s^{-1} by steps of 0.5 Jy beam^{-1} km s^{-1}). Bottom left: line velocity distribution (contour levels from -200 to 600 km s^{-1} by steps of 100). Bottom right: line width distribution (contour levels from 100 to 900 km s^{-1} by steps of 100).

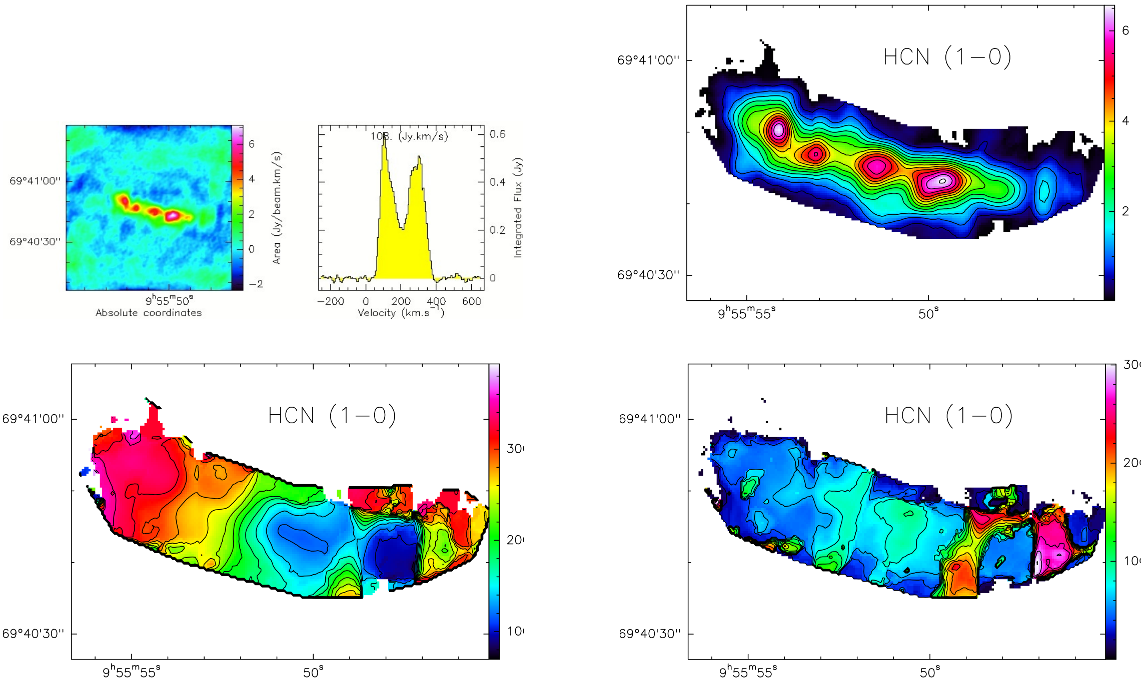

Figure C.3: HCN (1-0) at 88.632 GHz in M 82 .Top left: line image with its spectrum. Top right: line flux distribution (contour levels from 0.5 to 6.5 Jy beam^{-1} km s^{-1} by steps of 0.5 Jy beam^{-1} km s^{-1}). Bottom left: line velocity distribution (contour levels from 20 to 400 km s^{-1} by steps of 20). Bottom right: line width distribution (contour levels from 20 to 300 km s^{-1} by steps of 20).

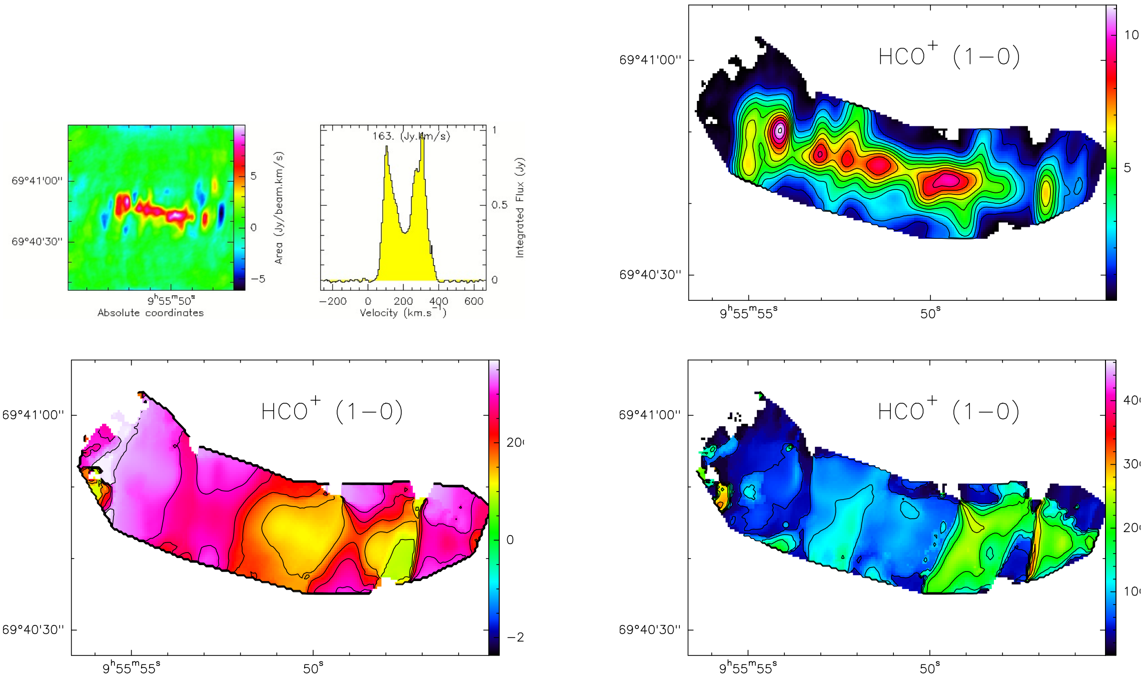

Figure C.4: HCO$^+$ at 89.189 GHz in M 82 .Top left: line image with its spectrum. Top right: line flux distribution (contour levels from 1 to 11 Jy beam^{-1} km s^{-1} by steps of 1 Jy beam^{-1} km s^{-1}). Bottom left: line velocity distribution (contour levels from -250 to 350 km s^{-1} by steps of 50). Bottom right: line width distribution (contour levels from 50 to 450 km s^{-1} by steps of 50).

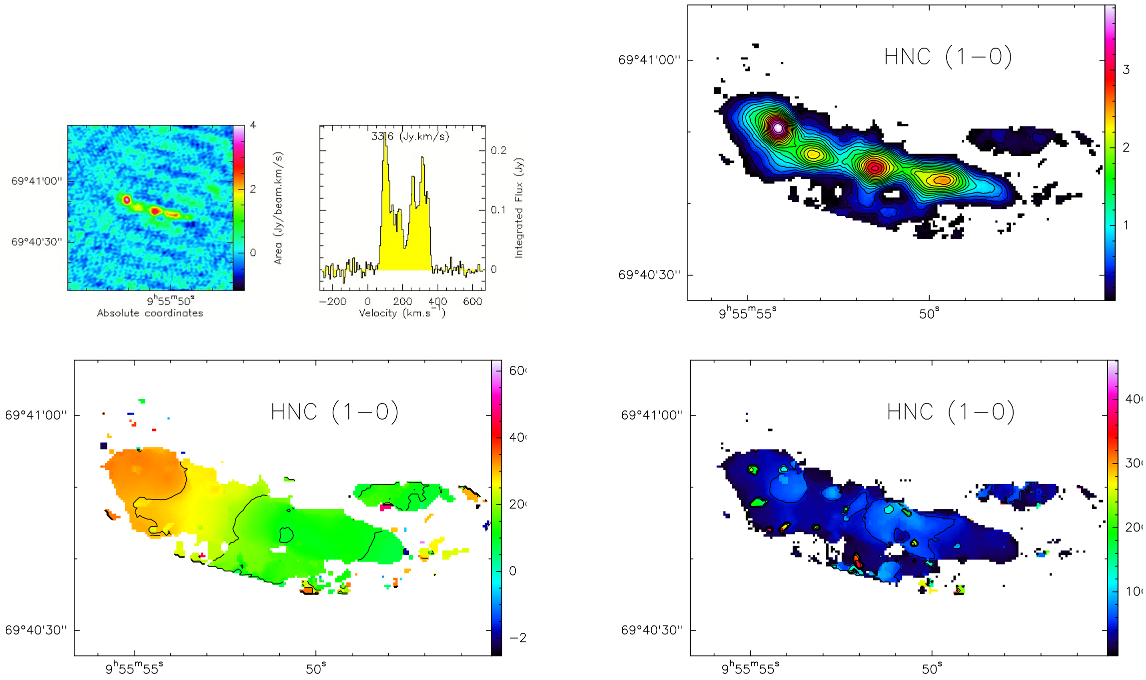

Figure C.5: HNC at 90.664 GHz in M 82 .Top left: line image with its spectrum. Top right: line flux distribution (contour levels from 0.2 to 3.8 Jy beam^{-1} km s^{-1} by steps of 0.2 Jy beam^{-1} km s^{-1}). Bottom left: line velocity distribution (contour levels from -300 to 600 km s^{-1} by steps of 100). Bottom right: line width distribution (contour levels from 50 to 450 km s^{-1} by steps of 50).

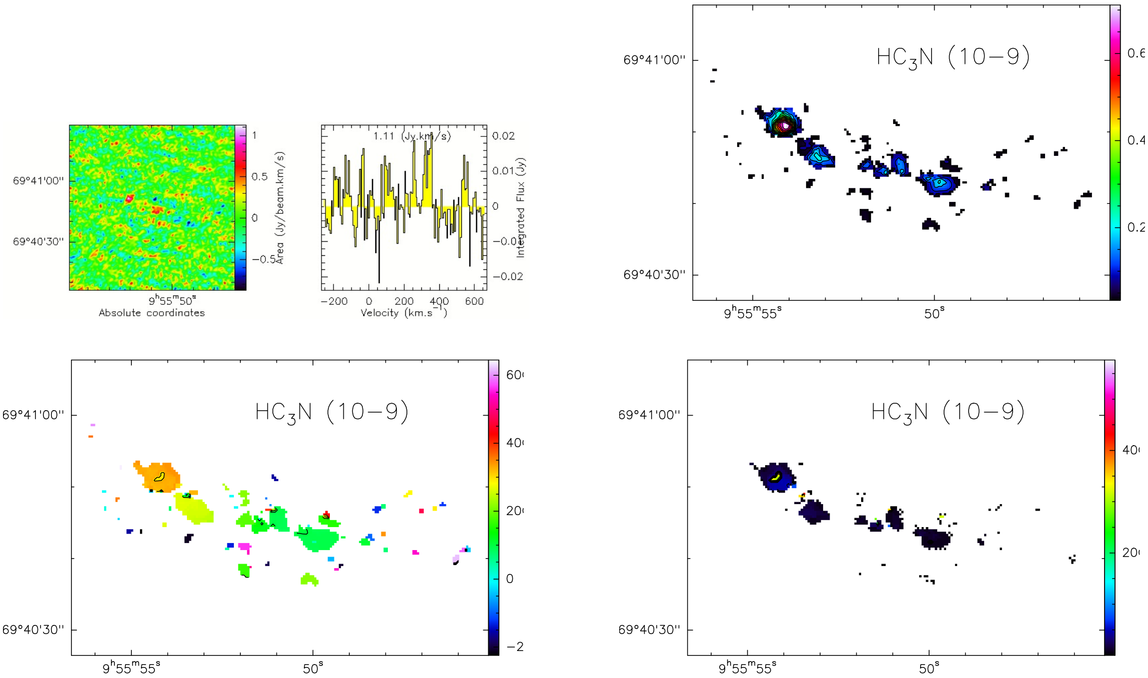

Figure C.6: HC$_3$N at 90.978 GHz in M 82 .Top left: line image with its spectrum. Top right: line flux distribution (contour levels from 0.05 to 0.7 Jy beam^{-1} km s^{-1} by steps of 0.05 Jy beam^{-1} km s^{-1}). Bottom left: line velocity distribution (contour levels from -200 to 600 km s^{-1} by steps of 100). Bottom right: line width distribution (contour levels from 50 to 600 km s^{-1} by steps of 50).

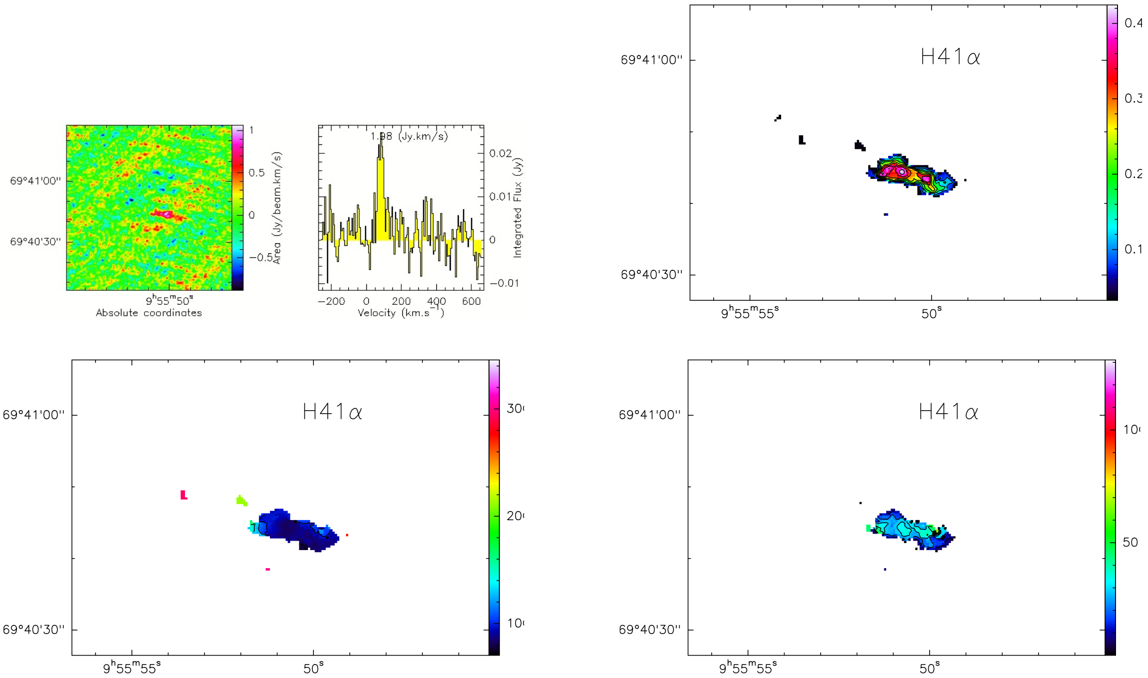

Figure C.7: H41α at 92.034 GHz in M 82 .Top left: line image with its spectrum. Top right: line flux distribution (contour levels from 0.05 to 0.4 Jy beam^{-1} km s^{-1} by steps of 0.05 Jy beam^{-1} km s^{-1}). Bottom left: line velocity distribution (contour levels from 20 to 340 km s^{-1} by steps of 20). Bottom right: line width distribution (contour levels from 10 to 130 km s^{-1} by steps of 10).

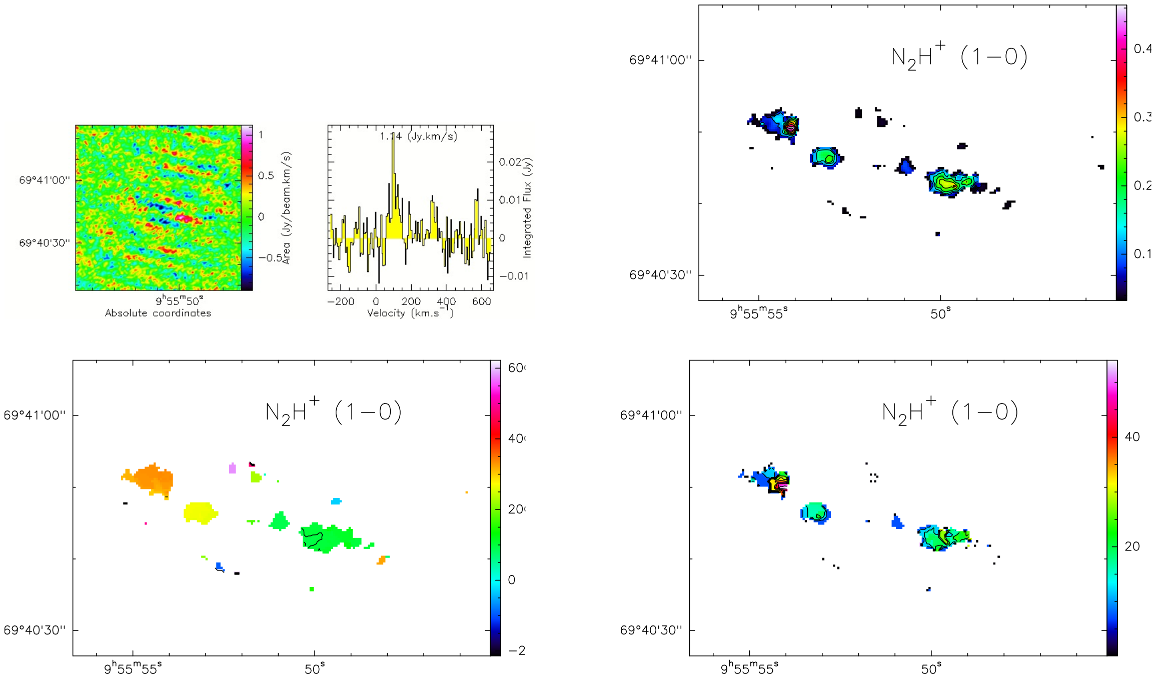

Figure C.8: N_2H^+ at 93.174 GHz in M 82 .Top left: line image with its spectrum. Top right: line flux distribution (contour levels from 0.05 to 0.45 Jy beam^{-1} km s^{-1} by steps of 0.05 Jy beam^{-1} km s^{-1}). Bottom left: line velocity distribution (contour levels from -200 to 600 km s^{-1} by steps of 100). Bottom right: line width distribution (contour levels from 5 to 55 km s^{-1} by steps of 5).

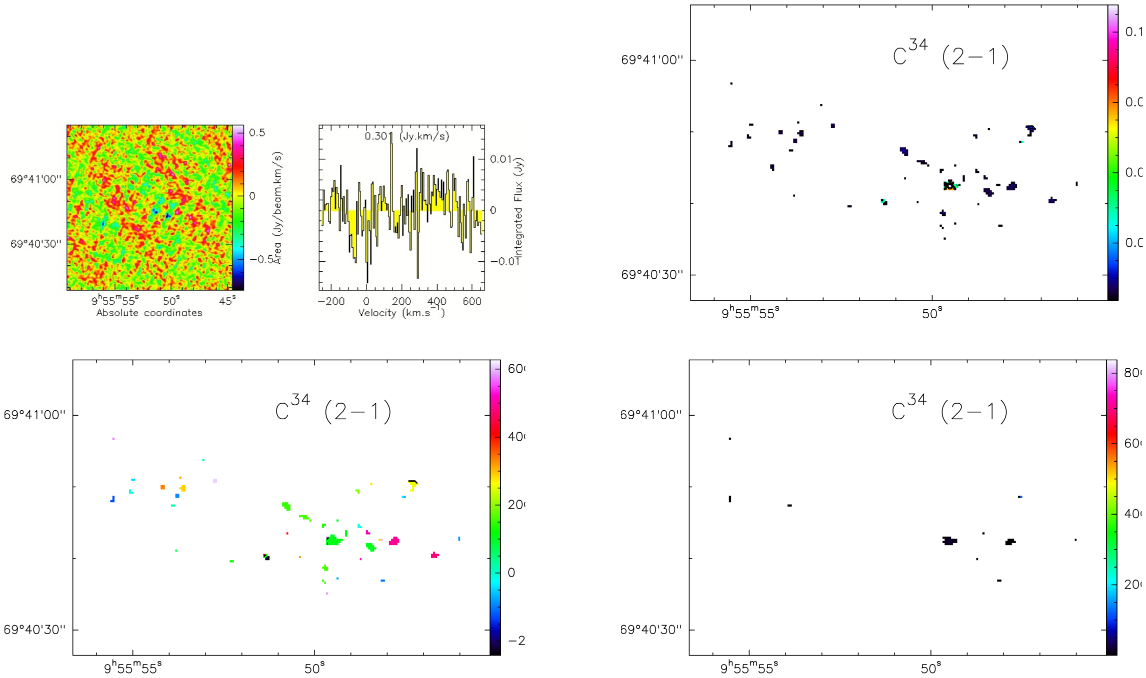

Figure C.9: C^{34}S at 96.413 GHz in M 82 .Top left: line image with its spectrum. Top right: line flux distribution (contour levels from 0.01 to 0.11 Jy beam^{-1} km s^{-1} by steps of 0.01 Jy beam^{-1} km s^{-1}). Bottom left: line velocity distribution (contour levels from -200 to 600 km s^{-1} by steps of 100). Bottom right: line width distribution (contour levels from 100 to 800 km s^{-1} by steps of 100).

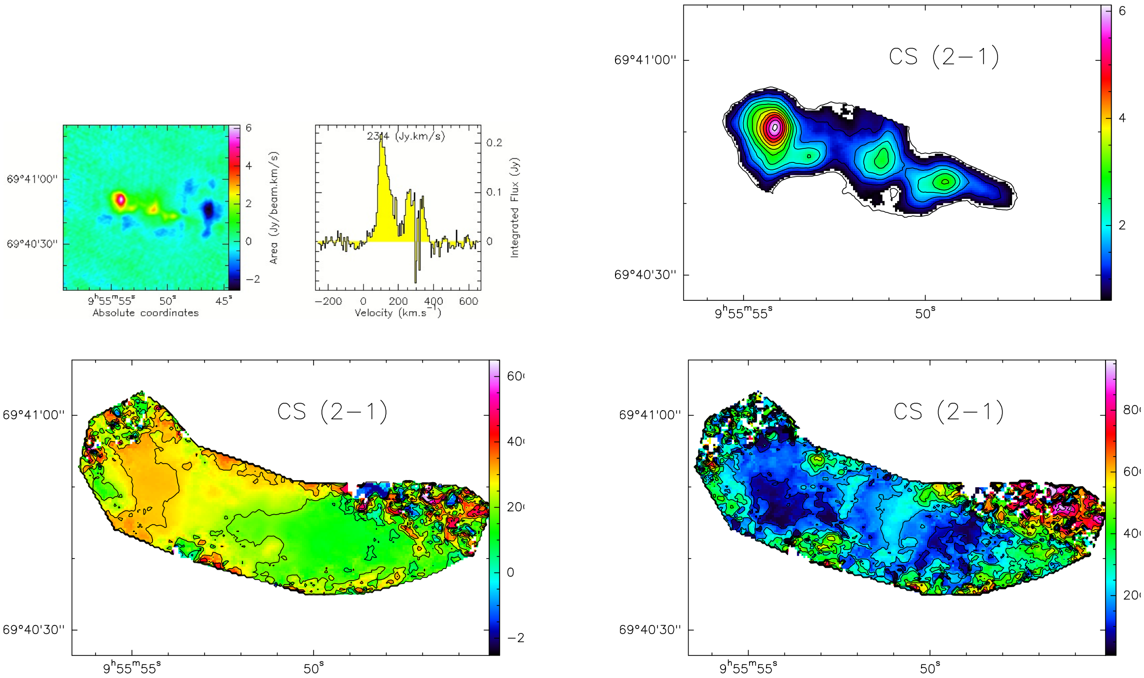

Figure C.10: CS at 97.981 GHz in M 82 .Top left: line image with its spectrum. Top right: line flux distribution (contour levels from 0.5 to 6.0 Jy beam^{-1} km s^{-1} by steps of 0.5 Jy beam^{-1} km s^{-1}). Bottom left: line velocity distribution (contour levels from -300 to 700 km s^{-1} by steps of 100). Bottom right: line width distribution (contour levels from 100 to 1000 km s^{-1} by steps of 100).

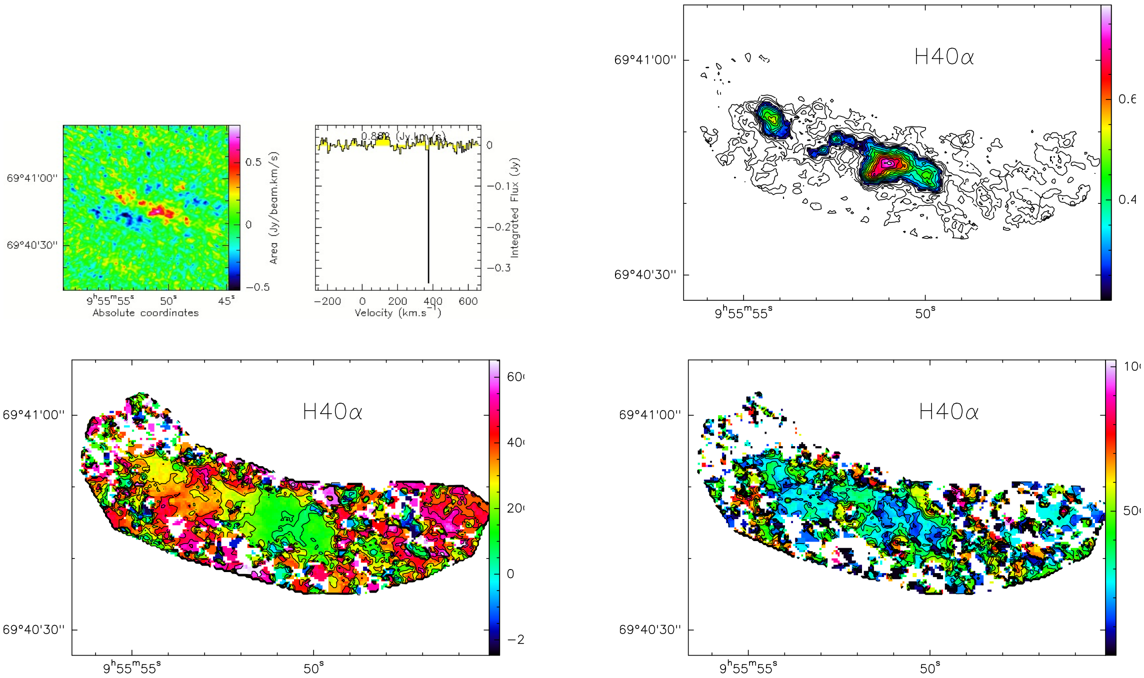

Figure C.11: H40α at 99.023 GHz in M 82 .Top left: line image with its spectrum. Top right: line flux distribution (contour levels from 0.05 to 0.8 Jy beam^{-1} km s^{-1} by steps of 0.05 Jy beam^{-1} km s^{-1}). Bottom left: line velocity distribution (contour levels from -200 to 700 km s^{-1} by steps of 100). Bottom right: line width distribution (contour levels from 100 to 1000 km s^{-1} by steps of 100).

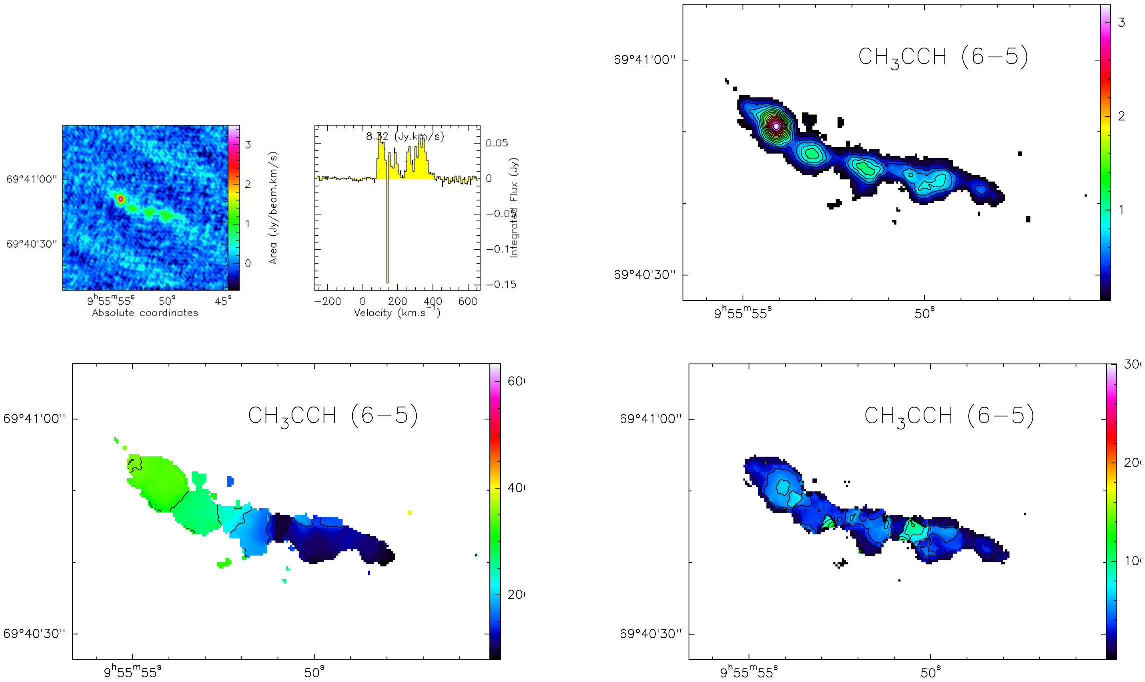

Figure C.12: CH$_3$CCH at 102.548 GHz in M 82 .Top left: line image with its spectrum. Top right: line flux distribution (contour levels from 0.2 to 3.2 Jy beam^{-1} km s^{-1} by steps of 0.2 Jy beam^{-1} km s^{-1}). Bottom left: line velocity distribution (contour levels from 50 to 650 km s^{-1} by steps of 50). Bottom right: line width distribution (contour levels from 20 to 300 km s^{-1} by steps of 20).

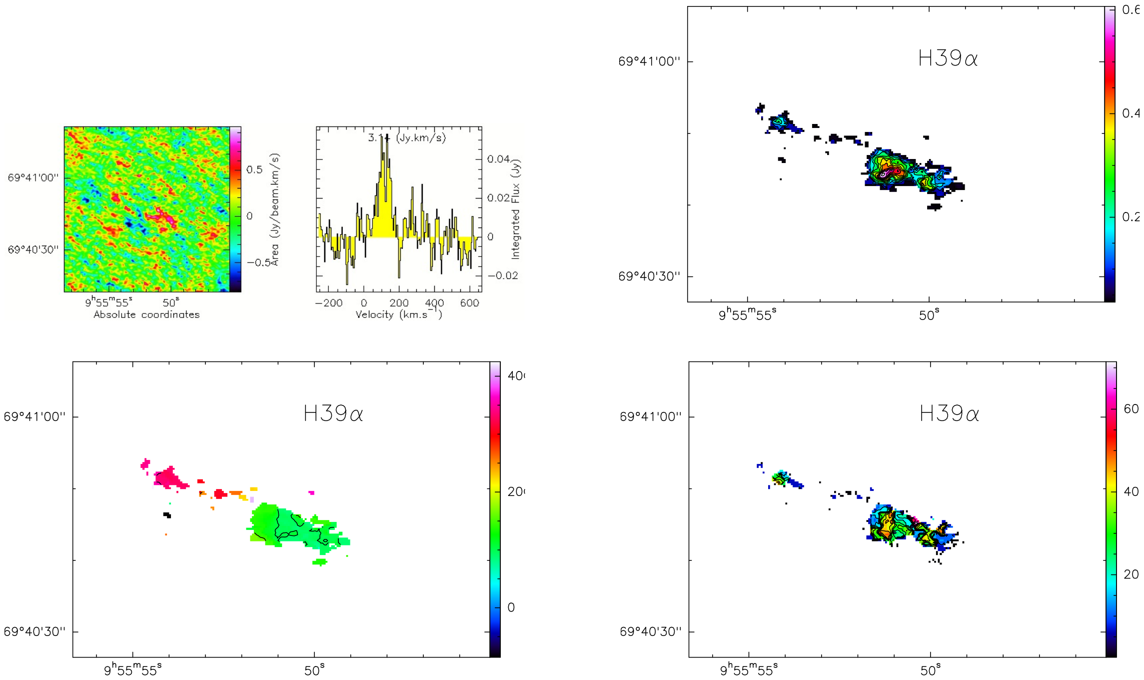

Figure C.13: H39α at 106.737 GHz in M 82 .Top left: line image with its spectrum. Top right: line flux distribution (contour levels from 0.05 to 0.6 Jy beam^{-1} km s^{-1} by steps of 0.05 Jy beam^{-1} km s^{-1}). Bottom left: line velocity distribution (contour levels from -100 to 400 km s^{-1} by steps of 50). Bottom right: line width distribution (contour levels from 5 to 70 km s^{-1} by steps of 5).

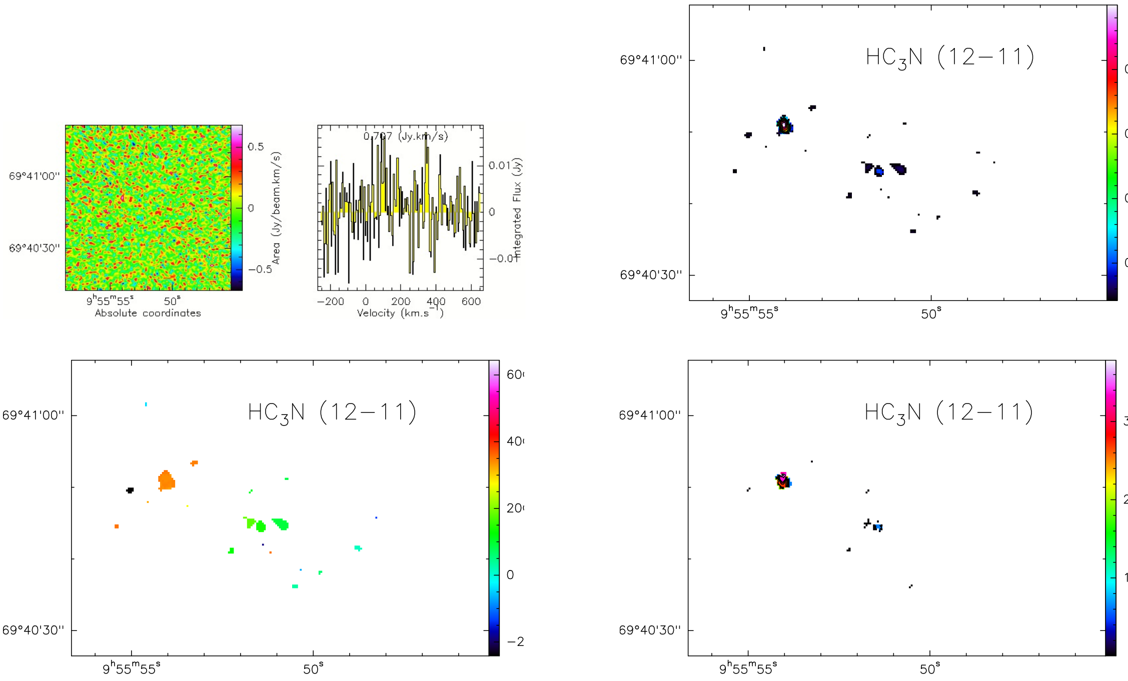

Figure C.14: HC$_3$N at 109.174 GHz in M 82 .Top left: line image with its spectrum. Top right: line flux distribution (contour levels from 0.05 to 0.5 Jy beam^{-1} km s^{-1} by steps of 0.05 Jy beam^{-1} km s^{-1}). Bottom left: line velocity distribution (contour levels from -200 to 600 km s^{-1} by steps of 20). Bottom right: line width distribution (contour levels from 2 to 38 km s^{-1} by steps of 2).

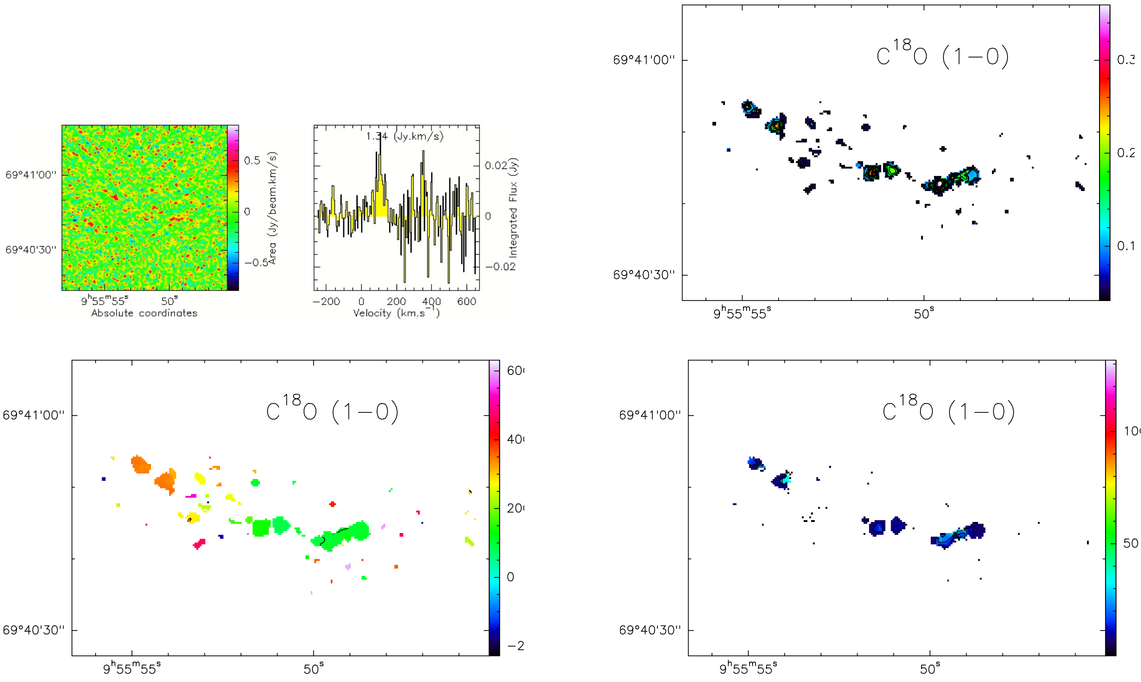

Figure C.15: C^{18}O at 109.782 GHz in M 82 .Top left: line image with its spectrum. Top right: line flux distribution (contour levels from 0.02 to 0.36 Jy beam^{-1} km s^{-1} by steps of 0.02 Jy beam^{-1} km s^{-1}). Bottom left: line velocity distribution (contour levels from -200 to 600 km s^{-1} by steps of 100). Bottom right: line width distribution (contour levels from 10 to 130 km s^{-1} by steps of 10).

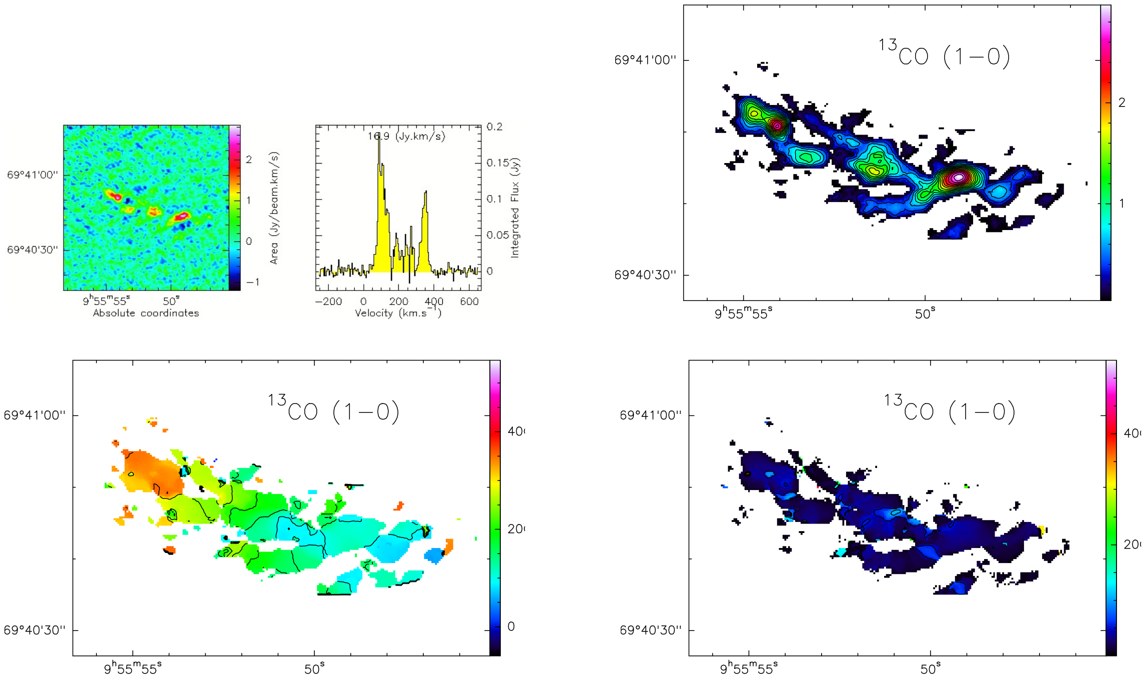

Figure C.16: ^{13}CO at 110.201 GHz in M 82 .Top left: line image with its spectrum. Top right: line flux distribution (contour levels from 0.2 to 3 Jy beam^{-1} km s^{-1} by steps of 0.2 Jy beam^{-1} km s^{-1}). Bottom left: line velocity distribution (contour levels from -50 to 550 km s^{-1} by steps of 50). Bottom right: line width distribution (contour levels from 50 to 550 km s^{-1} by steps of 50).

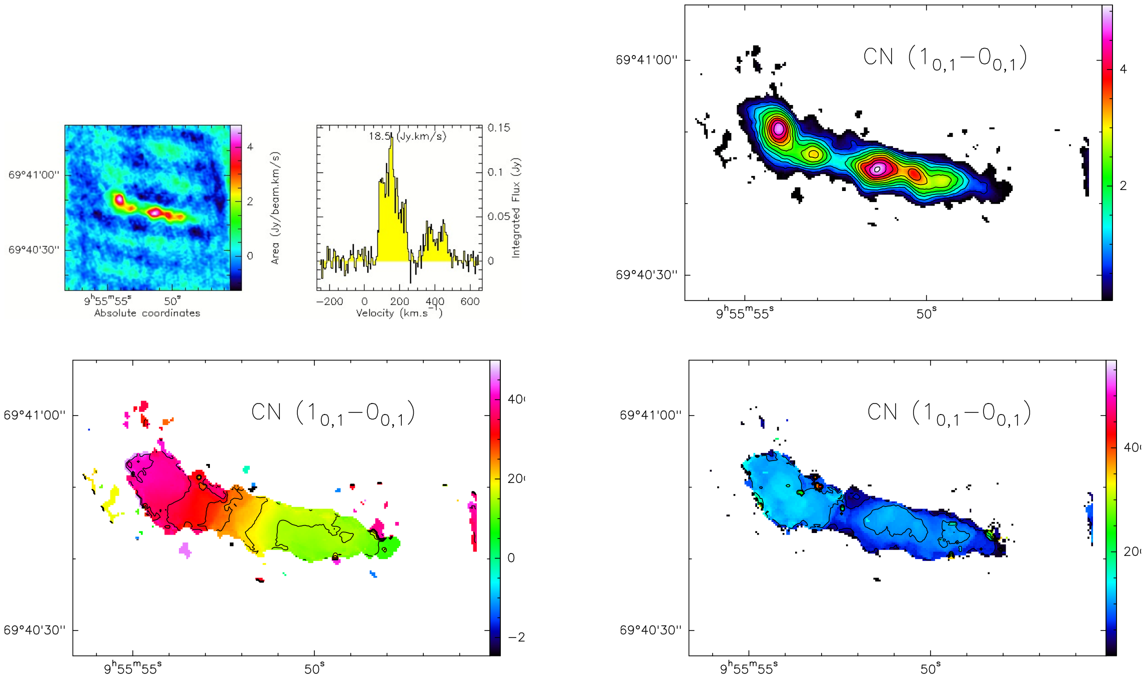

Figure C.17: CN at 113.191 GHz in M 82 .Top left: line image with its spectrum. Top right: line flux distribution (contour levels from 0.5 to 5 Jy beam^{-1} km s^{-1} by steps of 0.5 Jy beam^{-1} km s^{-1}). Bottom left: line velocity distribution (contour levels from -250 to 500 km s^{-1} by steps of 50). Bottom right: line width distribution (contour levels from 50 to 550 km s^{-1} by steps of 50).

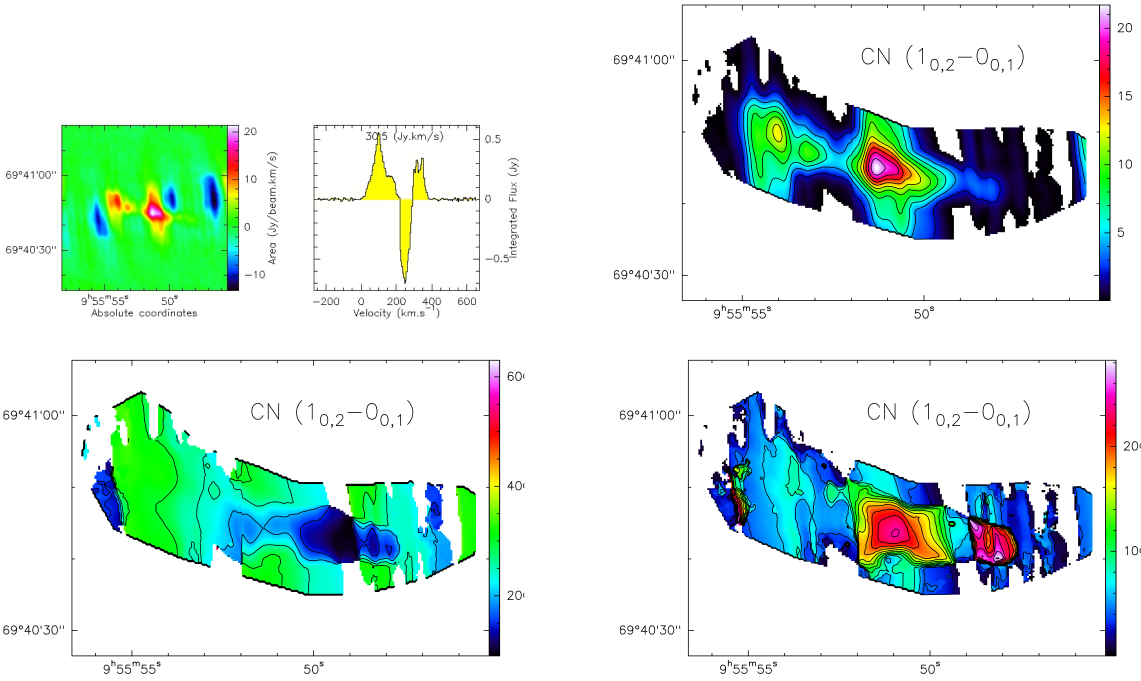

Figure C.18: CN at 113.491 GHz in M 82 .Top left: line image with its spectrum. Top right: line flux distribution (contour levels from 2 to 22 Jy beam^{-1} km s^{-1} by steps of 2 Jy beam^{-1} km s^{-1}). Bottom left: line velocity distribution (contour levels from 50 to 650 km s^{-1} by steps of 50). Bottom right: line width distribution (contour levels from 20 to 280 km s^{-1} by steps of 20).

C.2 IC 342

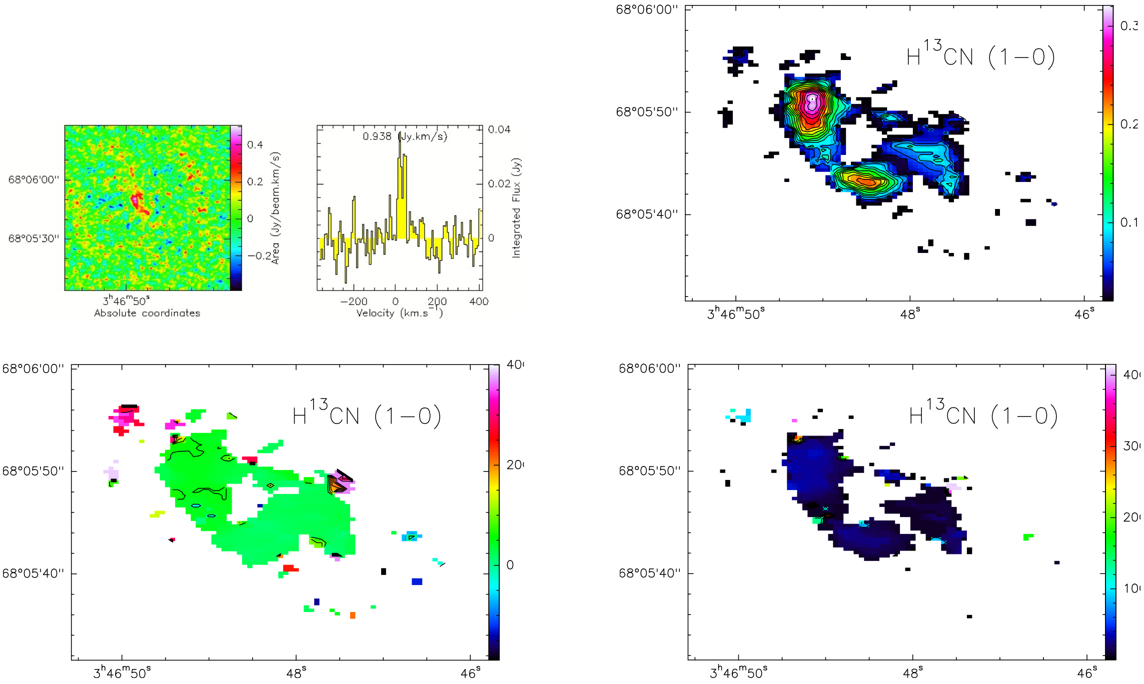

Figure C.19: H^{13}CN at 86.754 GHz in IC 342. Top left: line image with its spectrum. Top right: line flux distribution (contour levels from 0.02 to 0.32 Jy beam^{-1} km s^{-1} by steps of 0.02 Jy beam^{-1} km s^{-1}). Bottom left: line velocity distribution (contour levels from -200 to 400 km s^{-1} by steps of 50). Bottom right: line width distribution in (contour levels from 50 to 400 km s^{-1} by steps of 50).

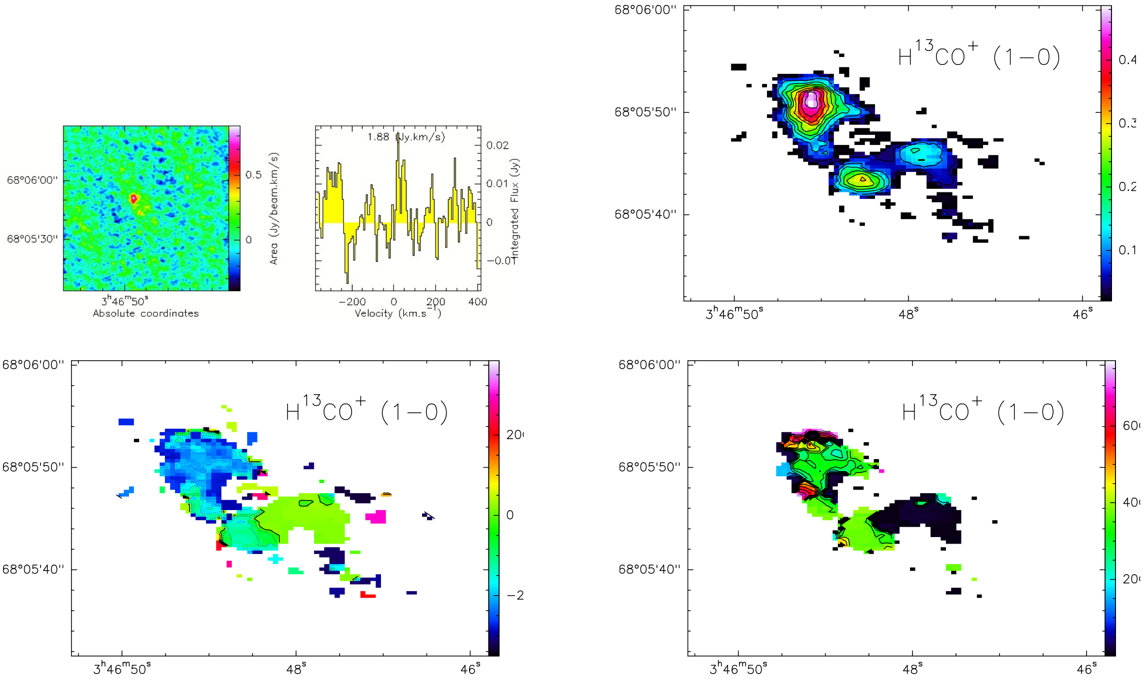

Figure C.20: H^{13}CO^{+} at 86.754 GHz in IC 342. Top left: line image with its spectrum. Top right: line flux distribution (contour levels from 0.05 to 0.5 Jy beam^{-1} km s^{-1} by steps of 0.05 Jy beam^{-1} km s^{-1}). Bottom left: line velocity distribution (contour levels from -350 to 400 km s^{-1} by steps of 50). Bottom right: line width distribution (contour levels from 50 to 750 km s^{-1} by steps of 50).

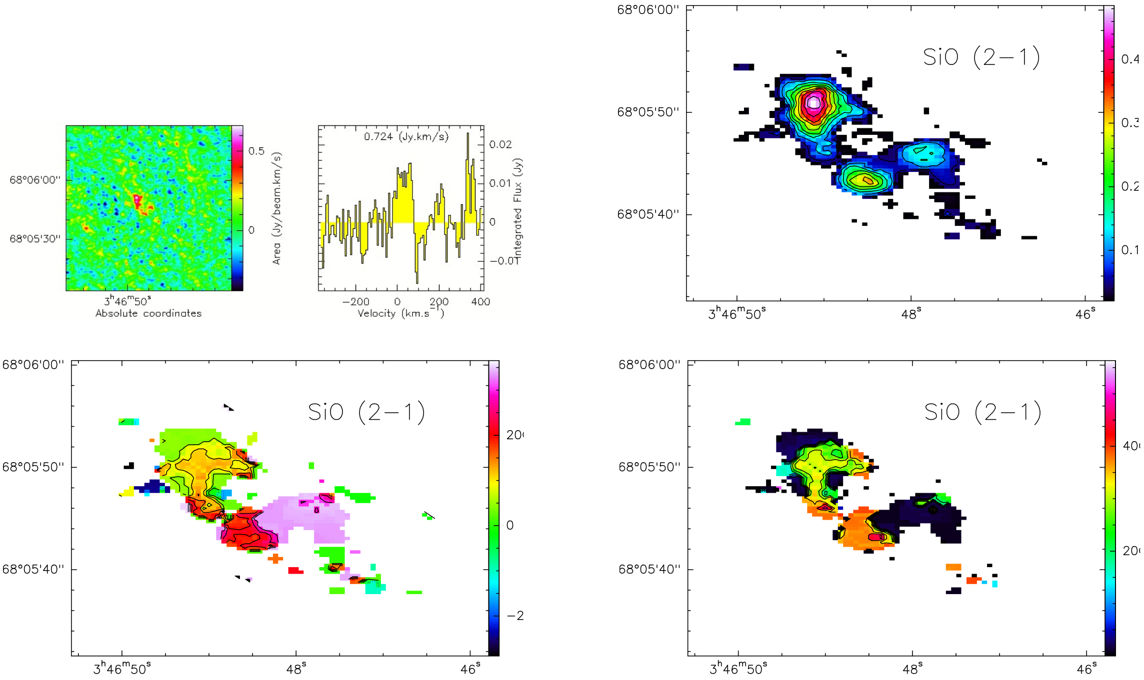

Figure C.21: SiO at 86.754 GHz in IC 342. Top left: line image with its spectrum. Top right: line flux distribution (contour levels from 0.05 to 0.5 Jy beam^{-1} km s^{-1} by steps of 0.05 Jy beam^{-1} km s^{-1}). Bottom left: line velocity distribution (contour levels from -300 to 350 km s^{-1} by steps of 50). Bottom right: line width distribution (contour levels from 50 to 550 km s^{-1} by steps of 50).

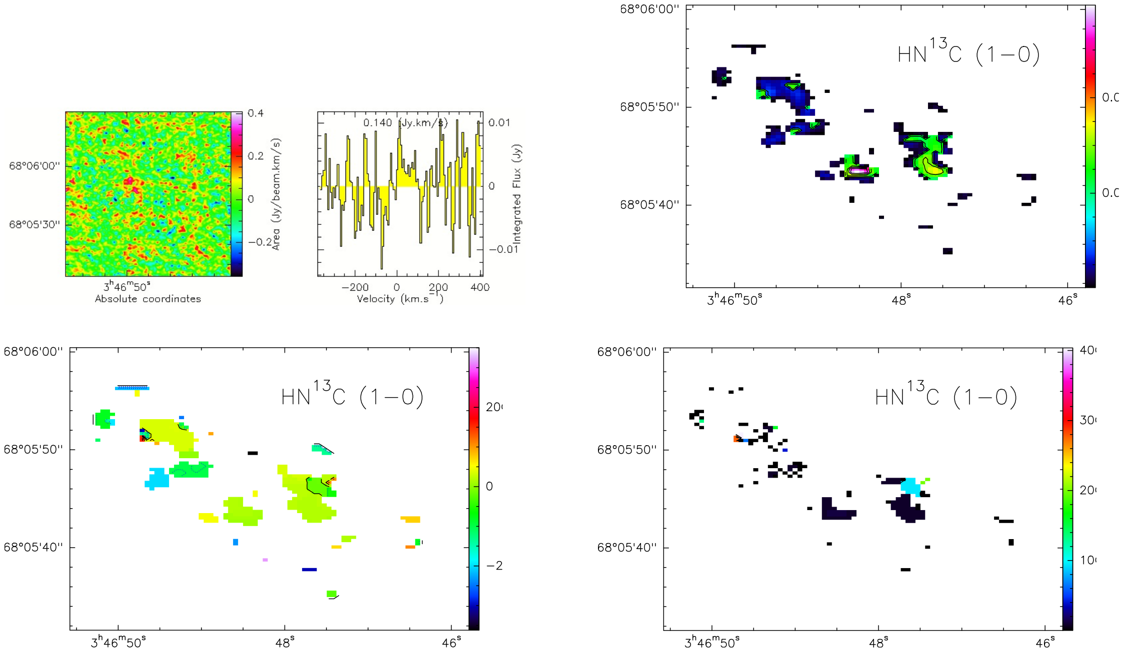

Figure C.22: HN^{13}C at 86.754 GHz in IC 342. Top left: line image with its spectrum. Top right: line flux distribution (contour levels from 0.01 to 0.08 Jy beam^{-1} km s^{-1} by steps of 0.01 Jy beam^{-1} km s^{-1}). Bottom left: line velocity distribution (contour levels from -350 to 500 km s^{-1} by steps of 50). Bottom right: line width distribution (contour levels from 50 to 400 km s^{-1} by steps of 50).

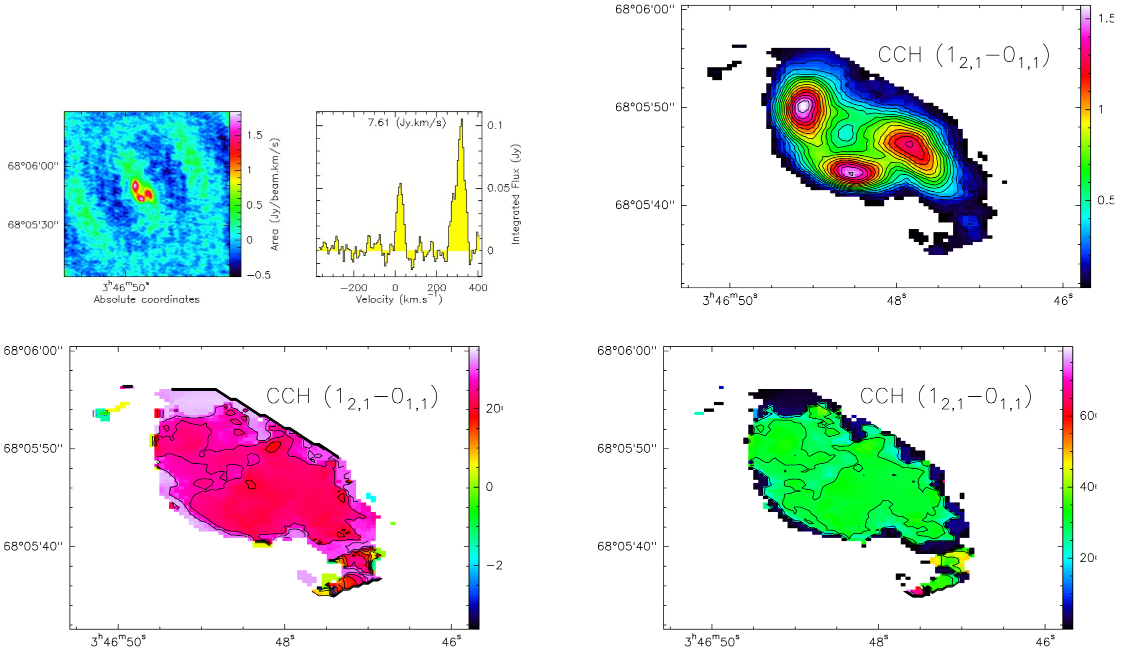

Figure C.23: CCH at 87.317 GHz in IC 342. Top left: line image with its spectrum. Top right: line flux distribution (contour levels from 0.1 to 1.38 Jy beam^{-1} km s^{-1} by steps of 0.1 Jy beam^{-1} km s^{-1}). Bottom left: line velocity distribution (contour levels from -180 to 100 km s^{-1} by steps of 20). Bottom right: line width distribution (contour levels from 10 to 170 km s^{-1} by steps of 10) (The velocity distribution and width distribution were plotted for the line at 87.402 GHz with a range of -200 to 200 km s^{-1}).

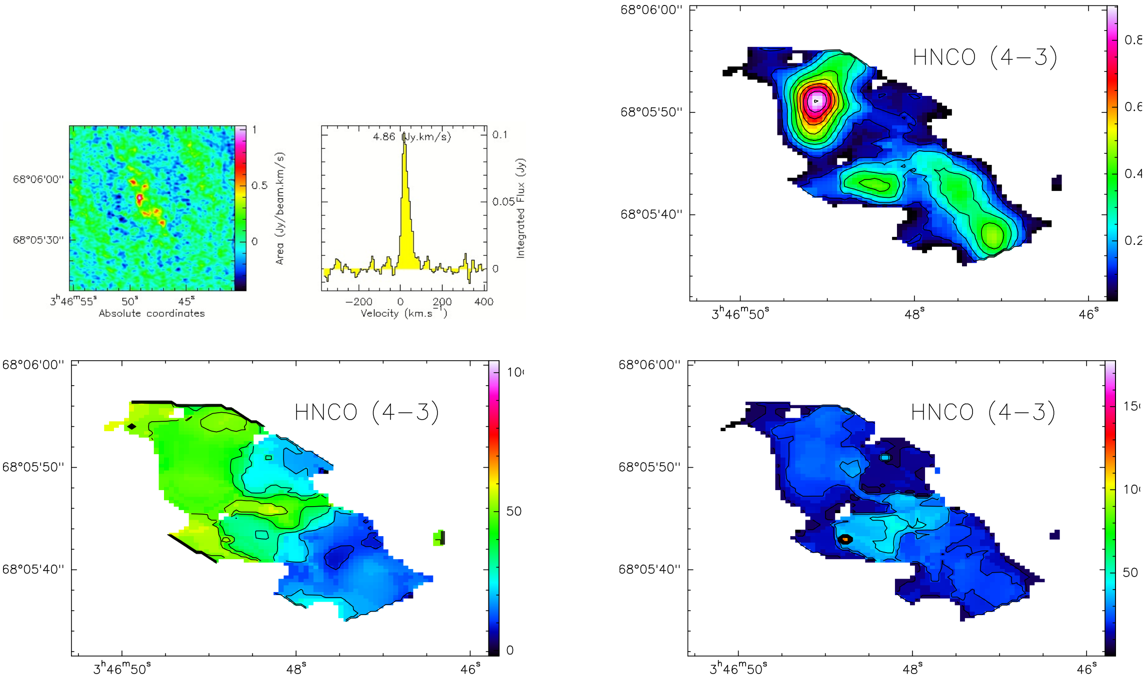

Figure C.24: HNCO at 87.925 GHz in IC 342. Top left: line image with its spectrum. Top right: line flux distribution (contour levels from 0.1 to 0.9 Jy beam^{-1} km s^{-1} by steps of 0.1 Jy beam^{-1} km s^{-1}). Bottom left: line velocity distribution (contour levels from 10 to 100 km s^{-1} by steps of 10). Bottom right: line width distribution (contour levels from 10 to 180 km s^{-1} by steps of 50).

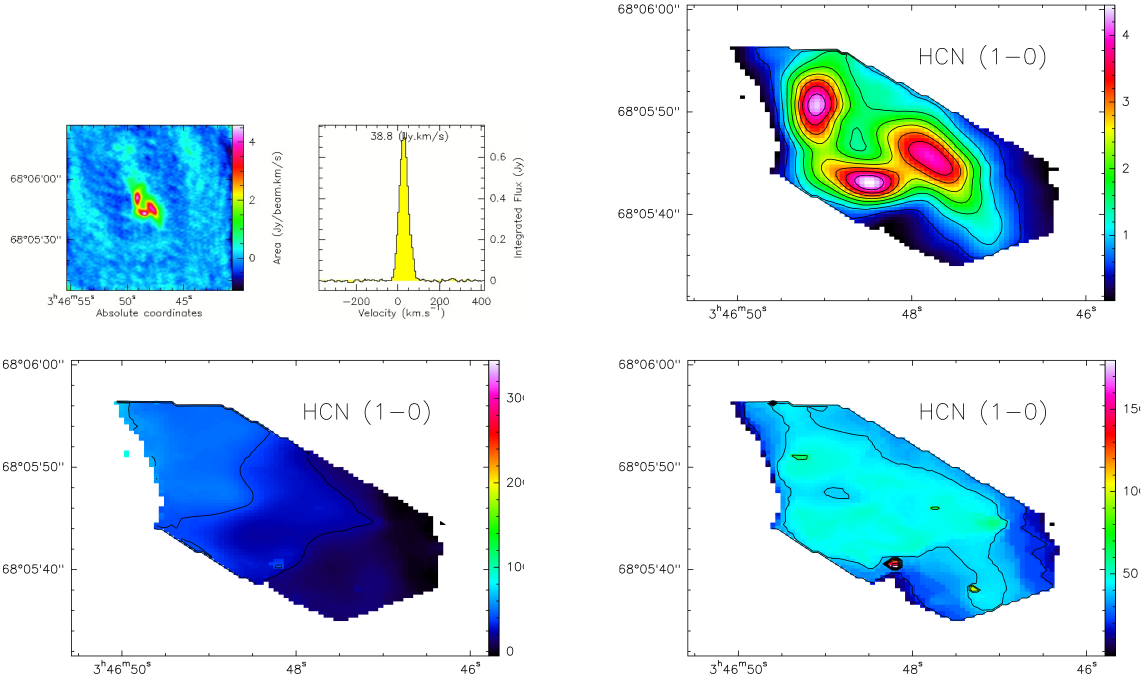

Figure C.25: HCN at 88.631 GHz in IC 342. Top left: line image with its spectrum. Top right: line flux distribution (contour levels from 0.5 to 4.5 Jy beam^{-1} km s^{-1} by steps of 0.5 Jy beam^{-1} km s^{-1}). Bottom left: line velocity distribution (contour levels from 20 to 340 km s^{-1} by steps of 20). Bottom right: line width distribution (contour levels from 20 to 180 km s^{-1} by steps of 20).

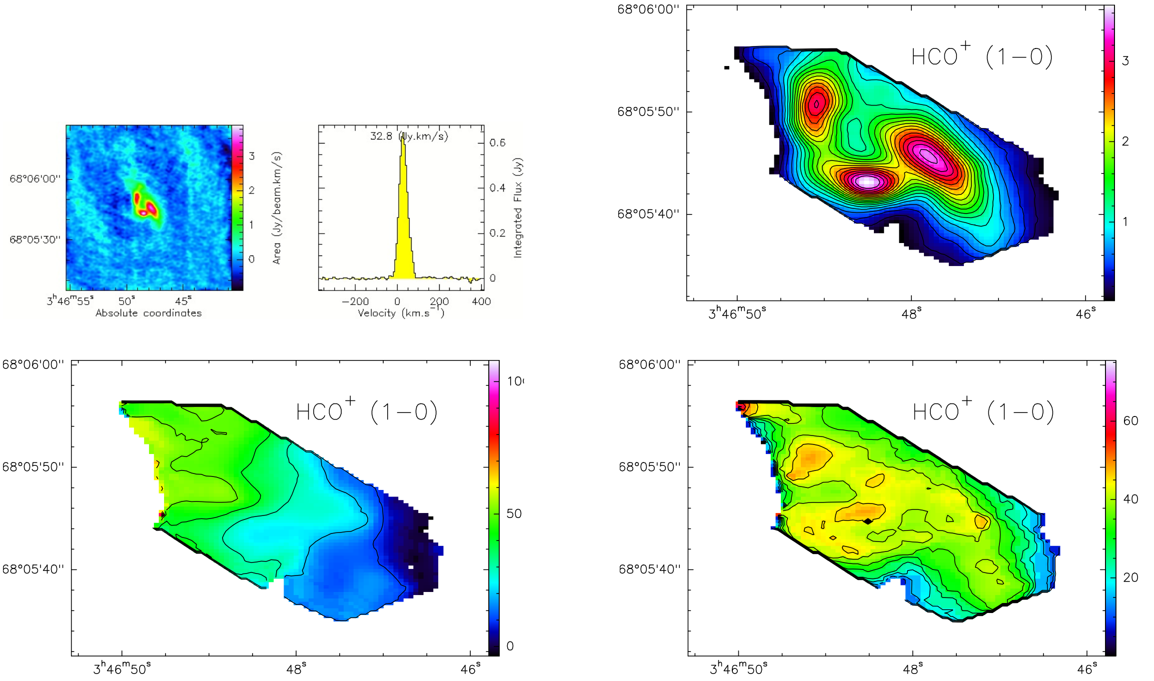

Figure C.26: HCO$^+$ at 89.188 GHz in IC 342. Top left: line image with its spectrum. Top right: line flux distribution (contour levels from 0.2 to 3.6 Jy beam^{-1} km s^{-1} by steps of 0.2 Jy beam^{-1} km s^{-1}). Bottom left: line velocity distribution (contour levels from 10 to 110 km s^{-1} by steps of 10). Bottom right: line width distribution (contour levels from 5 to 75 km s^{-1} by steps of 5).

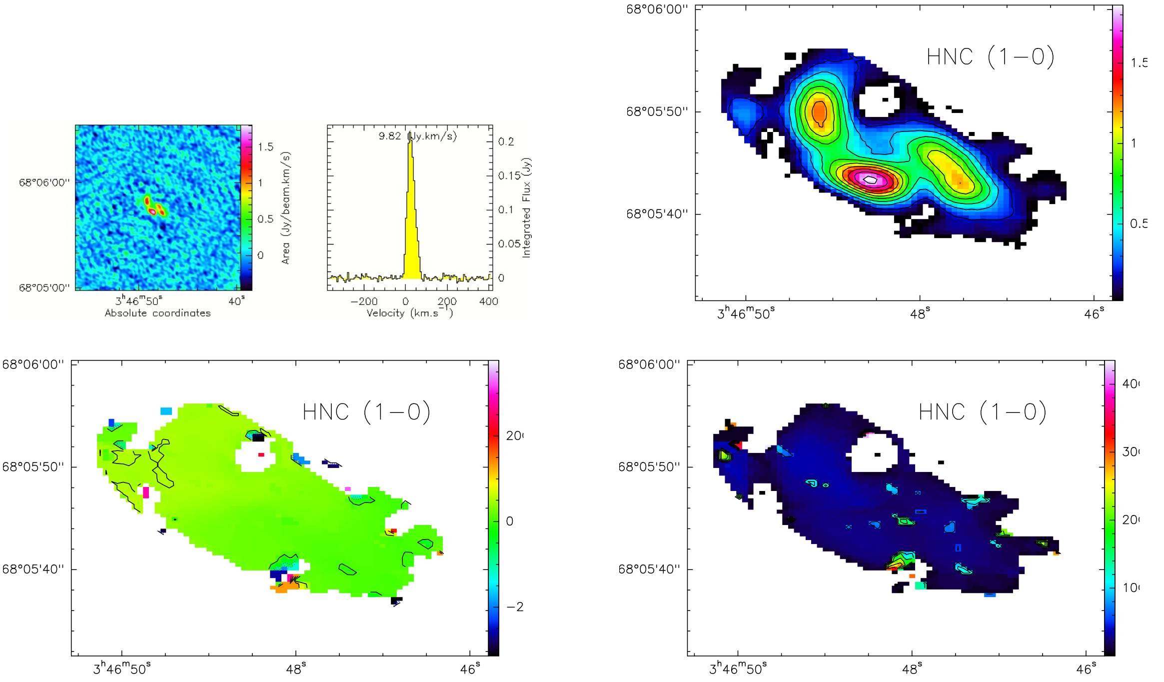

Figure C.27: HNC at 90.663 GHz in IC 342. Top left: line image with its spectrum. Top right: line flux distribution (contour levels from 0.2 to 1.8 Jy beam^{-1} km s^{-1} by steps of 0.2 Jy beam^{-1} km s^{-1}). Bottom left: line velocity distribution (contour levels from -300 to 400 km s^{-1} by steps of 50). Bottom right: line width distribution (contour levels from 50 to 450 km s^{-1} by steps of 50).

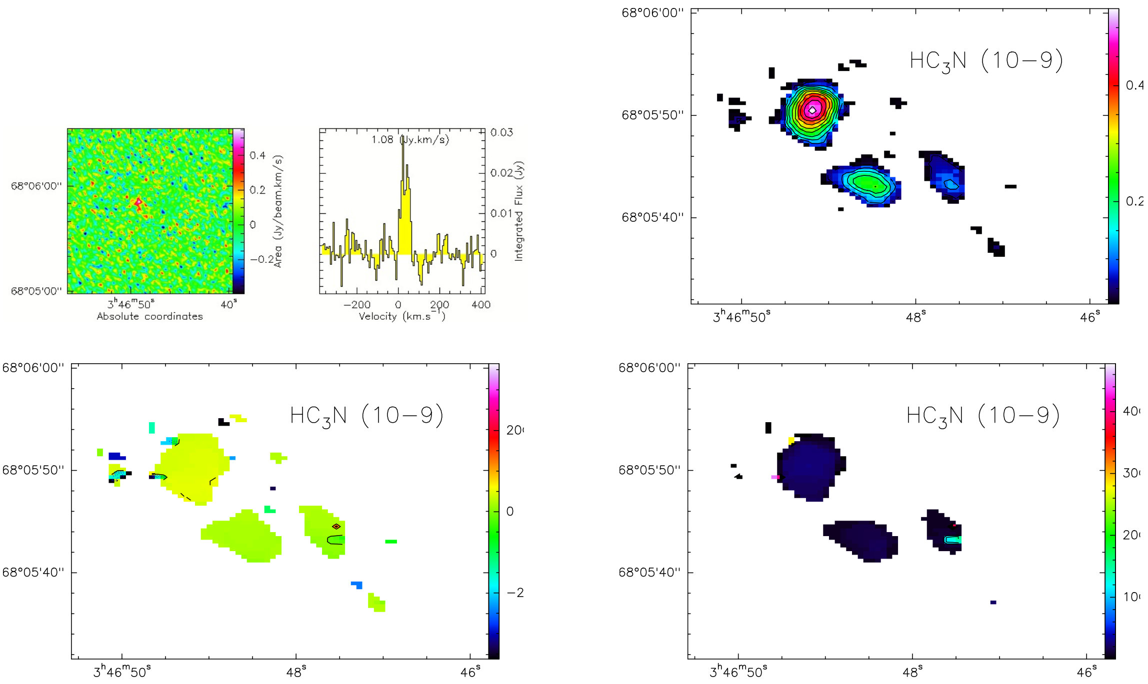

Figure C.28: HC_3N at 90.978 GHz in IC 342. Top left: line image with its spectrum. Top right: line flux distribution (contour levels from 0.05 to 0.55 Jy beam^{-1} km s^{-1} by steps of 0.05 Jy beam^{-1} km s^{-1}). Bottom left: line velocity distribution (contour levels from -350 to 350 km s^{-1} by steps of 50). Bottom right: line width distribution (contour levels from 50 to 500 km s^{-1} by steps of 50).

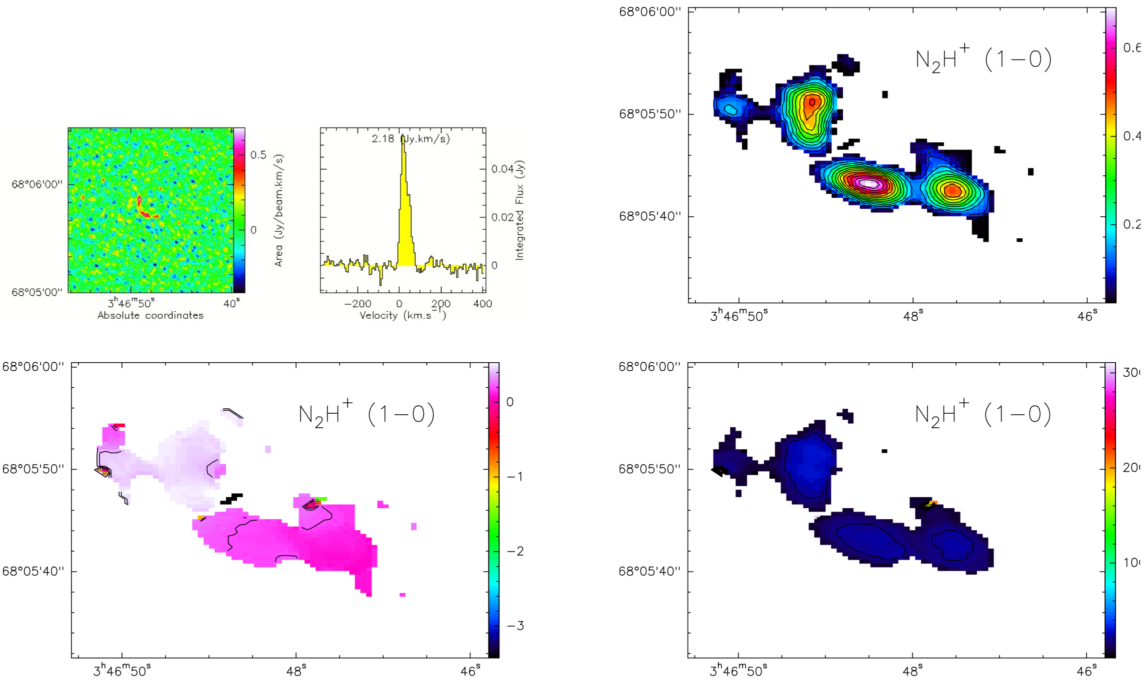

Figure C.29: N_2H^+ at 93.173 GHz in IC 342. Top left: line image with its spectrum. Top right: line flux distribution (contour levels from 0.05 to 0.7 Jy beam^{-1} km s^{-1} by steps of 0.05 Jy beam^{-1} km s^{-1}). Bottom left: line velocity distribution (contour levels from -340 to 60 km s^{-1} by steps of 20). Bottom right: line width distribution (contour levels from 20 to 320 km s^{-1} by steps of 20).

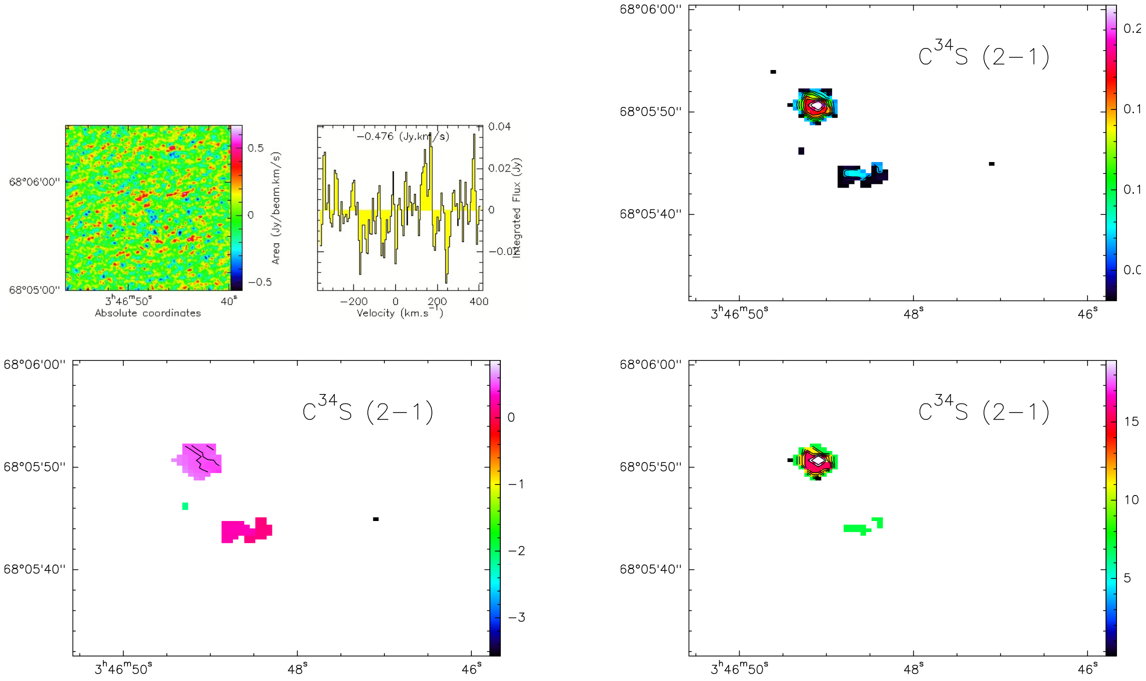

Figure C.30: $C^{34}S$ at 96.413 GHz in IC 342. Top left: line image with its spectrum. Top right: line flux distribution (contour levels from 0.02 to 0.22 Jy beam^{-1} km s^{-1} by steps of 0.02 Jy beam^{-1} km s^{-1}). Bottom left: line velocity distribution (contour levels from -350 to 100 km s^{-1} by steps of 50). Bottom right: line width distribution (contour levels from 2 to 18 km s^{-1} by steps of 20).

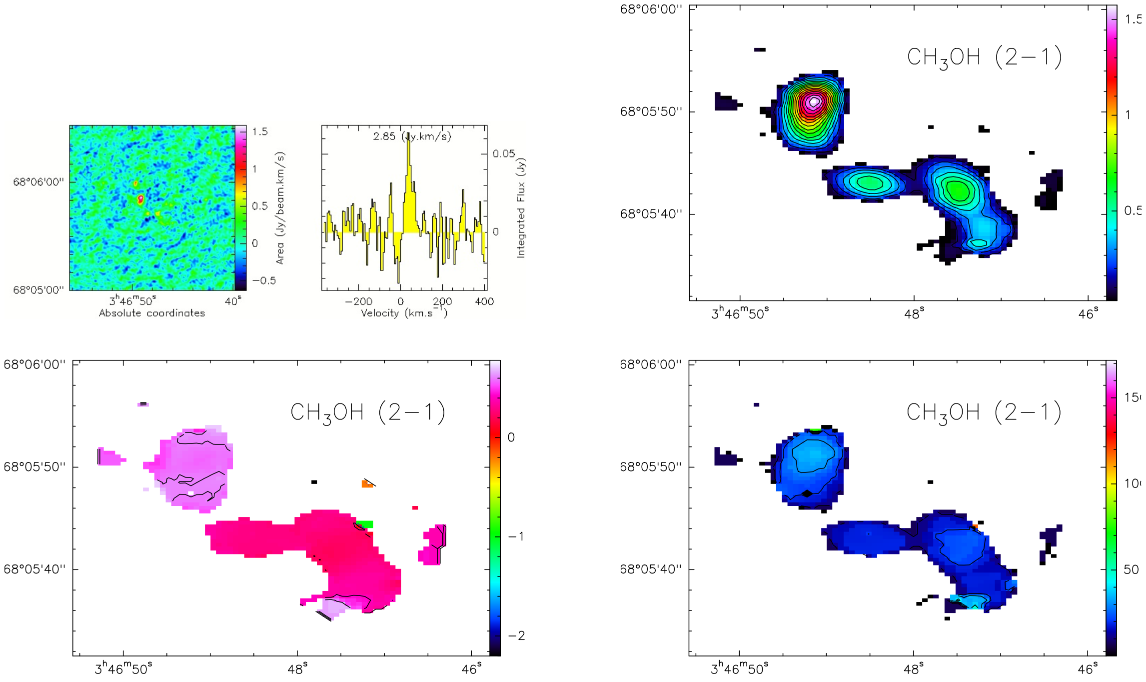

Figure C.31: CH_3OH at 86.754 GHz in IC 342. Top left: line image with its spectrum. Top right: line flux distribution (contour levels from 0.1 to 1.6 Jy beam^{-1} km s^{-1} by steps of 0.1 Jy beam^{-1} km s^{-1}). Bottom left: line velocity distribution (contour levels from -220 to 80 km s^{-1} by steps of 20). Bottom right: line width distribution (contour levels from 10 to 170 km s^{-1} by steps of 10).

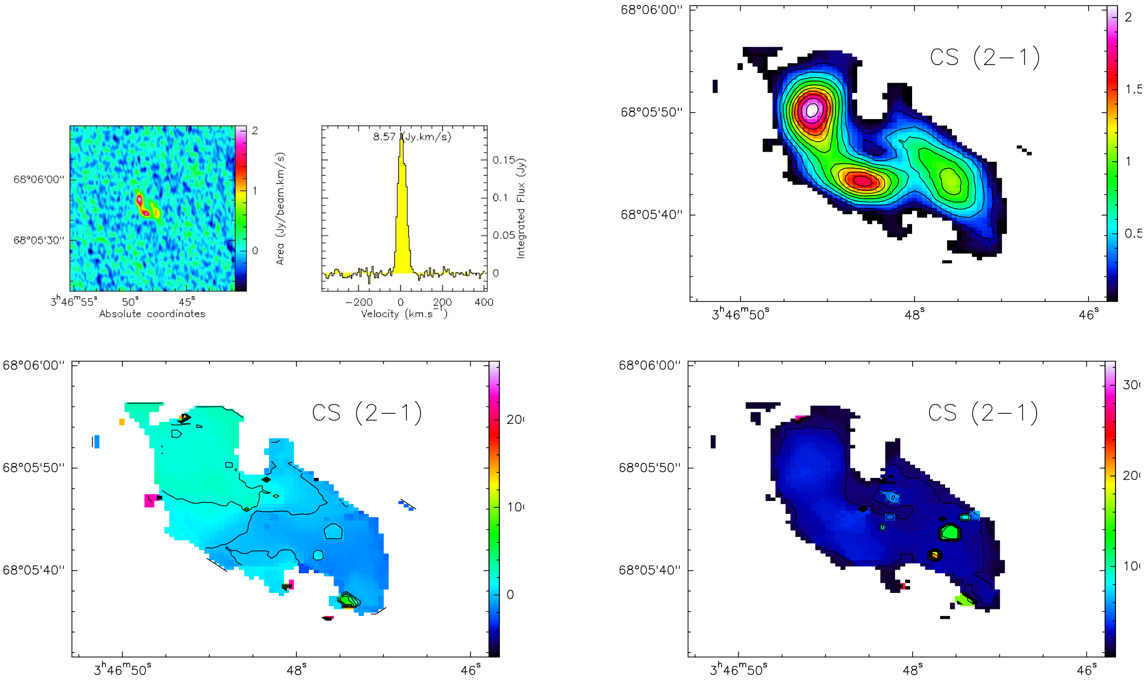

Figure C.32: CS at 97.973 GHz in IC 342. Top left: line image with its spectrum. Top right: line flux distribution (contour levels from 0.2 to 2 Jy beam^{-1} km s^{-1} by steps of 0.2 Jy beam^{-1} km s^{-1}). Bottom left: line velocity distribution (contour levels from -80 to 260 km s^{-1} by steps of 20). Bottom right: line width distribution (contour levels from 20 to 320 km s^{-1} by steps of 20).

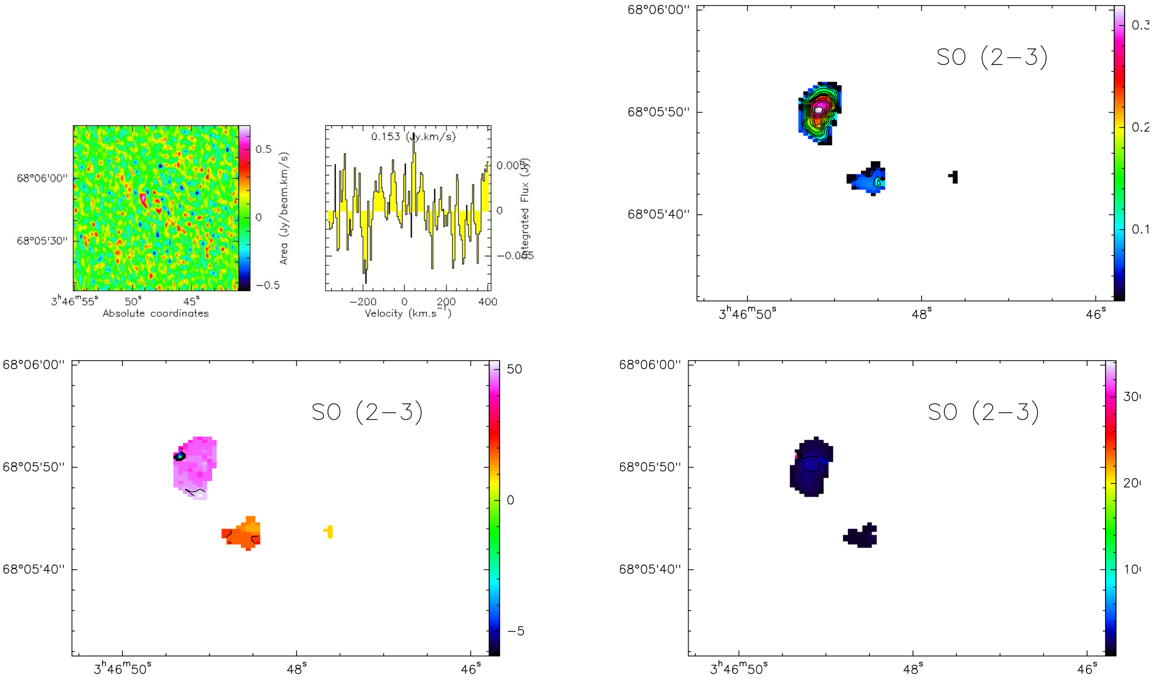

Figure C.33: SO at 99.299 GHz in IC 342. Top left: line image with its spectrum. Top right: line flux distribution (contour levels from 0.02 to 0.32 Jy beam^{-1} km s^{-1} by steps of 0.02 Jy beam^{-1} km s^{-1}). Bottom left: line velocity distribution (contour levels from -60 to 50 km s^{-1} by steps of 10). Bottom right: line width distribution (contour levels from 20 to 340 km s^{-1} by steps of 20).

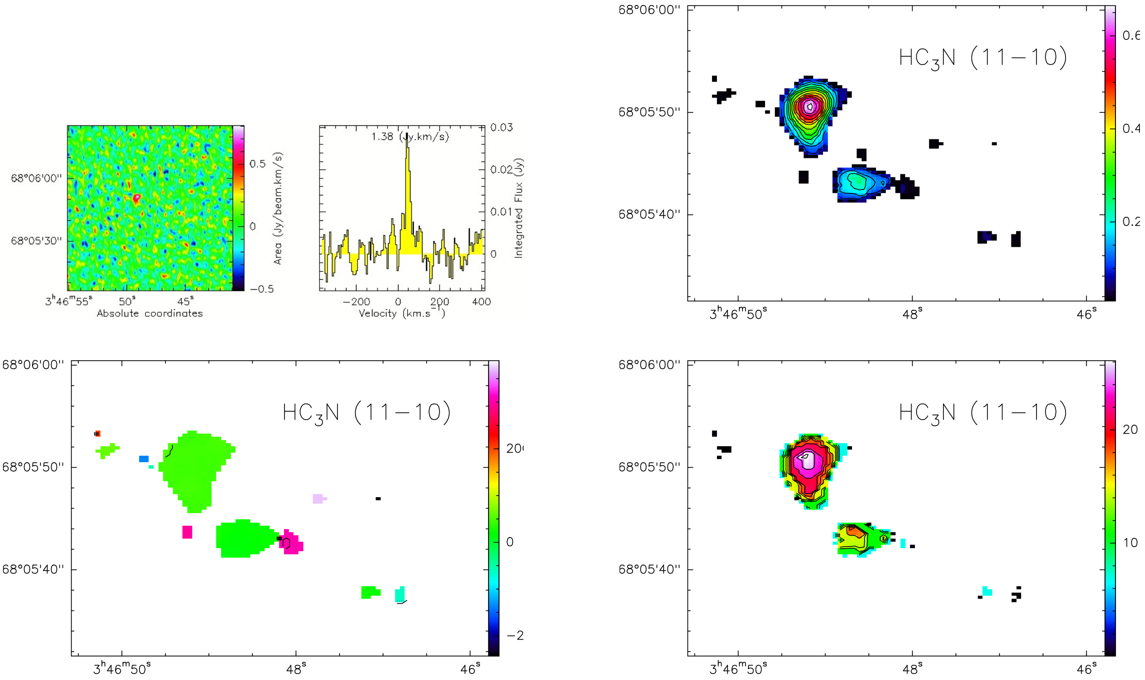

Figure C.34: HC$_3$N at 100.076 GHz in IC 342. Top left: line image with its spectrum. Top right: line flux distribution (contour levels from 0.05 to 0.65 Jy beam^{-1} km s^{-1} by steps of 0.05 Jy beam^{-1} km s^{-1}). Bottom left: line velocity distribution (contour levels from -250 to 400 km s^{-1} by steps of 50). Bottom right: line width distribution (contour levels from 2 to 26 km s^{-1} by steps of 2).

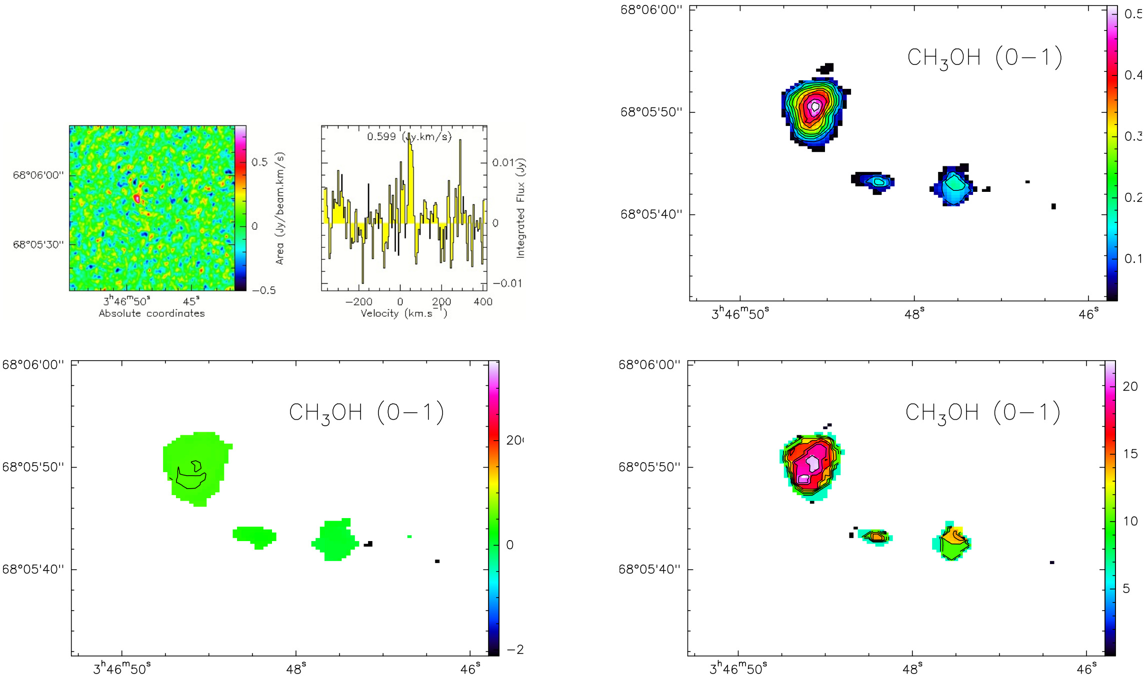

Figure C.35: CH$_3$OH at 108.894 GHz in IC 342. Top left: line image with its spectrum. Top right: line flux distribution (contour levels from 0.05 to 0.5 Jy beam^{-1} km s^{-1} by steps of 0.05 Jy beam^{-1} km s^{-1}). Bottom left: line velocity distribution (contour levels from -200 to 350 km s^{-1} by steps of 50). Bottom right: line width distribution (contour levels from 2 to 22 km s^{-1} by steps of 2).

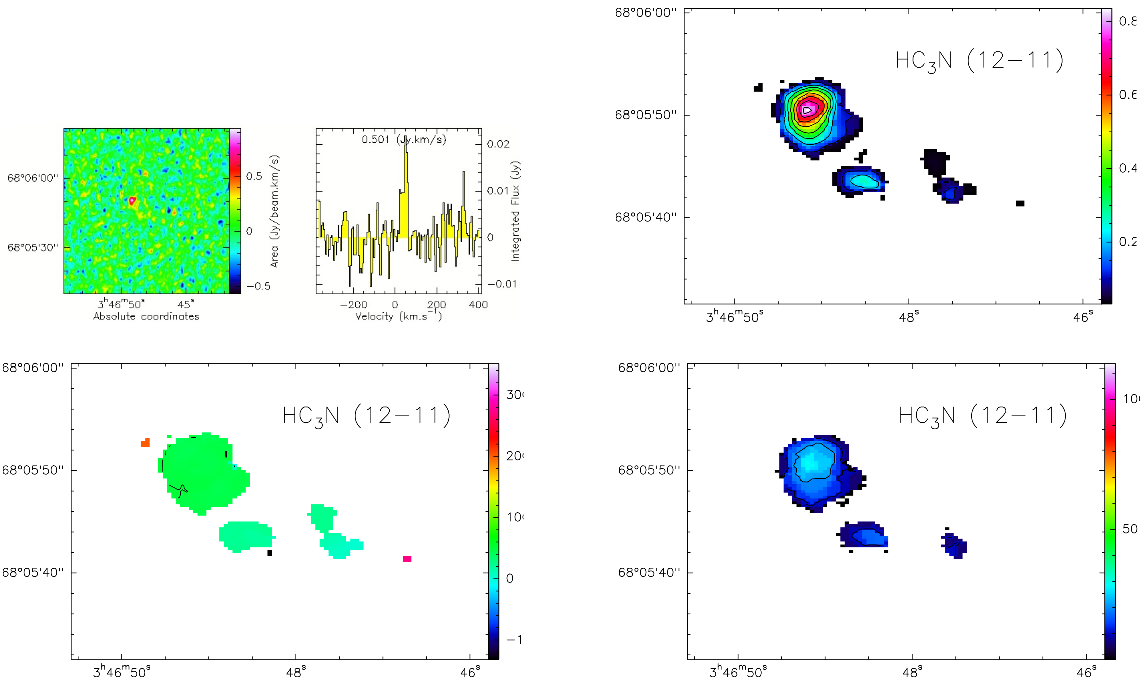

Figure C.36: HC$_3$N at 109.173 GHz in IC 342. Top left: line image with its spectrum. Top right: line flux distribution (contour levels from 0.1 to 0.8 Jy beam^{-1} km s^{-1} by steps of 0.1 Jy beam^{-1} km s^{-1}). Bottom left: line velocity distribution (contour levels from -150 to 350 km s^{-1} by steps of 50). Bottom right: line width distribution (contour levels from 10 to 110 km s^{-1} by steps of 50).

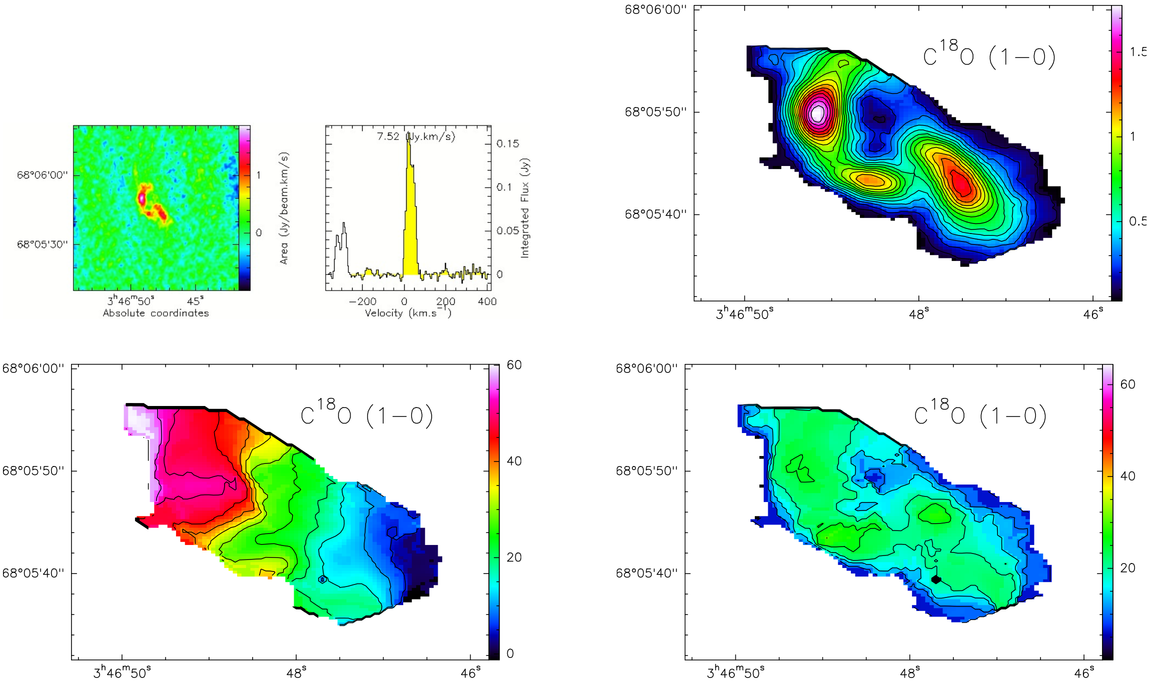

Figure C.37: C^{18}O at 109.782 GHz in IC 342. Top left: line image with its spectrum. Top right: line flux distribution (contour levels from 0.1 to 1.8 Jy beam^{-1} km s^{-1} by steps of 0.1 Jy beam^{-1} km s^{-1}). Bottom left: line velocity distribution (contour levels from 5 to 60 km s^{-1} by steps of 5). Bottom right: line width distribution (contour levels from 5 to 65 km s^{-1} by steps of 5).

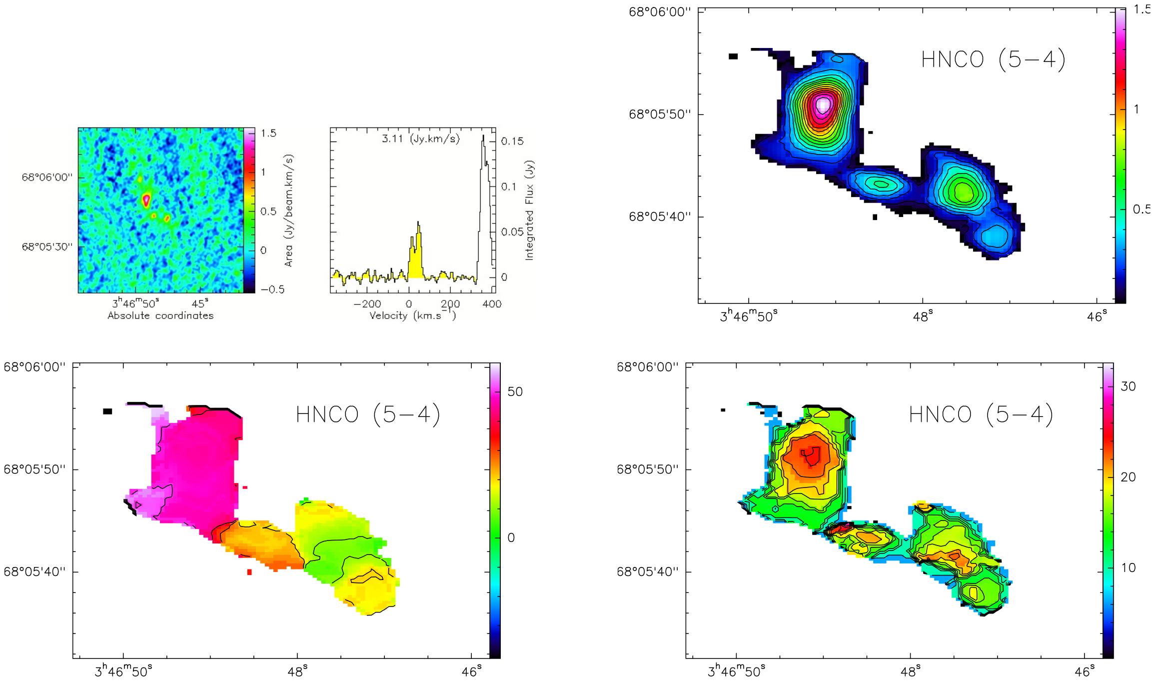

Figure C.38: HNCO at 109.905 GHz in IC 342. Top left: line image with its spectrum. Top right: line flux distribution (contour levels from 0.1 to 1.5 Jy beam^{-1} km s^{-1} by steps of 0.1 Jy beam^{-1} km s^{-1}). Bottom left: line velocity distribution (contour levels from -40 to 60 km s^{-1} by steps of 10). Bottom right: line width distribution (contour levels from 2 to 32 km s^{-1} by steps of 2).

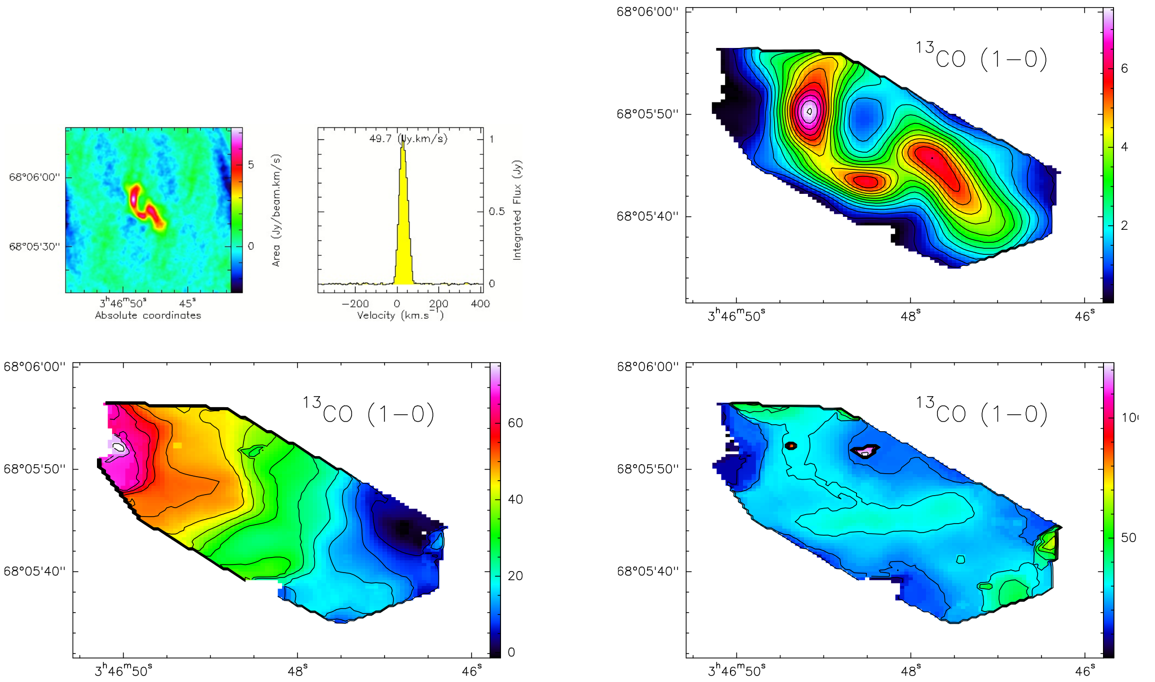

Figure C.39: ^{13}CO at 110.201 GHz in IC 342. Top left: line image with its spectrum. Top right: line flux distribution (contour levels from 0.5 to 7.5 Jy beam^{-1} km s^{-1} by steps of 0.5 Jy beam^{-1} km s^{-1}). Bottom left: line velocity distribution (contour levels from 5 to 75 km s^{-1} by steps of 5). Bottom right: line width distribution (contour levels from 10 to 120 km s^{-1} by steps of 10).

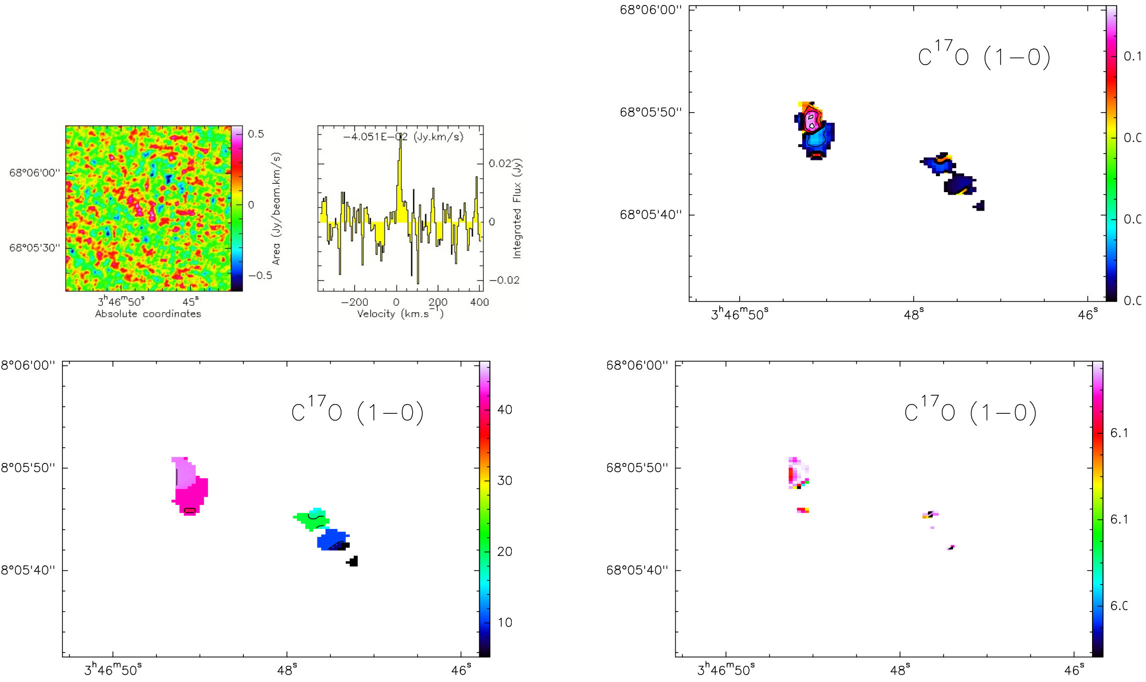

Figure C.40: C^{17}O at 112.358 GHz in IC 342. Top left: line image with its spectrum. Top right: line flux distribution (contour levels from 0.01 to 0.11 Jy beam^{-1} km s^{-1} by steps of 0.01 Jy beam^{-1} km s^{-1}). Bottom left: line velocity distribution (contour levels from 5 to 45 km s^{-1} by steps of 5). Bottom right: line width distribution (contour levels from 0.5 to 6 km s^{-1} by steps of 0.5).

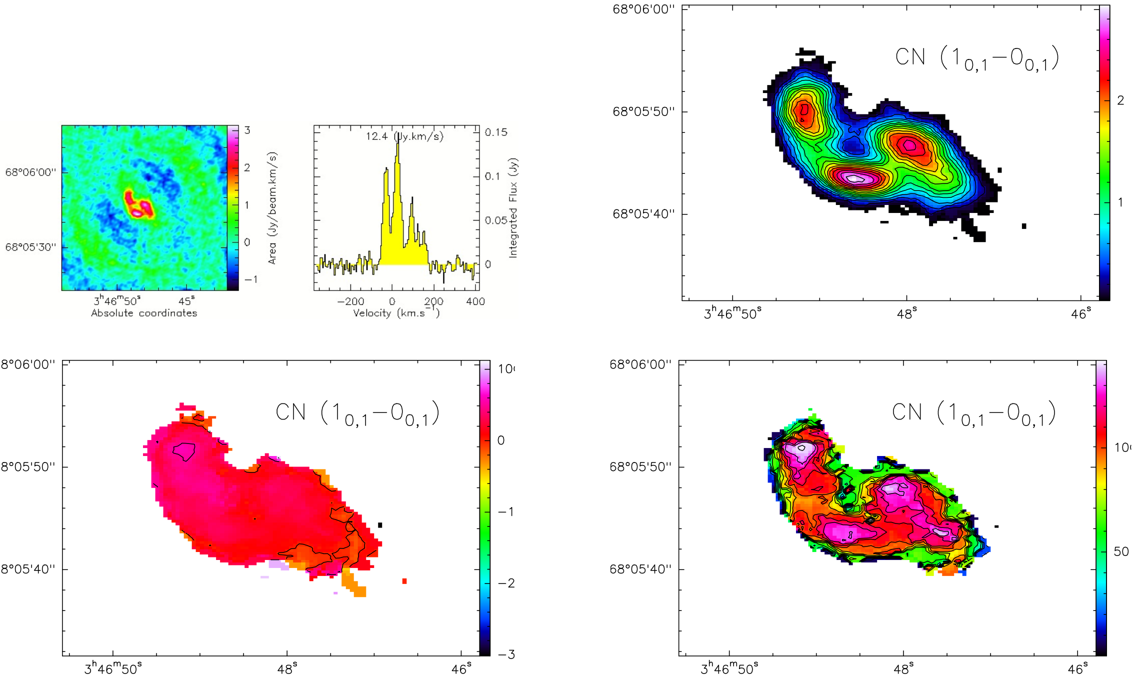

Figure C.41: CN at 113.191 GHz in IC 342. Top left: line image with its spectrum. Top right: line flux distribution (contour levels from 0.2 to 3 Jy beam^{-1} km s^{-1} by steps of 0.2 Jy beam^{-1} km s^{-1}). Bottom left: line velocity distribution (contour levels from -300 to 100 km s^{-1} by steps of 50). Bottom right: line width distribution (contour levels from 10 to 140 km s^{-1} by steps of 10).

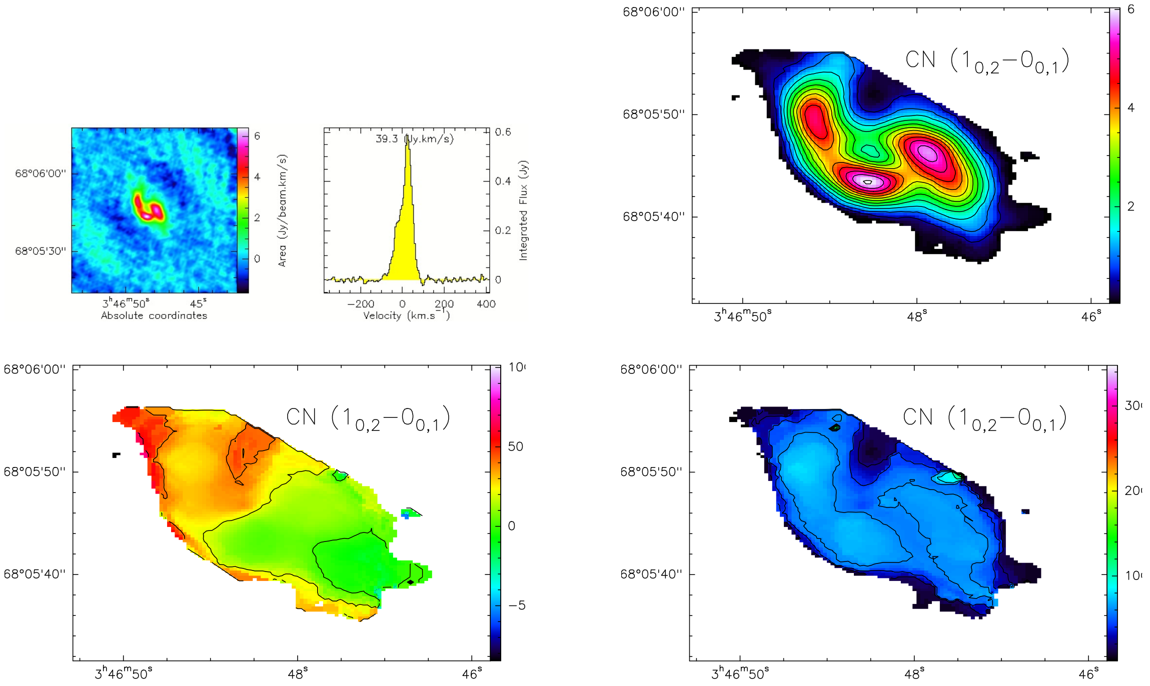

Figure C.42: CN at 113.491 GHz in IC 342. Top left: line image with its spectrum. Top right: line flux distribution (contour levels from 0.5 to 6 Jy beam^{-1} km s^{-1} by steps of 0.5 Jy beam^{-1} km s^{-1}). Bottom left: line velocity distribution (contour levels from -80 to 100 km s^{-1} by steps of 20). Bottom right: line width distribution (contour levels from 20 to 340 km s^{-1} by steps of 20).

Appendix D

Gaussian Fitting with GILDAS

D.1 M 82

D.1.1 Position A

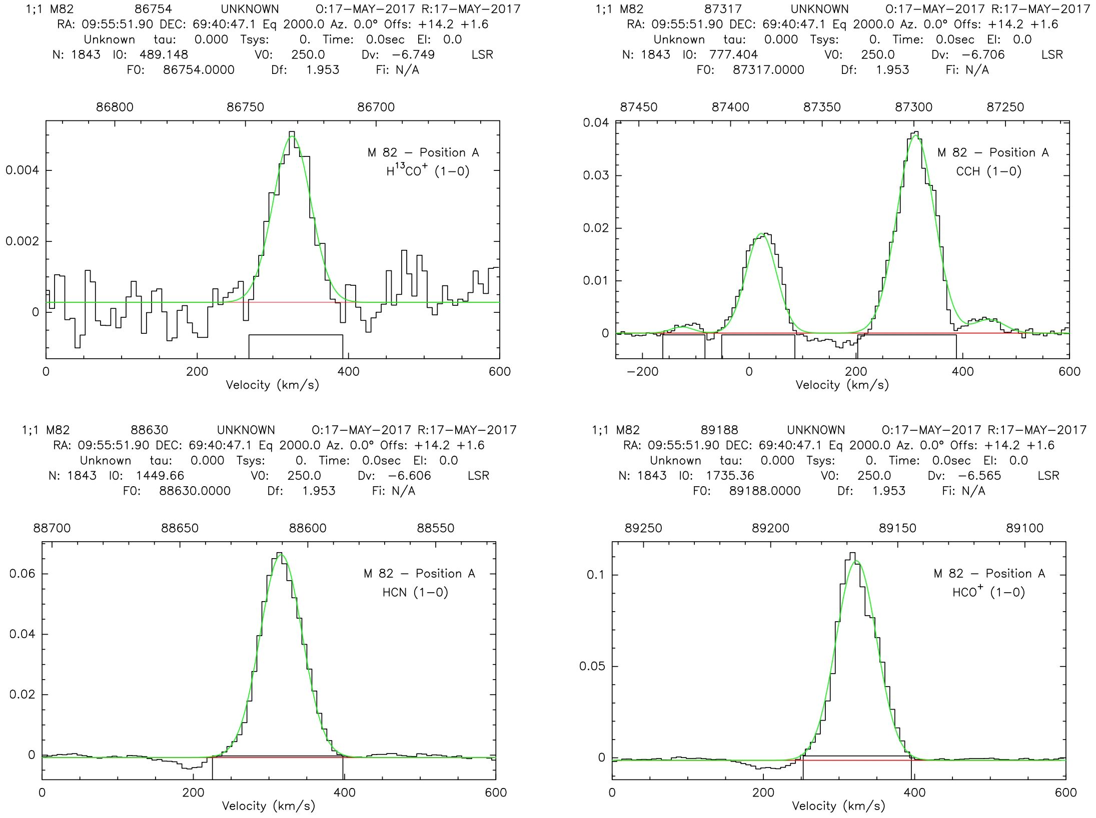

Figure D.1: M 82: Spectra and Gaussian fit of $\mathrm{H^{13}CO^{+}}(1-0)$ at 86.754 GHz, $\mathrm{CCH}(1-0)$ with 4 components at a central frequency of 87.317 GHz, $\mathrm{HCN}(1-0)$ at 88.630 GHz, and $\mathrm{HCO^{+}}(1-0)$ at 89.188 GHz. The top x-axis shows the frequency in MHz and the bottom x-axis shows the velocity in km s^{-1}. The y-axis shows the flux density in Jy. The central frequency is shown in the header.

Figure D.2: M 82: Spectra and Gaussian fit of $\mathrm{HNC}(1-0)$ at 90.663 GHz, $\mathrm{HC_3N}(10-9)$ at 90.979 GHz, $\mathrm{H41}\alpha$ at 92.034 GHz, $\mathrm{N_2H^+}(1-0)$ at 93.171 GHz, $\mathrm{C^{34}S}(2-1)$ at 96.413 GHz, $\mathrm{CS}(2-1)$ at 97.981 GHz, and $\mathrm{H40}\alpha$ at 99.023 GHz, $\mathrm{SO}(2-3)$ at 99.299 GHz. The axes are the same as in Fig. D.1.1

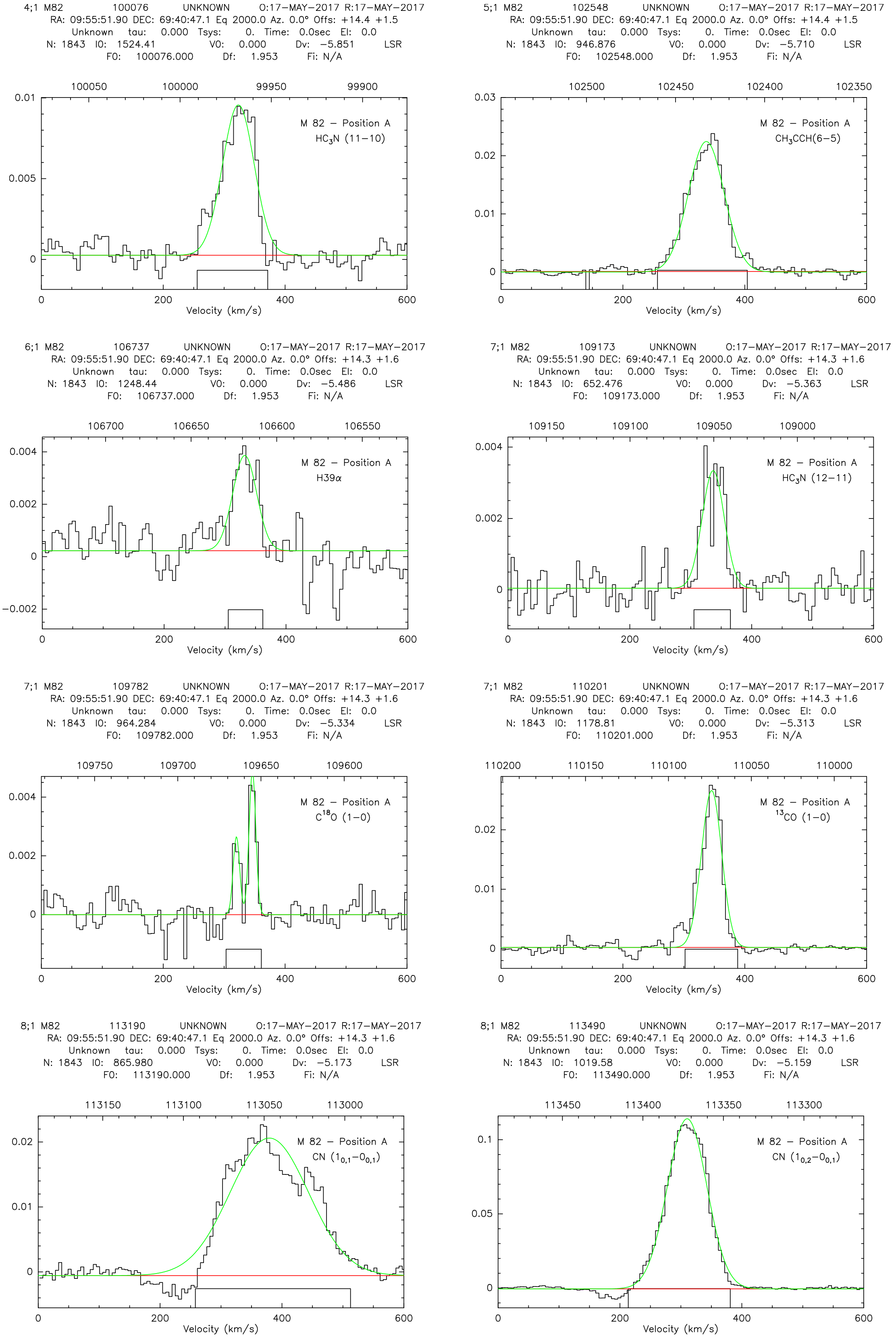

Figure D.3: M 82: Spectra and Gaussian fit of $\mathrm{HC_3N}(11-10)$ at 100.076 GHz, $\mathrm{CH_3CCH}(6-5)$at 102.548 GHz, $\mathrm{H39}\alpha$ at 106.737 GHz, $\mathrm{HC_3N}(12-11)$at 109.173 GHz, $\mathrm{C^{18}O}(1-0)$ with 2 components at a central frequency of 109.782 GHz, $^{13}\mathrm{CO}(1-0)$at 110.201 GHz, $\mathrm{CN}(1_{0,1}-0_{0,1})$ at 113.190 GHz, $\mathrm{CN}(1_{0,2}-0_{0,1})$ at 113.490 GHz. The axes are the same as in Fig. *D*.1.1

D.1.2 Position B

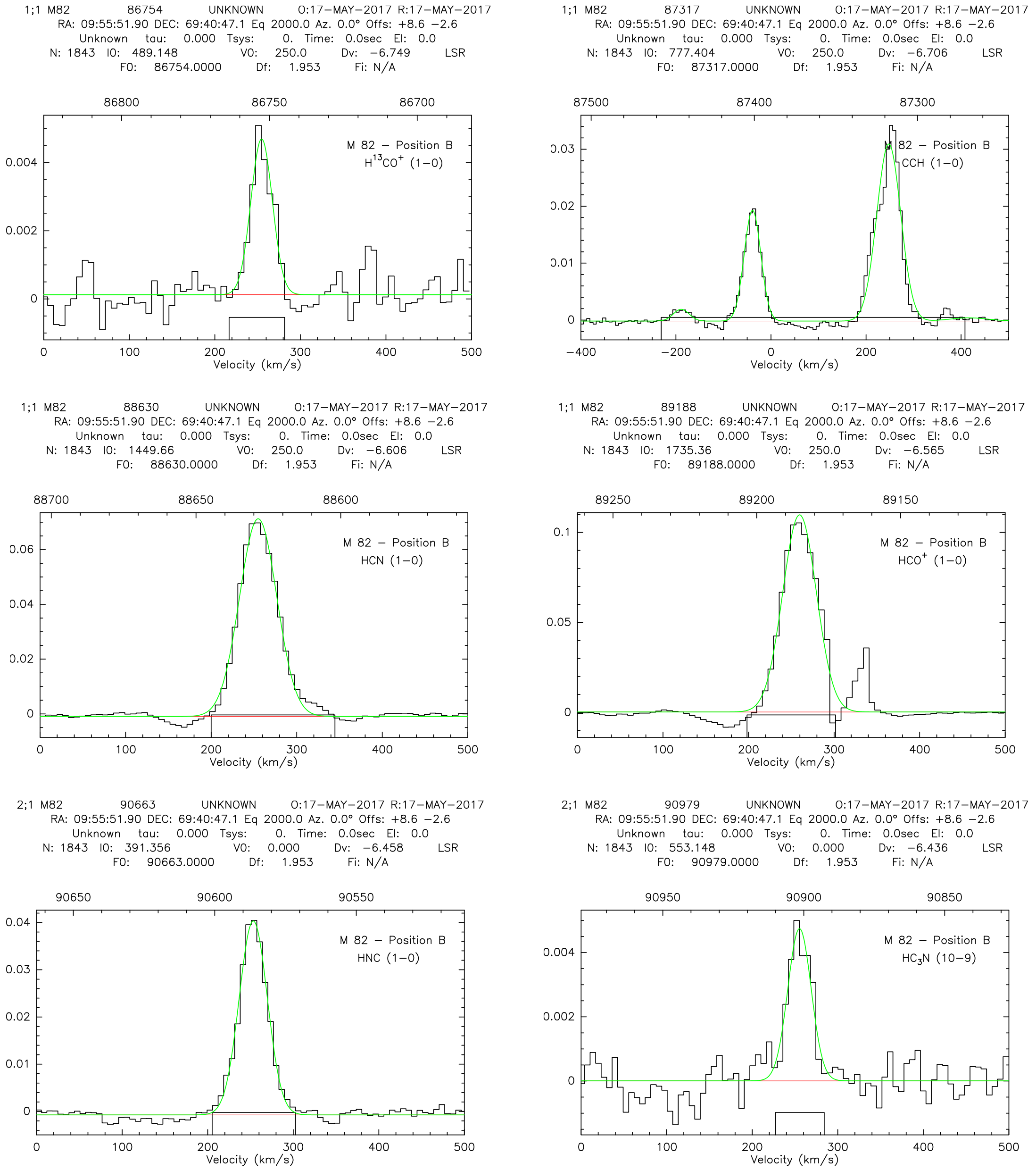

Figure D.4: M 82: Spectra and Gaussian fit of $\mathrm{H^{13}CO^{+}}(1-0)$ at 86.754 GHz, $\mathrm{CCH}(1-0)$ with 4 components at a central frequency of 87.317 GHz, $\mathrm{HCN}(1-0)$ at 88.630 GHz, $\mathrm{HCO^{+}}(1-0)$ at 89.188 GHz, $\mathrm{HNC}(1-0)$ at 90.663 GHz, and $\mathrm{HC_3N}(10-9)$ at 90.979 GHz. The axes are the same as in Fig. *D*.1.1

Figure D.5: M 82: Spectra and Gaussian fit of $\mathrm{H41}\alpha$ at 92.034 GHz, $\mathrm{N_2H^+(1-0)}$ at 93.171 GHz, $\mathrm{C^{34}S(2-1)}$ at 96.413 GHz, $\mathrm{CS(2-1)}$ at 97.980 GHz, $\mathrm{H40}\alpha$ at 99.023 GHz, $\mathrm{SO(2-3)}$ at 99.299 GHz, $\mathrm{HC_3N(11-10)}$ at 100.076 GHz, and $\mathrm{CH_3CCH(6-5)}$ at 102.548 GHz. The axes are the same as in Fig. *D*.1.1

Figure D.6: M 82: Spectra and Gaussian fit of H39α at 106.737 GHz, $HC_3N(12-11)$ at 109.173 GHz, $C^{18}O(1-0)$ at a central frequency of 109.782 GHz, $^{13}CO(1-0)$ at 110.201 GHz, $C^{17}O(1-0)$ at 112.359 GHz, $CN(1_{0,1}-0_{0,1})$ at 113.190 GHz, and $CN(1_{0,2}-0_{0,1})$ at 113.490 GHz. The axes are the same as in Fig. *D*.1.1

D.1.3 Position C

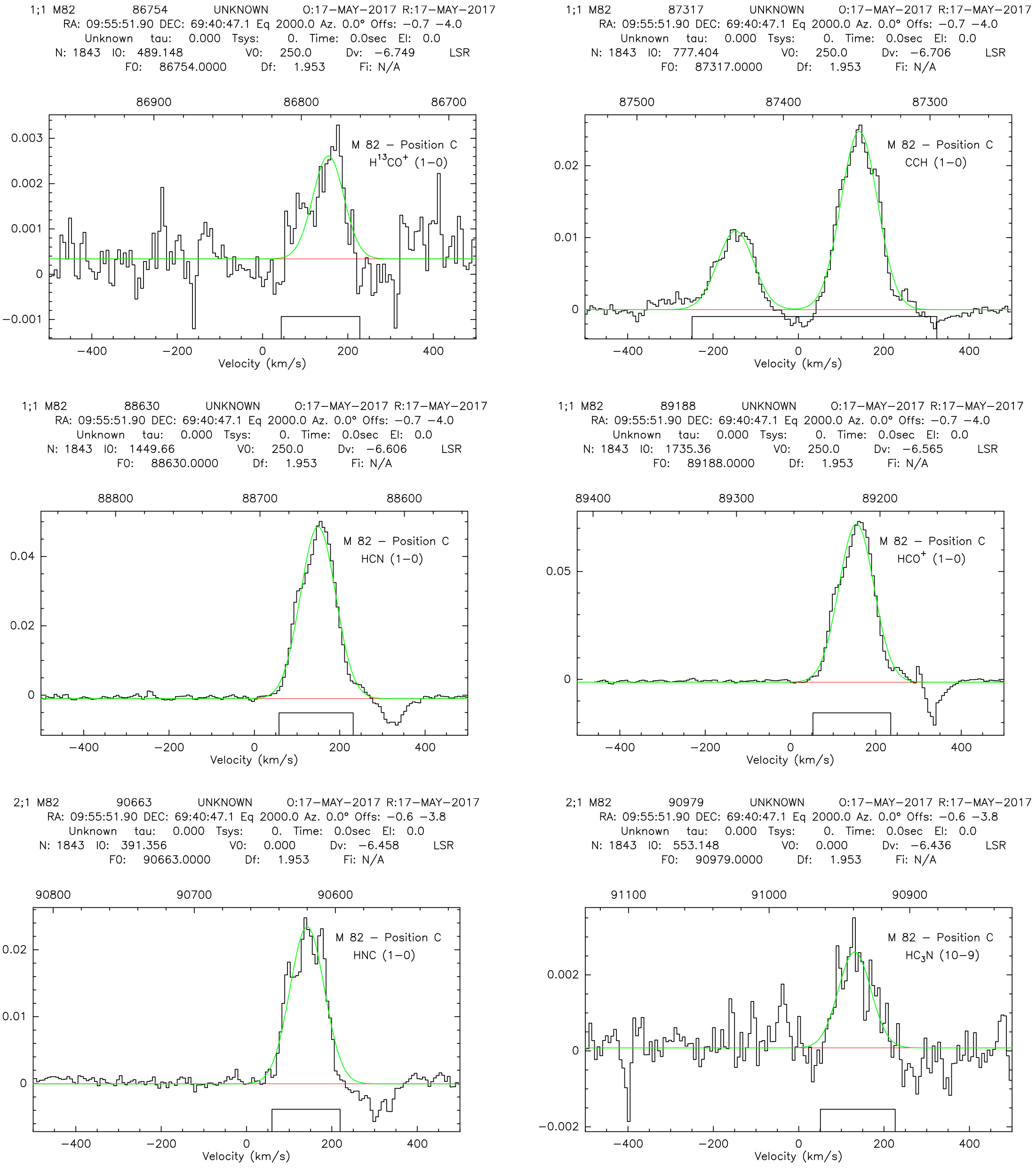

Figure D.7: M 82: Spectra and Gaussian fit of $\mathrm{H^{13}CO^{+}(1-0)}$ at 86.754 GHz, $\mathrm{CCH(1-0)}$ with 2 components at a central frequency of 87.317 GHz, $\mathrm{HCN(1-0)}$ at 88.630 GHz, $\mathrm{HCO^{+}(1-0)}$ at 89.188 GHz, $\mathrm{HNC(1-0)}$ at 90.663 GHz, and $\mathrm{HC_3N(10-9)}$ at 90.979 GHz. The axes are the same as in Fig. *D*.1.1

Figure D.8: M 82: Spectra and Gaussian fit of H41α at 92.034 GHz, $N_2H^+(1-0)$ at 93.171 GHz, $C^{34}S(2-1)$ at 96.413 GHz, $CS(2-1)$ with 2 components at a central frequency of 97.980 GHz, H40α at 99.023 GHz, $SO(2-3)$ at 99.299 GHz, $HC_3N(11-10)$ at 100.076 GHz, and $CH_3CCH(6-5)$ at 102.548 GHz. The axes are the same as in Fig. *D*.1.1

Figure D.9: M 82: Spectra and Gaussian fit of H39α at 106.737 GHz, $HC_3N(12-11)$ at 109.173 GHz, $C^{18}O(1-0)$ at 109.782 GHz, $^{13}CO(1-0)$ at 110.201 GHz, $CN(1_{0,1}-0_{0,1})$ at 113.190 GHz, and $CN(1_{0,2}-0_{0,1})$ with two components at a central frequency of 113.490 GHz. The axes are the same as in Fig. D.1.1

D.1.4 Position D

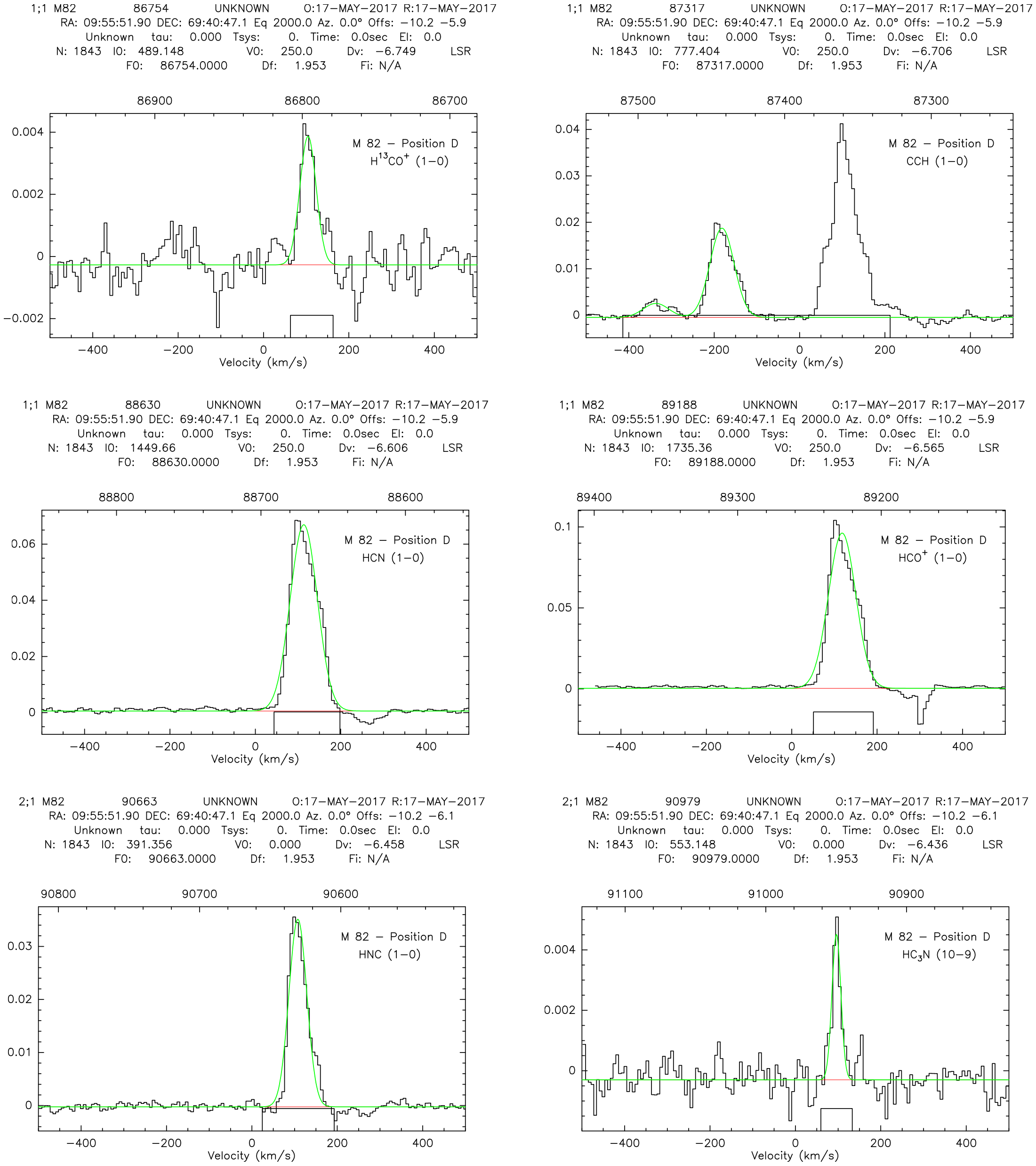

Figure D.10: M 82: Spectra and Gaussian fit of $\mathrm{H^{13}CO^{+}(1-0)}$ at 86.754 GHz, $\mathrm{CCH(1-0)}$ with 3 components at a central frequency of 87.317 GHz, $\mathrm{HCN(1-0)}$ at 88.630 GHz, $\mathrm{HCO^{+}(1-0)}$ at 89.188 GHz, $\mathrm{HNC(1-0)}$ at 90.663 GHz, and $\mathrm{HC_3N(10-9)}$ at 90.979 GHz. The axes are the same as in Fig. *D*.1.1

Figure D.11: M 82: Spectra and Gaussian fit of H41α at 92.034 GHz, $\mathrm{N_2H^+}(1-0)$ at 93.171 GHz, $\mathrm{C^{34}S}(2-1)$ 96.413 GHz, $\mathrm{CS}(2-1)$ at 97.981 GHz, H40α at 99.023 GHz, $\mathrm{SO}(2-3)$ at 99.299 GHz, $\mathrm{HC_3N}(11-10)$ at 100.076 GHz, and $\mathrm{CH_3CCH}(6-5)$ at 102.548 GHz. The axes are the same as in Fig. D.1.1

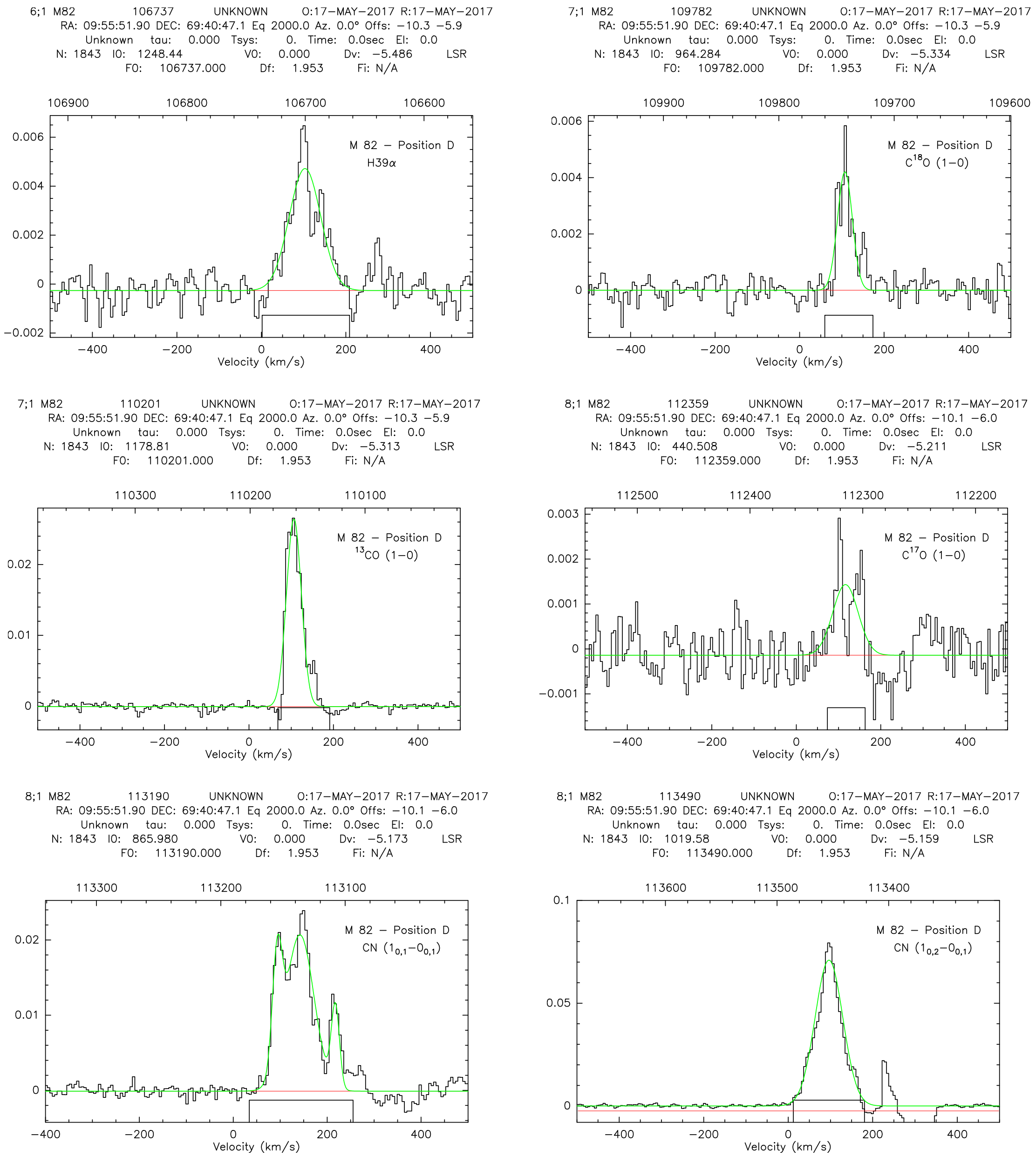

Figure D.12: M 82: Spectra and Gaussian fit of H39α at 106.737 GHz, $\mathrm{C}^{18}\mathrm{O}(1-0)$ at 109.782 GHz, $^{13}\mathrm{CO}(1-0)$ at 110.201 GHz, $\mathrm{C}^{17}\mathrm{O}(1-0)$ at 112.359 GHz, $\mathrm{CN}(1_{0,1}-0_{0,1})$ with 3 components at a central frequency of 113.190 GHz, and $\mathrm{CN}(1_{0,2}-0_{0,1})$ at 113.490 GHz. The axes are the same as in Fig. D.1.1

D.2 IC 342

D.2.1 Position A

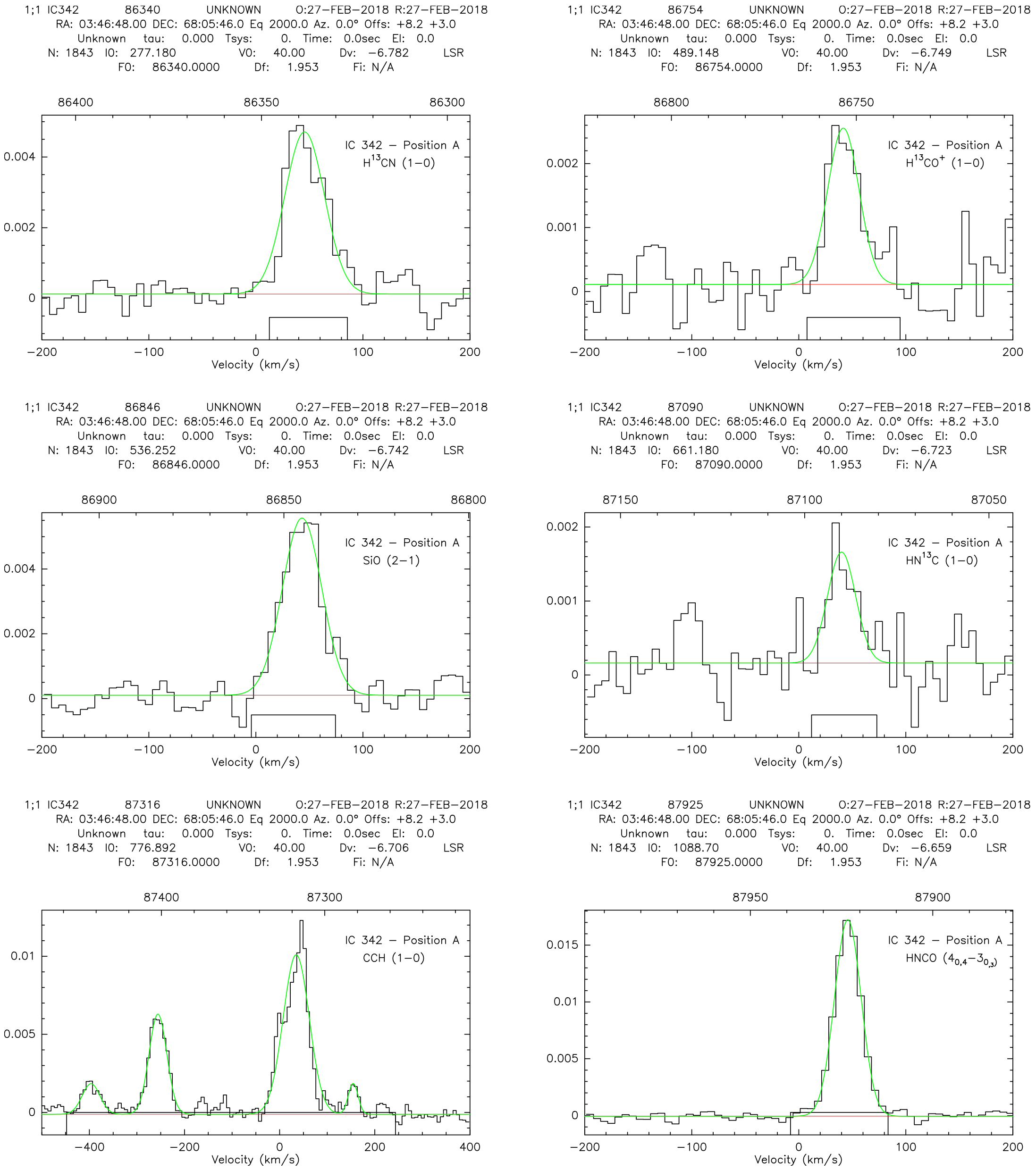

Figure D.13: IC 342: Spectra and Gaussian fit of $\mathrm{H^{13}CN}(1-0)$ at 86.340 GHz, $\mathrm{H^{13}CO^{+}}(1-0)$ at 86.754 GHz, $\mathrm{SiO}(2-1)$ at 86.846 GHz, $\mathrm{HN^{13}C}(1-0)$ at 87.090 GHz, $\mathrm{C_2H}(1-0)$ with 4 components at a central frequency of 87.317 GHz, and $\mathrm{HNCO}(4_{0,4}-3_{0,3})$ at 87.925 GHz. The axes are the same as in Fig. $D.1.1$

Figure D.14: IC 342: Spectra and Gaussian fit of $\mathrm{HCN}(1-0)$ at 88.631 GHz, $\mathrm{HCO}^{+}(1-0)$ at 89.188 GHz, $\mathrm{HNC}(1-0)$ at 90.663 GHz, $\mathrm{HC_3N}(10-9)$ at 90.978 GHz, $\mathrm{CH_3CN}(5_k-4_k)$ at 91.987 GHz, $\mathrm{N_2H}^{+}(1-0)$ at 90.978 GHz, $\mathrm{C^{34}S}(2-1)$ at 96.413 GHz, and $\mathrm{CH_3OH}(2_k-1_k)$ at 96.744 GHz. The axes are the same as in Fig. D.1.1

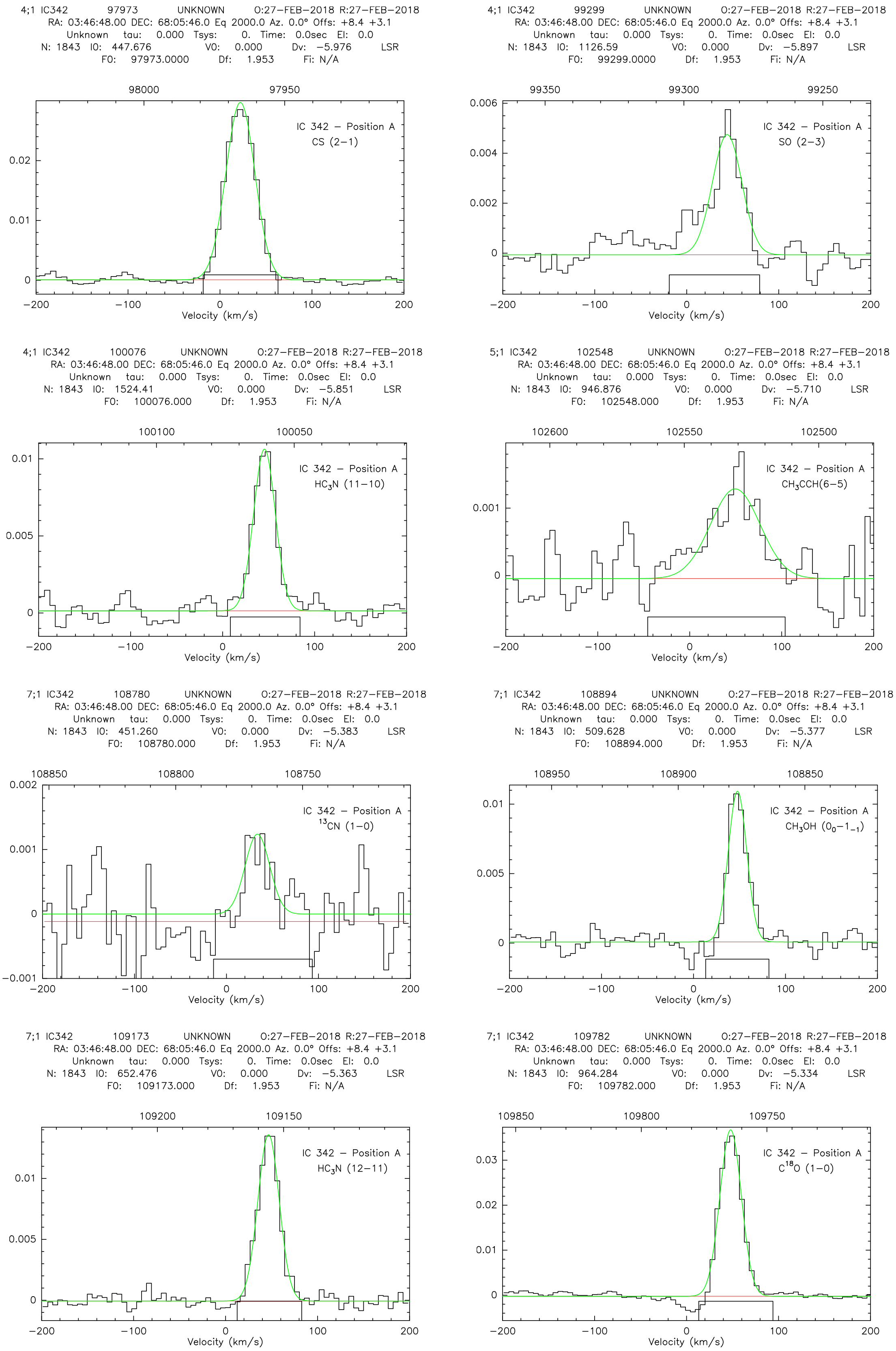

Figure D.15: IC 342: Spectra and Gaussian fit of $\mathrm{CS}(2-1)$ at 97.973 GHz, $\mathrm{SO}(2-3)$ at 99.299 GHz, $\mathrm{HC_3N}(11-10)$ at 100.076 GHz, $\mathrm{CH_3CCH}(6_k-5_k)$ at 102.548 GHz, $^{13}\mathrm{CN}(11-10)$ at 108.780 GHz, $\mathrm{CH_3OH}(0_0-1_{-1})$ at 108.894 GHz, $\mathrm{HC_3N}(12-11)$ at 109.173 GHz, and $\mathrm{C^{18}O}(1-0)$ at 109.782 GHz. The axes are the same as in Fig. *D*.1.1

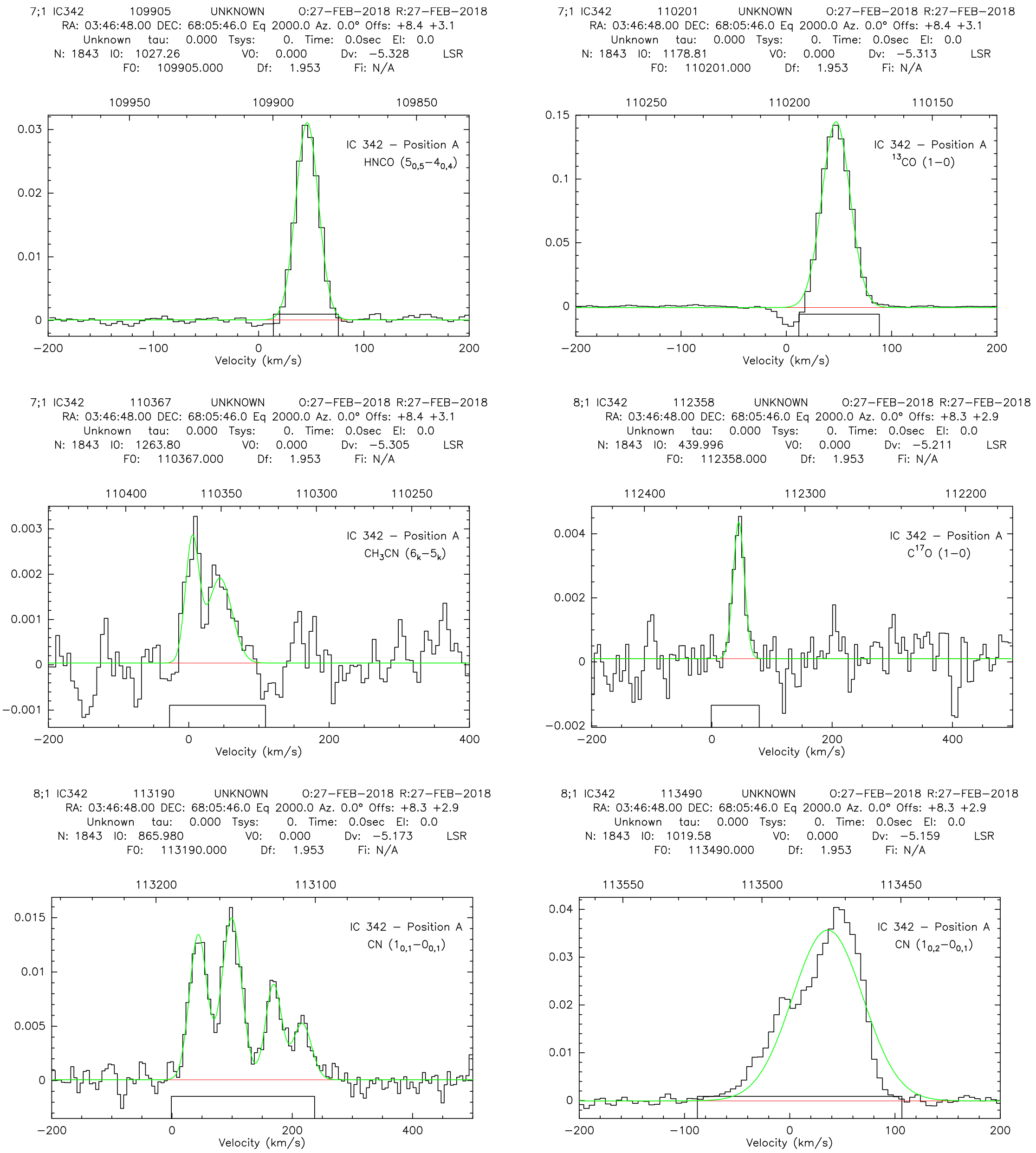

Figure D.16: IC 342: Spectra and Gaussian fit of $\mathrm{HNCO}(5_{0,5} - 4_{0,4})$ at 109.905 GHz, $^{13}\mathrm{CO}(1-0)$ at 110.201 GHz, $\mathrm{CH_3CN}(6_k - 5_k)$ at 110.384 GHz, $\mathrm{C}^{17}\mathrm{O}(1-0)$ at 112.358 GHz, $\mathrm{CN}(1_{0,1} - 0_{0,1})$ with 4 components at a central frequency of 113.190 GHz, and $\mathrm{CN}(1_{0,2} - 0_{0,1})$ at 113.490 GHz. The axes are the same as in Fig. D.1.1

D.2.2 Position B

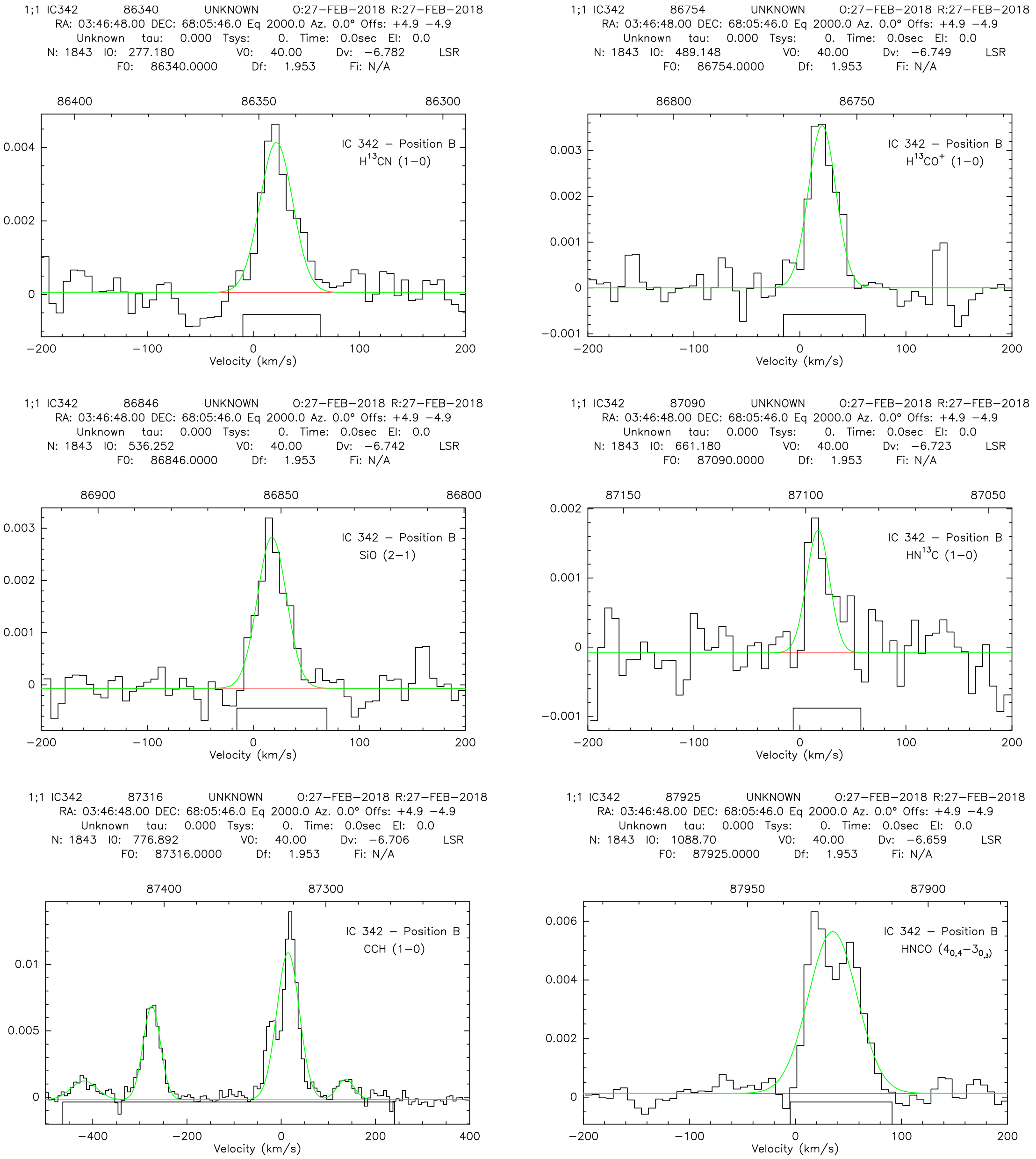

Figure D.17: IC 342: Spectra and Gaussian fit of $\mathrm{H^{13}CN}(1-0)$ at 86.340 GHz, $\mathrm{H^{13}CO^{+}}(1-0)$ at 86.754 GHz, $\mathrm{SiO}(2-1)$ at 86.846 GHz, $\mathrm{HN^{13}C}(1-0)$ at 87.090 GHz, $\mathrm{C_2H}(1-0)$ with 4 components at a central frequency of 87.317 GHz, and $\mathrm{HNCO}(4_{0,4}-3_{0,3})$ at 87.925 GHz. The axes are the same as in Fig. *D*.1.1

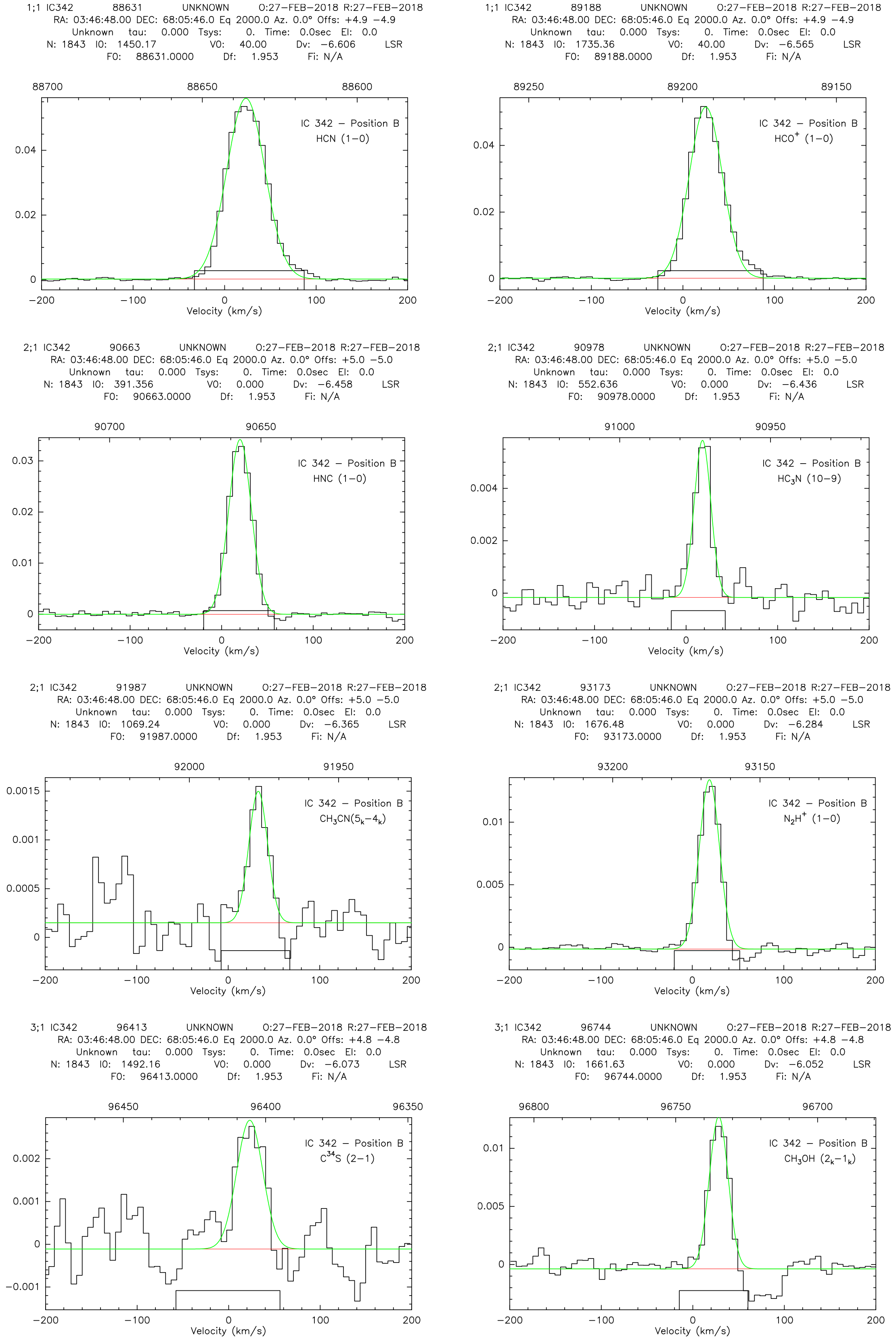

Figure D.18: IC 342: Spectra and Gaussian fit of $\mathrm{HCN}(1-0)$ at 88.631 GHz, $\mathrm{HCO}^{+}(1-0)$ at 89.188 GHz, $\mathrm{HNC}(1-0)$ at 90.663 GHz, $\mathrm{HC_3N}(10-9)$ at 90.978 GHz, $\mathrm{CH_3CN}(5_k-4_k)$ at 91.987 GHz, $\mathrm{N_2H}^{+}(1-0)$ at 90.978 GHz, $\mathrm{C^{34}S}(2-1)$ at 96.413 GHz, and $\mathrm{CH_3OH}(2_k-1_k)$ at 96.744 GHz. The axes are the same as in Fig. *D*.1.1

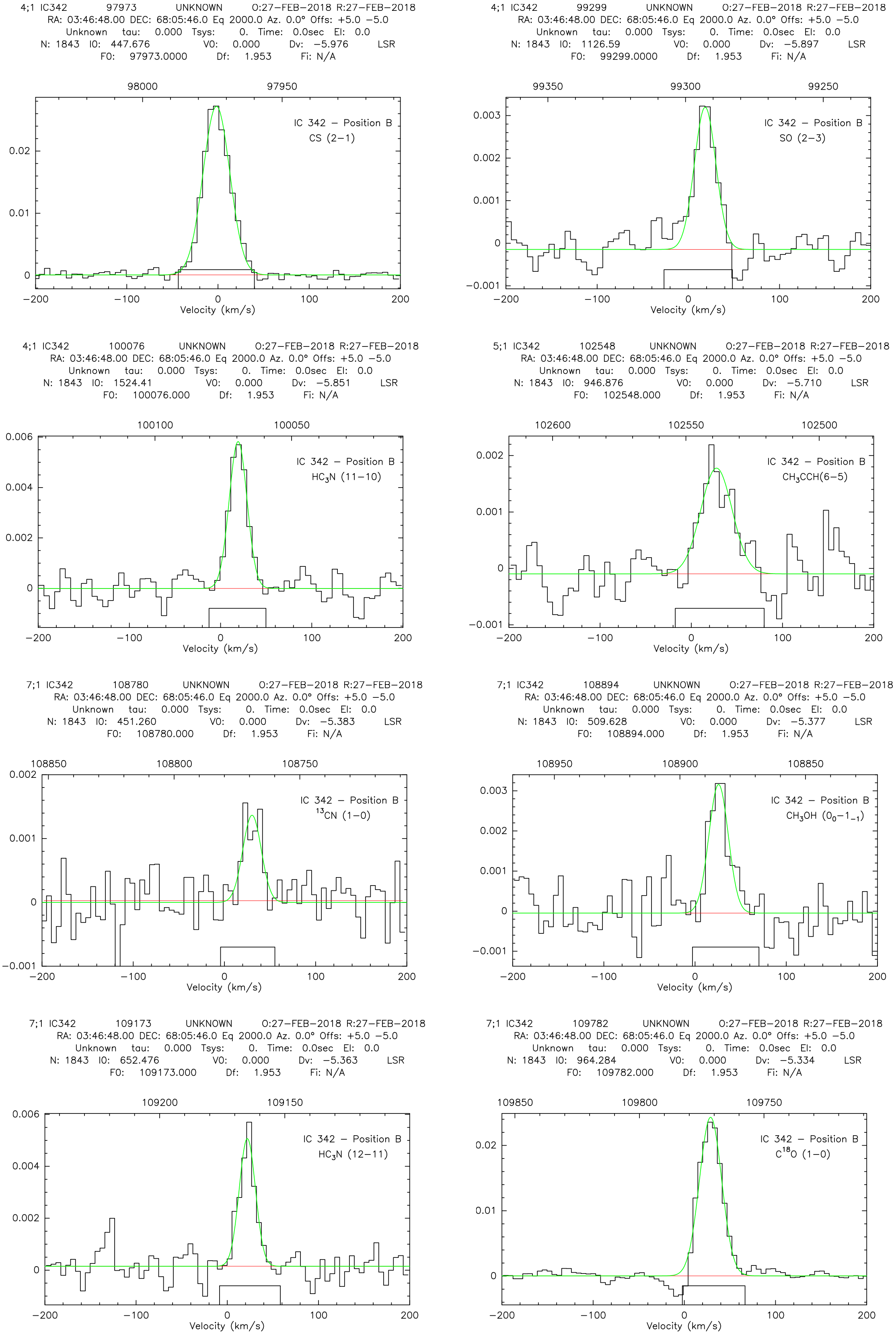

Figure D.19: IC 342: Spectra and Gaussian fit of $\mathrm{CS}(2-1)$ at 97.973 GHz, $\mathrm{SO}(2-3)$ at 99.299 GHz, $\mathrm{HC_3N}(11-10)$ at 100.076 GHz, $\mathrm{CH_3CCH}(6_k-5_k)$ at 102.548 GHz, $^{13}\mathrm{CN}(11-10)$ at 108.780 GHz, $\mathrm{CH_3OH}(0_0-1_{-1})$ at 108.894 GHz, $\mathrm{HC_3N}(12-11)$ at 109.173 GHz, and $\mathrm{C^{18}O}(1-0)$ at 109.782 GHz. The axes are the same as in Fig. D.1.1

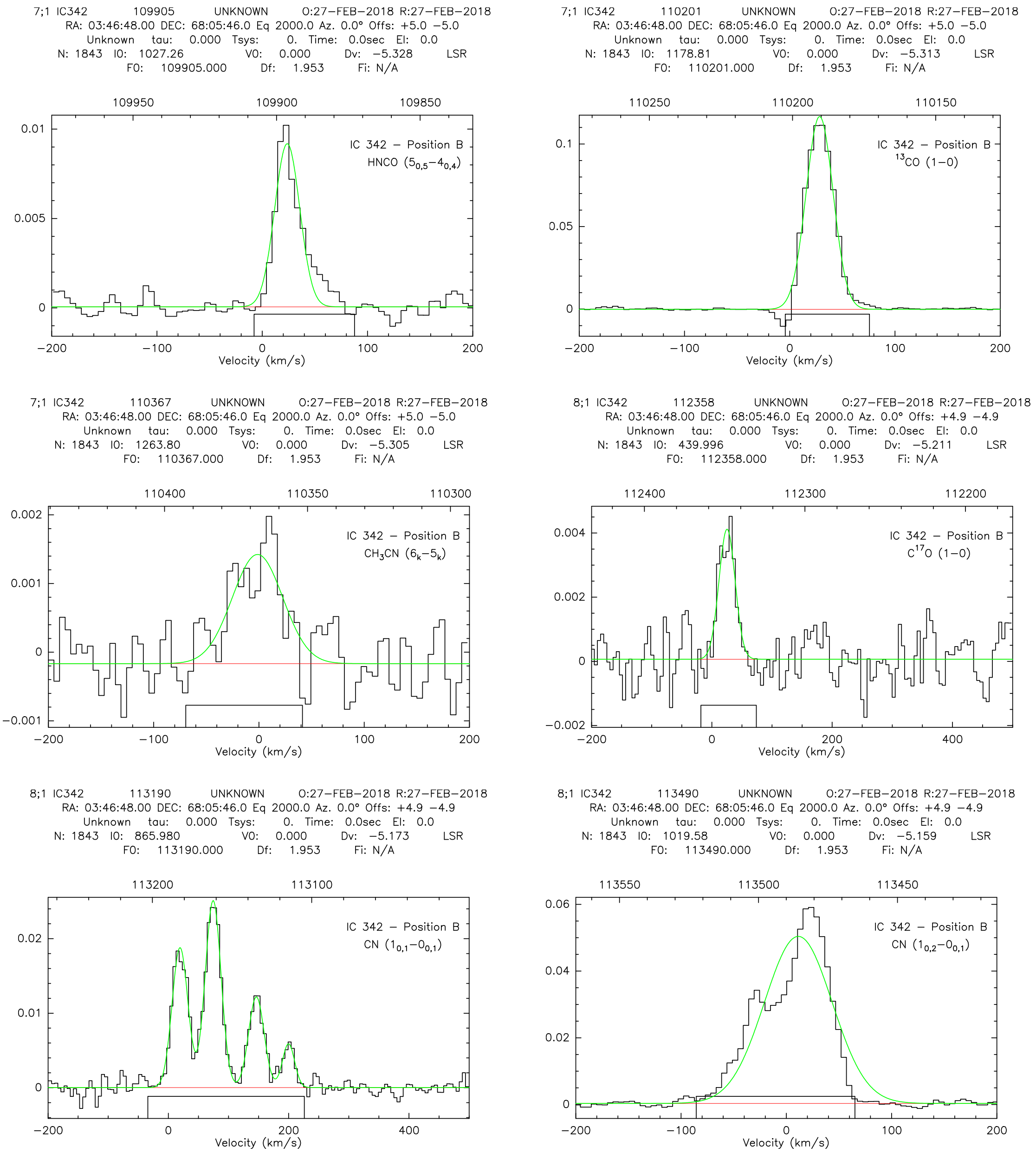

Figure D.20: IC 342: Spectra and Gaussian fit of $\mathrm{HNCO}(5_{0,5} - 4_{0,4})$ at 109.905 GHz, $^{13}\mathrm{CO}(1-0)$ at 110.201 GHz, $\mathrm{CH_3CN}(6_k - 5_k)$ at 110.384 GHz, $\mathrm{C^{17}O}(1-0)$ at 112.358 GHz, $\mathrm{CN}(1_{0,1} - 0_{0,1})$ with 4 components at a central frequency of 113.190 GHz, and $\mathrm{CN}(1_{0,2} - 0_{0,1})$ at 113.490 GHz. The axes are the same as in Fig. D.1.1

D.2.3 Position C

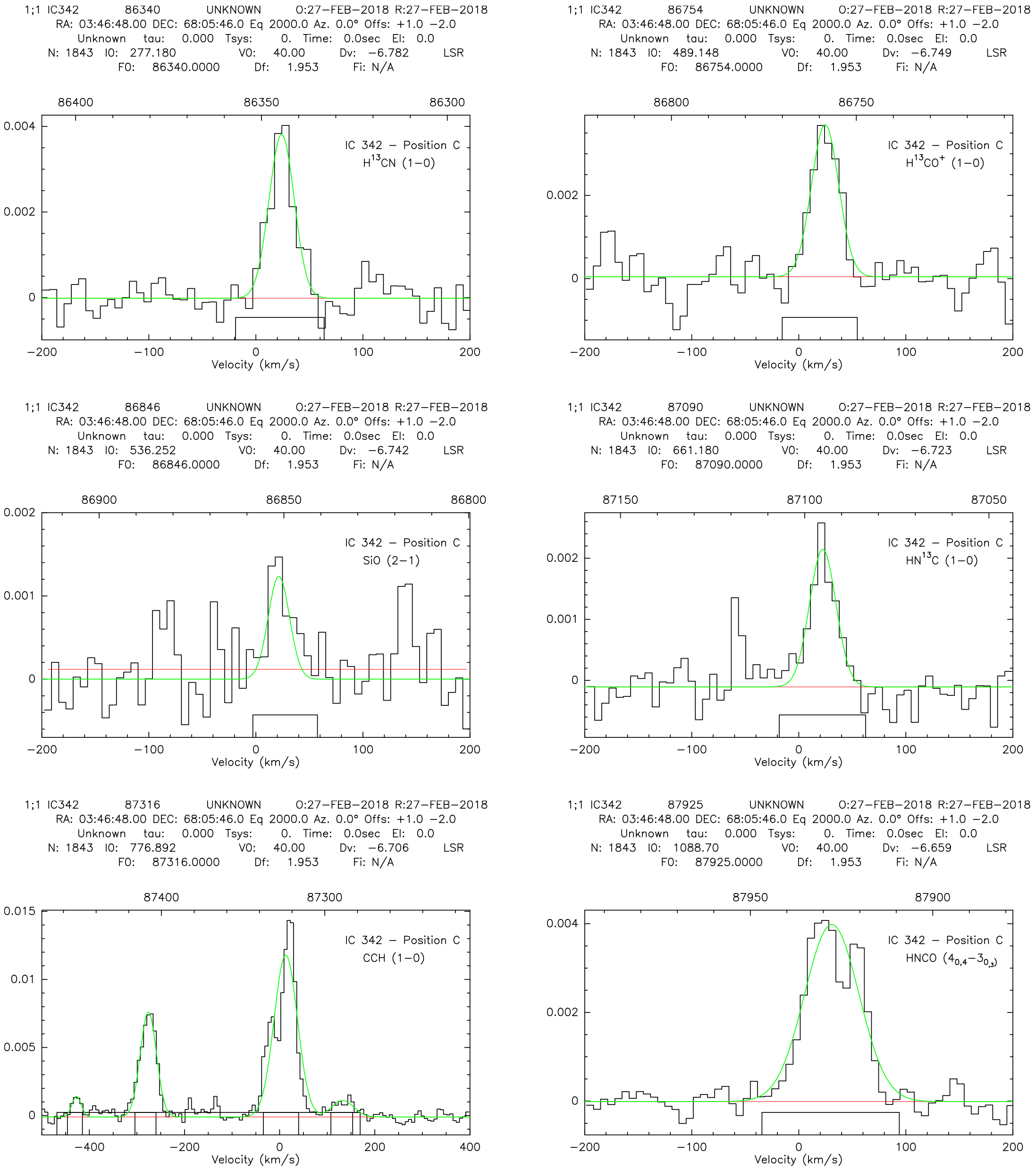

Figure D.21: IC 342: Spectra and Gaussian fit of $\mathrm{H^{13}CN}(1-0)$ at 86.340 GHz, $\mathrm{H^{13}CO^{+}}(1-0)$ at 86.754 GHz, $\mathrm{SiO}(2-1)$ at 86.846 GHz, $\mathrm{HN^{13}C}(1-0)$ at 87.090 GHz, $\mathrm{C_2H}(1-0)$ with 4 components at a central frequency of 87.317 GHz, and $\mathrm{HNCO}(4_{0,4}-3_{0,3})$ at 87.925 GHz. The axes are the same as in Fig. *D*.1.1

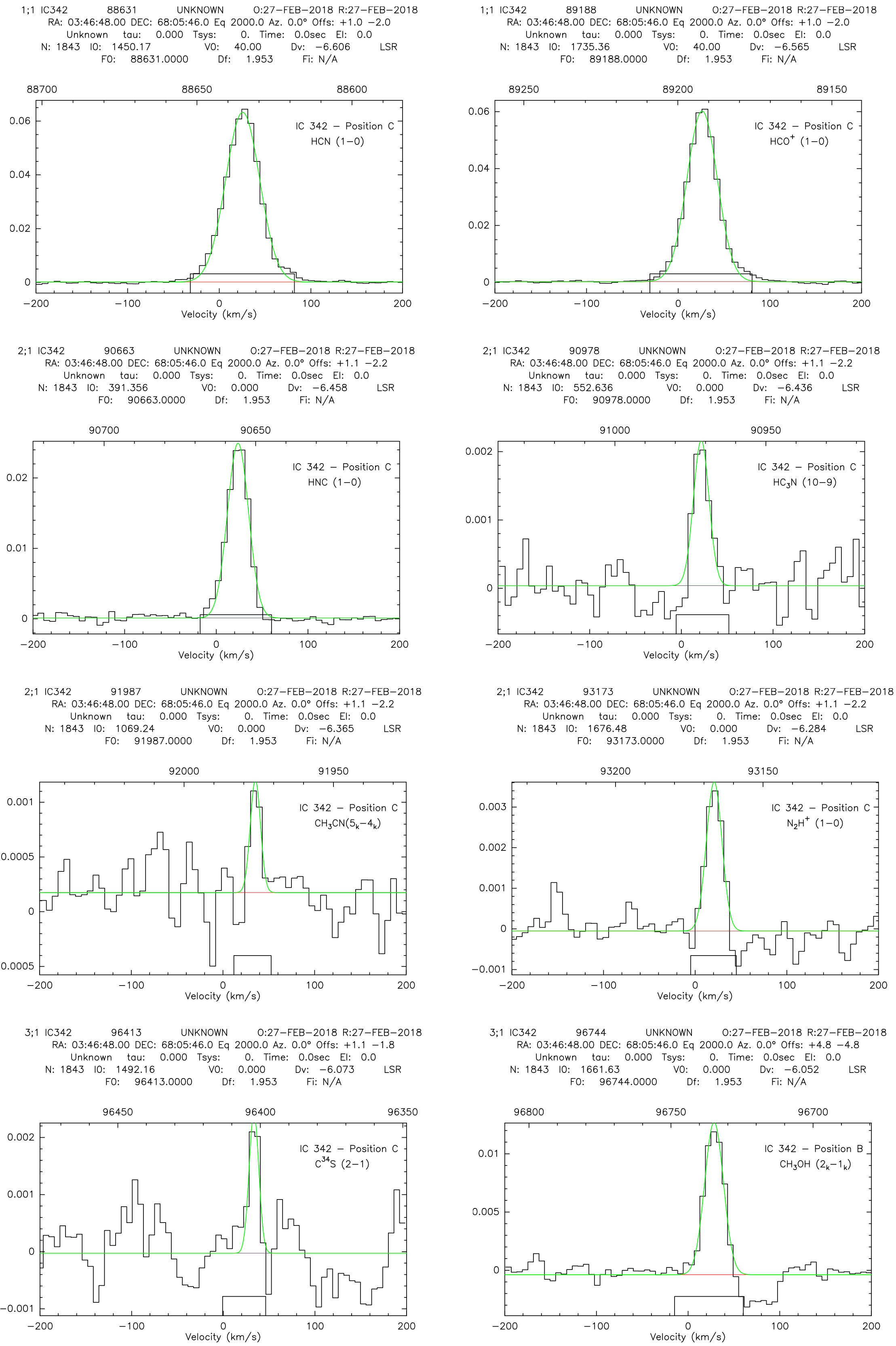

```
1;1 IC342        88631        UNKNOWN        0:27-FEB-2018 R:27-FEB-2018
RA: 03:46:48.00 DEC: 68:05:46.0 Eq 2000.0 Az. 0.0° Offs: +1.0 -2.0
Unknown    tau:   0.000  Tsys:      0.  Time:  0.0sec  El:  0.0
N: 1843  I0:  1450.17         V0:   40.00       Dv:  -6.606       LSR
F0:    88631.0000       Df:    1.953       Fi: N/A

1;1 IC342        89188        UNKNOWN        0:27-FEB-2018 R:27-FEB-2018
RA: 03:46:48.00 DEC: 68:05:46.0 Eq 2000.0 Az. 0.0° Offs: +1.0 -2.0
Unknown    tau:   0.000  Tsys:      0.  Time:  0.0sec  El:  0.0
N: 1843  I0:  1735.36         V0:   40.00       Dv:  -6.565       LSR
F0:    89188.0000       Df:    1.953       Fi: N/A

2;1 IC342        90663        UNKNOWN        0:27-FEB-2018 R:27-FEB-2018
RA: 03:46:48.00 DEC: 68:05:46.0 Eq 2000.0 Az. 0.0° Offs: +1.1 -2.2
Unknown    tau:   0.000  Tsys:      0.  Time:  0.0sec  El:  0.0
N: 1843  I0:  391.356         V0:   0.000       Dv:  -6.458       LSR
F0:    90663.0000       Df:    1.953       Fi: N/A

2;1 IC342        90978        UNKNOWN        0:27-FEB-2018 R:27-FEB-2018
RA: 03:46:48.00 DEC: 68:05:46.0 Eq 2000.0 Az. 0.0° Offs: +1.1 -2.2
Unknown    tau:   0.000  Tsys:      0.  Time:  0.0sec  El:  0.0
N: 1843  I0:  552.636         V0:   0.000       Dv:  -6.436       LSR
F0:    90978.0000       Df:    1.953       Fi: N/A

2;1 IC342        91987        UNKNOWN        0:27-FEB-2018 R:27-FEB-2018
RA: 03:46:48.00 DEC: 68:05:46.0 Eq 2000.0 Az. 0.0° Offs: +1.1 -2.2
Unknown    tau:   0.000  Tsys:      0.  Time:  0.0sec  El:  0.0
N: 1843  I0:  1069.24         V0:   0.000       Dv:  -6.365       LSR
F0:    91987.0000       Df:    1.953       Fi: N/A

2;1 IC342        93173        UNKNOWN        0:27-FEB-2018 R:27-FEB-2018
RA: 03:46:48.00 DEC: 68:05:46.0 Eq 2000.0 Az. 0.0° Offs: +1.1 -2.2
Unknown    tau:   0.000  Tsys:      0.  Time:  0.0sec  El:  0.0
N: 1843  I0:  1676.48         V0:   0.000       Dv:  -6.284       LSR
F0:    93173.0000       Df:    1.953       Fi: N/A

3;1 IC342        96413        UNKNOWN        0:27-FEB-2018 R:27-FEB-2018
RA: 03:46:48.00 DEC: 68:05:46.0 Eq 2000.0 Az. 0.0° Offs: +1.1 -1.8
Unknown    tau:   0.000  Tsys:      0.  Time:  0.0sec  El:  0.0
N: 1843  I0:  1492.16         V0:   0.000       Dv:  -6.073       LSR
F0:    96413.0000       Df:    1.953       Fi: N/A

3;1 IC342        96744        UNKNOWN        0:27-FEB-2018 R:27-FEB-2018
RA: 03:46:48.00 DEC: 68:05:46.0 Eq 2000.0 Az. 0.0° Offs: +4.8 -4.8
Unknown    tau:   0.000  Tsys:      0.  Time:  0.0sec  El:  0.0
N: 1843  I0:  1661.63         V0:   0.000       Dv:  -6.052       LSR
F0:    96744.0000       Df:    1.953       Fi: N/A
```

Figure D.22: IC 342: Spectra and Gaussian fit of $\mathrm{HCN}(1-0)$ at 88.631 GHz, $\mathrm{HCO}^+(1-0)$ at 89.188 GHz, $\mathrm{HNC}(1-0)$ at 90.663 GHz, $\mathrm{HC_3N}(10-9)$ at 90.978 GHz, $\mathrm{CH_3CN}(5_k-4_k)$ at 91.987 GHz, $\mathrm{N_2H}^+(1-0)$ at 90.978 GHz, $\mathrm{C^{34}S}(2-1)$ at 96.413 GHz, and $\mathrm{CH_3OH}(2_k-1_k)$ at 96.744 GHz. The axes are the same as in Fig. *D*.1.1

Figure D.23: IC 342: Spectra and Gaussian fit of $\mathrm{CS}(2-1)$ at 97.973 GHz, $\mathrm{SO}(2-3)$ at 99.299 GHz, $\mathrm{HC_3N}(11-10)$ at 100.076 GHz, $\mathrm{CH_3CCH}(6_k-5_k)$ at 102.548 GHz, $^{13}\mathrm{CN}(11-10)$ at 108.780 GHz, $\mathrm{CH_3OH}(0_0-1_{-1})$ at 108.894 GHz, $\mathrm{HC_3N}(12-11)$ at 109.173 GHz, and $\mathrm{C^{18}O}(1-0)$ at 109.782 GHz. The axes are the same as in Fig. *D*.1.1

Figure D.24: IC 342: Spectra and Gaussian fit of $\mathrm{HNCO}(5_{0,5}-4_{0,4})$ at 109.905 GHz, $^{13}\mathrm{CO}(1-0)$ at 110.201 GHz, $\mathrm{CH_3CN}(6_k-5_k)$ at 110.384 GHz, $\mathrm{C^{17}O}(1-0)$ at 112.358 GHz, $\mathrm{CN}(1_{0,1}-0_{0,1})$ with 4 components at a central frequency of 113.190 GHz, and $\mathrm{CN}(1_{0,2}-0_{0,1})$ at 113.490 GHz. The axes are the same as in Fig. *D*.1.1

Nomenclature

ALMA	Atacama Large millimetre/sub-millimetre Array
APEX	Atacama Pathfinder EXperiment
CDMS	Cologne Database for Molecular Spectroscopy
CLASS	Continuum and Line Analysis Single-dish Software
CLIC	Continuum and Line Interferometer Calibration
CMZ	Central Molecular Zone
CR	Cosmic Ray
DLR	Deutsches Zentrum für Luft- und Raumfahrt (German Aerospace Center)
FUV	Far ultra-Violet
FWHM	Full Width Half Maximum
GILDAS	Grenoble Image and Line Data Analysis Software
IRAM	Institut de Radioastronomie Millimétrique
ISM	Interstellar Medium
JPL	Jet Propulsion Laboratory
LTE	Local Thermodynamical Equilibrium
MADCUBA	MAdrid Data CUBe Analysis
MERLIN	Multi-Element Radio-Linked Interferometer Network
Mpc	Megaparsec (Astronomical distance measure)
MW	Milky Way
NASA	National Aeronautics and Space Administration
NOEMA	NOrthern Extended Millimetre Array
PCA	Principle Component Analysis
PdBI	Plateau de Bure Interferometre

PDRs	Photo-Dissociation Regions
SFR	Star Formation Rate
SLAIM	Spectral Line Atlas of Interstellar Molecules
SLIM	Spectral Line and Identification and Modelling
SN	Supernova
SOFIA	Stratospheric Observatory for Infrared Astronomy
SPH	Smoothed Particles Hydrodynamics
ULX	Ultra-Luminous X-ray Source
VLA	Very Large Array

List of Figures

List of Tables